Investigating the association between Lamin B1 and genomic instability in B cells

Filip Filipsky

Thesis submitted for the degree of
Doctor of Philosophy
at the Barts and the London School of Medicine and Dentistry, Queen Mary University of London

Centre for Haemato-Oncology
John Vane Science Centre
Barts Cancer Institute
Queen Mary University of London EC1M 6BQ
November 2022

Statement of Originality

I, Filip Filipsky, confirm that the research included within this thesis is my own work or that where it has been carried out in collaboration with, or supported by others, that this is duly acknowledged below, and my contribution indicated. Previously published material is also acknowledged below.

I attest that I have exercised reasonable care to ensure that the work is original and does not to the best of my knowledge break any UK law, infringe any third party's copyright or other Intellectual Property Right, or contain any confidential material.

I accept that the College has the right to use plagiarism detection software to check the electronic version of the thesis.

I confirm that this thesis has not been previously submitted for the award of a degree by this or any other university.

The copyright of this thesis rests with the author and no quotation from it or information derived from it may be published without the prior written consent of the author.

Signature: Filip Filipsky

Date: 16/11/2022

Funding

The work in the thesis was supported by Barts Cancer Institute, Queen Mary University of London and the following funding bodies:

- Key Kendal Leukaemia Fund
- Blood Cancer UK Lamin B1-mediated genomic instability in leukaemia and lymphoma

Presentations

The work was presented at the following events:

1. 5th TRR81 Symposium on "**Chromatin Changes in Differentiation and Malignancies"**, Bad Nauheim, Germany 2019

   Poster Presentation: **"Reduced Lamin B1 incorporation leads to increased genomic instability and proliferation in B cell lymphoma"**

2. PhD day – Barts Cancer Institute, QMUL 2020

   Poster presentation: "**Investigating the role of Lamin B1 in genomic instability in normal and malignant B cells"**

3. London PhD Cancer Network Conference 2021

   Oral presentation **"Nuclear lamina: Emerging protector of the genome"**

4. PhD day – Barts Cancer Institute, QMUL 2021

   Poster Presentation: **Nuclear lamina: "Emerging protector of the genome"**

5. Cambridge Lymphoma Symposium 2022

   Poster Presentation: **Nuclear lamina: "Emerging protector of the genome"**

Publications

Chapman K[*], Filipsky F[*], Peschke N, Gelléri M, Weinhardt V, Braun A, Hausmann M and Cremer C. (2022) **A comprehensive method to study the DNA's association with lamin and chromatin compaction in intact cell nuclei at super resolution**. Nanoscale. [Manuscript accepted] *joint first authors.

Filipsky F, Sallan M, Chapman K, Bloehdorn J, Wang J, Hausmann M, Cremer C, Gribben J, Klymenko T, Braun A. (2022) **Lamin B1 prevents genomic instability in normal and malignant B cells.** [Manuscript submitted]

Collaborations and Contributions

Data and results presented in this work were only possible with the help of our colleagues, collaborators, and staff at the Queen Mary University.

- Dr Marta Crespi Sallan has contributed to *in vitro* assays in Chapter 3, including immunofluorescence optimization, *in vivo work* in Chapter 5 by performing mouse genotyping and maintaining the mouse colony, samples processing, and optimization of flow cytometry protocol.
- Dr Findley Copley have helped with bioinformatics analysis using High Performance Computing for RNA-sequencing and sBLISS analysis.
- Dr. Oscar Maiques provided the optimised protocol for immunohistochemistry staining.
- Dr. Andrew Clear provided human DLBCL tissue microarrays for immunohistochemistry staining in Chapter 8.
- Dr. Alex Wang has performed whole-exome sequencing analysis, including processing of raw FASTQ files, and calling of single nucleotide variants in Chapter 3.
- Dr. Johannes Bloehdorn has performed analysis of GEP in CLL patients shown in Figure 1.3.5.
- Katarina Chapman and colleagues from Prof. Christoph's Cremer's and Prof. Michael Hausmann's lab has generated super-resolution microscopy imaging and performed the post-processing image analysis in Chapter 4.

Acknowledgements

I would like to firstly express my gratitude to my great friend and colleague Marta who has been my constant support over the four years. Marta's continual inflow of encouragement, motivation, ideas, as well as constructive criticism, have helped to further grow as a scientist and a colleague. I cannot thank you enough for teaching me various laboratory techniques, critically analysing generated data, helping me with complex experimental protocols, and taking care of the mouse colony. You shared your knowledge and past experiences, which has made this journey a great experience.

I appreciate everyone from the Haemato-Oncology department, flow cytometry facility, microscopy, and animal facilities at the Barts Cancer Institute. Many thanks to my former colleagues from the department, including Quentin, Annika, Henry, Fin, Erwin who helped me with data analysis and supported me outside of the laboratory environment. I would like to thank our collaborators Dr. Tanya Klymenko, Dr. Jun Wang, Dr. Johannes Bloehdorn, and Katarina Chapman, Prof. Michael Hausman, and Prof. Cristopher Cremer. Also, I would like to thank my friends and family who always encouraged me and supported me throughout this journey. Further, I would like to thank Olivia who stood by my side and continuously supported me during the ups and downs.

Lastly, I would like to thank my supervisor, Dr. Andrejs Braun for the opportunity to carry out this research in his lab and giving me the independence to implement my ideas into this project.

Abstract

Lamin B1 is a fundamental component of the nuclear meshwork, which regulates diverse cellular processes, including the stabilisation of the nucleus, chromatin organization, and gene regulation. More recent studies revealed that Lamin B1 is involved in the regulation of DNA damage repair and mutagenesis. In B cells, Lamin B1 epigenetically controls somatic hypermutagenesis in the immunoglobulin variable gene (IgV). Furthermore, decreased Lamin B1 is associated with a genomic instability signature and inferior survival of chronic lymphocytic leukaemia (CLL) patients. Despite the recent findings, the role of Lamin B1 in normal germinal centre (GC) B cells and malignant counterparts remains poorly understood.

The principal analysis of the whole exome sequencing data revealed a transient Lamin B1 knockdown in lymphoma cells induces *de novo* mutational clustering outside of the IgV region. Doxycycline-inducible shRNA mediated Lamin B1 knockdown *in vitro* lymphoma models demonstrated that the removal of Lamin B1 from the nuclear periphery leads to the spontaneous double-strand breaks (DSBs) and elevated localisation of 53BP1, a mediator of the non-homologous end joining (NHEJ) pathway. Lamin B1 depletion was accompanied by increased cell proliferation and altered transcriptional landscape in BL2 cells. To complement the *in vitro* findings, a GC B cell-specific Lamin B1 knockout ($Lamin\ B1^{fl/fl}C\gamma1^{cre/+}$) mouse model revealed that Lamin B1 depleted GC B cells undergo increased DNA damage without the impairment of humoral immune response. Interestingly, an increase of GC B cells and plasmablasts cells was observed in $Lamin\ B1^{fl/fl}C\gamma1^{cre/+}$ mice 21 days after immunisation. The sBLISS (in situ labelling and sequencing) identified DSBs hotspots were enriched around transcriptional start sites of highly expressed genes in Lamin B1 depleted B cells and colocalised with genes mutated in lymphoma. A high proportion of DSB locations in mouse GC B cells contained a DNA sequence motif associated with activation-induced deaminase (AID) mutational signature, suggesting the open chromatin is susceptible to AID-mediated DSBs. Contrary to the findings from the functional studies, high Lamin B1 expression correlates with γH2AX in tissues from diffuse large B cell lymphoma (DLBCL) patients. Clinicopathological analysis of Lamin B1 demonstrated that decreased Lamin B1 expression associates with the advanced diagnostic stages and inferior progression-free survival, particularly in DLBCL patients. this study provides further evidence of Lamin B1's involvment in the maintenance of genomic stability in B cells and has potential clinical applications in B cell-derived lymphomas.

Table of Contents

Chapter 3: Lamin B1 depletion induces spontaneous mutagenesis and DNA damage in B cells 84

List of Figures

List of Tables

Abbreviations

53BP1	53-Binding Protein-1
AB	Antibody
ABC	Activated B Cell-Like
ADLD	Autosomal Dominant Leukodystrophy
AICDA	Activation Induced Cγtosine Deaminase
AID	Activation Induced Deaminase
AIDS	Auto immunodeficiency syndrome
AML	Acute Myeloid Leukaemia
APOBEC	apolipoprotein B mRNA editing enzyme catalytic polypeptide like
ASC	Antibody Secreting cells
ATM	Ataxia Telangiectasia-Mutated
BCL2	B-cell lymphoma 2
BCL6	B-cell lymphoma 6
BCR	B Cell Receptor
BER	Base Excision Repair
BL	Burkitt's Lymphoma
bp	Base Pairs
BP	Biological processees
BSA	Bovine Serum Albumin
CAR	Chimeric Antigen Receptor
CC	Cellular Components
CDKN2A	Cγclin-Dependent Kinase Inhibitor 2A
ChIP	Chromatin Immune Precipitation
CHOP	Cγclophosphamide, hydroxydaunorubicin, Oncovin, Prednisolone
CGG	Chicken Gamma Globulin
cHL	Classical Hodgkin Lymphoma
CIN	Chromatin Instability
CLL	Chronic Lymphocytic Leukaemia
CLPs	Common Lymphoid Progenitors
CMPs	Common Myeloid Progenitors
COO	Cell of Origin
COSMIC	Catalogue of Somatic Mutations In Cancer
CPM	Counts Per Million
CR	Complete Response
CRISPR	clustered regularly interspaced short palindromic repeats

CSR	Class Switch Recombination
CT	Computational Topography
CTCT	CCCTC-binding factor
DamID	DNA adenine methyltransferase identification
DAPI	4′,6-diamidino-2-phenylindole
DCLR1EC	DNA Cross-Link Repair 1C
DDR	DNA Damage Repair
DDX6	DEAD-Box Helicase 6
DLBCL	Diffused Large B Cell Lymphoma
DMEM	Dulbecco
DNA	Deoxyribonucleic acid
DNA-PKcs	DNA dependent protein kinase, catalytic subunit
DOX	Doxycycline
DSB	Double-Strand Break
DSMZ	Deutsche Sammlung von Mikroorganismen und Zellkulturen
DZ	Dark Zone
E2A	E Box Binding Protein 2A
EBF1	Early B Cell Factor-1
EBV	Epstein-Barr Virus
EMT	Epithelial-Mesenchymal Transition
ES	Embryonic Stem
EZH2	Enhancer of zeste homolog 2
FACS	Fluorescence Associated Cell Sorting
fBALM	fluctuation-assisted Binding Activated Localisation Microscopy
FBS	Foetal Bovine Serum
fDC	Follicular Dendritic Cells
FDR	False Discovery Rate
FISH	Fluorescence *in Situ* Hybridization
FL	Follicular Lymphoma
FLIPI	Follicular Lymphoma International Prognostic Index
FMO	Fluorescence Minus One
FO	Follicular
FOXO1	Forkhead box protein O1
FPKM	Fragments Per Kilobase Million
GCB	Germinal Centre B Cell-like
GEP	Gene Expression Profile
GFP	Green Fluorescent Protein
GI	Genomic Instability
GO	Gene Ontology
GSEA	Gene Set Enrichment Analysis
H2AX	histone H2A variant H2AX
HBSS	Hanks' Balanced Salt Solution
HEK293	Human embryonic kidney cells
HIV	Human Immunodeficiency Virus
HR	Homologous Recombination
HRP	Horseradish Peroxidase
HSCs	Hematopoietic Stem Cells
IF	Immunofluorescence
Ig	Immunoglobulin
IGHV	Immunoglobulin Heavy Chain Variable
IgV	Immunoglobulin Variable
IPI	International Prognostic Index
IR	Ionizing Radiation
KDM2	human lysine (K)-specific demethylase
LADs	Lamina Associated Domains
LMNA	Lamin A/C
LMNB1	Lamin B1
LMNB2	Lamin B2
LZ	Light Zone
mCLL	Mutated Chronic Lymphocytic Leukaemia
MCL	Mantle Cell Lymphoma
MEME	Motif-based sequence analysis
MIN	microsatellite instability
MLL	Mixed-Lineage Leukaemia
MMEJ	Microhomology Mediated End Joining
MMR	Mismatch Repair
MPP	multipotent progenitor population
MRD	Minimal Residual Disease
mRNA	messenger RNA
MZ	Marginal Zone
MZL	Marginal Zone Lymphoma
NE	Neuroendocrine
NER	Nucleotide Excision Repair
NES	Normalised Enrichment Score
Nf-kB	nuclear factor kappa light chain enhancer of activated B cells
NGS	Next Generation Sequencing
NHEJ	Non-Homologous End Joining
nHL	non-Hodgkin Lymphoma
NIN	Nucleotide Instability
NK	Natural Killer
NL	Nuclear Lamina
NR	No Response
NP	4-Hydroxy-3-Nitrophenylacetyl Hapten
OIR	Oncogene Induced Replication
OIS	Oncogene Induced Senescence
OS	Overall Survival
OVA	Ovalbumin
PARP1	Poly (ADP-Ribose) Polymerase 1
PAX5	Paired Box Protein 5
PBS	Phosphate Buffered Saline
PBS-T	Phosphate Buffered Saline-Tween
PCI	Phenol Chloroform Isoamyl
PEL	Primary Effusion Lymphoma
PFA	Paraformaldehyde
PFS	Progression Free Survival
PIM1	Pim-1 Proto-Oncogene,Serine/Threonine Kinase
PMBL	Primary mediastinal B-cell lymphoma
PNA	Peanut Agglutinin Antigen
PR	Partial Response
PRKDC	Protein Kinase, DNA-Activated, Catalytic Subunit
Pre	Precursor
Pre-BCR	Pre-B Cell Receptor

Pro	Progenitor
PS	Penicillin/Streptomycin
qPCR	Quantitative Polymerase Chain Reaction
RAG1	Recombination activating gene 1
RAG2	Recombination activating gene 2
REL B	RELB proto-oncogene, NF-kB subunit
RET	Rearranged during Transfection
RNA	Ribonucleic Acid
RNA-Seq	RNA Sequencing
ROS	Reactive Oxygen Species
RPM	Revolutions Per Minute
RPMI	Roswell Park Memorial Institute medium
RT	Room Temperature
sBLISS	in-suspension breaks labelling in situ and sequencing
SBS	Single Base Substitution
scATAC-Seq	single-cell accessible transposase assay sequencing
SHM	Somatic Hypermutation
shRNA	Short-Hairpin RNA
SMLM	Single Molecule Localisation Microscopy
SNV	Single Nucleotide Variant
ssGSEA	Single Sample Gene Set Enrichment analysis
STAT6	Signal transducer and activator of transcription
TAD	Topologically associated domains
TBS	Tris Buffered Saline
TCGA	The Cancer Genome Atlas
TES	Transcription end site
TME	Tumour Microenvironment
TNFRs	Tumour necrosis factor receptors
TOP2	Topoisomerase 2
TOP2B	Topoisomerase 2 B
TP53	Tumour Protein 53
TS	Tumour Suppressor
TSS	Transcription start site
uCLL	Unmutated Chronic Lymphocytic Leukaemia
UK	United Kingdom
UMI	Unique Molecular Adaptor
UV	Ultraviolet
WXS	Whole Exome Sequencing
WB	Western Blotting
YAP1	Yes-associated Protein-1
XRCC4	X-Ray Repair Cross Complementing 4
XRCC5	X-Ray Repair Cross Complementing 5

Chapter 1: Introduction

1.1 Ontogeny and functional role of immune cells

1.1.1 Discovery and identification of B cells

B cells lymphopoiesis is a dynamic and vital component of a correctly functioning immune response, and its importance was recognised since the discovery of immunoglobulin (Ig) expressing cells, now termed B cells[1]. Since the 1940s, the identification of serum Ig proteins (antibodies) prompted a suggestion that a subset of B cells (plasma cells) are responsible for antibody production[2]. Our understanding of B cell lymphopoiesis began with identifying cells with self-renewal capacity, called hematopoietic stem cells (HSCs)[3]. Pluripotent HSCs serve as a reservoir of all cells repopulating the circulatory and lymphatic systems, central to adaptive immune response (Figure 1.1.1).

The first identification of different B cell subsets occurred during the 1960s in diverse experimental models, including chicken, murine models, and human clinical studies[4–6]. Antibody production was linked to B cells by demonstrating that immunoglobulin expression can characterise normal and leukemic B cells[7,8]. Studies in murine foetal livers and bone marrow identified precursor (pre)-B cells that arise from progenitor (pro)-B cells. Pre-B cells expressing cytoplasmic μ H chains were recognised as precursors to IgM+ B cells, which are found in the peripheral blood and secondary lymph organs[9,10]. Interestingly, B cell precursors begin to develop in the foetal murine liver, and at a very early stage of haematopoiesis during embryonic development within the yolk sac[11,12]. Furthermore, the haematopoietic niche begins to establish within the bone marrow before birth[13,14]. The first model of antibody variability driven by class switch recombination (CSR) and somatic hypermutations (SHM) were initially demonstrated in chicken models and later in human[15,16]. Novel immunophenotyping methods improved our understanding of B cell maturation and allowed for the identification and characterisation of normal B cells derived from peripheral blood[7,8]. Immunophenotyping of B cells eventually paved the path for diagnosing, classifying, and treating B cell-derived malignancies.

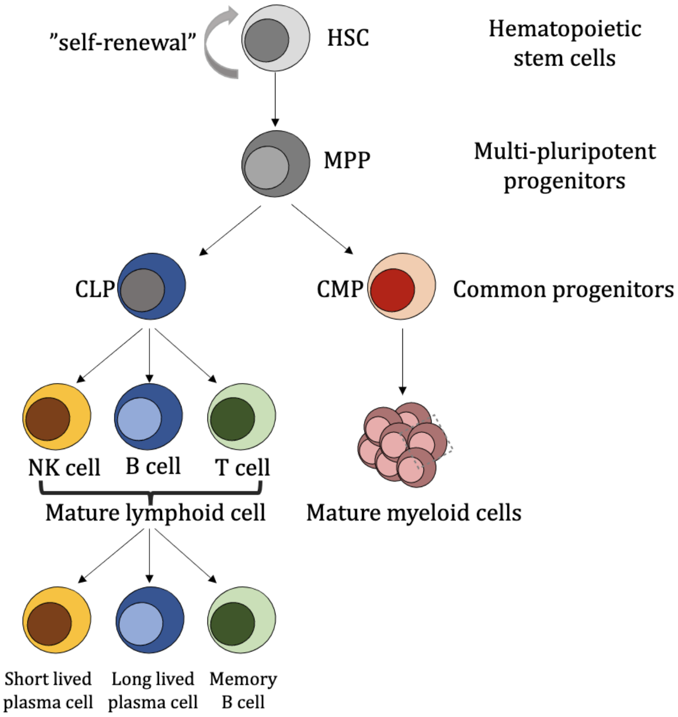

Figure 1.1.1 Hierarchical description of haematopoiesis and maturation of myeloid and lymphoid progenitors. In the bone marrow, haematopoiesis is initiated by the differentiation of HSCs into MPPs. MPPs commit to differentiate into lymphoid or myeloid progenitors which further undergo maturation steps and terminally differentiate in the secondary lymphoid organs.

1.1.2 Hierarchy of B cell maturation

B cell maturation is divided into two distinct stages: pre-B cell development in the bone marrow and subsequent maturation of B cells in the secondary lymphoid organs. HSCs give rise to a multipotent progenitor (MPP) population, which differentiates into common lymphoid progenitors (CLPs) or common myeloid progenitors (CMPs) in the bone marrow (Figure 1.1.1 & 1.1.2)[14]. CLPs further differentiate into three mature lymphoid lineages, including Natural Killer cells (NK), T cells, and B cells[17]. CLPs committed to B cell differentiation initially transform into progenitor (pro-B) cells under the control of transcription factors Early B cell Factor-1 (*EBF1*) and E box binding protein 2A (*E2A*)[18]. Subsequently, Paired box protein 5 (*Pax5*) is exclusively expressed within B-lymphoid lineages and is essential for B cell commitment by suppressing alternative lineage choices[19]. Moreover, *Pax5* is required for the initiation of the V(D)J recombination, the first programmed DNA damage necessary for B cell receptor (BCR) formation within the bone marrow[20]. The hallmark of B cells ultimately becomes the cell surface receptor BCR, known as Ig, whose expression is induced in pre-B cells within the bone marrow as the pre-B cell receptor (pre-BCR). Pro-B cells lack pre-BCR on the cell surface, therefore Recombination activating gene 1 (*RAG1*) and Recombination activating gene 2 (*RAG2*) enzymes are essential for the assembly of the antigen receptor by the recombination of V, D, and J gene segments in both B and T cells[21–23]. *RAG1/2* and the multifunctional transcription factor *Pax5* carry out sequential rearrangement events of heavy immunoglobulin genes essential for the formation of BCR. Pre-BCR is formed through the association of Ig light chain and Igα/β dimer on the surface of pre-B cells[24,25]. Pre-B cells further undergo V-J rearrangement of the Ig light chain, required to produce a fully functional BCR, which is then expressed as IgM on the cell surface of naive B cells[26]. B cells continue to differentiate upon translocating from the bone marrow to secondary lymphoid organs. Naive mature B cells undergo several transitional steps required for differentiation into long-lived mature follicular (FO) or marginal zone (MZ) B cells[27]. Alternatively, upon the antigen stimulation, B cells enter hyperproliferative germinal centres (GCs) to undergo clonal expansion, class-switch recombination (CSR), and somatic hypermutation (SHM) events within the Ig locus[28,29]. Positively selected clones further differentiate into diverse antibody-secreting cells, which reside in the secondary lymphoid organs (plasmablasts) or migrate to the bone marrow (plasma cells) and establish humoral immunity[27].

1.1.3 Role of B cells in adaptive immune response

As outlined above, immature B cells undergo several differentiation steps prior to the active participation in the adaptive immune response. After cells commit to the B lineage maturation within the bone marrow microenvironment, naïve mature B cells enter secondary lymphoid organs (Figure 1.1.2). Here, upon the antigen encounter and several highly ordered maturation steps, activated B cells can differentiate into antibody-secreting cells. Activation of a naïve resting B cell leads to the upregulation of essential transcription factors including *BCL6, FOXO1, and E2A*[30–32]. Then, activated B cells enter the dark zone (DZ) of GCs and undergo rapid proliferation, known as clonal expansion[33]. GC B cells, under the control of *BCL6*, are susceptible to high-frequency point mutations within the Ig variable (*IgV*) gene clusters. Activation Induced Deaminase (AID), also known as *AICDA* gene, highly expressed in DZ GC B cells, induces cytosine to thymine nucleotide substitutions resulting in these point mutations[34]. B cells then egress from the DZ to the light zone (LZ) of the GC to undergo the process of high-affinity selection driven by *Nf-kB* and *MYC*[35,36]. Alternatively, B cells undergo isotype class switching via CSR or re-enter the DZ for additional rounds of SHM driven by AID[35]. CSR occurs in the LZ of the GC, but studies have shown cells can undergo class-switching prior to GC entry[37,38]. Positively selected B cells displaying high-affinity Ig differentiate into memory B cells or plasma cells, which are essential for the humoral immunity.

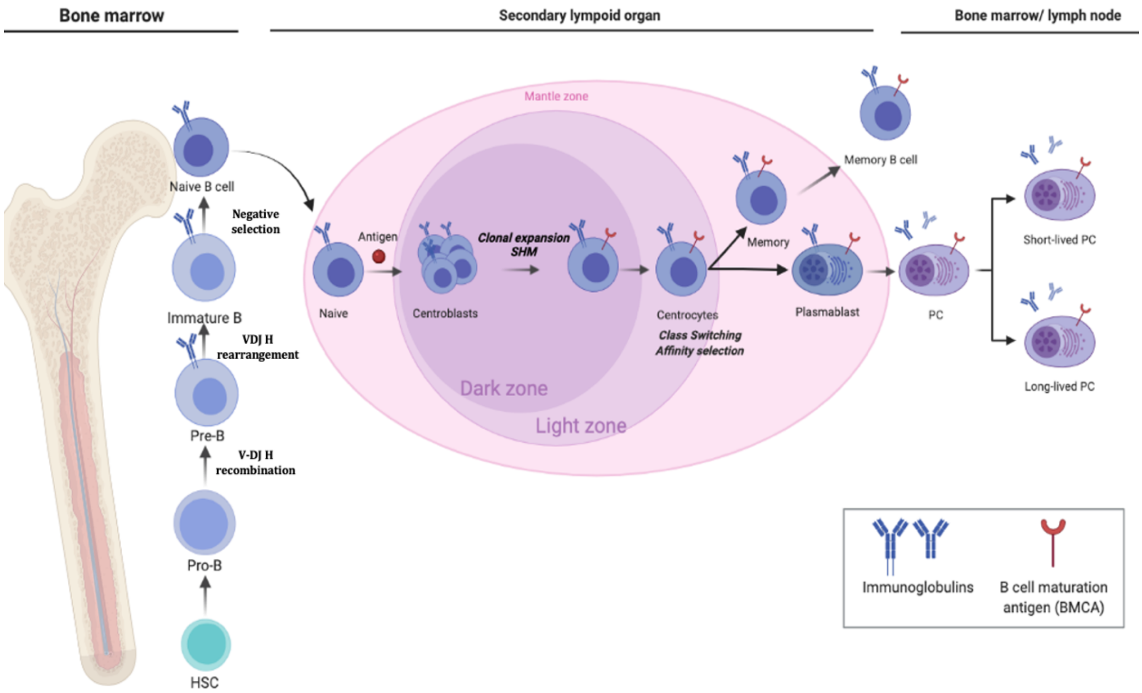

Figure 1.1.2 B cell maturation and differentiation hierarchy. Schematic representation of early antigen-independent B cell maturation in the bone marrow and further antigen-dependent B cell differentiation in the germinal centres of secondary lymphoid organs.

1.1.4 Mutagenic role of AID and APOBECs

The GC reaction is partly driven by the mutagenic activity of AID. AID, along with other members of APOBEC (apolipoprotein B mRNA editing enzyme catalytic polypeptide like) family, are cytidine deaminases, known DNA editing enzymes with diverse physiological functions[39]. Previous evidence has shown AID is a key enzyme responsible for antibody maturation and properly functioning adaptive immune response[40]. AID mediates point mutations within the IgV region and antibody class-switching. Outside of natural AID-mediated targeting of IgV cluster, the mutagenic activity of AID can also be detected in non-Ig genes. Studies have demonstrated AID is a critical facilitator of mutations and genomic rearrangements in essential transcription factors and oncogenes (*C-MYC, PAX5, DDX6*)[41–43]. APOBEC1 and APOBEC3 are fundamentally closest ancestors to AID[44]. WXS analysis uncovered APOBEC driven mutational signatures (dC>dT) across a broad spectrum of malignancies (lung adenocarcinoma, bladder, breast, cervix, B cell lymphomas, multiple myelomas, acute lymphocytic leukaemia), although some do not display APOBEC signatures[45] (Figure 1.1.3). High-frequency mutations mediated by APOBECs are linked to kataegis, mutational clustering throughout certain genomic regions[46]. Therefore, the expression of APOBECs and their mutational activity are tightly controlled.

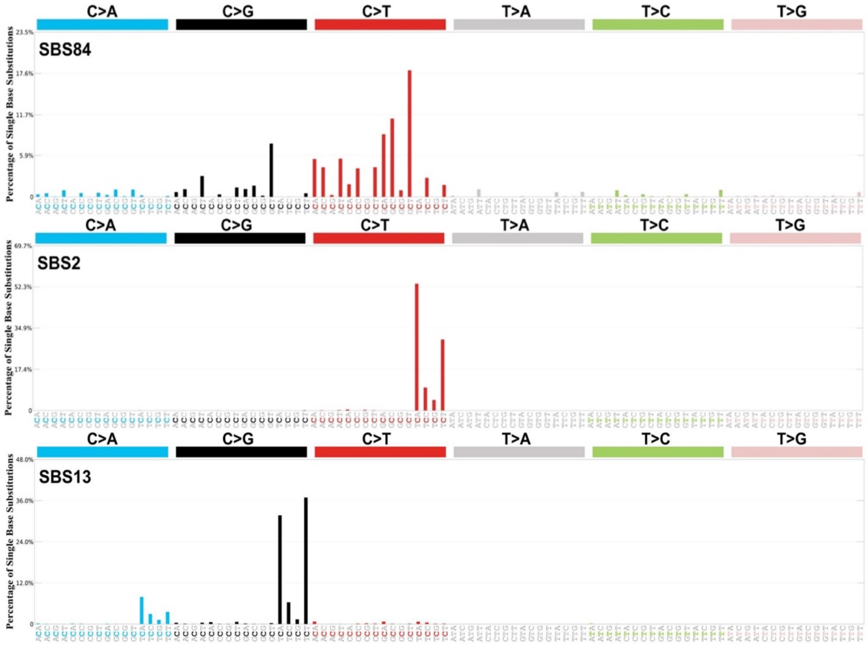

Figure 1.1.3 Single base substitution (SBS) mutational signatures. SBSs attributed to the enzymatic activity of activation-induced deaminase (AID) were obtained from COSMIC database. SBS signatures mediated by APOBECs are defined as a change of a nucleotide base, primarily a cytosine to thymine (C>T) mutation (SBS2 & SBS84). SBS13 is also attributed to activity of the AID/APOBEC family of cytidine deaminases (APOBEC3) based on similarities in the sequence context of cytosine mutations. There are only six different possible substitutions founded on Watson-Crick base pairs (C>A, C>G, C>T, T>A, T>C, and T>G). C= Cytosine, A=Adenosine, G=Guanine, T=Thymine).

1.1.5 Developmental regulation of B cell progenitors

Regulation of B cell development is dependent on negative and positive expression of cell surface receptors. B cell selection begins in the bone marrow, where immature B cells undergo positive selection based on the lambda light chain expression on the pre-BCR receptor during the pro-B and pre-B cell stages[47]. Further selection continues after BCR "maturation" prior to the exit of B cell from the bone marrow, where IgM crosslinking by autoantigens triggers negative selection to avoid cross-reactivity. Immature IgM+ B cells capable of cross-linking their BCRs then undergo negative selection by several mechanisms, including apoptosis, receptor editing, or deletion[48,49]. After migrating from the bone marrow to GC in the secondary lymphoid organs, negatively selected naïve mature B cells are primed to undergo clonal expansion upon antigen mediated by antigen activation[50]. Cells transiting through the GC are positively selected based on Ig receptors with the highest affinity towards the antigen. GC process induces a high cell turnover with non-specific clones towards the antigen undergoing apoptosis[51]. The relatively prolonged life cycle of B cells and susceptibility to genomic lesions linked to SHM and CSR increase the risk of potential malignant transformation.

1.1.6 Malignant transformation of B cells

Lymphoma is one of the most prevalent cancer types in the UK and the world[52]. Specifically, B cell malignancies account for 95% of all lymphoma cases, highlighting the susceptibility of normal B cells to undergo malignant transformation[52]. Normal B cells are highly prone to recombination events and mutagenesis as a part of the immune response, which increases the likelihood of malignant transformation. Several key events have been proposed as drivers of malignant B cell transformation, including chromosomal translocations, somatic mutagenesis, and B-cell receptor signalling[53]. Chromosomal translocations of immunoglobulin loci and proto-oncogene are commonly detected in B cell malignancies, which result in a constitutive proto-oncogene expression under the control of immunoglobulin promoter[53]. Chromosomal translocations are not restricted to GC events only, as one of the most commonly occurring translocations t(14;18)(q32;q21) arises from VDJ recombination process in pro/pre B lymphocyte, translocating B-cell lymphoma 2 (*BCL2)* gene to *IgH* locus[54–56]. Despite *BCL2;IgH* translocation being present in up to 50% of healthy individuals, this specific genetic lesion alone is not sufficient for malignant transformation as most *BCL2;IgH+* patients do not develop lymphoma[57,58]. However, the accumulation of additional genetic aberrations acquired via SHM and CSR events increases the likelihood of GC B cell transformation, as revealed by differential gene expression analysis between B cell lymphomas and normal GC B cells, which identified genes involved in lymphomagenesis[33,59].

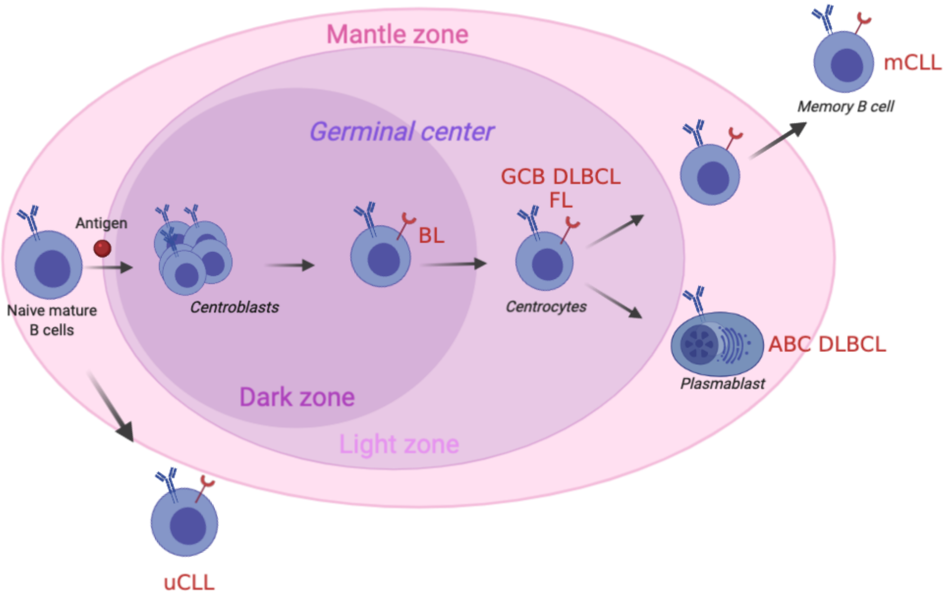

Figure 1.1.4 Origin of GC-derived B cell malignancies. Schematic figure demonstrating the likely cellular origin of nHL. Unmutated IGHV Chronic lymphocytic leukemic (uCLL) is derived from pre-GC B cell. B cell lymphoma resembling DZ GC B cell is Burkitt's lymphoma (BL). Follicular Lymphoma and GCB DLBCL are derived from the transformation of LZ GC B cells. Activated B cell-like (ABC) DLBCL arises from plasmablast-like activated late/post-GC B cell. The origin of NHL B cell lymphomas has been uncovered by analysis of gene transcription and genomic alteration, including acquired translocations, deletions, or mutations.

B cell differentiation involves a high cell turnover rate and increased likelihood of apoptosis, specifically within GCs. High proliferation and apoptosis rates require precise regulation of the anti-apoptotic pathway for the survival of normal B cells, which partially is dependent on BCR expression[60]. B cells constitutively displaying BCR prompted speculation as to whether B cell lymphomas are fully dependent on BCR expression. Aside from a few exceptions, including classical Hodgkin Lymphoma (cHL) and Primary mediastinal B-cell lymphoma (PMBL), most B cell lymphomas do express BCR[61,62]. B cells unable to form a functional BCR are less likely to survive and transform into lymphoma, suggesting BCR provides essential signalling for lymphomagenesis and cell survival[63,64]. Recent implementation of NGS analysis and gene expression profiling (GEP) led to the cellular origin identification of several B cell derived malignancies (Figure 1.1.4). Despite the latest advances in classification of blood malignancies, the cell origin of B cell derived lymphomas is not fully elucidated.

1.2 GC B cell derived malignancies

1.2.1 Introduction

Haematological malignancies are some of the most common cancers in the world. Despite a high prevalence, current treatments provide a reasonably positive survival outlook compared to other more aggressive malignancies, such as lung carcinoma, pancreatic ductal adenocarcinoma, or glioblastoma[65]. Blood cancers are classified based on the cell of origin into a myelogenous (leukaemia) or lymphocytic (lymphomas) subtype. Myelogenous leukaemia is classified as a group of diseases arising from the bone marrow and haematopoietic stem cells and affecting myelogenous white blood cells (neutrophils, macrophages, basophils)[53]. On the contrary, lymphomas, subclassified into B cell and T cell lymphomas, arise from the transformation of lymphoid cells (B cells, T cells, and NK cells) from the bone marrow or secondary lymphoid organs.

1.2.2 Germinal centre derived B cell lymphomas

Lymphomas are classified as classical Hodgkin lymphoma (cHL) or non-Hodgkin lymphomas (nHL). B cell lymphomas account for 85% of nHL making it one of the most prevalent cancer types globally and in the United Kingdom (UK)[66,67]. B cell lymphomas can be further classified into different subtypes depending on the cell of origin. Most B cell lymphomas are transformed GC B cells from the secondary lymphoid structures. GC derived B cell lymphoma is a genetically highly heterogeneous disease, comprising of several subtypes. The most prevalent subtypes include follicular lymphoma (FL) and the more aggressive diffuse large B cell lymphoma (DLBCL). Less commonly occurring but highly aggressive subtype is Burkitt's lymphoma (BL). Despite the cellular origin of chronic lymphocytic leukaemia (CLL) being still debated, several studies have provided evidence CLL arises from GC-experienced B cells[68]. More specifically, mutated immunoglobulin heavy-chain variable gene (*IGHV*) CLL (mCLL) resembles memory B cells (CD27+), and unmutated *IGHV* CLL (uCLL) is thought to originate from a pre-GC B cells (CD27-)[68]. GC derived B cell lymphomas often present with high heterogeneity and mutagenesis, which complicates diagnosis and treatment. Despite recent improvements in personalised treatment approaches, many nHL patients become treatment-resistant and eventually relapse[69].

1.2.3 Epidemiology

The nHL was the sixth most common cancer type in the UK as of 2017, with 14,000 newly diagnosed patients accounting for 4% of all new cancer cases[70] and approximately 90% of all nHL cases are GC-derived B cells lymphomas[66]. The most common form of nHL is DLBCL, an aggressive and fast progressing subtype of GC derived B cell lymphoma. Indolent FL subtypes comprise approximately 30% of the cases, often diagnosed in older individuals[58]. Together, DLBCL and FL account for more than half of the nHL cases, despite vastly different prognoses, course of the disease, and survival outcomes. The rarest but very aggressive form of nHL is BL, comprising about 3-4% of nHL cases that arise mainly in children, young individuals, and patients with HIV and Epstein-Barr virus infection[71]. The incidence of nHL cases in the United States and western-world countries saw an increase of nHL rates by 3–4% each year from 1973 to the mid 1990s[72]. Over the last two decades, innovations in diagnosis and treatment options have improved the survival of patients. However, a recent report projected a growth of nHL patients by an annual increase of 1.87%, from about 154,000 newly diagnosed cases in 2017 to 183,000 cases in 2027 in the seven major countries[73]. Therefore, the need for novel diagnostic tools and treatment options will be needed for the improvement of nHL patient treatment.

1.2.4 Diagnosing and monitoring B cell derived lymphomas

Diagnosis of nHL in patients is usually based on surgically excised biopsy from peripheral lymphoid tissues or splenectomy, allowing for histopathological assessment of the tissue by microscopical imaging. Surgical biopsy is an invasive method which may not always result in an accurate diagnosis with respect to subclassifications of nHL. Live cell aspiration from peripheral blood or bone marrow is used for immunophenotypic analysis by flow cytometry, fluorescence *in situ* hybridization (FISH) detection of chromosomal abnormalities, or molecular diagnostics such as next-generation sequencing (NGS)[74]. These diagnostic methods are generally used to complement immunohistochemistry (IHC), which improves diagnosis and treatment management. NGS can further improve the diagnoses by evaluating gene expression profiles used for the classification of germinal centre B cell-like (GCB) DLBCL, activated B cell-like (ABC) DLBCL, and BL[75].

Patients undergoing treatment should be followed up during the first 2 to 3 years for early relapse detection, as relapse is most likely to occur within 2 years after the onset of treatment regime. Computed tomography (CT) and biomolecular profiling are commonly used to assess the response in nHL patients, particularly those with worse prognosis. Treatment of nHL patients is monitored by CT/ positron emission tomography (PET) scans and assignment of International Prognostic Index (IPI) or Follicular Lymphoma International Prognostic Index (FLIPI) diagnostic scores[76,77]. Treated patients are traditionally assigned into one of three groups based on the achieved response to therapy: complete response (CR), partial response (PR), or no response (NR). Molecular analysis by flow cytometry and the polymerase chain reaction can be used to detect minimal residual disease (MRD) based on IGHV rearrangements in some subtypes of GC B cell lymphomas[64].

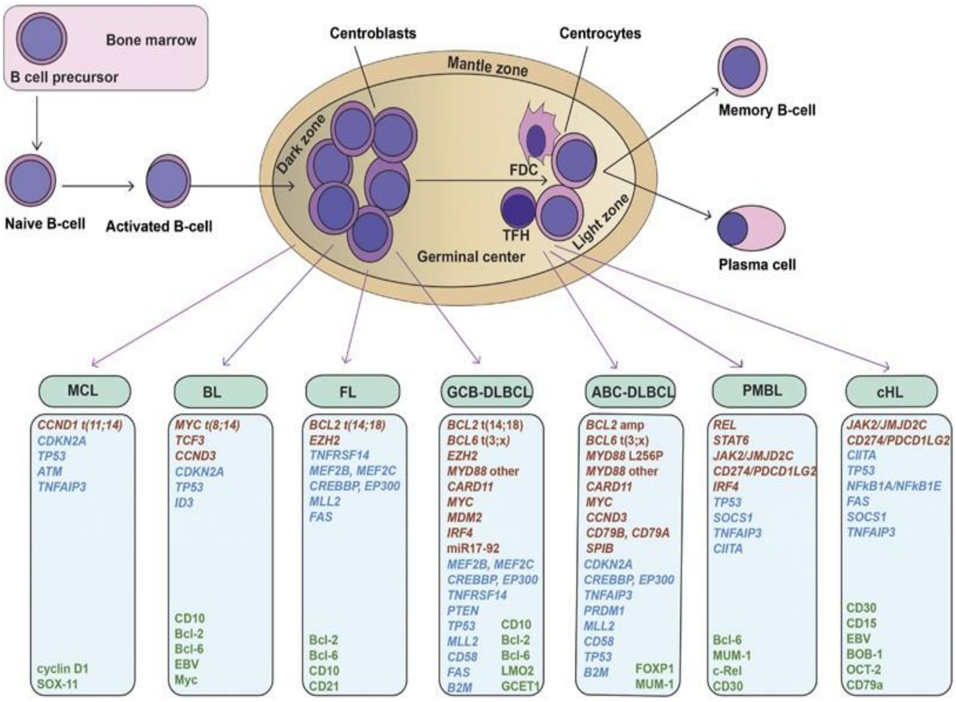

Figure 1.2.1 Genetic heterogeneity in B cell lymphomas. Most commonly occurring genetic aberration in B cell lymphoma subtypes. The figure was taken from Sun et al[78].

1.2.5 Molecular pathophysiology of B cell derived lymphomas

B cell lymphoma subtypes differ immunophenotypically, histologically, and genetically which result in a diverse clinical course associated with the disease subtype (Figure 1.2.1). Gene expression profiling and immunophenotyping revealed that DLBCL most likely originate from light zone GC B cells, whereas FL and BL resemble dark zone GC B cell origin[51,59]. Molecular cytogenetics revealed different chromosomal abnormalities, and *IGHV* rearrangement as hallmarks of GC derived nHL subtypes, which are commonly used in clinics for diagnosing and treating nHL patients[79].

1.2.5.1 Follicular lymphoma

FL is an indolent and slow-progressing GC derived lymphoma with cellular origin resembling a DZ GC B cell[59]. Despite a relatively high 5-year survival rate (~85%), FL is essentially an incurable disease associated with relapse and risk of transformation to a more aggressive form of lymphoma - DLBCL[80]. Morphological structures of FL biopsies share similarities with benign reactive lymph nodes, therefore accurate diagnosis is critical. Mutations within Ig gene, expression of *BCL6*, and *CD10* cell surface marker are shared hallmarks of normal GC B cell and FL[30,58]. Approximately 90% of FL patients present with chromosomal translocation t (14,18), the juxtaposition of *BCL2* gene and Ig locus, resulting from VDJ recombination process during B cell development in bone marrow[81]. However, additional oncogenic events are required for full malignant B cell transformation, as the majority of individuals carrying t(14,18) do not develop lymphoma[80]. Mutagenic lesions in *BCR, FOXO1, STAT6* genes and dysregulation of *KDM2* and *EZH2* are the most common drivers lymphomagenesis[59].

1.2.5.2 Diffuse Large B cell lymphoma

The most common and aggressive form of nHL is DLBCL, and accounts for approximately 40% of all cases. DLBCL cells are bigger in size, faster proliferating, and exhibit a greater heterogeneity as compared to FL cells. DLBCL can be classified into two main molecular subgroups GCB and ABC DLBCL based on the GEP[82]. Immunophenotypic and gene expression profile analysis revealed ABC DLBCL originates from a plasmablast-like B cell, while GCB DLBCL likely arises from an LZ GC cell that re-entered dark zone[83]. As a result, both subtypes display differences in genetic lesions, epigenetic and immunophenotypic signatures leading to diverse courses of the disease and survival outcome[83,84]. The most recurring genetic lesions in DLBCL are *BCL6*, *BCL2*, and *MYC* dysregulations arising from a chromosomal translocation to the close proximity of Ig loci[79,85,86]. Compared to FL, the majority of DLBCL present with some severe epigenetic reprogramming along with genetic lesions that drive tumorigenesis and lead to worse clinical outcomes.

1.2.5.3 Germinal centre B cell (GCB) DLBCL

GCB subtype comprises about 50% of all DLBCL cases and is associated with more favourable disease outcomes than ABC DLBCL[83,87]. Unlike other DLBCL subtypes, compiled evidence suggests GCB DLBCL originates from a malignant transformation of a normal GC B cell lacking the expression of early post-GC differentiation markers. Cytogenetic analysis demonstrated that GCB DLBCL cases are most often characterised by t(14;18) and t(8,14) chromosomal translocations, resulting in upregulation of oncogenic drivers *BCL2* (34%) and

MYC (14%), respectively[82,83]. The coexistence of these translocations presents as a double-hit lymphoma associated with a poor prognosis. In addition to chromosomal translocations, activating and loss-of-function mutations in epigenetic modulators *EZH2* (22%) and *TNFRs* (40%) are commonly found in GCB DLBCL [59,88].

1.2.5.4 Burkitt's lymphoma

BL is the least common but most aggressive form of nHL, affecting mainly children and young patients with Epstein-Barr Virus (EBV) infection or Autoimmune deficiency syndrome (AIDS)[66,89]. The first clinical case of BL was described in 1958, but the characteristic chromosomal translocation t(8,14) in BL cells was discovered nearly twenty years later[90]. Subsequent studies described this translocation as a juxtaposition of the human *MYC* gene and the *IG* locus, which serves as a hallmark of BL existing in the majority of patients[86,91,92]. *MYC*-driven tumorigenesis often leads to high staining of proliferative marker Ki-67 (95%), as well as tumour lysis syndrome and significantly elevated lactate dehydrogenase (LDH) in serum of BL patients[71]. Interestingly, *MYC* expression is completely silenced in proliferating dark zone GC centroblasts and increases only in light zone GC cells after egressing from the dark zone[35]. Contrary to this observation, gene expression profiling and immunophenotypic markers suggest BL cells originate from dark zone GC B cells[51].

1.2.5.5 Chronic lymphocytic leukaemia

Morphology and immunophenotype of CLL cells mostly resemble naïve mature GC B cells (CD5+). Even though recent NGS studies aiming to decipher the origin of CLL provided novel insights, there is no definite consensus on the cell-of-origin (COO) in CLL. In the clinical setting, the mutational status of *IGHV* is used to classify CLL into two major subtypes with a distinct prognosis and clinical outcome. Mutated *IGHV* CLL (mCLL) presents with genetic characteristics of GC experienced B cells, including mutated *BCL6* gene and elevated *AID* expression[67]. Additionally, mCLL cells express CD27+ marker specific for memory B cell, signifying the post-GC B cell of origin hypothesis[93]. Unlike mCLL, unmutated *IGHV* CLL (uCLL) cells do not express CD27 marker nor display IGHV mutations, suggesting a pre-GC cellular origin[68]. High mutational load is present in approximately 80% of CLL patients, including common deletions of 13q14 disrupting the expression of microRNA 15-a and 16-1; potent regulators of B cell apoptosis[94,95]. Additional inactivating mutations causing induction of genomic instability are mediated by the deletion of *ATM* (del11q22-q23) and *TP53*(del17p13), and are associated with poor prognosis[96,97]. Identifying the cellular origin of CLL and biomarkers for proper diagnosis and treatment management is necessary to achieve the best clinical outcome.

1.2.6 Disease progression

As nHL is not a single disease but rather a complex of several molecular subtypes, clinical courses vary accordingly. Low-grade FL is an indolent and slow-progressing disease that may take years to develop, affecting the older population. However, the risk of transformation to a more aggressive DLBCL increases by 3% per year[98]. A complete understanding of what drives FL transformation is not fully understood yet. While, alterations in epigenetic regulators have been proposed to be the initiator of transformation at the early stages, *NF-kB* and *EBF1* mutations were gained after the transformation stage[99,100]. Clonal evolution studies revealed linear and divergent modes of evolution, with all the evidence suggesting that the transformation of FL is associated with a divergent pattern of tumour evolution[101]. Adversely to FL, DLBCL is a high-grade and fast-growing aggressive large cell lymphoma. DLBCL patients generally have a faster and more pronounced response to treatment, although the number of non-responders and patients who relapse can be as high as 30-40%[102]. Similarly to DLBCL, BL progresses quickly and is often fatal if left untreated[103].

1.2.7 Treatment of nHL

The "watch and wait" approach, may benefit a group of patients with low-grade indolent FL. Conversely, for other lymphoma subtypes, treatment and survival outcomes of nHL patients have been dramatically improved by introducing combination chemotherapy in the 1980's[104,105]. The combination of Cyclophosphamide, Hydroxydaunorubicin, Oncovin, Prednisolone (CHOP) is still widely used for treatment of nHL[106]. Indeed, the administration of CHOP chemotherapy has been the cornerstone of nHL therapies for the last 40 years.

The CHOP treatment is curative only in approximately 40-60% of patients diagnosed with aggressive B cell lymphomas[105]. Therefore, the development of novel treatments, including immunotherapies and chimeric antigen receptor (CAR) T-cells, has been accelerated to meet the clinical need for more efficient therapies. The first significant improvement of CHOP therapy of nHL was achieved by the addition of anti-CD20 monoclonal antibody (Rituximab), which is now given as R-CHOP chemoimmunotherapy, or as Rituximab alone in patients with high expression of CD20 receptor[107–109]. Additional antibody therapies (anti-CD52, anti-CD30, anti-CD79b, anti-PDL1) have been approved for clinical use, but they failed to achieve clear-cut improvements compared to Rituximab[110]. In relapsed patients, combined treatment with R-CHOP and novel potential therapeutics, such as tyrosine kinase inhibitor (ibrutinib), proteasome inhibitor (bortezomib), or immunomodulators (lenalidomide) resulted in improved outcomes[69,110]. In recent years, chimeric antigen receptor (CAR) T-cell therapies have emerged on the front line of research for personalised medicine treatment. Despite the increased specificity, the high cost of treatment and severe side effects raise certain limitations on CAR-T cell therapies[111]. Further exploration of dysfunctional cellular pathways and discovery of novel diagnostic and prognostic biomarkers may improve treatment outcomes.

1.2.8 Resistance and relapse

A common phenomenon in high-grade nHL is disease relapse and resistance to treatment. The best survival outcome is achieved with R-CHOP as a first-line treatment in most GC derived nHL. However, treatment fails in approximately 35-50% of DLBCL patients due to resistance (15-25%) and relapse (20-30%)[65,69]. Many non-responders are classified as double-hit lymphomas (DHL), containing two oncogenic translocations (*MYC+BCL2/BCL6*)[81,112]. Although FL is an indolent disease, approximately 45% of patients are in high risk of transformation to more aggressive DLBCL counterpart[80]. Non-responders and relapse patients are given a second line treatment or bone marrow transplant if the secondary treatment fails to achieve remission. Despite a relatively high 3-year survival (80%) of immediately treated high-grade BL patients, 30-40% are associated with relapse or no response six months after the treatment[113], while relapsed and refractory BL patients have a poor prognosis (OS = 2.8 months)[114]. Because most of the effective pre-clinical treatments fail to be translated into the clinical setting, the generation of more advanced models recapitulating nHL disease is required for the discovery of novel treatment and diagnostic approaches.

1.2.9 Normal B cell and B cell lymphoma derived experimental models

The first studies deciphering the development of B cells and establishment of the immune system were conducted in the chicken bursa of Fabricius and murine models[4,9]. Murine models have remained widely used in B cell research due to their similarities to human physiology and the development of immune response. The generation of transgenic mouse models capable of recapitulating specific subtypes of nHL has broadened the understanding of lymphomagenesis. The *most* widely used murine models of spontaneous nHL development include E*μ*-*MYC*, Iμ-HABCL6, and *Vav*P-*BCL2* - genes often dysregulated in nHL[115–117]. Overexpression of *MYC* under the control of *IgH* may result in two phenotypes: an early phenotype resembling Burkitt's lymphoma arising from immature B cells, and delayed onset of DLBCL-like phenotype, most likely originating from mature B cells[115]. DLBCL often display chromosomal alterations deregulating the expression of *BCL6*, a transcriptional activator required for GC formation. Iμ-HABCL6 model results in increased GC formation and development of lymphoproliferative syndrome, eventually progressing to DLBCL-like human lymphoma[116]. The ability to recapitulate tumour development in mouse models allowed for deciphering key mechanisms associated with lymphomagenesis.

In addition to mouse models, immortalised human lymphoma cell lines are widely used in preclinical studies. The establishment of suspension lymphoma cell lines by routine tissue culture techniques was a challenge in the 1970's, except for Burkitt's lymphoma, which traditionally transformed by EBV, fundamental for immortalization of cells *in vitro*[118]. Alternatively, EBV negative lymphoma cell lines derived from non-BL patients were established using B cell growth factor[119]. Despite recent advances in disease phenotype recapitulation using various models, heterogeneity and genomic instability in lymphoma prove to be still a challenge in the clinical setting.

1.2.10 Genomic instability as a hallmark of cancer

Genomic instability (GI) is one of the well-established hallmarks of cancer. GI can be induced by several endogenous factors (replication stress, reactive oxygen species (ROS)) and by exogenous factors (ultraviolet light, X-rays, ionising radiation) summarised in Figure 1.2.2[120,121]. GI is the likely cause of malignant transformation of cells lacking properly functioning DNA damage repair (DDR) mechanisms[121]. DDR is a critical protecting mechanism against malignant transformation and subsequent mutagenesis of cancer cells. Within this context, B cell differentiation requires properly regulated DNA damage and repair for generation of antibody-secreting cells[122]. A controlled and functioning DNA repair mechanism is essential for highly ordered and targeted genomic instability necessary for generating Ig repertoire during B cell differentiation.

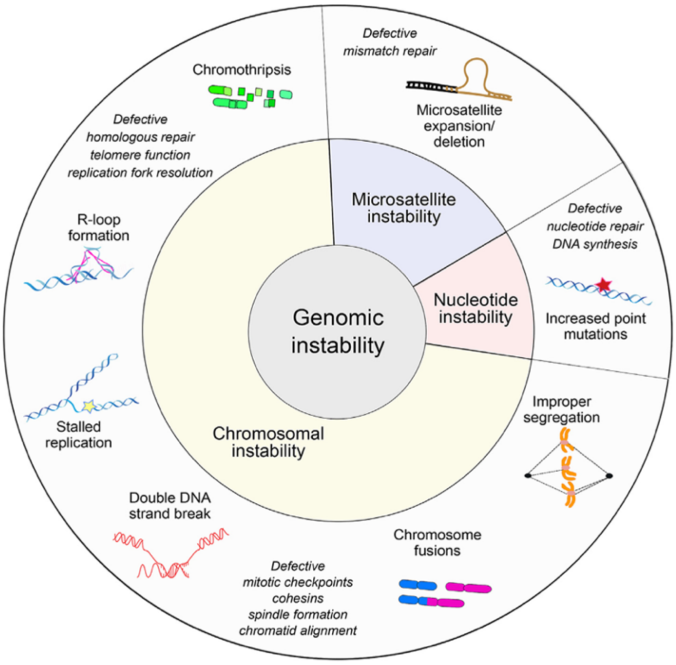

Figure 1.2.2 Exogenous and endogenous processes contributing to genomic instability. Diagram of mechanisms resulting in CIN (chromosomal instability), MIN (microsatellite instability), or NIN (nucleotide instability). Figure taken from Cunningham et al.[123]

1.2.11 Mutagenesis and genomic instability in B cell lymphomas

As described in Chapter 1.1, mutagenic processes, such as SHM, CSR, and V(D)J recombination, are specific to B cell maturation. These cellular processes result in DNA breaks, which are subsequently repaired, leading to high-frequency mutations and isotype switching[28,39]. B cell lymphomas, specifically antigen-experienced subtypes, display point mutations at the *IGV* gene, which increases their tumorigenic potential[122]. Loss of function in DNA damage repair (DDR) genes can lead to genomic instability, mutagenesis, and malignant transformation (Figure 1.2.3)[124]. The most frequent mutations in B cell lymphomas are present in important DDR factors, including *TP53*, *ATM*, and *PARP1*[125]. Less frequently mutated genes involved in DNA mismatch repair (*EXO1*, *MSH2*, *MSH6*), non-homologous end joining (NHEJ) genes (*DCLRE1C/ARTEMIS*, *PRKDC/DNA-PKcs*, *XRCC5/KU80*, and *XRCC6/KU70*), and homologous recombination (HR) pathways were detected in DLBCL patients[125]. In addition to the dysfunctional DDR, proto-oncogenes (*MYC*, *BCL2*, *BCL6*) driven genomic instability arises due to the replicative stress and accumulation of DNA damage during S phase of the cell cycle[125].

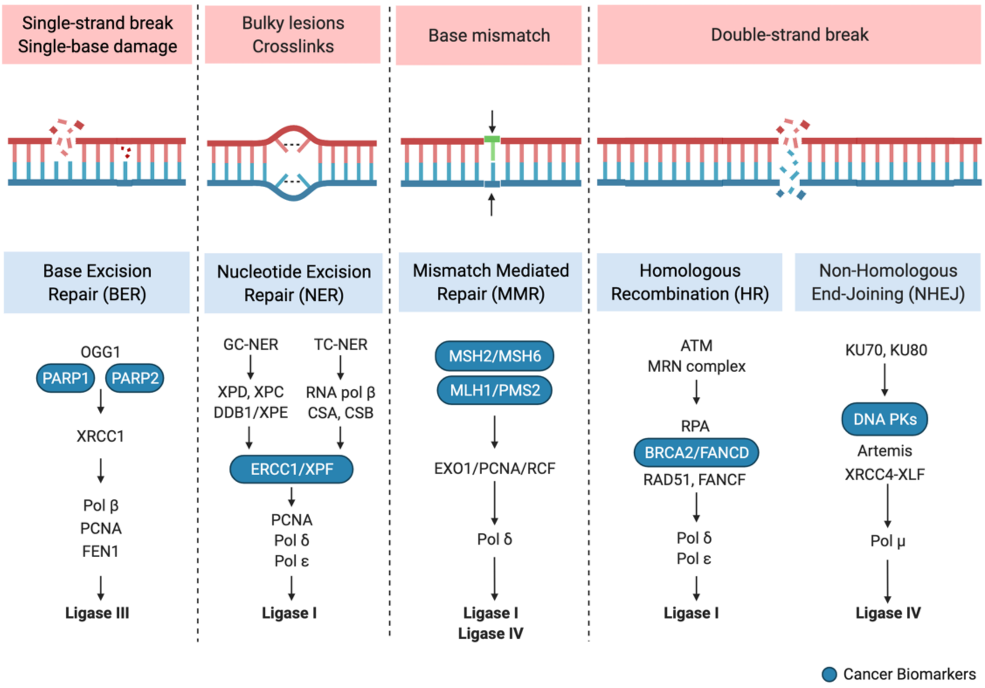

Figure 1.2.3 Cellular pathways involved in DNA damage repair. Common DNA repair mechanism pathways utilised in response to a specific DNA damage.

Consequently, the accumulation of DNA damage in B cells with improperly functioning DDR drives tumorigenesis and leads to poor clinical prognosis[126]. Two-fold increase in chromosome mis-segregation was associated with a 24% and 48% decrease in overall survival (OS) and progression-free survival (PFS) in DLBCL patients, respectively[126]. Immunohistochemistry (IHC) analysis revealed a constitutive activation of DDR components and GI in B cell lymphomas, particularly BL and DLBCL[127]. Phosphorylation of H2AX at serine 139 (*γH2AX*), and marker of DNA double strand breaks, was detected in 47% of analysed

DLBCL cases and 23% of BL cases, while indolent B cell lymphomas showed significantly lower positivity in DDR activity[127]. Interestingly, γH2AX was co-expressed with *c-MYC* activity in DLBCL patients, suggesting that replicative stress correlates with genomic instability and worse clinical outcomes. Analysis of γH2AX in B cell lymphoma cell lines revealed upregulation of γH2AX phosphorylation in GCB and BL subtypes, signifying the association of genomic instability with GC derived B cell lymphomas[127].

Diverse antibody repertoire is a result of controlled genomic instability carried out by SHM and CSR in normal GC B cells. Predictably, malignant B cells can undergo off-target recombination and mutagenesis of frequently dysregulated genes in lymphomas, including *BCL6*, *MYC*, *BCL2*, and *PIM1*[41,128,129,130]. Recently our group has demonstrated that targeted point mutations within *IGHV* in GC B cells are dependent on the release chromatin domains from Lamin B1 suppressive environment at the nuclear periphery[131]. Our data proposes Lamin B1, a nuclear lamina component, acts as an upstream epigenetic regulator of chromatin dynamics and mutagenesis.

1.3 Genome organisation is controlled by nuclear lamina

1.3.1 Controlling gene expression and cellular signalling through the spatial organization of the genome

Over the last decade, studies demonstrated gene transcription is not solely dependent on the activation of promoters and enhancers within the gene regulatory networks, but rather a more complex chromatin accessibility and reorganisation[132]. Genome organisation is an important factor that contributes to the regulation of gene transcription, cell differentiation, and genome integrity[133–135]. Three-dimensional chromatin is precisely organised into compartments known as topologically associated domains (TADs)[132]. TADs are several megabases long genomic regions, which undergo constant reorganizations during cell differentiation, cell cycle, and malignant transformation[136–138]. The major TAD compartments (TAD "A", TAD "B") are dependent on the spatial localisation and transcriptional state[139,140]. Chromatin undergoes rapid changes during transcription and replication, which are often coupled with chromosomal rearrangements[141,142]. Recent studies revealed chromosome loop anchors bound by CCCTC-binding factor (CTCF) and cohesin are susceptible to topoisomerase 2B (TOP2B)-mediated DSBs[133,143]. These DSBs form clusters localised along both sides of TADs, which demonstrates that the chromatin conformation and structure maintains genome integrity[143]. Reorganisation of chromatin allows DNA repair complexes and chromatin remodellers to access DNA[135]. Mammalian genomes are guarded via hierarchical organisation of chromatin and 53BP1, which prevents an excessive resection of DNA ends[144]. An excessive localisation of 53BP1 takes place at compact chromatin corresponding to TADs[135,144]. TADs comprising of transcriptionally silent genes located around the nuclear periphery and in close contact with the nuclear lamina form so-called lamina associated domains (LADs)[145,146]. To my knowledge, no studies have investigated the role of LADs in maintaining genome integrity.

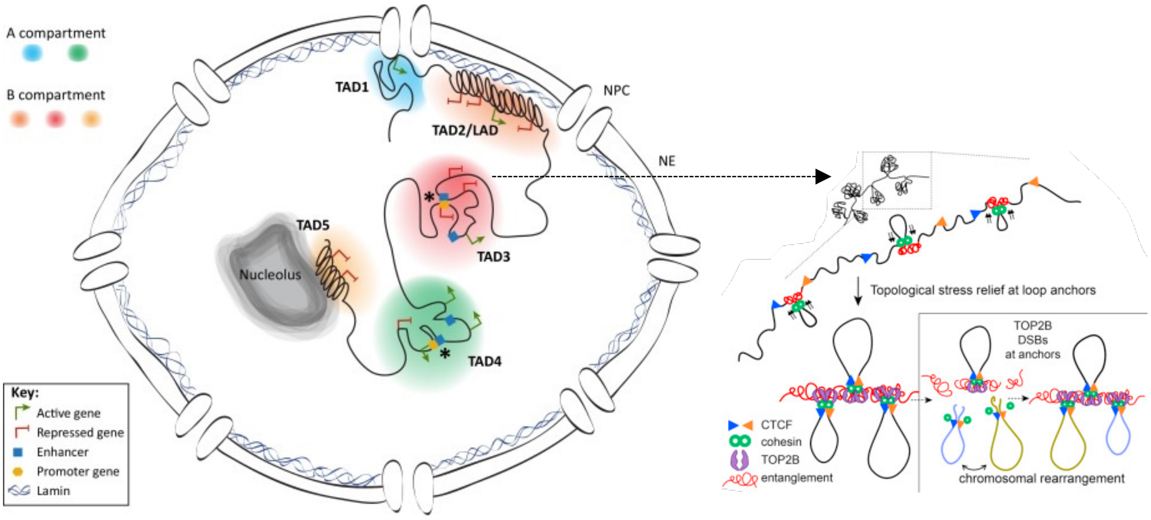

Figure 1.3.1 Spatial genome organization via topologically associated domains. Genome is organised into hierarchical compartments which control gene transcription. The figure was taken from Gonzalez-Sandoval et al. and Canela et al.[132,143].

1.3.2 The spatial organisation of the genome at the nuclear periphery

The nuclear lamina is a structural component of the cell that organises the genome landscape and provides mechanical support by stabilising the nuclear envelope (Figure 1.3.1)[147]. In addition to the formation of the nucleoskeleton, the nuclear lamina modulates chromatin organisation and gene transcription[148]. The nuclear lamina is a thin meshwork of intermediate filaments, which are in close contact with densely packed heterochromatin and nuclear pore complexes located on the inner nuclear membrane[146,149]. Interestingly, LADs are widely conserved between species LADs and contribute to epigenetic regulation of gene transcription from early developmental stages[150,148]. LADs often undergo conformational changes in transformed malignant cells mediated by the collapse of the nuclear lamina, resulting in the formation of micronuclei and chromosomal instability in cancer cells[151,152]. Interestingly, LADs have been described as hotspots for genomic lesions, which proposes that highly dynamic heterochromatin structures may prevent the access of DNA repair complexes[153].

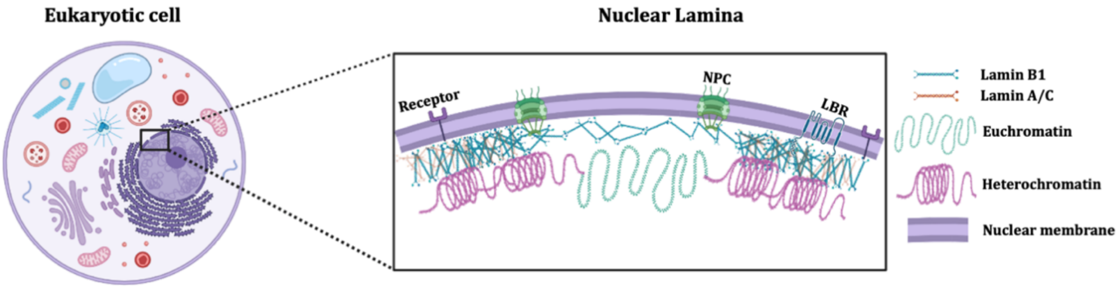

Figure 1.3.2 Graphic representation of nuclear lamina organizations. Nuclear lamina localises on the inner nuclear membrane, which contains several nuclear pore complexes (NPC), ion channels, and Lamin B receptor (LBR). Figure was generated in Biorender software.

1.3.3 Nuclear lamins

Lamins are evolutionary conserved type V intermediate filaments located primarily within the nucleus, concentrating at the nuclear periphery after assembling into more stable polymers[152,154]. Nuclear lamins can be subdivided to A-type (LMNA) and B-types (LMNB1, LMNB2) which both contribute to the compaction of chromatin at the nuclear periphery, forming transcriptionally repressive environment. Therefore, the interaction between lamins (B1 and A/C) and chromatin directly contributes to the regulation of gene transcription, DNA replication, cell cycle, and chromatin organisation[148,155]. While Lamin A/C expression fluctuates in cells during differentiation, Lamin B1 is continuously expressed and tightly regulated within every cell type throughout all developmental stages, including HSCs, neuroendocrine (NE) and embryonic stem (ES) cells, and immune cells[146,155,156]. All lamins assemble into same coiledcoil dimers and higher-order structures (proto-filaments), but differential expression suggests diverse molecular functions of A-type and B-type lamins[157]. The constant expression and stability of Lamin B1 in close association with the nuclear lamina is likely due to post-translational modifications (PTMs) at the C-terminus domain of Lamin B1. PTMs, including farnesylation, carboxymethylation, and phosphorylation of Lamin B1 prevent rapid degradation and allow for its retainment at the nuclear periphery (Figure 1.3.2 and 1.3.3)[158–160].

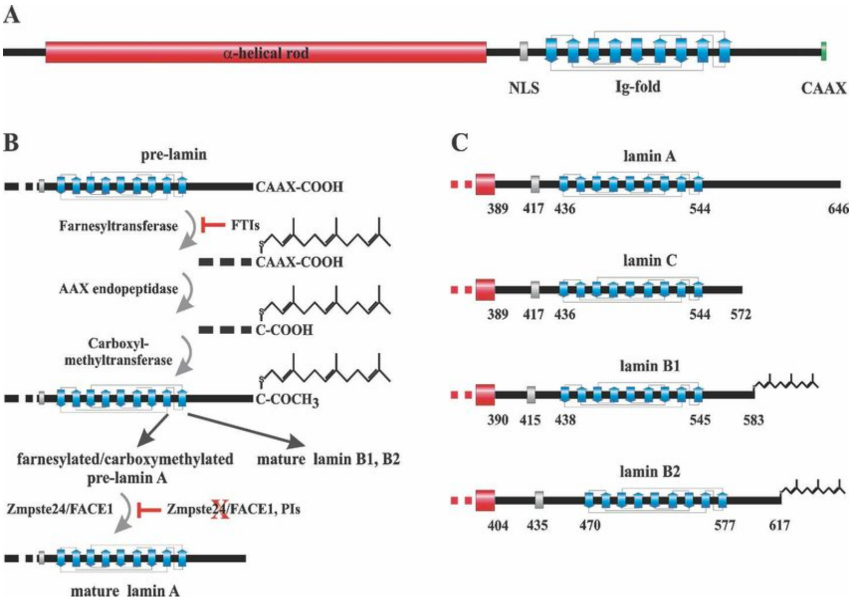

Figure 1.3.3 Structure of nuclear lamins. **(a)** Drawing of a pre-lamin polypeptide chain assembled of the central-helical rod domain (red) and the C-terminal –CAAX box (green). **(b)** Post-translational processing of pre-lamin B1 by addition of a farnesyl group to the cysteine residue of the –CAAX box **(c)** Schematic drawings of the C-terminal tail domains of mature lamins A, C, B1, and B2. Only Lamin B1 and B2 can be farnesylated and carboxymethylated, while Lamins A and C do not undergo these post-translational modifications. The figure was adapted from Dechat et al 2008[152].

1.3.4 The structure and function of Lamin B1

Lamin B1 forms parallel dimers which assemble into stable filaments through the interaction of central rod domains creating antiparallel nonpolar filaments. Nuclear localisation signal is found within the C-terminal tail and CAAX-box

(Figure 1.3.3)[161]. CAAX-box undergoes the above-mentioned post-translational modifications, which stabilise Lamin B1 and serve as anchorage of the protein filament to the nuclear membrane. Post-translational modification of Lamin B1 results in high stability, low turnover rate, and an average half-life of 1552 hours in B cells[162]. Lamin B1 expression is vital in the early stages of development, as shown by several Lamin B1 knockout studies *in vivo*[163,164]. Deletion of Lamin B1 in mice led to detrimental genetic defects and spontaneous malignant transformation of lung tissue[164]. Despite Lamin B1 expression being detected essentially in all cells regardless of the differentiation stage, fluctuation of Lamin B1 expression suggests regulation occurs at the protein level. Given a tight regulation of Lamin B1, several mechanisms of Lamin B1 degradation have been proposed[159,160,165,166].

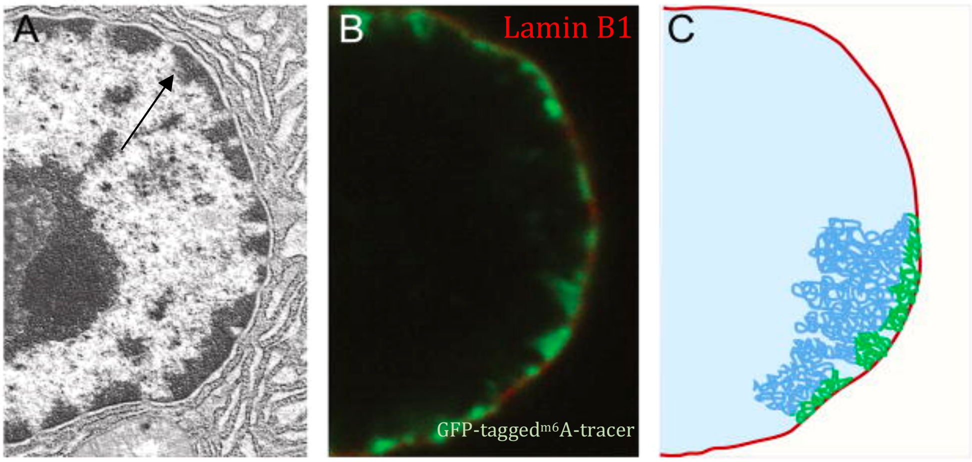

Figure 1.3.4 Visualization of LADs and Lamin B1. **(a)** Electron micrograph image mouse cell nucleus. Arrow indicates densely stained chromatin is closely associated with the nuclear lamina. Image provided by Kenneth M. Bart. **(b)** Labelling of DNA–NL contacts by co-expression of DAM-Lamin B1 and a GFP-tagged m6A-tracer protein associated with adenine-methylated DNA (green). Lamin B1 is shown in red. **(c)** Cartoon model illustrating how chromosome (blue) interacts with the NL through multiple LADs that form a heterochromatin layer (green). Figure adapted from Guellen et al.[146]

Lamin B1 expression was shown to be decreased upon oncogene-induced senescence (OIS) when p53 or Rb is activated, consequently leading to increased turnover of Lamin B1 protein and mRNA in senescent cells[167]. Lamin B1 was removed from the nuclear periphery and degraded via autophagic machinery upon OIS in human fibroblasts[165]. Alternatively, miRNA-23 was shown to act as a negative regulator of Lamin B1 in oligodendrocyte development and myelin formation, suggesting a cell type-specific mechanism of Lamin B1 regulation[168]. In line with this hypothesis, our group demonstrated induction of SHM in BL2 cells led to the removal of Lamin B1 from the nuclear periphery, allowing for point mutations to occur specifically within the *IGHV* region[131]. Lamin B1 protein expression was also reduced in splenic GCs of immunised mice, emphasising the importance of Lamin B1 in B cell biology, adaptive immune response, and genomic instability.

1.3.5 LADs regulate gene expression via Lamin B1

LADs were initially identified by DNA adenine methyltransferase identification (DamID) as gene-poor and transcriptionally silent regions covering approximately 40% of the genome across different cell types (Figure 1.3.4)[169,170]. Recent studies revealed LADs are enriched with developmentally regulated genes and genes associated with cell homeostasis[146,169]. LADs regulate cell-type specific gene expression profiles corresponding to cell differentiation, malignant transformation, or senescence (Figure 1.3.5)[148]. Genome-wide studies of Lamin B1 revealed a weak interaction with genomic regions within LADs leading to a large-scale chromatin relaxation[148]. Loss of Lamin B1 and repressive epigenetic modifications are essential to chromatin relaxation and transcriptionally active euchromatin[171,172]. However, some genes remain inactive upon chromatin relaxation and relocation away from the NL[172]. Kumaran et al. reported no difference in transcriptional rates upon trans-localisation of gene transcription reporter to NL, suggesting not all gene promoters associated with LADs are linked to lower transcription rates[173].

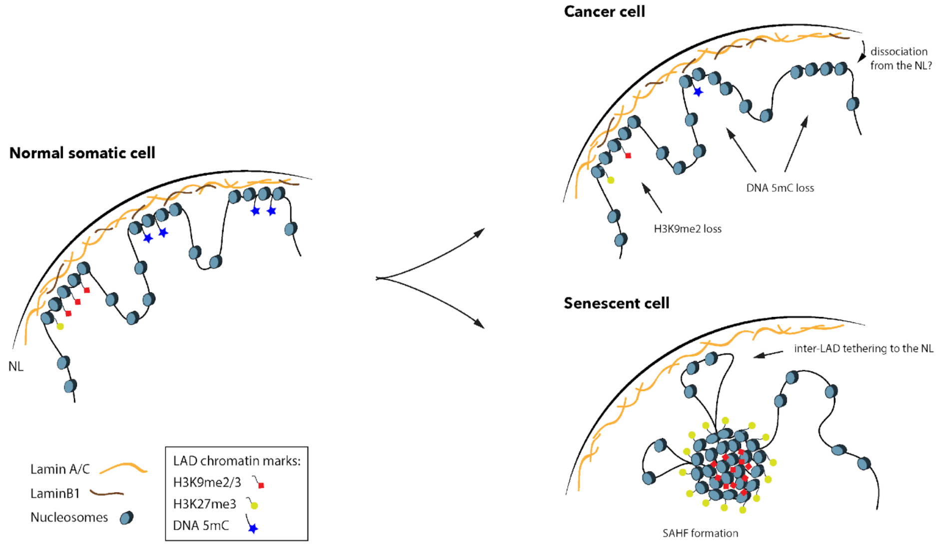

Figure 1.3.5 Proposed dynamics of LADs in normal and transformed cells. Transformation of cells is associated with the relocation of LADs upon dissociation from NL because of lamin depletion. The figure is taken from Lochs et. al 2019[148].

While Lamin B1 and Lamin A/C are mainly located at the nuclear periphery, nuclear lamins are associated with active euchromatin in the nucleoplasm[174,175]. Recently, Pascual-Reguant et al. demonstrated that Lamin B1 interacts with euchromatin in the nucleoplasm undergoing epithelial-to-mesenchymal transition (EMT) transcriptional signature in mice, which confirms Lamin B1 is not associated only with heterochromatin[160]. In addition to the well-documented Lamin B1 functions across different cell types and differential stages, novel evidence proposes that Lamin B1 has additional roles in regulating cell proliferation, DNA repair, differentiation, and genomic instability.

1.3.6 Role of Lamin B1 in DNA damage and repair

Fluctuating Lamin B1 expression has been linked to abnormal nuclear structure[33], reduced cell proliferation, and senescence[168,176–178]. Moreover, studies found Lamin B1 expression to be associated with chromatin instability and modulated DNA damage response (Table 1.3) in some cancer cell lines, including osteosarcoma (U2OS) and colorectal carcinoma cell lines (HCT166)[176,179–181]. Lamin B1 knockdown in these cell lines led to reduced proliferation and accumulation of cells in the S-phase as a direct result of stalling and collapse of the replication fork[176]. Furthermore, reducing Lamin B1 incorporation contributed to changes in the DNA repair genes, particularly the upregulation of NHEJ and decrease of

RAD51. ChIP-qPCR revealed Lamin B1 interacts with RAD51 and BRCA1 promoters, regulating the expression of these genes[176]. Additionally, radiation-induced DNA damage in Lamin B1-depleted cells revealed a delay in response of nucleotide excision repair pathway, further implicating the role of Lamin B1 in genome stability[181].

Lamin B1 expression	Cell line	Pathways involved
Acetylation	U2OS	Blockage of DNA repair[179]
High	U2OS	Inhibition of NHEJ[180]
Low	U2OS HCC	Chromatin instability[176]
Low	U2OS Hela	Restricted homologous recombination[182]
Low	U2OS	Inhibition of nucleotide excision repair[181]

Table 1.3 Lamin B1 is involved in the regulation of DNA repair pathways. Summary of studies demonstrating modulating Lamin B1 expression and post-translation modification influences DNA damage response and repair.

1.3.7 Decreased Lamin B1 is associated with GI signature in CLL

As described in Chapter 1.2, tightly controlled mutagenesis in B cells is vital for proper adaptive immune response. Despite recent reports, Lamin B1 dynamics within the context of DNA damage and repair in B cells remain unknown. Comprehensive analysis of mutations and gene expression obtained from CLL-8 cohort revealed Lamin B1 mRNA expression was downregulated in CLL patients classified as "genomically instable" (Figure 1.3.7 a,b). Furthermore, gene expression profiling revealed an increased expression of APOBEC members and cosmic signature 2 activation in GI and (I)GI (inflammatory) CLL subtypes, respectively (Figure 1.3.7 c).

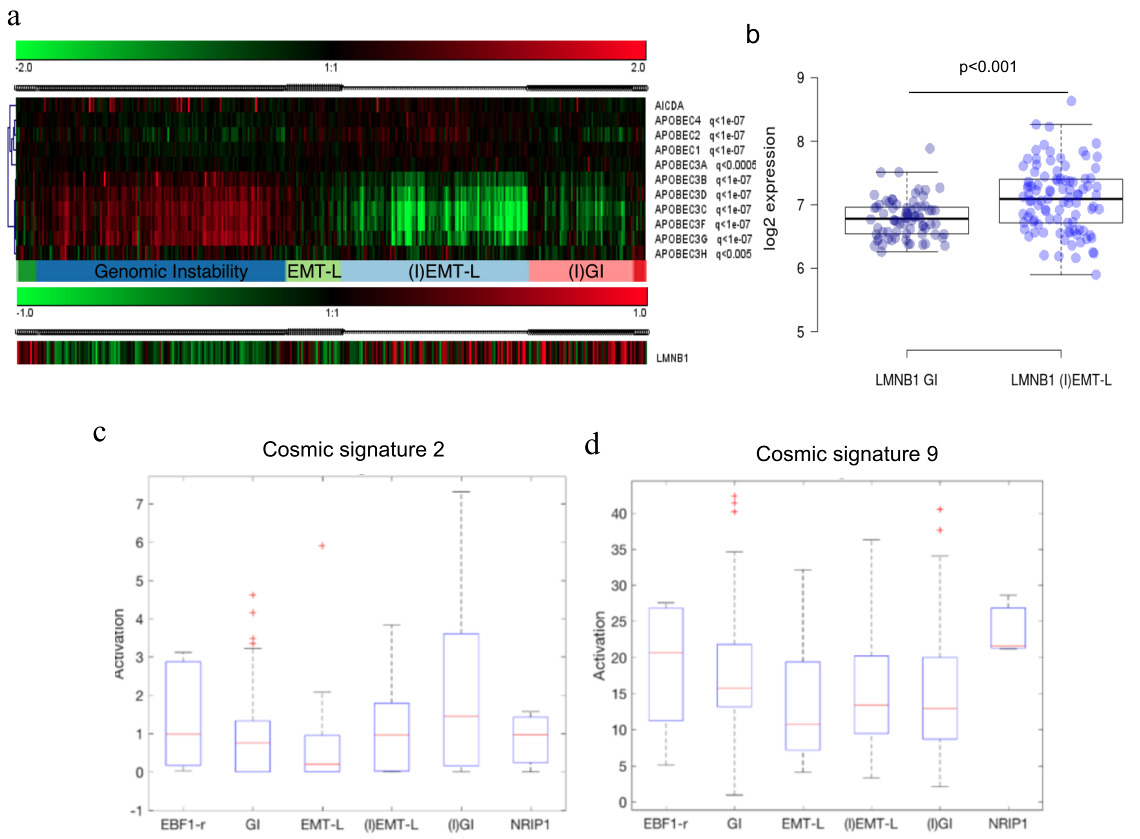

Figure 1.3.7 Genomically instable (GI) patients display decreased *LMNB1* and elevated expression of APOBECs. **(a)** Genomic instability signature negatively correlates with Lamin B1 expression in the CLL-8 cohort (817 patients). Data analysis was performed by Dr. Jonannes Bloehdorn. **(b)** Log2 CPM expression of *LMNB1* in GI and (I)EMT-L CLL subtype. N = 173. Mantel-Cox test was used for the statistical analysis. **(c-d)** Activation score of COSMIC **(c)** signature 2 and **(d)** signature 9 in CLL patients stratified based on mutational and gene expression profiles.

1.3.8. Role of Lamin B1 in adaptive immune response

Lamin B1 is known to be involved in chromatin remodelling and gene expression regulation via LADs[175,183,184]. Our group has demonstrated the importance of Lamin B1's role in GC B cells and adaptive immune response[131]. Lamin B1 was decreased in germinal centres of human lymphoid follicles and upon *in vivo* immunisation in mouse spleens (Figure 1.3.8.1). Lamin B1 ChIP-seq analysis revealed IgV domains were released from LADs' suppressive environment upon B cell activation, as demonstrated by decreased Lamin B1 DNA binding. Consequently, the release of the IgV gene from LADs allowed for high-frequency point mutations to occur within this region, allowing proper antibody generation driven by SHM and CSR events.

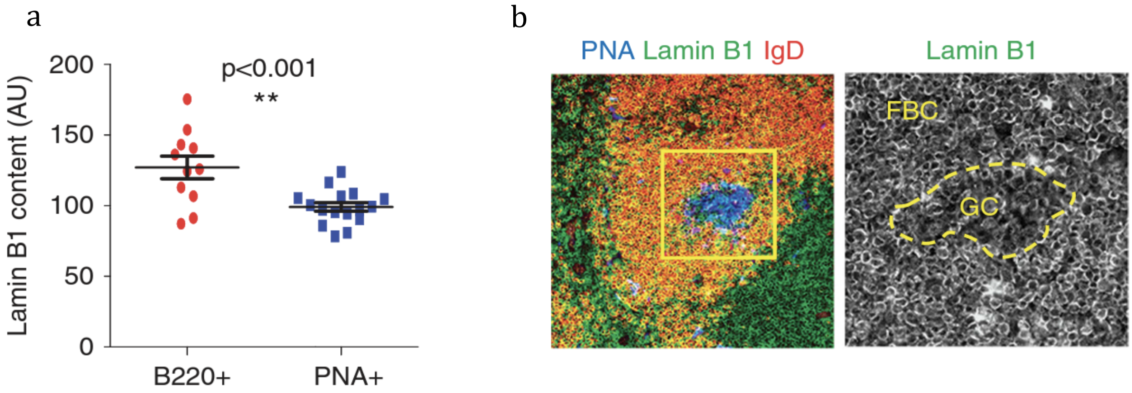

Figure 1.3.8.1 Lamin B1 is reduced in GC B cells compared to non-GC B cells. **(a)** Fluorescence intensity of the Lamin B1 within (PNA+ areas) or outside (B220+ or IgD+ PNA-areas) the GCs. At least 10 GCs from three spleens were analysed, and Lamin B1 fluorescence was compared with a similar number of randomly selected extra-GC areas of the same size. **(b)** Spleen GCs were stained with anti-Lamin B1 antibodies (AlexaFluor 488, green channel), Peanut Agglutinin (PNA) (Pacific Blue, blue channel), and anti-B220 or anti-IgD antibodies (AlexaFluor 594, red channel). The figure was adapted from Klymenko et al. 2018.

SHM is an essential part of the adaptive immune response required for the point mutations within the IgV region and antibody diversification[130]. Upon the antigen stimulation, somatic mutagenesis is initiated by the deamination of cytidine to uracil in the DNA sequence mediated by AID (Figure 1.3.8.2)[169]. The enzymatic activity of AID induces DNA lesions, which are subsequently repaired by DNA repair complexes, including mismatch repair (MMR), base excision repair (BER), and DNA polymerases[185]. AID lesions targeted specifically within the IgV region are repaired with lower fidelity than those in *Myc, Pax5,* and *Ebf1*, further suggesting the complexity and specificity of DNA repair machinery in GC B cells[186]. The second important step of adaptive immune response is CSR. CSR reaction is carried out through an intrachromosomal deletional recombination, which replaces a constant region in the immunoglobulin (Ig) heavy chain[28,187]. CSR is initiated by AID-induced deamination of cytosines in S regions, resulting in DNA single-strand breaks and subsequently converted to double strands by BER and MMR machinery[188]. The essential part of CSR is a programmed joining of double-strand DNA breaks carried out via NHEJ or microhomology-mediated end joining (MMEJ) pathway[189]. NHEJ is active in all phases of cell cycle, but particularly in G1 phase, while MMEJ is likely to be active in the S phase of the cell cycle[190,191]. Deficiencies in DSB repair mechanisms, including ataxia telangiectasia-mutated (ATM) and 53-binding protein-1 (53BP1), can result in impaired CSR and mutagenesis in B cell lymphoma[192,193]. However, Chapman et al. demonstrated that B cells can undergo robust CSR despite the lack of 53BP1-Rif-1 complex, an essential component of NHEJ[193].

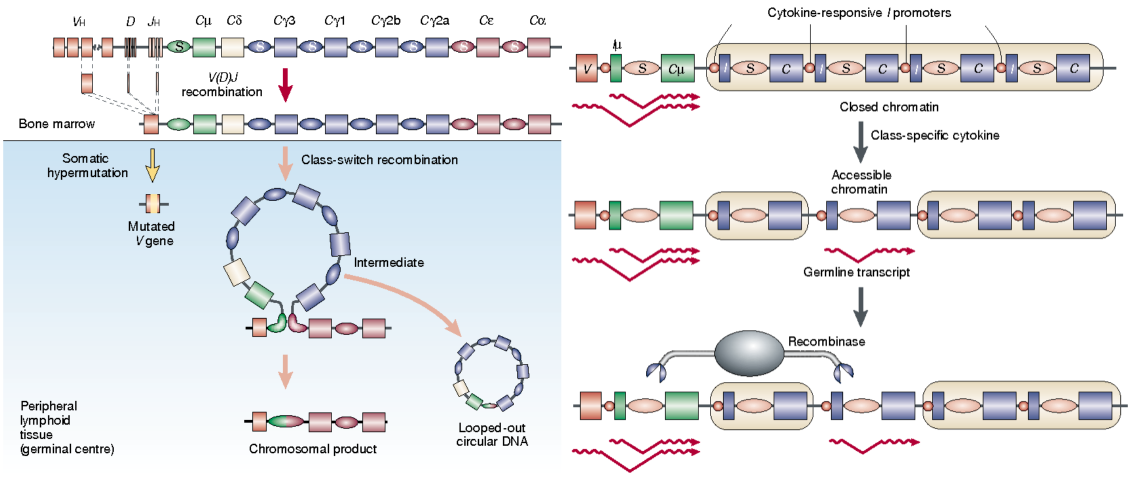

Figure 1.3.8.2 AID mediated mechanism of mutagenesis within the Ig region. Organization of IGHV gene. AID-driven SHM introduces frequent mutations in the rearranged V exon. Class-switch recombination brings the downstream constant (C) region exon in the proximity of the V exon by deletion between S*μ* and another S region upstream of the target C region[186].

1.3.9 Pathogenesis associated with dysregulation of Lamin B1

While the loss of function mutation in the LMNB1 gene has not been described nor associated with human malignancies, duplication in the LMNB1 locus has been established as the cause of a hereditary neurological disease, autosomal dominant leukodystrophy (ADLD)[194]. More recent studies demonstrate that Lamin B1 may indeed play an important role in tumorigenesis and could be used as a prognostic marker in cancer (Figure 1.3.9). For example, increased expression of Lamin B1 was shown to be a negative prognostic marker in colorectal cancer, pancreatic cancer, prostate cancer, and liver carcinoma[195–198].

On the contrary to these studies, decreased Lamin B1 expression was associated with high-grade lung carcinoma, acute myeloid leukaemia (AML), breast cancer, and worse clinical outcome in CLL and gastric cancer[131,164,199,200]. Specifically, Jia et al. 2019 have shown that Lamin B1 plays a tumour suppressor role in lung cancer by epigenetically controlling RET and suppressing metastasis[164]. Based on the current evidence, the clinical prognostic value of Lamin B1 appears to be highly cell-type specific, particularly in lung cancers and GC-derived B cell lymphomas.

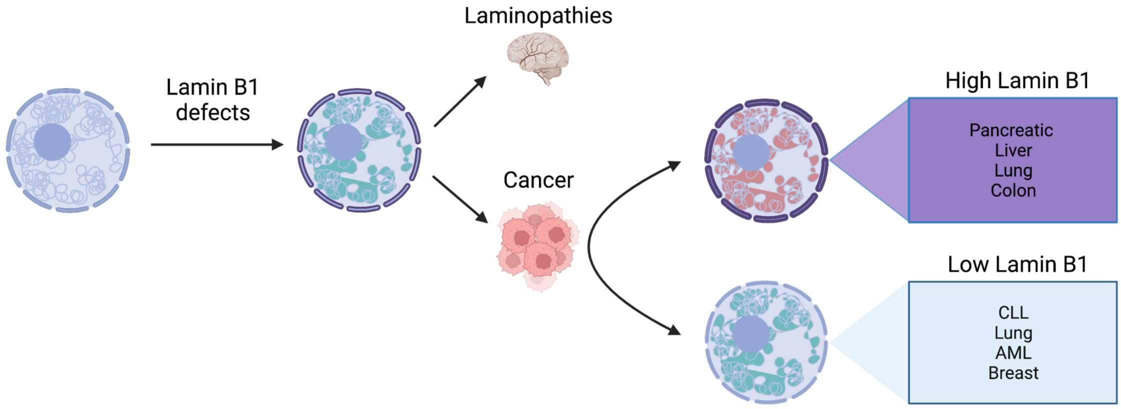

Figure 1.3.9 Pathology associated with dysregulated Lamin B1 expression. Fluctuating Lamin B1 is commonly linked to laminopathies and several cancer types.

1.3.10 Decreased Lamin B1 expression is a negative prognostic marker in CLL patients

Our group has previously shown the expression of Lamin B1 is a negative prognostic marker in CLL patients (Figure 1.3.10.1)[131]. Lamin B1 mRNA expression was associated with inferior progression-free and overall survival of CLL patients enrolled in the CLL-8 trial (Figure 1.3.10.1). Patients were dichotomised based on Lamin B1 expression, and a univariate Cox regression analysis was performed as a factor of the treatment regime. The analysis confirmed Lamin B1 is associated with a worse prognosis regardless of the given treatment. Lamin B1 comparison in diagnostic biopsies versus transformed counterparts revealed a decrease in Lamin B1 protein expression and a negative correlation with FL transformation (Figure 1.3.10.2). These findings suggest Lamin B1 expression and phenotype associated with Lamin B1 are cell type dependent.[129]

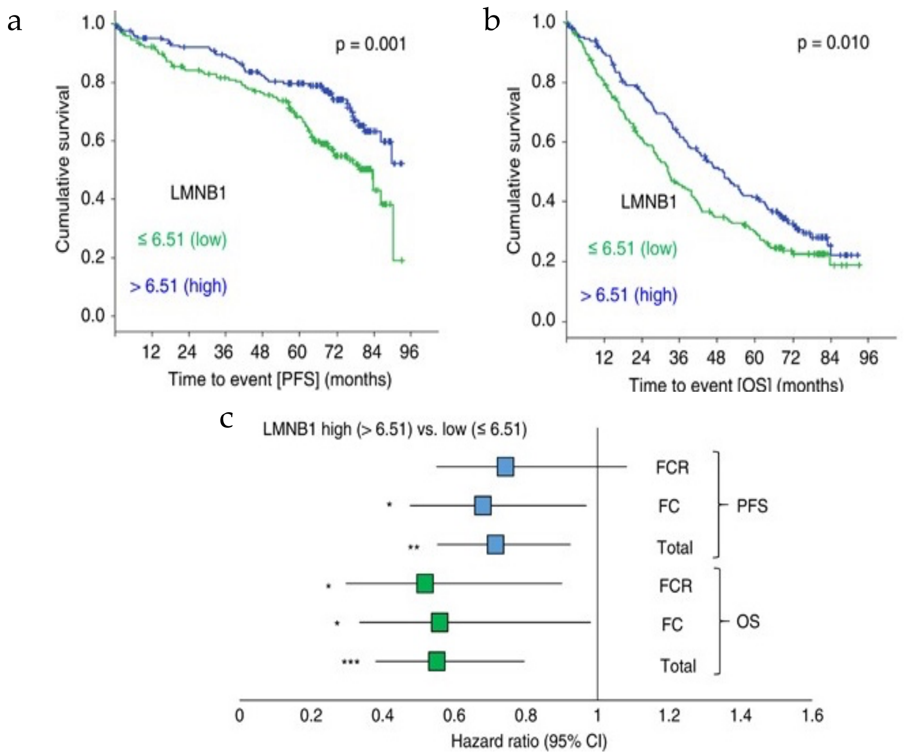

Figure 1.3.10.1 Lamin B1 expression is a prognostic marker in the CLL. **(a)** Kaplan–Meier estimates of progression-free (PFS) and overall (OS) **(b)** of CLL patients enrolled on the CLL8-trial as a factor of LMNB1 expression, dichotomised by the median (>6.51, *N*=168 and ⩽6.51, *N*=169). **(c)** Univariate Cox regression analysis comparing low (⩽6.51, *N*=169) and high (>6.51, *N*=168) LMNB1 expressing CLL patients as a factor of the treatment regime (FC or FCR) applied. *$P<0.05$, **$P<0.01$, ***$P<0.001$. Figure taken from Klymenko et al 2018[131].

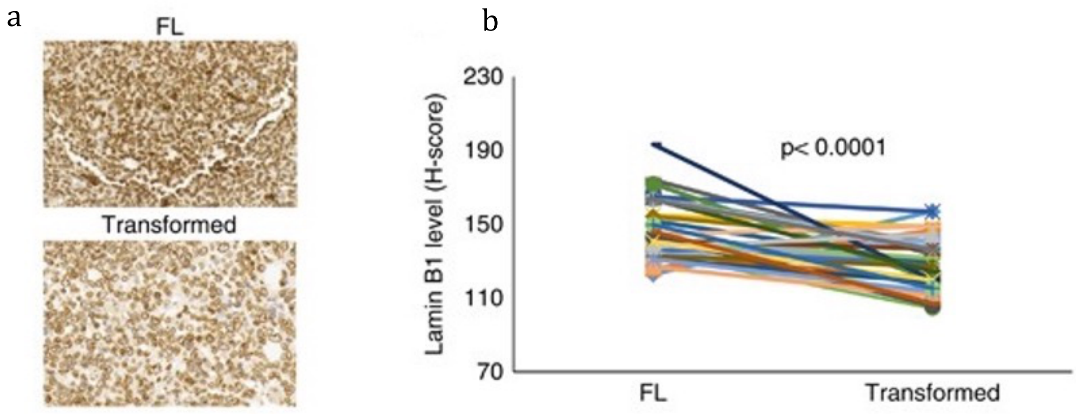

Figure 1.3.10.2 Decrease of Lamin B1 occurs in transformed follicular lymphoma patients. **(a)** Lamin B1 immunoreactivity in sequential biopsies from FL patients (top image) that later underwent FL transformation (bottom image). **(b)** Lamin B1 H-score values of 43 FL biopsies and their transformed counterparts. Each line connects two sequential biopsies from the same patient. Figure taken from Klymenko et al[131].

1.4 Project aims and hypothesis

The experimental work in this study was designed to define and evaluate the association of Lamin B1 and genomic instability in B cells using a comprehensive scope of experimental models (Figure 1.4). With clearly defined aims, I addressed the preliminary data generated by our group and provided further evidence of Lamin B1-mediated mutagenesis in B cells. Here, using advanced genetic engineering, I aimed to establish novel models precisely modulating Lamin B1 expression. Taking advantage of the expertise of our collaborators and institution, I aimed to define the consequences of Lamin B1 depletion using cutting edge NGS methods. I hypothesised Lamin B1 depletion in GC B cells would lead to genomic instability and modulation of the humoral response. By using conditional Lamin B1 hypomorphic *in vitro* and *in vivo* models, I aimed to identify genomic regions susceptible to DNA damage with respect to Lamin B1 and DNA accessibility. Lastly, to bring clinical relevance into this project, with a straightforward approach, I translated findings from our function studies into a clinical setting to evaluate Lamin B1 as a prognostic marker of survival in DLBCL patients.

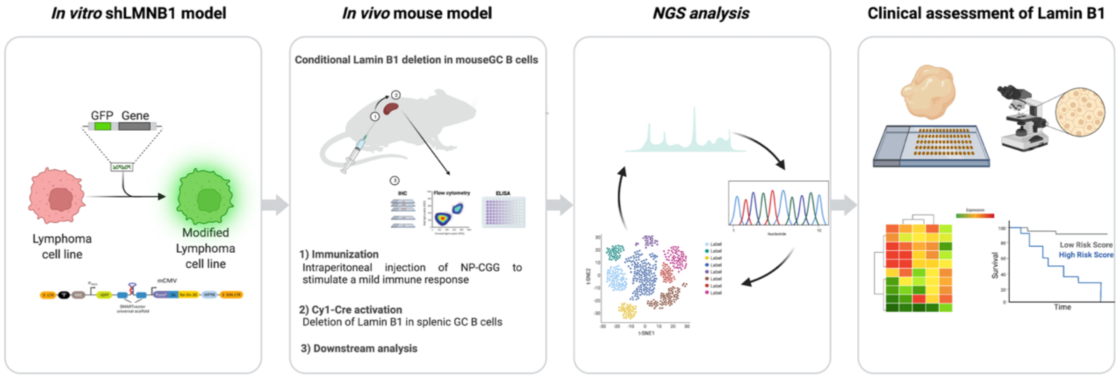

Figure 1.4 Graphical abstract of experimental aims and methods. Incorporation of a wide range of experimental models to elucidate the role of Lamin B1 in the normal and malignant B cells.

Experimental objectives of the project:

1. Analysis of Lamin B1 mediated mutagenesis in B cell lymphoma cells upon Lamin B1 silencing

2. Establishing of stable Lamin B1 knockdown model and assessment of genomic instability and gene expression upon Lamin B1 depletion

3. Generation of germinal centre B cell-specific Lamin B1 knockout mouse model and subsequent analysis of genomic instability and humoral response

4. Translation of *in vivo and in vitro* findings into the clinical setting and defining the value of Lamin B1 as a prognostic marker in GC-derived B cell lymphoma patient

5. Genome-wide analysis of DNA DSB profile upon Lamin B1 depletion in normal and malignant B cells

Chapter 2: Methods and Materials

2.1 Cell Lines

Burkitt's lymphoma cell line (BL2), germinal centre B cell (GCB) derived DLBCL cell line (OCI-Ly8), and Human embryonic kidney cells (HEK293) were obtained from the German Collection of Microorganisms and Cell culture (Deutsche Sammlung von Mikroorganismen und Zellkulturen, DSMZ). BL2 and OCI-Ly8 were cultured in the Roswell Park Memorial Institute 1640 (RPMI) medium supplemented with L-Glutamine, 10% foetal bovine serum (FBS), 1% Penicillin/Streptomycin (PS). HEK293 cells were maintained in Dulbecco's Modified Eagle's Medium (DMEM) supplemented with 10% FBS and 1% PS unless otherwise noted in the experimental protocol. Cell lines were kept at 37°C with 5% CO_2, passaged every 48 hours, and never cultured past passage number 20. Cells were routinely screened for mycoplasma contamination every 4 weeks. Cell lines used in the previously generated WXS experiment included BL2 AID$^{-/-}$ cells (provided by Claude-Agnes Reynaud (INSERM U1151, Paris)) and PCL12 (chronic lymphocytic leukaemia), obtained from DSMZ.

2.2 Generation of a stable Lamin B1 knockdown lymphoma model

To study the effects of reducing Lamin B1 nuclear incorporation in B cells, I generated stable cell lines expressing doxycycline-inducible shRNAs targeting Lamin B1 (Figure 2.1). Calcium phosphate transfection protocol was used to generate lentiviral particles containing specific shRNA sequences targeting Lamin B1 mRNA. HEK293 were transfected using Dharmacon trans-lentiviral shRNA Packaging kit with Calcium phosphate transfection reagents (TLP5913). $CaCl_2$ and 2 x HBSS were pre-warmed in a 37°C water bath. For a 100mm cell culture plate, the transfection mix was prepared by mixing 42 μg of lentiviral shRNA transfer vector, 30 μL of trans-lentiviral packaging, and x μL of H_2O to reach a total volume of 945 μL. After brief mixing, 105 μL of CaCl2 and 1050 μL of 2X HBSS were added to the transfection mix and incubated at RT for 3 minutes. Next, 10 mL of FBS-free DMEM (1 % PS, 0.15 μM chloroquine) was carefully added to the culture plate containing HEK293 cells. The transfection solution was added dropwise onto the culture dish carefully to prevent HEK293 from detaching. Transfected HEK293 cells were incubated at 37°C with 5 % CO_2 for 10 hours after which the media was replaced with fresh DMEM (1 % PS) and incubated for 48 hours. After 48 hours, viral supernatant was collected by centrifugation at 2000 *g* for 15 minutes at 4°C. The supernatant was passed through a 0.22 μm filter and immediately used for transduction of the target cell line, or aliquoted in 1.5 mL Eppendorf tubes and store at -80°C. BL2 or OCI-Ly8 cells were transduced with lentiviruses containing shRNAs (shLMNB1 #1: 5′-TTGGAGACAGCTTCAACCT-3′ [V3SH11252-224783461], shLMNB1 #2: 5′-CAACAACCACTCCAGCTGC-3′ [V3IHSMCG_8167334]). For transduction, viral supernatant was diluted with RPMI (8 μg/mL Polybrene) at a 1:1 ratio and centrifuged for 15 minutes at 1200 RPM at 4°C. After 48 hours, transduced cells were selected with puromycin at a 2.5 μg/mL concentration. To confirm the successful transduction of cells, 500ng/mL of doxycycline was used to induce the expression of fluorescent reporter protein (GFP) contained in the lentiviral transfer vector. As an indicator of transfection efficiency and positive shRNA induction, a percentage of GFP-expressing cells was assessed by flow cytometry 24 hours after the addition of doxycycline. Once the selection was completed, cells were cultured in the standard RPMI media described above. Cell counts and viability were measured with acridine orange/propidium iodide staining on Luna dual fluorescent cell counter (Logos Biosystems).

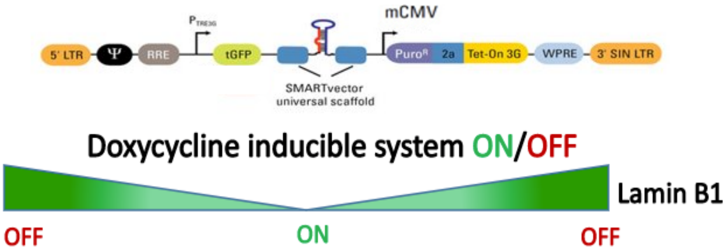

Figure 2.1 Schematic representation of doxycycline-inducible Lamin B1 knockdown lentiviral vector. SMARTvector inducible lentiviral shRNAs containing mouse Cytomegalovirus (mCMV) promoter, puromycin resistant gene, TurboGFP reporter, and Tet-On 3G doxycycline-inducible promoter were obtained from Dharmacon and used for transduction of target cell lines.

2.3 Doxycycline inducible silencing of Lamin B1

To perform and assess the Lamin B1 knockdown, transduced BL2 or OCI-Ly8 cells were seeded into a 6-well plate at a concentration of 2 x 10^5 cells/mL, and shRNA expression was induced by incubating cells with doxycycline at a concentration of 500 ng/mL. Cells were assessed for GFP expression by flow cytometry 24 hours after doxycycline induction. RPMI media containing doxycycline was replaced every 48 hours. Lamin B1 nuclear incorporation and total protein levels were assessed by immunofluorescence and western blotting, respectively. I selected two suitable shRNAs, which resulted in approximately 40 to 60% reduction of total Lamin B1 protein levels 72 hours after incubation with doxycycline.

2.4 Immunofluorescence

For immunofluorescence imaging, 2x10^5 cells were washed 3x with ice-cold phosphate-buffered saline (PBS) and spun onto a poly-l-lysine coated slide for 5 minutes at 400 rpm in Shandon Cytospin centrifuge (#22004). Immediately after centrifugation, cells were fixed in 4% paraformaldehyde (PFA) at RT for 15 minutes, subsequently washed with PBS, and permeabilised with 0.2% Triton-X/PBS for 15 minutes at RT. Slides were washed with PBS and blocked with 3% bovine serum albumin (BSA)/PBS-T (0.2%Tween) for one hour at RT. Slides were simultaneously incubated with primary antibody at specifically optimised concentration and time duration according to Table 2.1. Secondary fluorescently conjugated antibodies AlexaFlour-488 or AlexaFlour-594 were incubated and 4′,6-diamidino-2-phenylindole (DAPI) at 1 μg/mL for 45 minutes at RT in the dark. Following three washes with PBS-T, slides were mounted using an antifading solution and images were taken on Nikon Ci-L fluorescent microscope (for γH2AX), or with a confocal Zeiss LSM710 (for RAD51 and 53BP1) or LSM880microscope. ImageJ software was used to quantify foci were counted using MATLAB FoCo script.

Antigen	Antibody dilution and incubation time	Time	Species	Manufacturer and item number
Lamin B1	1:800 (1°) 1:600 (2°)	1 hour 45 minutes	Rabbit	Abcam ab16048
Lamin B1	1:400 (1°) 1:600 (2°)	Overnight 45 minutes	Mouse	Abcam ab8982
H2A.X phospho-Ser139	1:200 (1°) 1:500 (2°)	1 hour 45 minutes	Mouse	Abcam ab26350
Anti-53BP1	1:200 (1°) 1:500 (2°)	1 hour 45 minutes	Mouse	Novus Biologicals NBP2-25028
Anti-Rad51	1:200 (1°) 1:500 (2°)	1 hour 45 minutes	Rabbit	Invitrogen PA5-31144

Goat Anti-Mouse IgG H&L (Alexa Fluor® 647)	1°Ab dependent	1 hour	Mouse	Abcam ab150115
Goat Anti-Rabbit IgG H&L (Alexa Fluor® 488)	1°Ab dependent	1 hour	Rabbit	Abcam ab150077
Goat Anti-Mouse IgG H&L (Alexa Fluor® 594)	1°Ab dependent	1 hour	Mouse	Life Technologies A11005
Goat Anti-Rabbit IgG H&L (Alexa Fluor® 594)	1°Ab dependent	1 hour	Rabbit	Life Technologies A11037

Table 2.1 Primary and secondary antibodies used for immunofluorescence microscopy. For dual-colour fluorescent microscopy, both antibodies were used simultaneously at indicated concentrations. DAPI was used as a nuclear stain at a concentration of 1 μg/mL. Incubation with fluorescent antibodies was performed in the dark. All antibodies were stored as directed by the manufacturer's instructions.

2.5 Western Blotting

Total cell lysates were prepared by resuspending cells in NuPAGE LDS Sample buffer with the addition of protease and phosphatase inhibitors. Lysates were sonicated for 15 cycles (30 seconds ON/OFF) using Bioruptor Pico (B01060010). An equal amount of total lysate (~ 1 x 10^5) was loaded into each well and denatured at 95°C for 5 minutes, followed by electrophoresis separated by 4%-12% SDS-PAGE at 200 V for 35 minutes in a NuPAGE MES SDS running buffer (ThermoFisher, #NP0002). Separated proteins were transferred onto a methanol-activated PVDF membrane by wet transfer at 300mA for 1 hour. To prevent non-specific antibody binding, the membrane was blocked with 3% BSA/TBS-T for 1 hour at RT and incubated with primary antibody according to specified dilution and duration (Table 2.2). Following the incubation with the primary antibody, the membrane was washed 3x with TBS-T and incubated for 1 hour with corresponding secondary horseradish peroxidase (HRP)-linked secondary antibody, anti-rabbit IRDye 680RD secondary antibody, or anti-mouse IRDye 800RD secondary antibody (Table 2.2). The membrane was washed 3x with TBS-T before imaging. Images were developed using Pierce ECL Substrate (ThermoFisher #32106) and Amersham Imager 600RGB system or Li-Cor imaging system. Images were processed in Image Studio or ImageJ.

Antigen	Antibody dilution	Time	Species	Manufacturer and item number
Lamin B1	1:2000	1 hour	Rabbit	Abcam ab16048
H2A.X phospho-Ser139	1:500	Overnight	Mouse	Abcam ab26350
Anti-53BP1	1:500	Overnight	Rabbit	Novus Biologicals NBP2-25028
Anti-Rad51	1:1000	Overnight	Rabbit	Invitrogen PA5-31144
GAPDH	1:10000	1 hour	Mouse	SigmaAldrich G8795
Tubulin	1:10000	1 hour	Mouse	Cell Signalling #2125S
HRP-secondary linked anti-rabbit IgG antibody	1:10000	1 hour	Goat	Cell Signalling #7074
HRP-secondary linked anti-mouse IgG antibody	1:10000	1 hour	Goat	Cell Signalling #7076
IRDye® 680RD Donkey anti-Rabbit IgG (H + L)	1:10000	1 hour	Donkey	Li-Cor 926-68073
IRDye® 800RD Donkey anti-Mouse IgG (H + L)	1:10000	1 hour	Donkey	Li-Cor 926-32212

Table 2.2 Primary and secondary antibodies used for western blotting. All antibodies were diluted in a 3% BSA (TBS-T) solution. Diluted antibodies were applied directly onto the nitrocellulose membrane and placed on a roller for the indicated duration. Overnight incubations were carried out at 4°C.

2.6 Single-cell electrophoresis

Single-cell electrophoresis (COMET) assay was used to measure DNA breaks in BL2 cells upon Lamin B1 knockdown. The COMET protocol was adapted from the Trevigen Comet Assay kit (4250-050-K) with minor adjustments described below. Harvested cells were pelleted and washed with ice-cold PBS and mixed with 1% low-melting-point molten agarose (37°C) in a 1:10 cell to agarose ratio. Immediately after mixing of cells with agarose, 50 µL of suspension (~1000 cells) was spread evenly onto pre-chilled CometSlide and let to cool down at 4°C for at least 20 minutes in the dark before the immersion into lysis solution at 4°C overnight. Slides were briefly washed in PBS and incubated in a freshly made 4°C alkaline solution (pH > 13) for an hour in the dark. The electrophoresis was carried out in 4°C alkaline electrophoresis solution with an electric potential set to 21 volts for 20 minutes. The volume of the electrophoresis solution was adjusted to maintain an electric current of 300 mA. Immediately after electrophoresis, slides were washed in H_2O for 5 minutes and immersed in

70% ethanol for additional 5 minutes. To bring cells into a single plane for an easier comet visualization, slides were airdried at 37°C for at least 15 minutes. SYBR Gold (1/10000) was used to stain DNA for 30 minutes at RT in the dark. Slides were then washed 3x for 5 minutes, air-dried in the dark, and images were taken using Nikon Ci-L upright fluorescent microscope at 20X magnification. TriTex CometScore 2.0 automatic comet assay software was used to assess DNA damage as a proportion of a tail moment (% of DNA in tail * Tail Length) measurement obtained from the comet scoring software. At least 100 comet tails were analysed per condition. Cells with a tail moment > 250 were filtered out as apoptotic cells.

2.7 Cell proliferation assay

Cell proliferation was assessed by FACS using Click-iT Plus EdU Flow cytometry Alexa Fluor 488 Imaging Kits (Invitrogen/Thermo-Fisher, Paisley, UK). Cells were plated onto a six-well plate at a concentration of 5×10^5 cells per mL, twenty-four hours before EdU incubation. Logarithmically growing BL2 cells were incubated with 10 μM EdU for 2 hours and processed according to the manufacturer's protocol. The proportion of EdU+ cells was assessed by flow cytometry. For the assessment of the cell cycle distribution, cells were washed with PBS three times and fixed with ice-cold 70% ethanol for 1 hour at -20°C. Cells were washed with Wash/Stain buffer three times and incubated with DAPI (1 μg/mL) for 20 minutes in the dark. At least 10,000 cells were acquired for the analysis by flow cytometry, and data were analysed in FlowJo software.

2.8 Flow cytometry analysis

For GFP flow cytometry analysis in shLMNB1 cell lines, 1×10^6 live cells were washed with PBS and stained with DAPI (1/1000) before flow cytometry analysis. At least 10,000 cells were analysed for GFP expression. For γH2AX-ser139 analysis, 1×10^6 cells were washed with PBS (3% BSA), fixed with ice-cold 70% Ethanol, and placed at -20°C for 1 hour. Cells were washed three times with PBS (3% BSA) and stained with anti-γH2AX (ser139) antibody for 30 minutes at 4°C. Cells were washed twice with PBS (3% BSA), incubated with DAPI (1/1000) for 20 minutes, and analysed by flow cytometry for γH2AX and cell cycle analysis.

2.9 WXS and topology mapping

Whole exome sequencing (WXS) was performed to test whether Lamin B1 mediated mutagenesis is specific to IgV clusters as described by Klymenko et al. Control or siRNA-treated cells were used to assess mutational burden upon LaminB1 transient knockdown. WXS was carried out HiSeq 2x150bp and with an average sequencing depth 500X for BL2 AID^{wt}, BL2 AID$^{-/-}$, and PCL12^{wt} cells 48 hours after transfection with siRNAs targeting *LMNB1*, as described by Klymenko et al. 2018[131]. Raw reads were paired and trimmed adapters using fastp. Reads were mapped to the hg38 reference genome by BWA-MEM. Single nucleotide variants were called with Mutect2 (v3.5) and deconstructSigs was used for signature deconvolution. Mutational clustering was performed using karyoplotR (v1.22.0) package. To assess mutational signature, I utilised a comprehensive mutational catalogue COSMIC (v83) by analysing characteristics of mutational patterns and different substitutions (official COSMIC patterns: C > A, C > G, C > T, T > A, T > C, and T > G). Dr Jun Wang helped with the analysis of FASTQ files and the calling of mutations using Mutect2.

2.10 RNA isolation

RNA extraction was carried out using RNeasy Qiagen Kit. Briefly, 2x10^6 BL2 cells were harvested and pelleted in a 1.5mL Eppendorf tube. The cell pellet was resuspended in 350 µL of RLT buffer, then added and mixed in 350 µL of 70% ethanol to the lysate. Up to 700 µL of the sample was transferred to RNeasy Mini spin column, placed in a collection tube and centrifuged for 15s at 8000 *g*. After discarding the flow-through, 700 µL of RW1 was added to the RNeasy spin column and centrifuged for 15s at 8000*g* and the same step was repeated twice with 500 µL of RPE buffer. RNeasy spin column was centrifuged for 1 minute at maximum speed to dry the membrane. Isolated RNA was quantified by Nanodrop and submitted to Genewiz for library preparation and pair-end sequencing.

2.11 RNA sequencing

RNA was extracted using RNeasy Qiagen Kit according to the manufacturer’s protocol. Briefly, 2 x 10^6 BL2 cells were harvested for RNA extraction and library preparation. Pair-end sequencing was performed using Illumina HiSeq 2500 with a minimum of 30 million reads per sample. Briefly, adapter sequences in raw FASTQ files were trimmed using TrimGalore (v0.6.3) and then aligned to the human genome (hg19) with HISAT2 (v2.1.0). QualiMap (v2.2.2) was used to assess the quality of alignment and raw read counts were quantified with FeatureCounts (v1.6.4) and used for downstream analysis (Figure 2.2).

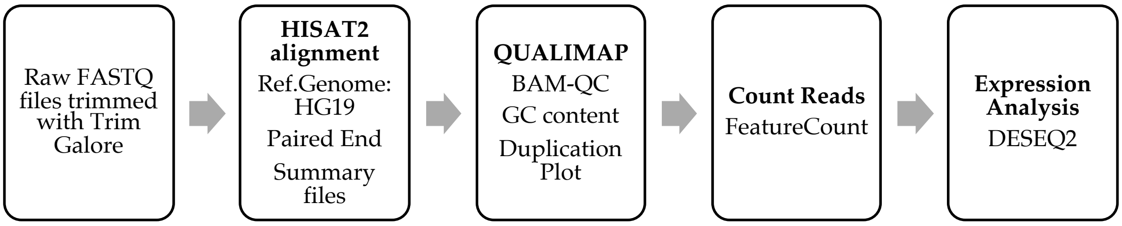

Figure 2.2 Streamlined workflow of RNA-seq analysis of BL2 cells

2.12 Differential gene expression analysis and GSEA

Differential gene expression analysis was computed by the DeSEQ2 (v1.28.1) package in R. Significant differentially expressed genes (DEG) were filtered based on p-adjusted (padj) value less than 0.05 and log2 fold change (log2FC) greater than 0.58 or less than -0.58. GSEA was performed using fgsea (v1.14) package and default setting. For GSEA, pathways were considered significantly enriched with a normalised enrichment score (NES) greater than 1.0 or less than 1.0 and padj less than 0.05.

2.13 *In vivo* experiments and procedures

2.13.1 Deletion of Lamin B1 in mouse splenic germinal centre B cells

All mice were on the C57BL/6 background. I utilised the *Cre/loxP* system, which engages *Cre*-mediated deletion of Lamin B1 (Figure 2.4). GC-specific LMNB1 deletion was accomplished by crossing C57BL/6N-Lmnb1$^{\mathrm{tm1c(EUCOMM)Wtsi}}$/WtsiH (referred to as Lamin B1$^{\mathrm{fl/fl}}$) strain, obtained from EMMA (EM:10615), and B6.129P2(Cg)-*Ighg1*$^{tm1(cre)Cgn}$/J (referred as $C\gamma 1^{+/cre}$) kindly provided by Dr. Dinis Calado (Crick Institute, UK) depicted in Figure 2.5. $C\gamma 1^{+/cre}$ mouse model specifically activates constitutive expression of *Cre* recombinase from the transcription of endogenous immunoglobulin heavy constant gamma 1 locus, Ighg1,($C\gamma1$) gene which transcribed in GC B cells[201]. Therefore, the generation of transgenic $C\gamma1^{+/cre}$ x $LaminB1^{fl/fl}$ mouse model allowed me to study the effect of Lamin B1 deletion specifically in GC B cells. *Cre* recombinase activation was induced by stimulation of immune response by NP-CGG immunization (Scheme 2). *Cγ1-Cre* were used as heterozygous for Ighg1<tm1(cre)Cgn> gene, and $\mathrm{LaminB1}^{fl/fl}$ strain was homozygous for $\mathrm{Lmnb1}^{tm1a(EUCOMM)}$/WtsiH. All experiments involving mice were performed under Queen Mary of London Veterinary oversight with UK Home Office authorization. All control and experimental mice were randomised among littermates. Marta Crespi-Sallan helped with the *in vivo* experiments and the maintenance of the mouse colony. Mouse tissue was obtained from each animal by ear clipping, and tissue samples were processed by Transnetyx.

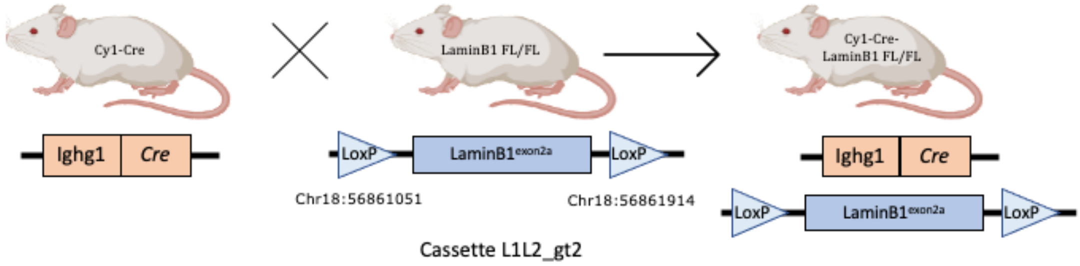

Figure 2.4 Generation of inducible GC B cell-specific Lamin B1 knockout mouse model.

2.13.2 Mice immunization

Mouse models used for the experimental procedures were males and females of 8-12 weeks old. Stimulation of mild immune response was prompted by intraperitoneal (IP) injection of 100 μL ImjectTM Alum Adjuvant with 100 μg of NP-CGG (Chicken Gamma Globulin) Ratio 10-19 (N-5055B-1, 2B Scientific) at a concentration 0.5 mg/mL. The drug was resuspended before IP injections, and animals were monitored regularly immediately after the drug administration.

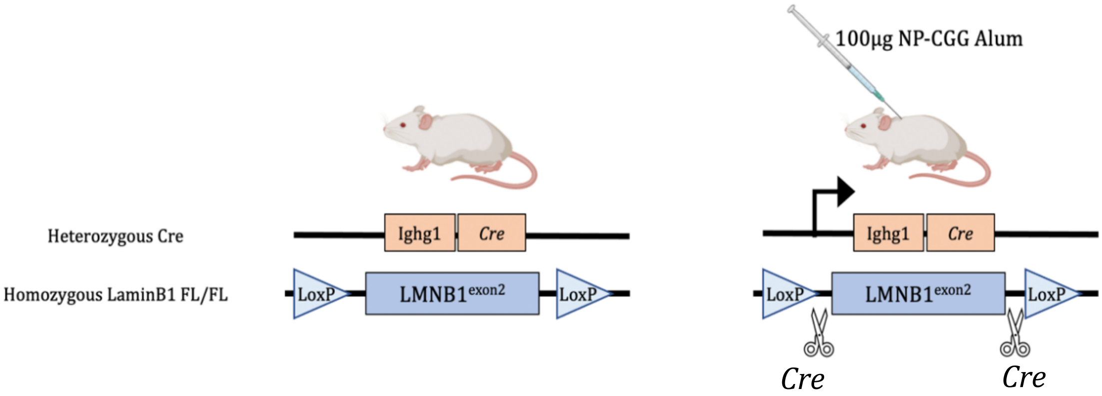

Figure 2.5 Generation of a GC B cell-specific Lamin B1 knockout model. Lamin B1 deletion specifically in GC B cells is achieved by Cre recombinase activity in GC B cells expressing Ighg1 gene.

2.13.3 Histology

Immediately after the end of mouse experiments, spleens were dissected before fixation in 10% neutral buffer formalin for 24 hours. Fixed spleens were placed in 70% ethanol for a minimum of 24 hours before embedding in paraffin blocks and sectioned for immunohistochemistry staining.

2.13.4 Flow cytometry of B cell membrane surface markers to assess B cell differentiation

To label cell surface B cell differentiation markers, single-cell splenocyte suspension was made by disaggregating fresh spleen tissue using the 70 µM strainer and resuspending cells in PBS (10% FBS). Cells were centrifuged for 10 minutes at 1500 RPM at 4°C. After discarding the supernatant, red blood cells were lysed with 1x RBLB for 5 minutes at RT. Cells were washed with ice-cold PBS and centrifuged for 10 minutes at 1500 RPM at 4°C. Live cells were then washed with PBS and resuspended in PBS (2% FBS) containing fluorochrome-labelled antibodies (Table 2.3). After 20 min incubation at 4°C, cells were washed with PBS and assessed by FACScalibur analyser (BD Biosciences, Oxford, UK). Single stains and FMOs were used for setting up compensation parameters and gating strategies, respectively. At least 10,000 cells were analysed per sample.

Antigen	Dilution	Item number
PE Rat Anti-Mouse T- and B-Cell Activation Antigen clone GL7	1:100	BD Biosciences #561530
FITC Rat Anti-Mouse IgM clone R6-60.2	1:100	BD Biosciences #553408
PerCP-Cγ™5.5 Rat Anti-Mouse IgD clone 11-26c.2a	1:100	BD Biosciences #564273
APC anti-mouse CD19 Antibody 1D3/CD19	1:100	BD Biosciences #550992
BV421 Rat Anti-Mouse CD138 clone 281-2	1:100	BD Biosciences #566289
FITC anti-mouse IgG1 Antibody clone RMG1-1	1:100	BD Biosciences #406605
BV786 Rat Anti-Mouse CD45R/B220 clone RA3-6B2	1:100	BD Biosciences #563894
FITC Hamster Anti-Mouse CD95 clone Jo2	1:100	BD Biosciences #554257
PE Rat Anti-Mouse CD38/ clone 90/CD38	1:100	BD Biosciences #553764
BV421 Rat Anti-Mouse CD138/ clone 281-2	1:100	BD Biosciences #562610
BV711 Rat Anti-Mouse CD86/ clone GL1	1:50	BD Biosciences #740688
PerCP anti-mouse CD19 Antibody 6D5 Rat IgG2a, κ	1:100	Biolegend #115532
APC anti-mouse CD95 (Fas)	1:100	Biolegend #152603
Fixable Viability Dye eFluor 780	1:100	eBioscience #65-0865-14
APC Rat anti-Mouse CD184 Clone 2B11/CXCR4	1:50	BD Biosciences #558644

Table 2.3 Fluorophore-conjugated antibodies and reagents used for B cell surface marker analysis by flow cytometry analysis. AbC™ Total Antibody Compensation Bead Kit (Invitrogen A10513) was used for the compensation and voltage adjustment.

2.14 Immunohistochemistry

Paraffin embedding samples were dewaxed twice in 100% Xylene for 3 minutes, followed by single incubation in 100% ethanol for 3 minutes and twice in 100% ethanol (3% H_2O_2) for 3 minutes to block endogenous peroxidases. Before the antigen retrieval step, samples were placed in 100% ethanol and deionised H_2O for 3 minutes. Antigen retrieval was carried out by boiling the samples at a maximum temperature in the pressure cooker in the presence of 1 x antigen unmasking solution (Tris-Based or Citrate-based) for a minimum of 10 minutes. Slides were then placed in 1x DAKO wash buffer and followed by staining with primary and secondary antibody staining. Secondary HRP-linked antibody signal detection was carried out by incubating samples with VIP reagent for a maximum of 10 minutes and immediately placing them in H_2O to remove excess colour. Samples were placed in Haematoxylin for 3 minutes and rinsed with water, followed by three dips in acid alcohol and 3 minutes in Scott's solution. To dehydrate samples, slides were placed in three tanks containing 100% ethanol for 3 minutes and incubated in 100% xylene. Slides were then mounted with coverslips, allowed to air dry, and scanned with digital slide scanner NanoZoomer S210 (Hamamatsu C13239-01) at 20 x original magnification. Multiplex immunohistochemistry on the same tissue section was performed by stripping the previous staining and performing the protocol described above with different staining, which allowed subsequent probing with several antibodies on the same tissue (Figure 2.6). Spleens were firstly stained with Haematoxylin for QuPath single-cell detection, Ki-67 staining was used as a proliferation marker of GC B cells, and subsequently, tissues were stained for Lamin B1 and γH2AX-ser139 (Table 2.4). At least four randomly selected GCs per spleen from a minimum of four different mice were selected and used for analysis. Human DLBCL tissue microarrays were stained for CD20, Lamin B1, and γH2AX. Each staining procedure contained negative control (no primary antibody), which was used to confirm the stripping of previous staining and no background staining effect. Raw images were processed and analysed in QuPath (0.2.3) and Fiji (2.0.0).

Antigen	Dilution	Time	Species	Manufacturer and item number
Lamin B1	1:800	45 minutes	Rabbit	Abcam ab16048
H2A.X phospho-Ser139	1:200	45 minutes	Mouse	Abcam ab26350
Ki67	1:200	1 hour	Rat	Dako M7249
CD20	1:200	1 hour	Mouse	Dako M0755

Table 2.4 Primary and secondary antibodies used for IHC on human and mouse tissues. Indicated concentration and incubation times were optimised for each tissue type.

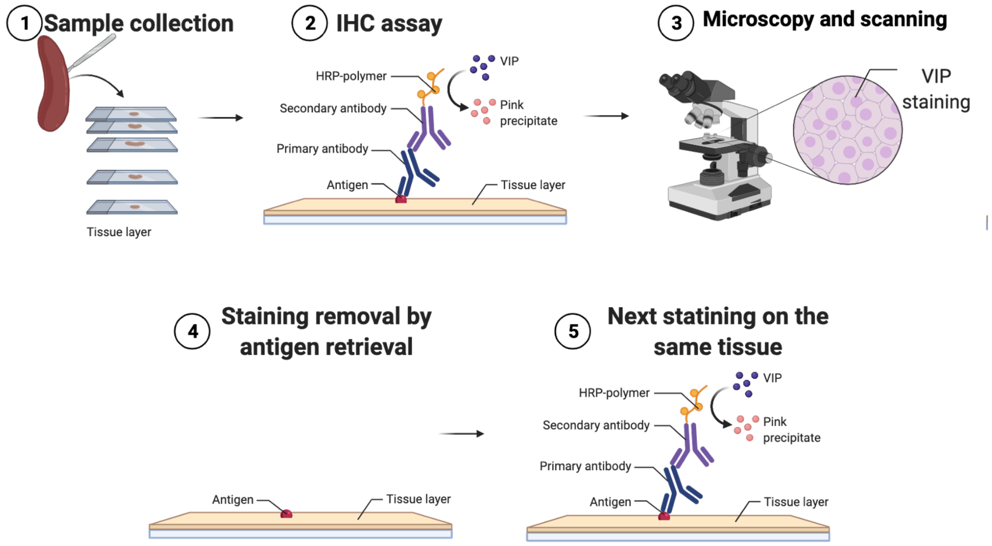

Figure 2.6 Schematic representation of multiplex IHC staining procedure. Slides were scanned with S210 Nanozoomer at 40 X magnification and raw images were processed in QuPath and Fiji.

2.15 fBALM microscopy SMLM microscopy

2.15.1 Immunofluorescence staining protocol

BL2 shLMNB1 were incubated for 72 hours with doxycycline to induce Lamin B1 gene knockdown. Cells were washed with 1 × PBS+Ca/Mg, cyto-spun onto poly-l-lysine coated slides, and fixed with 4% formaldehyde for 10 minutes at 37°C. Cells were rewashed three times in 1× PBS+Ca/Mg permeabilised with 0.2% Triton X-100 in 1 × PBS+Mg/Ca for 10 min. Slides were incubated in blocking solution (2% BSA in 1 × PBS+Mg/Ca) for 1 hour and subsequently incubated with the primary antibody at room temperature for 1 hour. The antibody concentrations were optimised specifically for this cell line for confocal microscopy The primary antibody was washed off three times in 1 × PBS+Mg/Ca on a shaker for 5 min. Samples were incubated with the secondary antibody at room temperature in the dark for 45 min. The cells were also stained with the DNA-binding fluorescent stain DAPI (1/1000). Slides were then embedded in ProLong Gold medium on a new slide and covered with coverslips and left to was left to polymerise for 24 hours at room temperature before sealing the coverslips. Images were acquired and processed by Katarina Chapman using the microscope built by Dr. Wladimir Schaufler located at the Light Microscopy Facility of the German Cancer Research Centre (DKFZ).

2.15.2 DNA-binding with Sytox Orange for fBALM imaging

Imaging of intranuclear proteins and DNA was performed with dual-colour staining in combination with the DNA-binding dye Sytox Orange, a DNA intercalator that binds to double-stranded DNA. Prior to Sytox Orange staining, the cells were treated with an RNA digestion buffer (RNAase A) diluted at a ratio of 1:1000 in PBS at 37°C for 15 minutes. Sytox Orange was added to the sample (1 μg mL^{-1}) for 30 min at 37°C. Then, the cells were washed 3 times with 1× PBS and 0.1% Tween-20, incubated with PBS and sealed with coverslips. Samples stained with Sytox Orange were imaged by DNA structure fluctuation-assisted BALM (fBALM). Before imaging, samples were incubated with a glucose oxidase (GLOX) based oxygen-scavenging buffer as described by Szczurek et al 2017.

2.15.3 SMLM Data analysis

Images were reconstructed by localizing fluorophores using the previously established algorithm program SMLM.py[202] and the open-source program ThunderSTORM. The dual-colour localisation precision of fBALM measurements were imaged in ProLong Golg. ThunderSTORM settings were as follows: a wavelet filter for image filtering, detection of local maxima with a threshold (1x Standard deviation) of the intensity values from the first wavelet deviation and the approximate localisation of fluorophores. Symmetric 2D Gaussian function for the subpixel localisation approximated with the least-squares method. Cross-correlation was used for drift correction with the default settings (bin number and magnification set to 5, merging molecules) for post-processing of the images. Analysis was performed by Katarina Chapman.

2.15.4 Cluster analysis

The algorithm density-based spatial clustering of applications with noise (DBSCAN) developed by Ester et al. was implemented for the detection of clusters with an arbitrary shape, different from noise signal[203]. We also detected the number of points per cluster, the number of clusters per nucleus, the cluster areas and cluster densities. The spatial distribution of clusters was assessed by the distance frequency of points within clusters, and the centre of mass of the clusters. To compare clusters detected in the control and shLMNB1 nuclei, the same parameters were chosen for uniform detection in both samples. Analysis was performed by Katarina Chapman.

2.15.5 Voronoi Analysis

Voronoi tessellation of point clouds was applied to SMLM data to segment regions according to the Euclidean distance between observed molecules. The area of cells is inversely proportional to the density of the points. A python-implemented program written by Nicolas Peschke, Cremer group, IMB Mainz, was used for the Voronoi density analysis. Localisation of the data points transformed into the polar coordinates (the centre of mass of the nucleus being the coordinate system's origin) to visualise the Voronoi analysis as a function of the nucleus's radius r or angle θ. by dividing by the number of localisations. Analysis was performed by Katarina Chapman.

2.15.6 Line Profile Analysis and Colocalisation Analysis

To specifically study the density distribution of LaminB1 proteins as a line profile along the nuclear periphery, a program was written to show the LaminB1 intensity in a selected radial interval as a function of the polar angle θ. This gave detailed information about whether the LaminB1 line is continuous or has recurring interruptions. For dual-colour images of samples stained with both LaminB1 and the DNA DSB marker γH2AX, the angular relationship between the two proteins was derived. For the colocalisation of Lamin B1, γH2AX, and Sytox Orange, the program 2-channel-analysis.py (written by Charlotte Neitzel and Martin Gote). Distances between two distinct signal localisations were computed to assess the correlation between the two signals. Further, nearest neighbour distances were calculated according to the defined number of nearest neighbouring points. A threshold of 95 nm was chosen as the maximal distance between two different signal molecules for it to be considered a localised event. Further, an alternative method, dual-colour ThunderSTORM data were analysed with an algorithm developed by Malkusch and Endesfelder[204]. A coordinate-based colocalisation value was defined as values between -1 and 1. Analysis was performed by Katarina Chapman.

2.16 IgG1 antibody affinity maturation analysis

Whole blood was collected from mice by tail vein bleeding at different time points. Collected blood samples were kept at RT for at least 20 minutes and centrifuged for 10 minutes at 3000 RPM. A clear upper-phase serum layer was collected into a clean Eppendorf tube and stored at -80°C until further use. Nunc MaxiSorp 96-Well plate was coated with 50 μL of high (NP-9) and low affinity (NP-27) substrate 24 hours prior to performing the ELISA assay. Non-specific antigen binding was blocked by incubating ELISA NP-coated plate with PBS (1% BSA) for 2 hours, shaking at 400 RPM followed by three washes with 100 μL of PBS-T (0.5% Tween-20). Serum samples were diluted 1:16000 with 1x PBS, added in duplicates to ELISA NP-coated plate for 1 hour at 37°C and washed three times with 100 μL of PBS-T. The plate was incubated with mouse anti-IgG1 (1/1000)-HRP linked antibody for 1 hour at 37°C and washed three times with 100μL of PBS-T. Room temperature equilibrated 1-Step™ Ultra TMB-ELISA Substrate Solution (100 μL /well) was added for 25 minutes at RT, and the reaction was terminated using Stop Solution (100 μL /well). Immediately after, the absorbance was measured at OD 450nm and 570nm.

2.17 Gene expression analysis of DLBCL patients

I utilised a publicly available dataset from TCGA (phs001444) for differential gene expression analysis, Lamin B1 expression, and clinical outcome of 481 DLBCL patients[205] (Appendix Table 10.6.1). Normalised Log2CPM and clinical data were obtained from TCGA, and cell-of-origin subtype stratification was obtained from a study published by Schmitz et al. For Kaplan-Meier survival analysis, progression-free survival (PFS) was used as a factor of LMNB1 mRNA expression in all DLBCL patients (n=485), GCB subtype (n=139), and ABC subtype (n=243) at multiple PFS cut-off intervals. Furthermore, LMNB1 expression (Log2 CPM+1) was used for diagnostic stage analysis. Gene expression dataset for single-sample (ss) GSEA was applied to assess differentially enriched pathways after dichotomising patients based on Lamin B1 expression.

2.18 In-suspension breaks labelling in situ and sequencing (sBLISS)

To identify the genome-wide scale of DSBs, the sBLISS methodology was adapted to label DSBs in fixed cells after Lamin B1 hypomorphic *in vitro* and *in vivo* models (Figure 2.7).

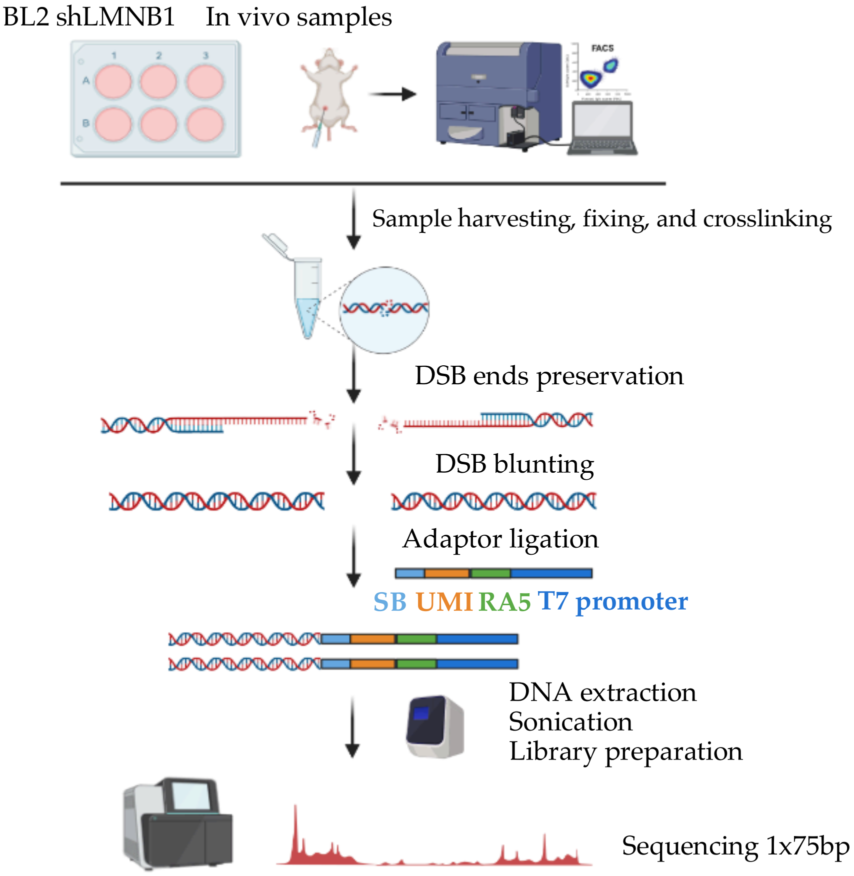

Figure 2.7 Schematic representation of sBLISS workflow. Experimental samples were harvested, fixed, and processed as described in the sBLISS protocol. SB = sample barcode, UMI = unique molecular adaptor.

2.18.1 sBLISS Experimental design

For the BL2 shLMNB1 *in vitro* samples, BL2 cells were plated at 2x10^5 cells/mL in RPMI media in triplicates and were left untreated or incubated with 500 ng/mL of doxycycline for 72 hours to induce shRNA mediated Lamin B1 knockdown. After 72 hours, cells were assessed for GFP expression, Lamin B1 knockdown, and DNA damage. As a positive control of DSB inductions, BL2 cells were treated with 20 μM of Etoposide for 2 hours and immediately processed for the generation of sBLISS template. Three biological replicates were processed per each condition.

2.18.2 GC B cell and Naïve B cell *in vivo* samples

For mouse samples, $C\gamma 1^{+/cre}$ and $LaminB1^{fl/fl}$ $C\gamma 1^{+/cre}$ mice were immunised with 100 µg of NP-CGG for 10 days. On day 10, mice were sacrificed, and spleen tissues were immediately harvested and processed for FACS. GC B cell population (B220+, GL7+, CD95+) was sorted from at least four different animals per condition at two separate immunisations (Figure 2.8). The naïve B cell population from $C\gamma 1^{+/cre}$ mice were used as a negative control. Single-cell splenocyte suspension was made by disaggregating fresh spleen tissue using the 70 µM strainer and resuspending cells in PBS (10% FBS). Cells were centrifuged for 10 minutes at 1500 RPM at 4°C. After discarding the supernatant, red blood cells were lysed with 1x red blood cell lysis buffer (RBLB) for 5 minutes at RT. Cells were washed with ice-cold PBS and centrifuged for 10 minutes at 1500 RPM at 4°C. For faster and more efficient cell sorting, I enriched the GC B cell population using Germinal Centre B Cell MicroBead Kit according to the manufacturer's protocol. Immediately after enrichment, cells were counted and stained with GC B cell or Naïve B cell markers. Cells were stained in the dark for 20 minutes, and washed with PBS (2% FBS) immediately sorted by FACS.

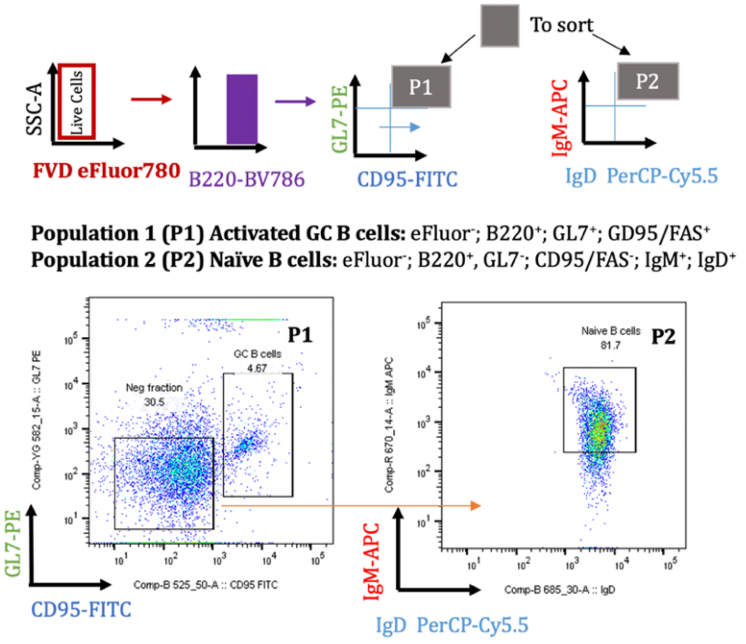

Population 1 (P1) Activated GC B cells: eFluor$^-$; B220$^+$; GL7$^+$; GD95/FAS$^+$
Population 2 (P2) Naïve B cells: eFluor$^-$; B220$^+$, GL7$^-$; CD95/FAS$^-$; IgM$^+$; IgD$^+$

Figure 2.8 Sorting of murine splenic GC B cells and Naïve B cells by FACS. Live splenic cells were stained with an antibody cocktail containing CD95-FITC, GL7-PE, IgM-APC, IgD-PerCP-Cγ5.5, B220-BV786, and viability dye eFluor780.

Library	Sample	Barcode Sequence	Organism
BL1	controlR1	CGTGTGAG	Homo Sapiens
	shLMNB1R1	GACACGAG	Homo Sapiens
	etoposideR1	ATGTGGAG	Homo Sapiens
BL2	controlR2	CGTGTGAG	Homo Sapiens
	shLMNB1R2	GACACGAG	Homo Sapiens
	etoposideR2	ATGTGGAG	Homo Sapiens
BL3	controlR3	CGTGTGAG	Homo Sapiens
	shLMNB1R3	GACACGAG	Homo Sapiens
	etoposideR3	ATGTGGAG	Homo Sapiens
M1	CYR1	CGTGTGAG	Mus musculus
	LaminB1FLR1	GACACGAG	Mus musculus
	negcontrolR1	ATGTGGAG	Mus musculus
M2	CYR2	CGTGTGAG	Mus musculus
	LaminB1FLR2	GACACGAG	Mus musculus
	negcontrolR2	ATGTGGAG	Mus musculus

Table 2.5 sBLISS library design and barcode sequence matched sequence per sample.

2.18.3 sBLISS protocol

Before the sBLISS template preparation, the lyophilised single-stranded phospho-oligonucleotide(s) were dissolved to create a 100 µM stock solution. Compatible reverse and forward oligonucleotides were mixed and placed in a thermal block for the following annealing reaction (Step 1: 95°C for 5 min, Step 2: Cool to 25°C at -1.5°C per minute, Step 3: 25°C Hold). Annealing of oligonucleotides was confirmed by analysis on TapeStation, and double-stranded oligonucleotides were stored at -20°C. The sBLISS template preparation was carried out as follows.

Briefly, FACS-sorted mouse splenic germinal centre B cells, or BL2 cells cultured in culture dishes, were counted, and 1x10^6 were centrifuged at 300 x g for 10 minutes in a pre-warmed medium (10% FBS) to obtain 10^6 cells per mL. Cells were immediately fixed with 16% PFA (10% FBS/1× DPBS+) (Electron

Microscopy Sciences, catalog no. 15710) diluted to reach a 4% final concentration in the cell suspensions. Cells were left on a roller at RT for precisely 10 minutes, and PFA was quenched by the addition of 2 M glycine (Molecular Dimensions, catalog no. MD2-100-105) to a final concentration of 125 mM. The suspension was incubated at RT for 5 minutes and then placed on ice for additional 5 minutes. Glycine and PFA were washed twice with ice-cold PBS and stored at 4 °C until template preparation. Fixed cells were transferred to 1.5-mL Protein LoBind Eppendorf tube and lysed with 200 µL Lysis buffer #1 (10mM Tris-HCl, 10 mM NaCl, 1 mM ethylenediaminetetraacetic acid and 0.2% Triton X-100 (pH 8)) for 1 hours on the ice, followed by lysis in lysis buffer #2 (10 mM Tris-HCl, 150 mM NaCl, 1 mM ethylenediaminetetraacetic acid and 0.3% sodium dodecylsulfate (pH 8)) shaking at 37°C for 1 hour at 400rpm. Lysed cells were centrifuged and washed with 1x CSTX buffer before DSB blunting and adaptor ligation. Lysed cells were incubated with 100 µL blunting master mix for 60 min at room temperature, shaking at 400 RPM, followed by two washes with 200 µL of CSTX buffer. Each sample was incubated with 4 µL of the unique adaptor (100 mM) and mixed with 96µL of ligation mastermix and placed at 4°C overnight. Ligated samples were centrifuged at 300 g for 10 minutes and washed twice with CSTX buffer. The pelleted sample was resuspended in 100 µL of tail buffer, followed by the addition of 10 µL of proteinase K, and incubated overnight at 55°C shaking at 800 RPM. The next day, 10 µL of proteinase K was added to each sample for another hour at 55°C shaking at 800 RPM. Proteinase K was inactivated by 10minute incubation at 95°C and cooled at RT. Genomic DNA was isolated by phenol-chloroform-based extraction. Into each tube, 120 µL of room-equilibrated fresh PCI was added, and sample tubes were shaken for 30s. Samples were centrifuged at 20,000 *g* for 15 min at room temperature. The upper phase was transferred into a 1.5-mL DNA LoBind Eppendorf tube and an equal volume of chloroform was added to the transferred upper phase, followed by vigorous shaking for 30 s. Samples were centrifuged at 20,000 *g* for 15 min at RT. Into the transferred upper phase layer, 0.1x volume of 3 M sodium acetate was added and followed by the addition of 5 µL glycogen (20 mg/mL). Lastly, 2.45× volumes of ice-cold 100% ethanol were added into each tube, vortexed, and stored overnight at –80°C. The following day, samples were centrifuged at 30,000 *g* for 90 min at 4°C. Pelleted samples were washed twice with 70% ice-cold ethanol and centrifuge at 30,000 *g* for 15 min at 4°C. Air-dried pellets were then dissolved in

102 µL of TE. Exactly 100 µL of the sample was transferred to a 0.5-mL DNA LoBind tube, and samples were sonicated with Bioruptor for 7 cycles (30 seconds ON, 60 seconds OFF) for BL2 samples and 5 cycles for mouse samples. The sBLISS template was quantified by DNA content. Prepared templates were concentrated and cleaned with AMPure XP beads. The sBLISS containing different barcode sequences were pooled for library preparation according to Table 2.5. IVT was performed using SuperScript IV Reverse Transcriptase for 50 min at 50°C. Finally, libraries were amplified with NEB's Next Ultra II Q5 Master and the RP1 common primer (10uM) and a 20 µL of uniquely selected index primer. Eight cycles were performed for 100ng input (in vitro samples); 12 cycles for ~10ng input (in vivo samples). Generated libraries were cleaned and purified with AMPure XP beads, followed by quantification with DNA Tapestation4200. Libraries were sequenced as single-end (1 × 75 bp) reads on the NextSeq platform.

Figure 2.9 sBLISS analysis workflow for the experiment described in Chapter 7.

2.18.4 Pre-processing of sequencing data

Data analysis was performed using a publicly available script created for the sBLISS analysis. Raw FASTQ files were merged, and reads were filtered according to the associated sample barcode allowing for a maximum of one mismatch in the barcode sequence (Figure 2.9 & Table 2.6). Prefixes in each read were trimmed, and sequences were aligned to the hg19 reference genome using BWA-MEM. Aligned reads with a mapping quality score ≤60 were removed. Additionally, reads determined as PCR duplicates by SAMtools were filtered out based on the criteria described in the published script. After filtering low-quality aligned reads and PCR duplicates, a BED file containing unique DSB locations was obtained and used in the further downstream analysis.

2.18.5 Identification of sequence motifs around DSB breakpoints

Motif discovery and enrichment around DSB breakpoints were performed using MEME Suite. First, FASTA files sequences of different lengths (± 10bp, ± 7bp) around DSB breaks were retrieved from BED files. Retrieved sequences were used as input for simple enrichment analysis (SEA) of a given list of motifs associated with recruitment, accessibility, and targeting by AID. SEA compared sequences of all breakpoints from shLMNB1 treated samples and control samples. To compute the probability of a specific motif being present near or at the DSB end, I used the CentriMo algorithm, which identifies motifs that show a significant preference for a particular location in our DNA sequences derived from the sBLISS. The STREME algorithm was used to perform discriminative motif discovery, and enrichment analysis of sequences around DSB found in experimental conditions compared to control sequences with a minimum E value <0.05.

2.18.6 Hotspot detection

Detection of the sBLISS hotspots Macs2 (version2.1.1.20160309) (Zhang et al.,2008) was used to call peaks from the BED files of UMI-DSB. BED files containing one UMI-DSB entry per detected DSB break in the BED file were used as input for the Macs2 algorithm (no background model, no cross-correlation between strands around the hotspots, shift reads by -100bp and extend by 200bp). The hotspots were defined as the peaks identified by Macs2 with q-value < 0.05, fold enrichment > 4, pileup >10. Circos plots were used to visualise the detected sBLISS hotspots and highly mutated genomic locations from WXS analysis, and genes mutated in nHL patients.

2.19 Clinical data from DLBCL patients

Limited clinical data for the survival analysis were obtained from a study by Schmidt et al.[205](Appendix Table 10.5.2). TMA DLBCL samples and clinical data were obtained from Barts Cancer Institute tissue bank, London, UK. Ethical approval was confirmed by the East London & The City Health Authority Local Research Ethics Committee (Reference number 10/H0704/65), and written informed consent was also obtained in accordance with the Declaration of Helsinki.

2.20 Study approval

All animal studies were conducted in compliance with UK Home Office approved licences (Animals (Scientific Procedures) Act 1986 and the EU Directive 2010). Animals were maintained in local facilities and experiments were approved by local ethical committees under Home Office license P68650650.

2.21 Statistical analysis

For IF, IHC, and western blotting analysis, raw images were processed in Fiji, QuPath. RNA-seq analysis was performed with Galaxy and R 3.8.1 (R Foundation). Foci counting was done with Fiji or FociCounter algorithm in MATLAB (Mathworks). Survival analysis was performed in R using the survival plot function. All other numerical data were analysed and plotted on Prism v8.3 (GraphPad Software, Inc.). Statistical analysis was performed using Prism (GraphPad Software, Inc.). P values were calculated using a two-tailed unpaired test unless stated otherwise. Kaplan-Meier survival curve statistics were determined using the Log-rank (Mantel-Cox) test in GraphPad or using ggsurvplot package. All charts of the results presented are the mean values and the standard errors of the mean from separate experiments unless otherwise stated in the figure description. RNA-seq data were considered significant with a p-adjusted value of < 0.05.

Materials	Supplier	Storage
Comet Assay Kit	Trevigen 4250-050-K	RT
EdU Click-it Kit	Thermofisher C10337	N/A
Intercept blocking buffer	Licor #927-70001	4°C
PBS	SigmaAldrich S-014-M	RT
DMEM	ThermoFisher	4°C
RPMI 1640	ThermoFisher	4°C
Antifading solution	Sigma S7114	RT
4% PFA in PBS	Santa Cruz 30525-89-4	4°C
Germinal centre B cell (PNA) microbead kit, mouse	Miltenyibiotec 30-110-479	4°C
LS columns	Miltenyibiotec	RT

MS collums	Miltenyibiotec 130-042-201	RT
(Acridine Orange / Propidium Iodide (AO/PI) Cell Viability Kit	Labtech International Ltd F23001	4°C
Antigen Unmasking Solution, Tris-Based	Vector labs H-3301	4°C
Antigen Unmasking Solution, Citric Acid Based	Vector labs H-3300	4°C
ImmPRESS® HRP Anti-Goat IgG (Peroxidase) Polymer Detection Kit, made in Horse	Vector labs MP-7405-15	4°C
ImmPRESS® HRP Anti-Rabbit IgG (Peroxidase) Polymer Detection Kit, made in Goat	Vector labs MP-7451-15	4°C
ImmPRESS® HRP Goat Anti-Rat IgG Polymer Detection Kit, Peroxidase	Vector Labs MP-7444-15	4°C
ImmPRESS® HRP Anti-Mouse IgG (Peroxidase) Polymer Detection Kit, made in Goat	Vector Labs MP-7452-15	4°C
NP-CGG (Chicken Gamma Globulin), Ratio 10-19	2BScientific N-5055B-1	4°C
RBC Lysis Buffer (10X)	Biolegend 420301	4°C
Wash Buffer 10x, Concentrate, 1 L	Agilent Dako S3006	4°C
Fluoromount™ Aqueous Mounting Medium	Sigma F4680-25ML	RT
Adhesion slides, SuperFrost Plus	VWR 631-0108	RT
Shandon Filter Cards Brown	Thermo Fisher 5991023	RT
Quick Blunting™ Kit	NEB E1201S	4°C/-20°C
T4 DNA Ligase (5 U/μL)	ThermoFisher EL0011	-20°C
ATP SOLUTION 100mM	ThermoFisher R0441	-20°C
UltraPure™ BSA (50 mg/mL)	ThermoFisher AM2616	-20°C
Proteinase K, Molecular Biology Grade	NEB P8107S	-20°C
UltraPure™ Phenol:Chloroform:Isoamyl Alcohol (25:24:1, v/v) 100mL	ThermoFisher 15593031	4°C
Glycogen from Mussels	SigmaAldrich 10901393001	-20°C
AMPure XP, 5 mL	VWR A63880	4°C
CutSmart Buffer 5ML	NEB B7204S	-20°C
Sodium Acetate	ThermoFisher AM9740	RT
Protein LoBind 1.5mL	Eppendorf 30108442	RT
NuPAGE™ 3-8% Tris-Acetate Protein Gels, 1.0 mm, 10-well	ThermoFisher EA0375BOX 10 gels	4°C
NuPAGE™ Tris-Acetate SDS Running Buffer (20X)	ThermoFisher LA0041	4°C
Phospho-Histone H2A.X (Ser139) (D7T2V) Mouse mAb #80312 100uL	Cell signalling 80312S	-20°C
Recombinant Anti-DNA PKcs (phospho S2056) antibody [EPR5670]	Abcam ab124918	-20°C
Western Blotting Filter Paper, Extra Thick, 8.5 cm x 9 cm	Thermo Fisher #88610	RT
FITC anti-H2A.X Phospho (Ser139) Antibody	Biolegend 613404	4°C
Cell Staining Buffer (500mL)	Biolegend 420201	4°C
Anti-Lamin B1 antibody [119D5-F1] - Nuclear Envelope Marker (ab8982)	Abcam ab8982	-20°C
Anti-GAPDH antibody, Mouse monoclonal	Sigma Aldrich G8795	-20°C
Color Prestained Protein Standard, Broad Range (10-250 kDa)	New England Biolabs P7719S	-20°C

ImmEdge® Hydrophobic Barrier PAP Pen	Vector Labs H-4000	RT
COVER SLIPS 22 X 40 MM NO. 1	VWR 631-0135	RT
DNA LoBind® Tubes, DNA LoBind®, 1.5 mL, PCR clean, colorless, 250 tubes (5 bags × 50 tubes)	Eppendorf 30108051	RT
DNA LoBind® Tubes, DNA LoBind®, 0.5 mL, PCR clean, colorless	Eppendorf 30108035	RT
NaCl (5 M), RNase-free	Invitrogen AM9760G	RT
MgCl2 (1 M)	Invitrogen 10418464	RT
UltraPure™ BSA (50 mg/mL)	Invitrogen AM2618	-20°C
RNase-free Microfuge Tubes (2.0 ml)	Invitrogen M12425	RT
Nuclease-Free Water (not DEPC-Treated) 5 x 100 mL	ThermoFisher AM9939	RT
NuPAGE™ LDS Sample Buffer (4X)	ThermoFisher NP0007	RT
Pierce™ ECL Western Blotting Substrate	ThermoFisher 32109	4°C
PVDF Transfer Membrane, 0.45 μm, 26.5 cm x 3.75 m	ThermoFisher 88518	RT
Bovine Serum Albumin (100g)	Sigma A2153	4°C
anti-Mouse IgG1 HRP	ThermoFisher A10551	-20°C
NP-BSA (Bovine Serum Albumin), Ratio 5-9	LGC Biosearch Technologies N-5050L-10	4°C
NP-BSA (Bovine Serum Albumin), Ratio > 20	LGC Biosearch Technologies N-5050H-10	4°C
AEC Substrate Kit, Peroxidase (HRP), (3-amino-9-ethylcarbazole)	Vector Labs SK-4200	4°C
1-Step™ Ultra TMB-ELISA Substrate Solution	ThermoFisher 34028	4°C
DEPC-Treated Water	AM9916	RT
NP-BSA (Bovine Serum Albumin), Ratio 10-19	LGC Biosearch Technologies N-5050M-10	4°C
Goat Anti-Mouse IgG H&L (Alexa Fluor® 594)	Abcam ab150116	4°C
ProLong™ Gold Antifade Mountant (2mL)	ThermoFisher P10144	RT
AbC™ Total Antibody Compensation Bead Kit	ThermoFisher	4°C
53BP1 Antibody (6B3E10)	NOVUS biologicals NBP2-25028	-20°C
Penicillin-Streptomycin	Sigma P0781-100ML	-20°C
SMARTvector Inducible Human LMNB1 mCMV-TurboGFP shRNA	V3SH11255-01EG4001	-20°C

Table 2.6 Materials used in this study annotated with manufacturer, item number, and storage conditions.

Chapter 3: Lamin B1 depletion induces spontaneous mutagenesis and DNA damage in B cells

3.1 Introduction

Germinal centre (GC) B cells are more susceptible to genetic lesions due to a high number of mutational and recombination events required for the B cell maturation as part of the adaptive immune response[206]. These genetic lesions are chromosomal translocations, nucleotide substitutions, amplifications, and deletions, which can lead to gain-of or loss-of-function mutations[206]. Accumulation of these genetic lesions predisposes normal GC B cells to malignant transformation[59]. B cells are programmed to tolerate targeted DNA damage[207] within specific genomic regions (e.g. Ig genes). Our primary interest was to investigate the association of Lamin B1 with mutagenesis in benign and malignant GC B cells. Activation-induced deaminase (AID) is a master regulator of somatic hypermutation (SHM) specifically expressed in GC B cells so SHM is programmed to occur primarily during B cell activation[208,40]. The rate of mutational load within the immunoglobulin variable (IgV) region is dependent on several factors, including DNA accessibility and local DNA sequence[46]. Our group previously demonstrated that Lamin B1 removal from the nuclear periphery, particularly the IgV region, regulates SHM[131]. The mutational load within the IgV region is attributed to the activity of AID, but not necessarily to the modulated expression of AID upon Lamin B1 removal[131]. This prompted the notion of other mechanisms regulating mutagenesis to exist in B cells, including the removal of Lamin B1 at the nuclear periphery.

Recent studies demonstrated the involvement of Lamin B1 in maintaining chromatin stability and DNA damage response[176,182]. Our group has previously shown that transient Lamin B1 silencing leads to spontaneous SHM-mediated point mutations within the IgV region and dysregulation of several signalling pathways in BL2 cells. To our knowledge, no studies have addressed the effect of Lamin B1 expression on genomic instability in B cells. Our group has previously failed to establish a stable Lamin B1 knockdown model, most likely due to the long half-life and low turnover of Lamin B1 in B cells and insufficient lentiviral transduction rates of B cell lymphoma cells. To overcome some of these limitations, I aimed to establish a novel stable Lamin B1 knockdown *in vitro* B cell model and assess the effect of Lamin B1 silencing on genomic instability.

3.2 Chapter aims and hypothesis:

In this chapter, I aimed to address the impact of Lamin B1 reduction on mutagenesis and genomic instability in B cells by utilizing whole exome sequencing and establishing novel Lamin B1 knockdown *in vitro* B cell models. Upon the successful generation of the Lamin B1 knockdown model, I assessed downstream phenotype, including DNA damage response and proliferation.

Chapter aims:

1. Analysis of mutational load using WXS after Lamin B1 reduction
2. Generation of a stable and inducible shRNA Lamin B1 knockdown *in vitro* lymphoma models
3. Assessment of DNA damage response upon depletion of Lamin B1 in B cell lymphoma cells
4. Cell cycle and proliferation analysis in BL2 shLMNB1 cells

3.3 Results

3.3.1 WXS reveals *de novo* mutational patterns after depletion of Lamin B1 in lymphoma cell lines

Lamin B1 removal from the nuclear periphery leads to the acquisition of AID-mediated point mutations in the IgV region[131]. I aimed to assess whether the observed Lamin B1-associated mutagenesis is restricted to the IgV region by genome-wide topological analysis of mutations after Lamin B1 silencing in several B cell lymphoma cells. For this, I utilised previously generated WXS data from B cell-derived lymphoma cell lines with differential *AID* expression upon transient Lamin B1 knockdown. The WXS analysis was performed in BL2 AID^{wt}, AID$^{-/-}$, and PCL12 cell lines upon the transfection with siRNAs against Lamin B1 for 48 hours (Figure 3.3.1.1), as previously described by Klymenko et al[131].

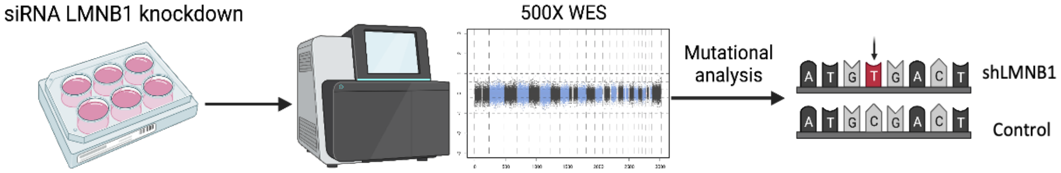

Figure 3.3.1.1 Schematic representation of the experimental approach for the assessment of the mutation load upon Lamin B1 silencing.

After the read alignment, somatic variant caller Mutect2 was used to detect *de novo* single nucleotide variants (SNVs) in control and siLMNB1 samples. Mutations found in siLMNB1 samples were used as an input for the downstream mutational analysis, including the frequency and type of nucleotide substitution. More than 300 SNVs were detected in siLMNB1 samples across the genome. COSMIC database and mutational signatures analysis of single nucleotide variants (C>A, C>G, C>T, T>A, T>C, and T>G) were used for the quantification and topological analysis[209]. My first finding was consistent with the mutational activity of AID, which revealed the enrichment C>T nucleotide substitution in siLMNB1 samples (Figure 3.3.1.2), suggesting that AID is the primary driver of mutagenesis associated with Lamin B1 silencing. Therefore, I expected that the observed phenotype is dependent on *AICDA* expression in BL2 AID^{wt}.

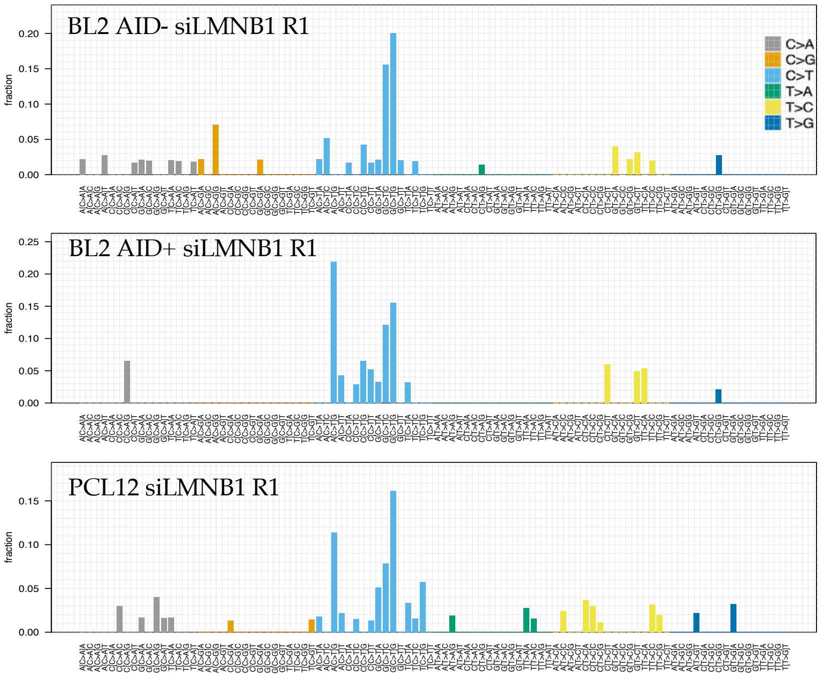

Figure 3.3.1.2 WXS analysis reveals Lamin B1 knockdown increases mutational load in B cell lymphoma cell lines. Representative analysis of single base substations (SBS) detected in Lamin B1 knockdown cell lines shows a preference for C>T nucleotide substitution. Processing of raw sequencing files and mutation calling was performed by Dr. Alex Wang.

3.3.2 Increase of cytosine to thymine nucleotide substations is not attributed to AID enzymatic activity

Next, I compared nucleotide substitution patterns in BL2 AID+ and AID- cell lines, which revealed no significant differences in the proportion of C>T present in AID+ (54%) and AID- (52%) samples (Figure 3.3.2.1 a). Analogous mutagenesis in AID+ and AID- samples may suggest that AID alone is not responsible for the induced *de novo* C>T mutations. Other apolipoprotein B mRNA editing enzymes, catalytic polypeptide-like (APOBEC) family members are known contributors to the C>T mutagenic signature[45]. Within this context, I assessed the expression of other APOBEC cytosine deaminases in BL2 cells using the GEP generated in Chapter 6. Several members of the APOBEC family are expressed in BL2 cells and DLBCL patients (Figure 3.3.2.1 & Appendix Figure 10.1.5). Particularly, *APOBEC3G* and *APOBEC3C* were among other cytosine deaminases expressed in BL2 cells, which have been implicated with increased mutagenesis[46,210].

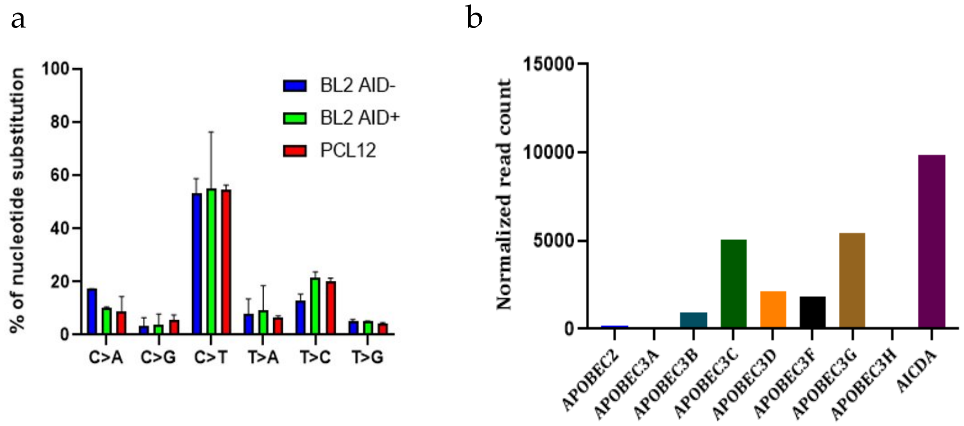

Figure 3.3.2.1 Analysis of single nucleotide variants and APOBEC expression BL2 cells. **(a)** The proportion of SNVs called with Mutect2 in siLMNB1 cells based on the COSMIC mutational pattern. Bar chart shows the proportion of SNVs from two independent WXS experiments in BL2 AID+, BL2 AID-, and PCL12 cells. Error bars represent +/- s.e.m. Mutation calling was performed by Dr. Alex Wang. **(b)** Relative expression of APOBECs cytosine deaminases in BL2 cells. Raw read counts were obtained from RNA-seq analysis in Chapter 6.

AID is known to induce point mutations within the exons of IgV and Immunoglobulin Heavy (IgH) switch regions[28]. However, several studies demonstrated that AID can also mediate off-target mutations and DNA breaks, which can subsequently lead to chromosomal translocations[128,211]. As a result, I assessed the enrichment of SNVs with respect to the genome coding region.

Approximately 60% of detected mutations were detected within the non-coding DNA sequence, and the remaining 40% - were within the gene-coding DNA sequences. Comparing the proportions of SNVs within the genomic regions revealed similar distribution across all samples. (Figure 3.3.2.2).

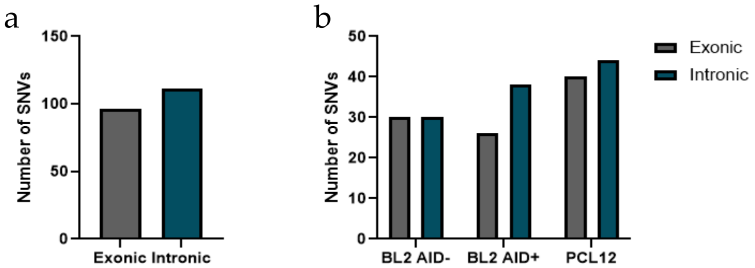

Figure 3.3.2.2 Analysis of SNV distribution gene coding regions in BL2 siLMNB1 cells. **(a)** Bar chart showing the total number of SNVs located within the intronic or exonic gene-coding regions across all Lamin B1 knockdown cell lines. **(b)** Bar chart shows the total number of SNVs across genomic regions in all cell lines.

3.3.3 Lamin B1 depletion induces kataegis in B cells

Next, I assessed whether detected mutations follow a random distribution across the genome. For this, I mapped all SNVs according to the associated chromosomal locations. Topological mapping of *de novo* mutations in siLMNB1 cells was performed using Phenogram software, which revealed the clustering of mutations within specific genomic locations. Mutational clusters were called with a recently developed clustering tool, in collaboration with Filip Sadlo's Lab. Mutation clusters were observed particularly in chr1, chr10, chr15, chr18, and chr20 (Figure 3.3.3.1). A comparison of mutations revealed a minimal overlap in BL2 AID+ (blue) and AID- (green) samples (Figure 3.3.3.2). However, there were five common clusters, which suggest that these regions may be more prone to genetic lesions, which is independent of AID-driven mutagenesis. Conclusively, these results suggest that Lamin B1 is involved in the maintaining of genomic stability in B cells and that Lamin B1 depletion increases the susceptibility to spontaneous mutations in certain genomic regions. Therefore, to further elucidate Lamin B1 mediated mutagenesis, I proposed to develop a more efficient and controllable *in vitro* Lamin B1 knockdown model, which would be used to study the effects of Lamin B1 mediated genomic instability in GC-derived B cell lymphoma.

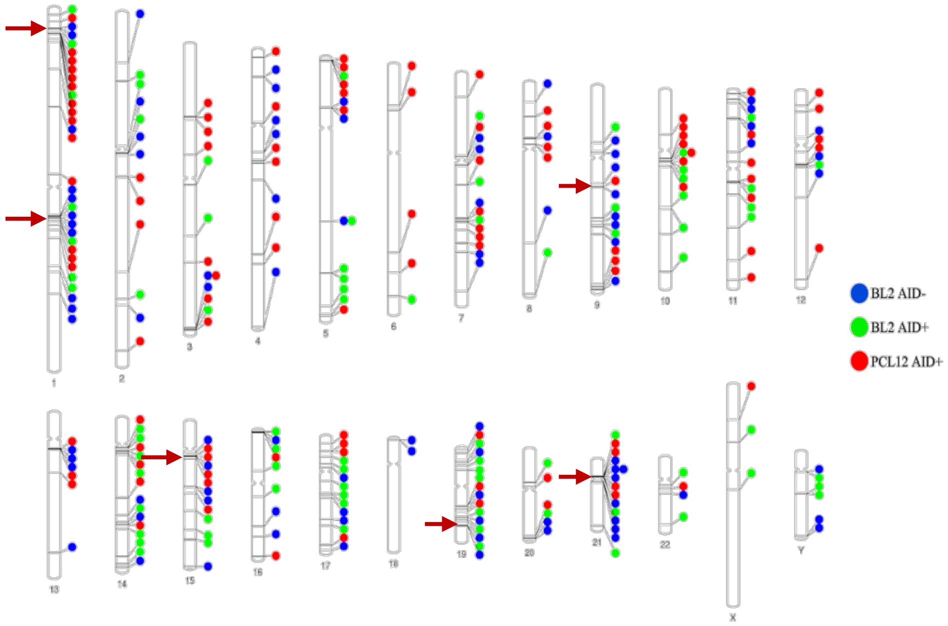

Figure 3.3.3.1 WXS analysis reveals Lamin B1 knockdown increases the mutational load in B cell lymphoma cell lines. Mutational topology of all SNVs detected uniquely in siLMNB1 treated BL2 AID+, BL2 AID-, and PCL12 samples. Phenogram software and hg38 were used for chromosome visualisation.

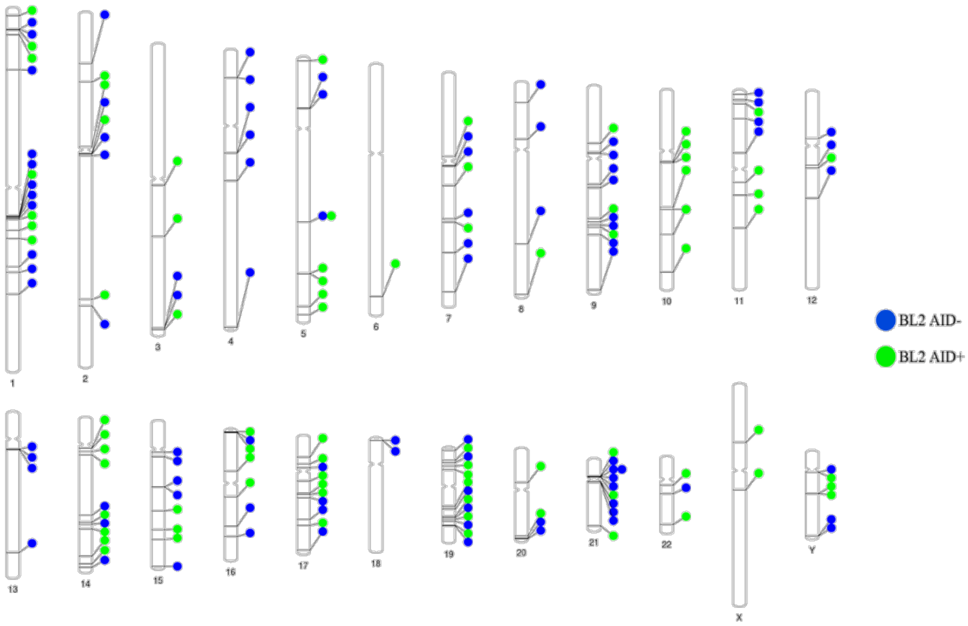

Figure 3.3.3.2 WXS analysis reveals Lamin B1 knockdown increases the mutational load in AID+ and AID- BL2 cells. Mutational topology of all SNVs detected uniquely in siLMNB1 treated BL2 AID+ (green) and AID- (blue) samples. Phenogram software and hg38 were used for chromosome visualisation.

3.3.4 Generation of a doxycycline-inducible shRNA Lamin B1 lymphoma cell lines

Our group has previously established siRNA-mediated transient silencing of LaminB1 in BL2 cells, but the prior attempts of generating a stable Lamin B1 knockdown model by clustered regularly interspaced short palindromic repeats (CRISPR)-Cas9 or shRNA approach was not successful. Due to the limited duration and variable transfection efficiency of siRNA-mediated silencing, I proposed to establish a more controllable and efficient in vitro model, which utilises a doxycycline (DOX) inducible shRNA lentiviral vector targeting Lamin B1 (Figure 3.3.4.1). I transduced a target cell line with a lentiviral vector containing puromycin resistant gene, which allowed for a positive selection of cells with an integrated vector. Additionally, the vector contained a Green Fluorescent Protein (GFP) reporter for the monitoring of transduction efficiency and shRNA activation by flow cytometry. After a 48-hour puromycin selection, positively selected transduced cells were incubated with DOX to induce the expression of the shRNA vector.

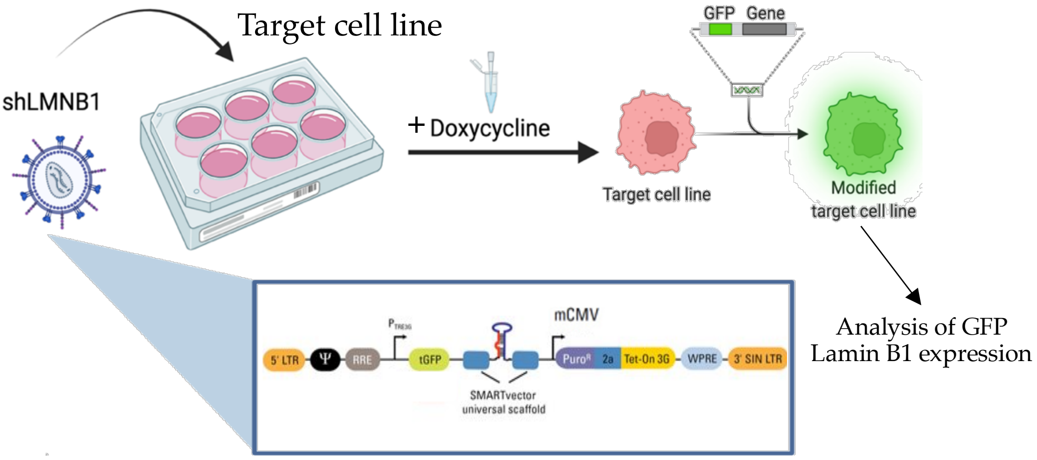

Figure 3.3.4.1 Principal scheme of engineering inducible Lamin B1 knockdown cell line. Lentivirus containing puromycin resistant gene and DOX inducible shRNA GFP promoter transduced into target B cell line lymphoma cell line. After puromycin selection of transduced cells, shRNA induction and Lamin B1 knockdown efficiency were assessed by flow cytometry and western blotting.

Cells expressing shRNAs were assessed by flow cytometry upon the addition of DOX to induce the CMV promoter. I utilised two unique shRNA constructs that targeted different LMNB1 mRNA sequences. Both shRNAs displayed more than 90% GFP positivity (Figure 3.3.4.2 a). The efficacy of shRNA-mediated Lamin B1 knockdown was assessed by the western blot analysis of total Lamin B1 protein levels, which showed a decrease of total Lamin B1 protein by as much as 60% after incubating cells with DOX for 72 hours (Figure 3.3.4.2 b). In addition to the western blot analysis, reduced localisation of Lamin B1 at the nuclear periphery was observed by immunofluorescence (IF) microscopy (Figure 3.3.4.3).

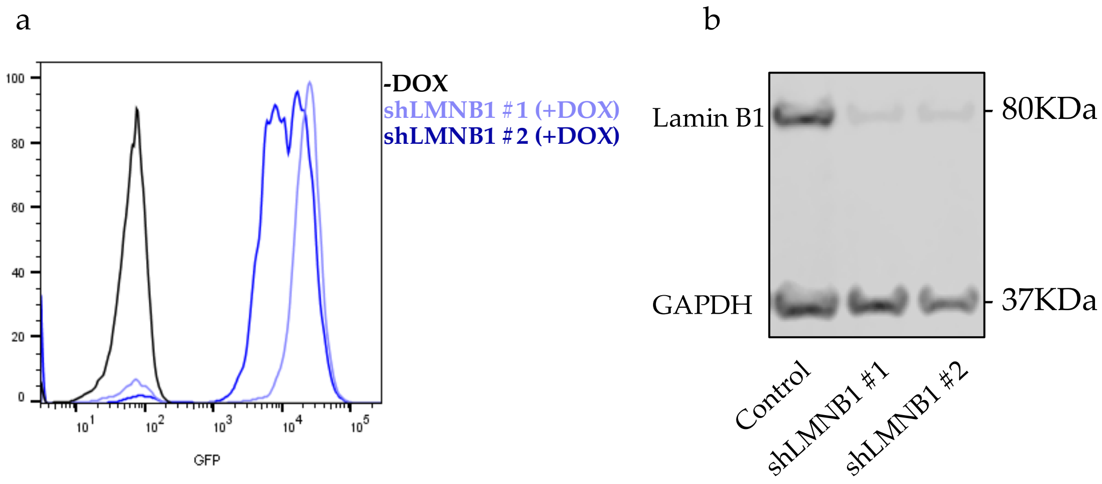

Figure 3.3.4.2 Doxycycline inducible shRNA mediated Lamin B1 knockdown in BL2 assessed by flow cytometry and western blotting. **(a)** Representative flow cytometry charts show the transduction efficiency by measuring the percentage of GFP+ BL2 cells expressing shLMNB1 #1 and shLMNB1 #2 as early as 24 hours after incubating with DOX. Untreated cells were used as a GFP- control. **(b)** Western blot image confirming a reduction of total Lamin B1 protein levels after 72 hours after DOX induction. GAPDH was used as a loading control.

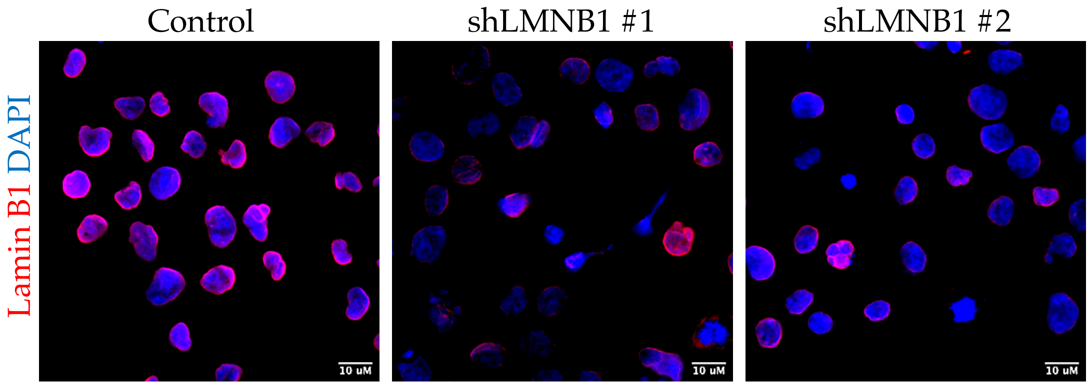

Figure 3.3.4.3 Localisation of Lamin B1 in the nucleus was assessed by IF microscopy 72 hours after DOX induction. BL2 cells were fixed and stained against Lamin B1 and a secondary fluorescent antibody Alexa594. A prominent decrease in Lamin B1 nuclear incorporation was observed by IF microscopy. DAPI was used as a nuclear staining marker. Scale bar represents 10 µm.

After confirming that both shRNAs led to an efficient Lamin B1 depletion, the kinetics of Lamin B1 depletion were studied at different timepoints. BL2 cells were incubated with 500 ng /mL of DOX to induce shRNAs (shLMNB1 #1) for 24, 48, and 72 hours. Lamin B1 nuclear incorporation was assessed by IF microscopy and quantified by Metamorph software (Figure 3.3.4.4). IF analysis shows that Lamin B1 incorporation is reduced in a time-dependent manner resulting in a 1.3-fold reduction 24 hours after incubation with DOX. After 48 and 72 hours, Lamin B1 incorporation was reduced by 1.6 and 2.4-fold, respectively (Figure 3.3.4.4 b). Further qualitative analysis of Lamin B1 localisation at the nuclear periphery was performed using a line scan and surface plot profile in ImageJ, which confirmed the removal of Lamin B1 mainly from the nuclear periphery (Figure 3.3.4.5). As a result, for the first time, I generated a stable and efficient Lamin B1 shRNA-mediated knockdown B cell model. Therefore, the following *in vitro* experiments described in this thesis were carried out using BL2 shLMNB1 cell line incubated with 500 ng/mL of DOX for 72 hours.

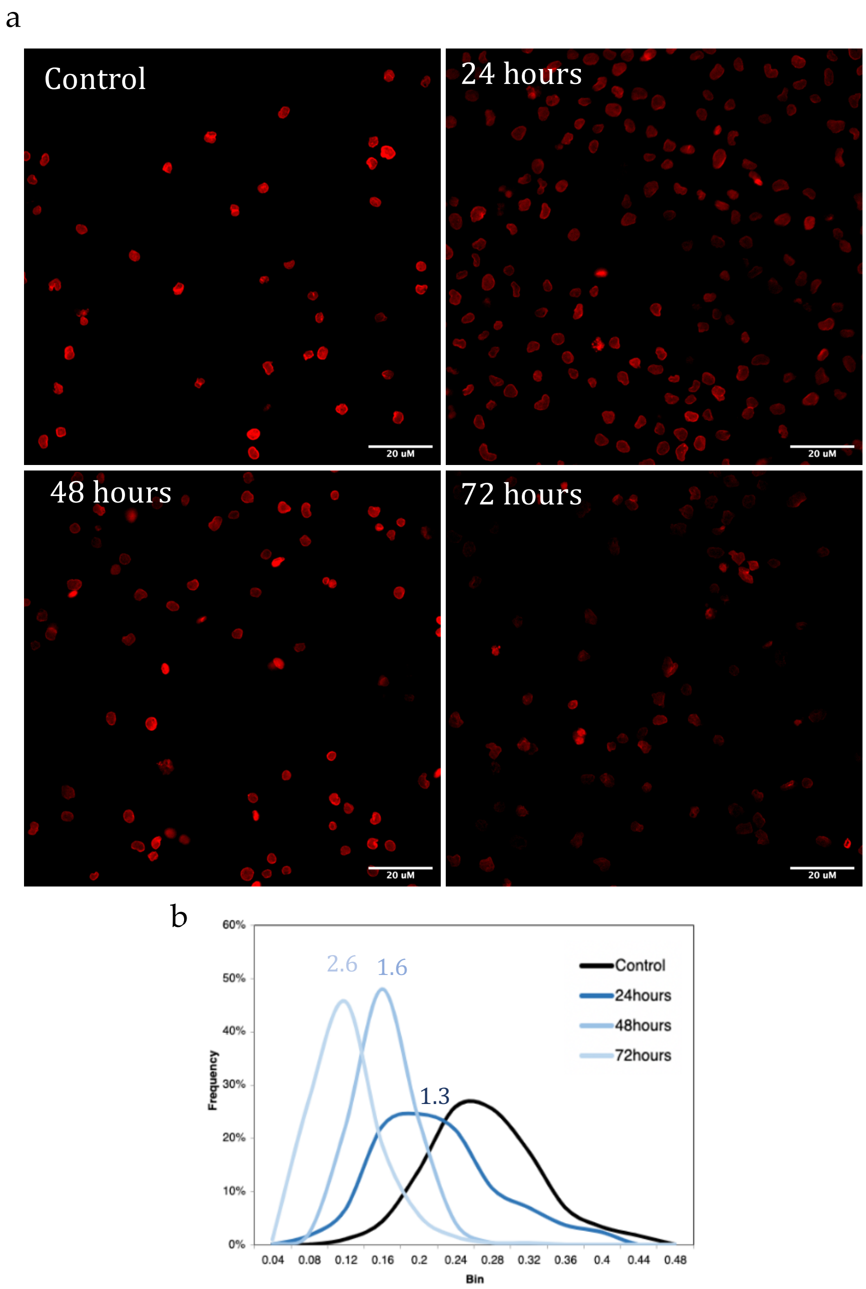

Figure 3.3.4.4 Lamin B1 incorporation at different time points after the incubation with DOX. **(a)** BL2 cells were fixed and stained against Lamin B1 and a secondary antibody Alexa594 at 24, 48, and 72, hours after the addition of DOX. Scale bar represents 20 µm. **(b)** MetaMorph software was used to measure Lamin B1 intensity. At least 100 nuclei were analysed in each condition. Values represent fold changes relative to control.

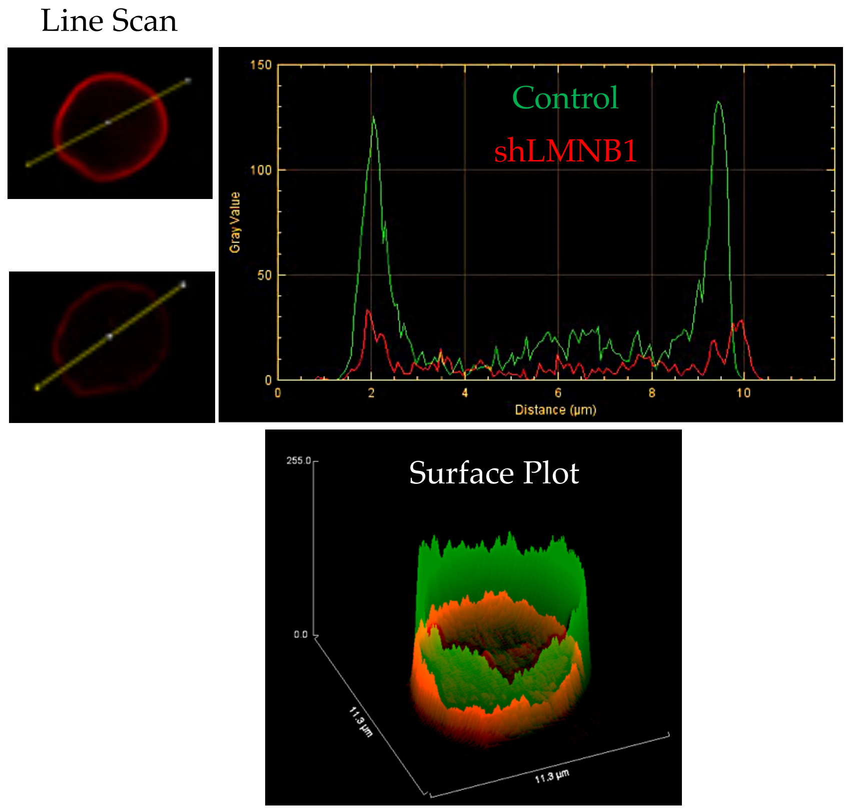

Figure 3.3.4.5 Assessing Lamin B1 incorporation at the nuclear periphery. Fiji image analysis software was used for the line scan and surface plot of two selected cells stained with Lamin B1-Alexa594.

3.3.5 Reducing Lamin B1 expression leads to spontaneous DNA damage in B cell lymphoma cells

After the successful generation of a stable and efficient Lamin B1 knockdown model in BL2 cells, I further addressed the preliminary data summarised in Chapter 1.3.and Chapter 3.3. I hypothesised that Lamin B1 depletion would lead to increased genomic instability in B cell lymphoma cells. I directly assessed the amount of DNA damage upon Lamin B1 depletion by performing several assays evaluating DNA damage. First, I utilised single-cell electrophoresis (COMET) assay to directly quantify the number of DNA breaks in individual cells (Figure 3.3.5)[212,213]. COMET analysis showed significantly higher tail moments (length of tails and percentage of DNA in tails) in BL2 shLMNB1 compared to control cells (Figure 3.3.5). Etoposide treatment was used as a positive control of DSB induction (Figure 3.3.5 and Appendix 10.1.4). The COMET assay has been designed to measure single-stranded and double-stranded breaks. Therefore, these results were confirmed by analysing the phosphorylation of histone variant

H2AX at serine residue 139 (γH2AX), a marker of DNA double-strand breaks (DSBs)[214,215].

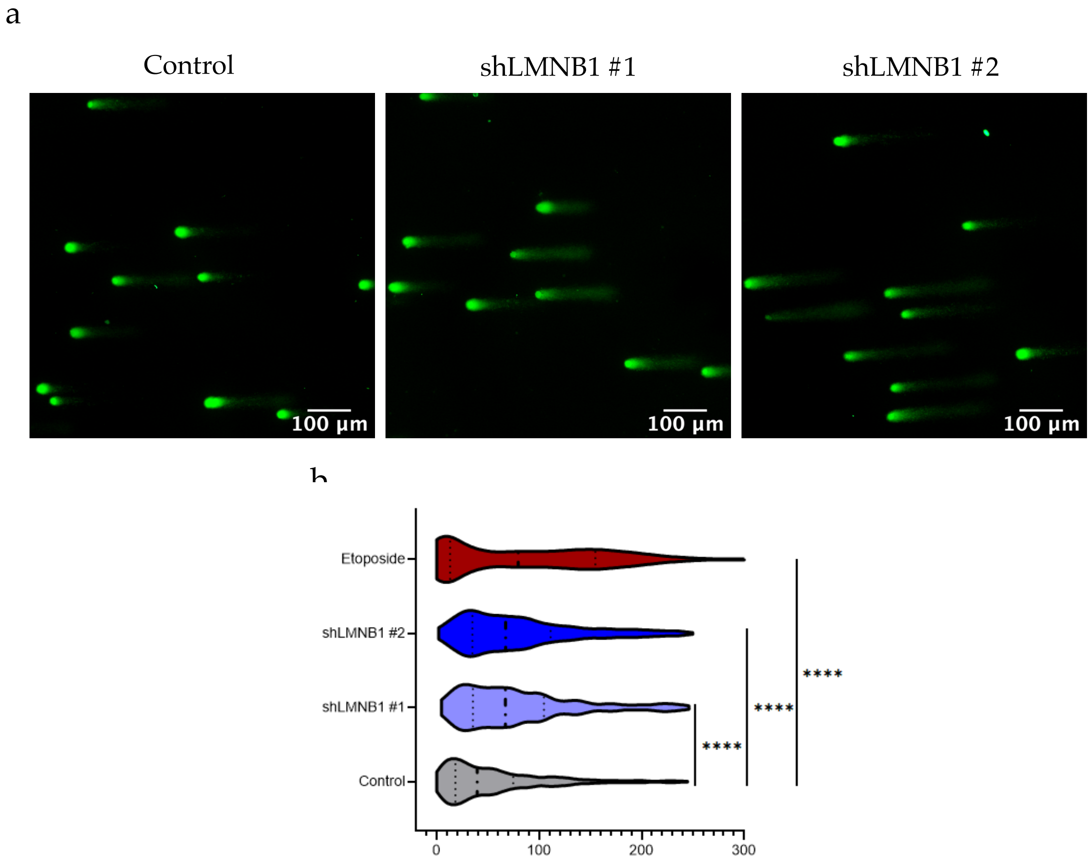

Figure 3.3.5 Reducing Lamin B1 induces DNA damage in lymphoma cells. **(a)** Representative COMET images of cells after single-cell electrophoresis. SYBR gold was used to stain DNA content and assess DNA breaks as a measure of tail moment. Scale bar represents 100 µm**.** **(b)** Quantification of tail moments (% of DNA in tail x tail length) by TriTek CometScore software showing increased tail moments in BL2 shLMNB1 #1 (n = 4) and BL2 shLMNB1 #2 (n = 3) cells compared to control (n = 4) samples. 20 µM Etoposide treatment was used to induce DSBs (n = 3). Dashed lines represent the mean and 95% confidence interval. Unpaired t-test was used for the statistical analysis. ****$P \leq 0.001$.

3.3.6 Elevated levels of γH2AX upon Lamin B1 silencing in B cell lymphoma cells

Intracellular staining of γH2AX (FITC or PE) in fixed BL2 control and shLMNB1 cells was performed to evaluate γH2AX levels after inducing shLMNB1 mediated knockdown (Figure 3.3.6.1). DAPI staining was used to exclude dead cells from the analysis. Flow cytometric analysis revealed an elevated γH2AX signal in BL2 shLMNB1 cells (mean γH2AX=4500) compared to control BL2 cells (mean γH2AX=3200) (Figure 3.3.6.1 b). Cells were treated with 20 µM Etoposide for 2 hours as a positive control of DSBs induction. I observed an increased proportion of γH2AX^{high} cells in BL2 shLMNB1 samples compared to controls, suggesting that there are cells with low LaminB1 which are undergoing a higher number of DSBs. Therefore, I confirmed these findings by analysing Lamin B1 and γH2AX foci formation by IF microscopy.

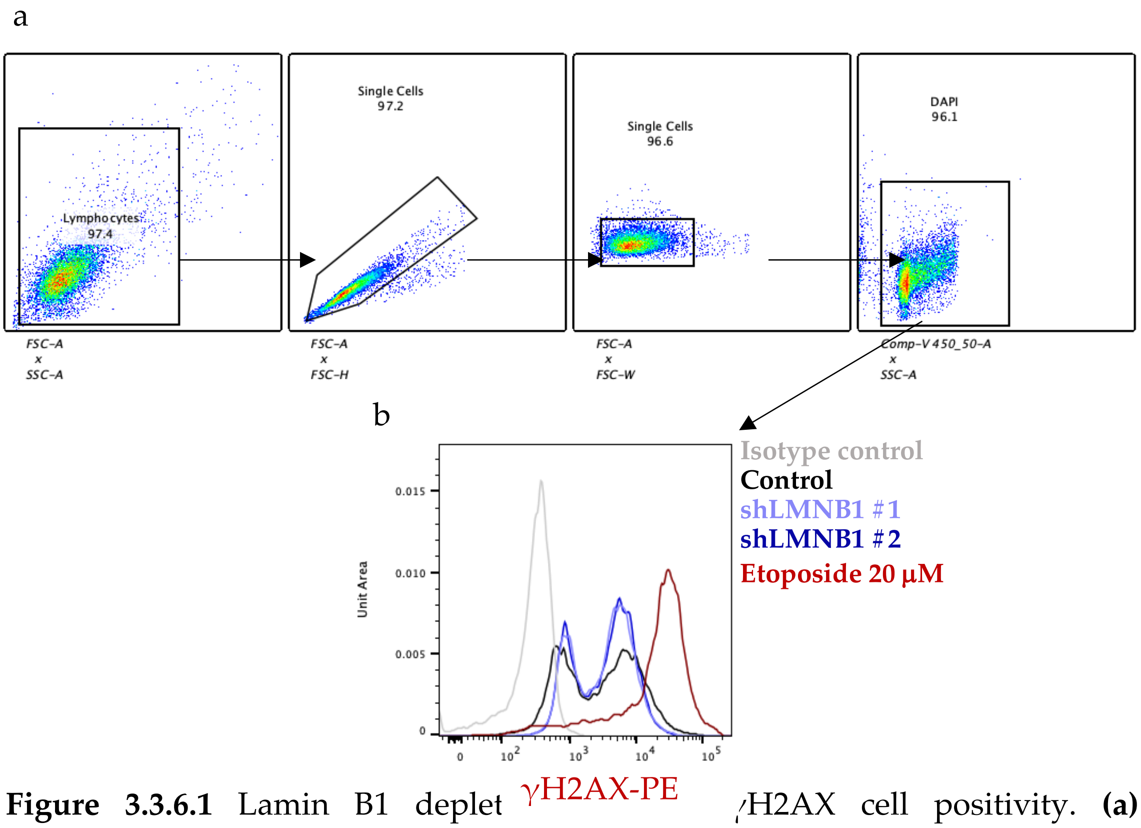

Figure 3.3.6.1 Lamin B1 deplet H2AX cell positivity. **(a)** Representative flow cytometry gating strategy of cell population used for the assessment of γH2AX in BL2 cells. Fixed BL2 cells were stained with γH2AX antibody conjugated to PE and DNA stain DAPI. **(b)** Normalised cell count histogram demonstrates an increased proportion of cells with higher fluorescent intensities of the γH2AX-PE channel, specifically in BL2 shLMNB1 cells. Etoposide-treated cells were used as a positive control of DNA DSB induction.

Fixed BL2 cells were stained in parallel against Lamin B1 (Alexa-594) and γH2AX (Alexa-488) to evaluate Lamin B1 nuclear localisation and quantify the number of γH2AX foci present in individual cells. In agreement with γH2AX flow cytometry analysis, both shLMNB1 treated BL2 cells displayed a higher number of γH2AX foci per cell than control BL2 cells (Figure 3.3.6.2 b), confirming the results from COMET assay. To complement IF and flow cytometry analysis, western blotting was used to confirm depletion of Lamin B1 is negatively associated with total γH2AX (Figure 3.3.6.2 c).

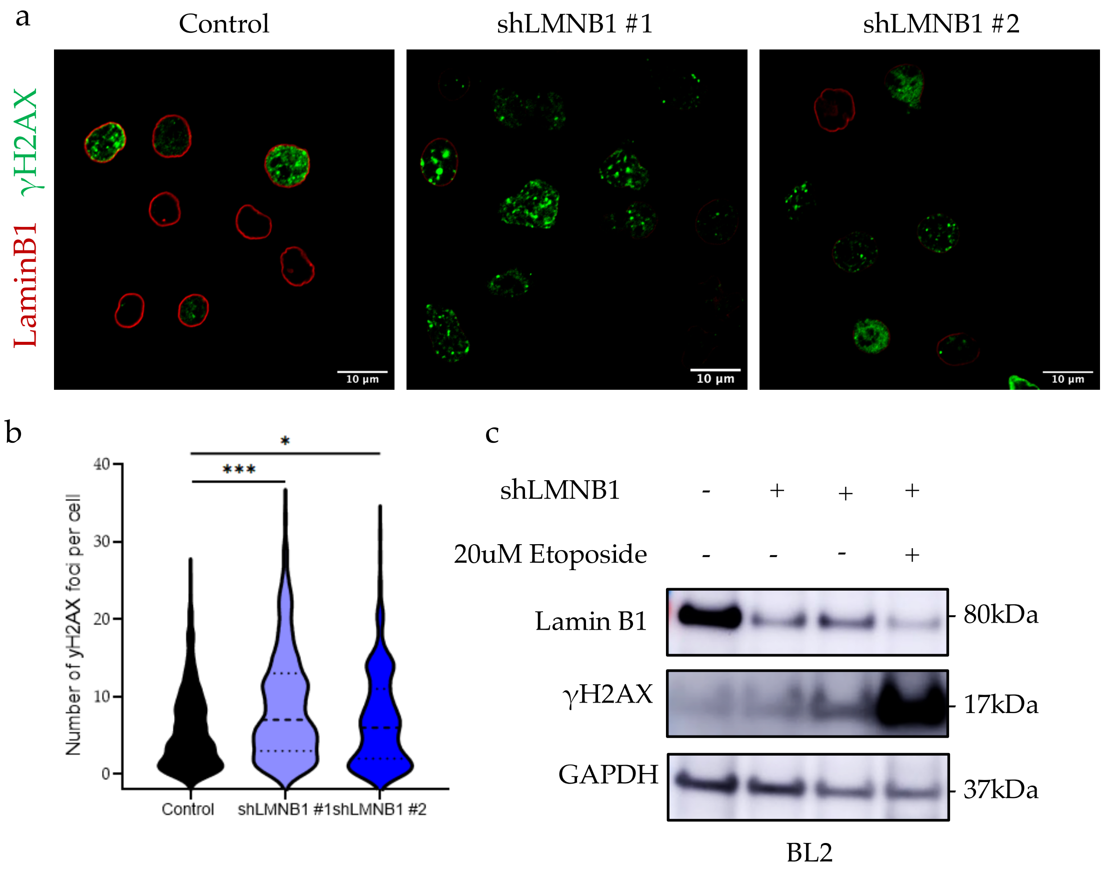

Figure 3.3.6.2 Lamin B1 downregulation increases γH2AX. **(a)** Fixed BL2 cells were stained with anti-Lamin B1 (Alexa594) and anti-γH2AX (Alexa488). Scale bar represents 10 µm. Shown images were acquired with Zeiss LSM710 confocal microscope. **(b)** Violin plots shows γH2AX distribution as a number of γH2AX per cell in control and shLMNB1 BL2 cells. Images foci analysis were acquired using a Nikon Ci-L upright fluorescence microscope and NIS elements software. At least 100 nuclei were analysed and analysed in ImageJ. **(c)** Immunoblot image of Lamin B1 and γH2AX from cell lysates extracted from BL2 control or shLMNB1 cells. GAPDH was used as a loading control. Cell lysate from Etoposide-treated cells were used as positive control of DSBs. Unpaired t-test was used for the statistical analysis. *$P \leq 0.05$; ***$P \leq 0.001$.

3.3.7 DNA damage induced by Lamin B1 depletion does not modulate homologous recombination

Next, I aimed to elucidate the cellular response to endogenous DNA damage induced by Lamin B1 depletion. Eukaryotic cells utilise two main repair pathways in response to DNA DSB, including HR or NHEJ. Unlike NHEJ, the HR pathway is a slow and error-free way to repair DSB. HR pathway utilises a homolog DNA strand as a substrate to facilitate repair, mainly restricted to the S and G2 phases of the cell cycle[216]. As a result, HR repair of DSBs was assessed by quantifying RAD51, a well-established marker of HR[87]. I found no changes in HR response as detected by the number of RAD51 foci per cell using IF microscopy (Figure 3.3.7.1). Complementary to IF analysis, total RAD51 protein levels were analysed by western blot and no changes were observed between BL2 shLMNB1 and controls cells (Figure 3.3.8.2). This led me to hypothesise that cells with a decreased Lamin B1 expression utilise alternative repair mechanisms.

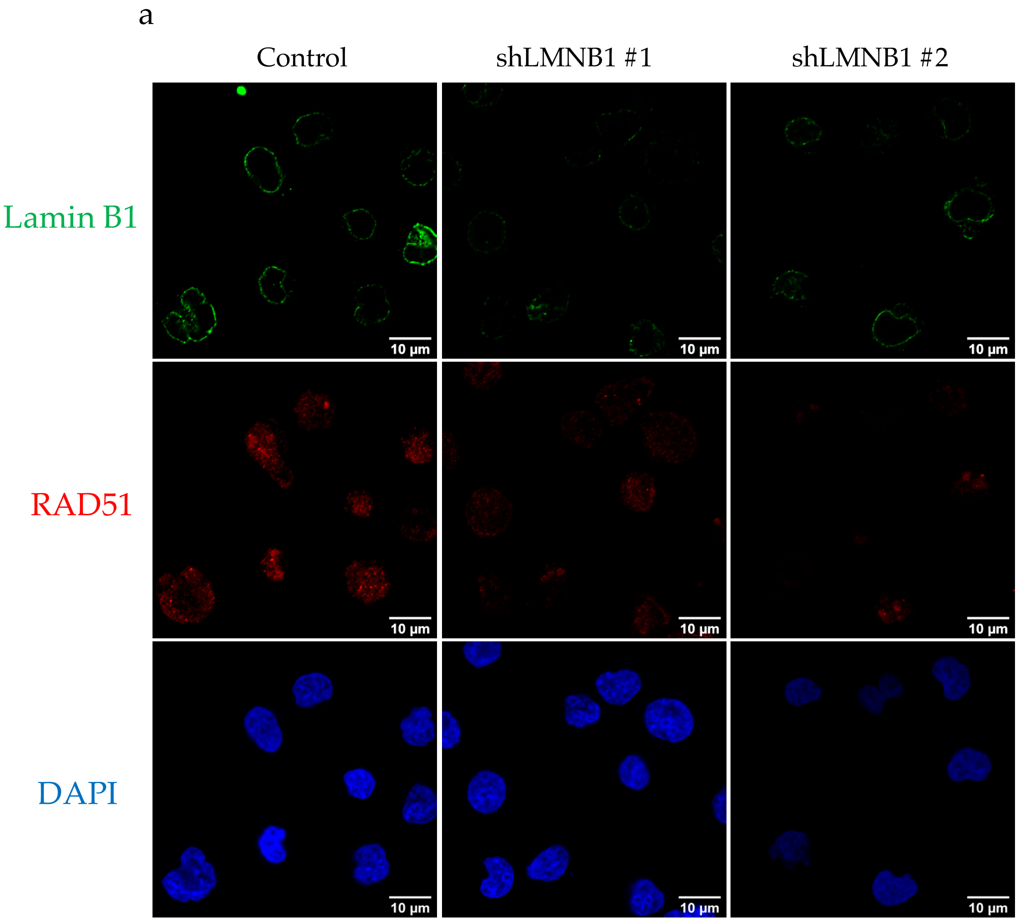

b

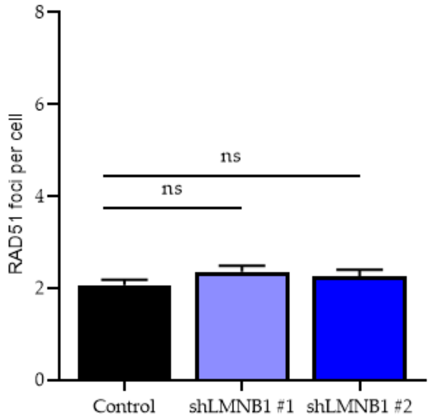

Figure 3.3.7.1 Lamin B1 depletion does not promote HR repair. **(a)** Fixed BL2 cells were stained with anti-Lamin B1(Alexa488) and anti-RAD51(Alexa594). DAPI was used as a nuclear stain. Scale bar represents 10 µm **(b)** RAD51 foci were counted in control (n = 4) and shLMNB1 BL2 cells (n = 3). At least 100 nuclei were analysed using the ImageJ mask. Bar charts represent the mean from four independent experiments, and error bars represent s.e.m. ns, not significant.

3.3.8 Increased localisation of 53BP1 in response to DSB breaks in shLMNB1 BL2 cells

The alternative pathway involved in DNA DSB repair is NHEJ, which can be engaged when an intact DNA template is not available for HR. Consequently, NHEJ can facilitate the repair of DSBs regardless of the cell cycle phase; although NHEJ is most often utilised in G1 and S phases. Mechanistically, NHEJ is a faster but more error-prone process frequently upregulated in B cells[87,217]. I investigated whether NHEJ plays a role in response to Lamin B1-mediated DNA damage. I assessed the response of a key chromatin-based mediator, 53BP1, which is known to facilitate the end joining of distal broken DNA ends[218]. I first utilised IF microscopy to quantify 53BP1 foci formation upon Lamin B1 depletion. As revealed in Figure 3.3.8.1, I detected a significant increase in the number of 53BP1 foci per cell in BL2 shLMNB1 (shLMNB1 #1 $p<0.05$, shLMNB1 #2 $p<0.05$) as compared to control cells (Figure 3.3.8.1). IF microscopy findings were further validated by western blot analysis, confirming the negative correlation between Lamin B1 and 53BP1 (Figure 3.3.8.2). These findings are consistent with data published by Butin-Israeli et al. 2016, which similarly described the upregulation of 53BP1 and NHEJ after decreasing Lamin B1 in U2OS and HCC cells[176]. I next evaluated the cell cycle distribution and percentage of actively proliferating cells to address whether Lamin B1 knockdown affects cell growth rate.

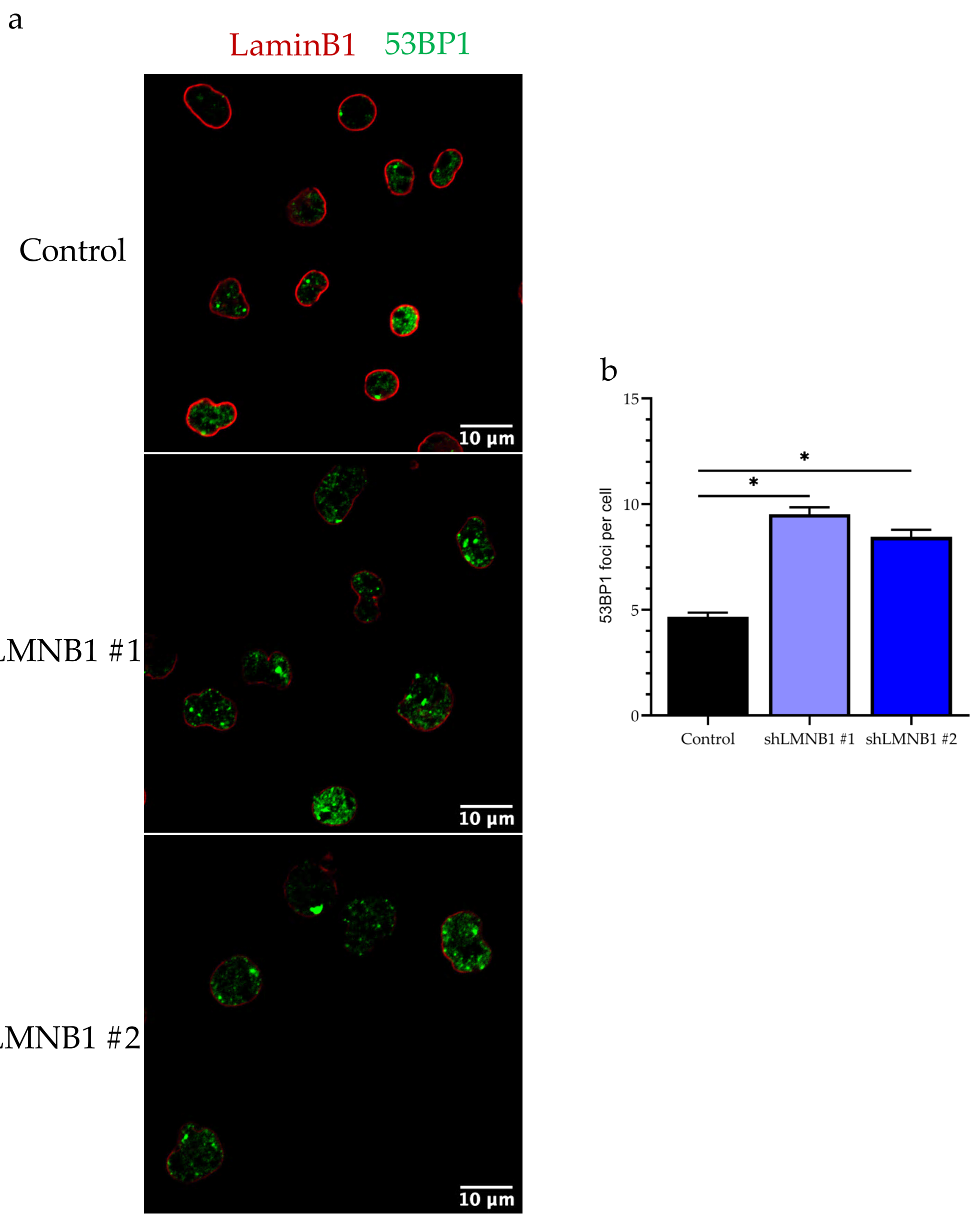

Figure 3.3.8.1 Lamin B1 knockdown induces 53BP1 foci formation as a response to DNA DSBs. **(a)** Fixed BL2 cells were stained with anti-Lamin B1 (Alexa594) and anti-53BP1 (Alexa488). Scale bar represents 10 µm. **(b)** Quantification of 53BP1 foci counted in control (n=4) and shLMNB1 BL2 cells (n=4). At least 100 nuclei were analysed, and foci was counted using the ImageJ mask. Bar charts represent the mean from at least independent experiments, and error bars represent s.e.m. Unpaired t-test was used for the statistical analysis. *$P \leq 0.05$.

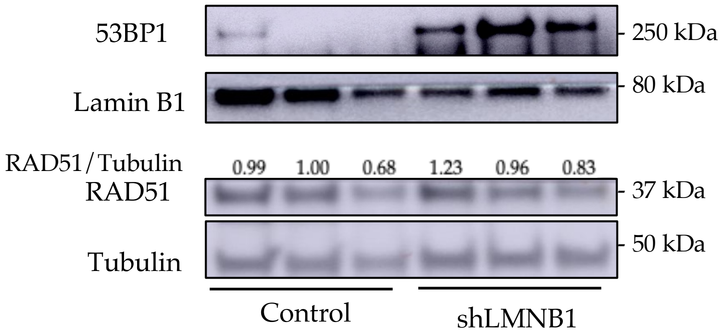

Figure 3.3.8.2 53BP1 expression is elevated in Lamin B1 depleted lymphoma cells. Immunoblot image of Lamin B1, 53BP1, and RAD51 from cell lysates extracted from BL2 control and shLMNB1 cells. Tubulin was used as a loading control. RAD51 expression is shown as a ratio normalised to Tubulin.

3.3.9 Lamin B1 knockdown increases the proliferative capacity of BL2 cells

Fluctuation of Lamin B1 levels is commonly associated with changes in proliferation[168], senescence induction[165], or enhanced cell migration[164]. Naturally, increased DNA damage can lead to cell cycle arrest until adequately repaired, which, in turn, impairs proliferation[219]. Our group had previously demonstrated that siRNA LaminB1 knockdown enhances the proliferation of BL2 cells[131]. Therefore, EdU (5-Ethynyl-2'-deoxyuridine) incorporation assay was used to assess the effect of Lamin B1 depletion on the proliferation in the BL2 shLMNB1 model. EdU is incorporated into the newly synthesised DNA strand and can be used to measure the proportion of actively proliferating cells (EdU+) by flow cytometry. Logarithmically growing cells were incubated with 10 μM EdU for 2 hours and stained with anti-EdU Pacific Blue conjugated antibody to label EdU+ cells. Flow cytometry analysis revealed a significant increase of EdU+ cells between control and shLMNB1 BL2 cells (Figure 3.3.9.1). The proportion of actively proliferating cells was up to 12% higher in BL2 shLMNB1 cells (48%) compared to the control (37%) (Figure 3.3.9.1 b). The increase of cell proliferation in BL2 shLMNB1 cells was further confirmed by cell counts at 72 hours after induction of the shRNA vector. BL2 cells are highly proliferative with a doubling time of ~18 hours, therefore the proliferation surge attributed to Lamin B1 depletion suggests a transcriptional dysregulation of genes involved in cell growth.

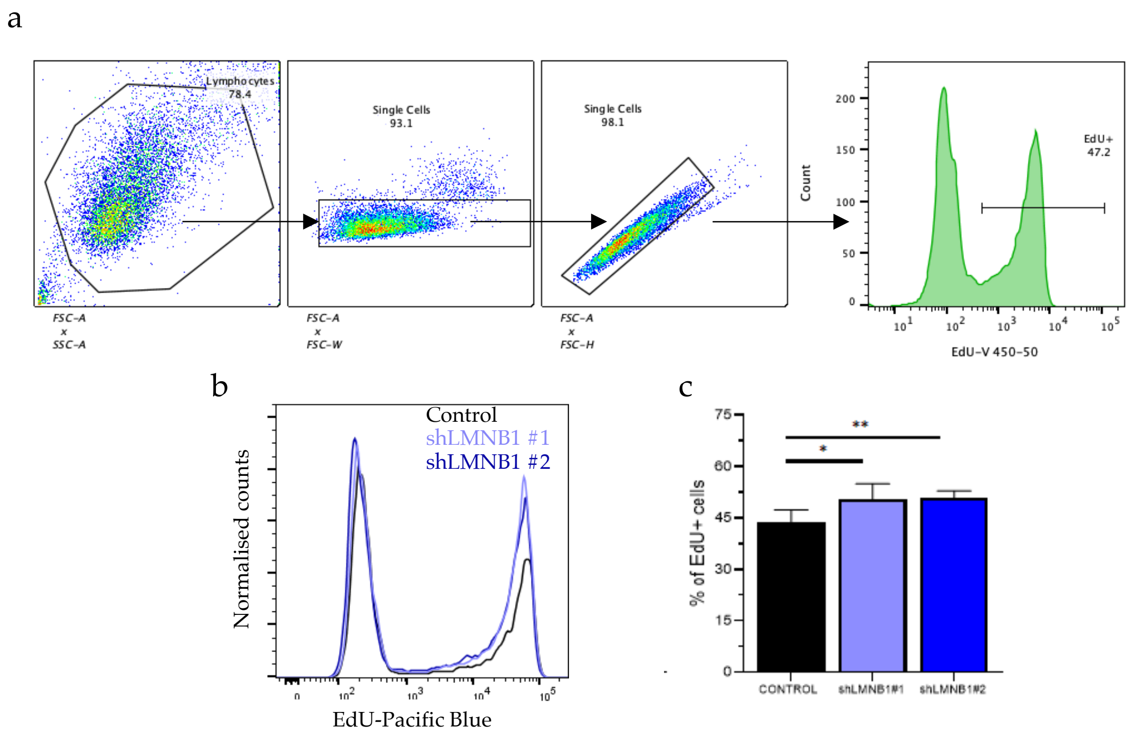

Figure 3.3.9.1 Increased proliferation in BL2 shLMNB1 cells. **(a)** Representative flow cytometry gating strategy of cell population used for EdU incorporation analysis. **(b)** Normalised cell counts flow cytometry histograms representing an increased number of BL2 shLMNB1 cells positive for EdU-Pacific Blue. **(c)** Bar chart showing the mean percentage of EdU+ cells in control (n=4) and Lamin B1 deficient BL2 samples (n=4). Error bars indicates s.e.m. Unpaired t-test was used for the statistical analysis. *$P \leq 0.05$; **$P \leq 0.01$; ns, not significant.

Cell cycle analysis was used to further determine whether Lamin B1 knockdown and increased DNA damage impair cell cycle progression. BL2 cells were fixed and stained with DAPI for analysis by flow cytometry (Figure 3.3.9.2). As expected, I detected an increased proportion of shLMNB1 BL2 cells in the S phase (48%), and a decrease in the G1 phase (30%) compared to control BL2 cells (Figure 3.3.9.2). Interestingly, there was no change in the proportion of cells in the G2/M phase (Figure 3.3.9.2). Taken together, the data indicate that LaminB1 knockdown does not cause phase-specific cell cycle arrest. Our findings are in line with previous reports by our group and are now demonstrated in a DOX-inducible shRNA vector. In addition to experimental data from BL2 cells, I further validated our findings in a GCB-derived DLBCL cell line OCI-LY8. Contrary to studies showing Lamin B1 decrease leads to inhibition of proliferation, our results agree with data published by Klymenko et al., showing increased B cell proliferation upon Lamin B1 depletion[131].

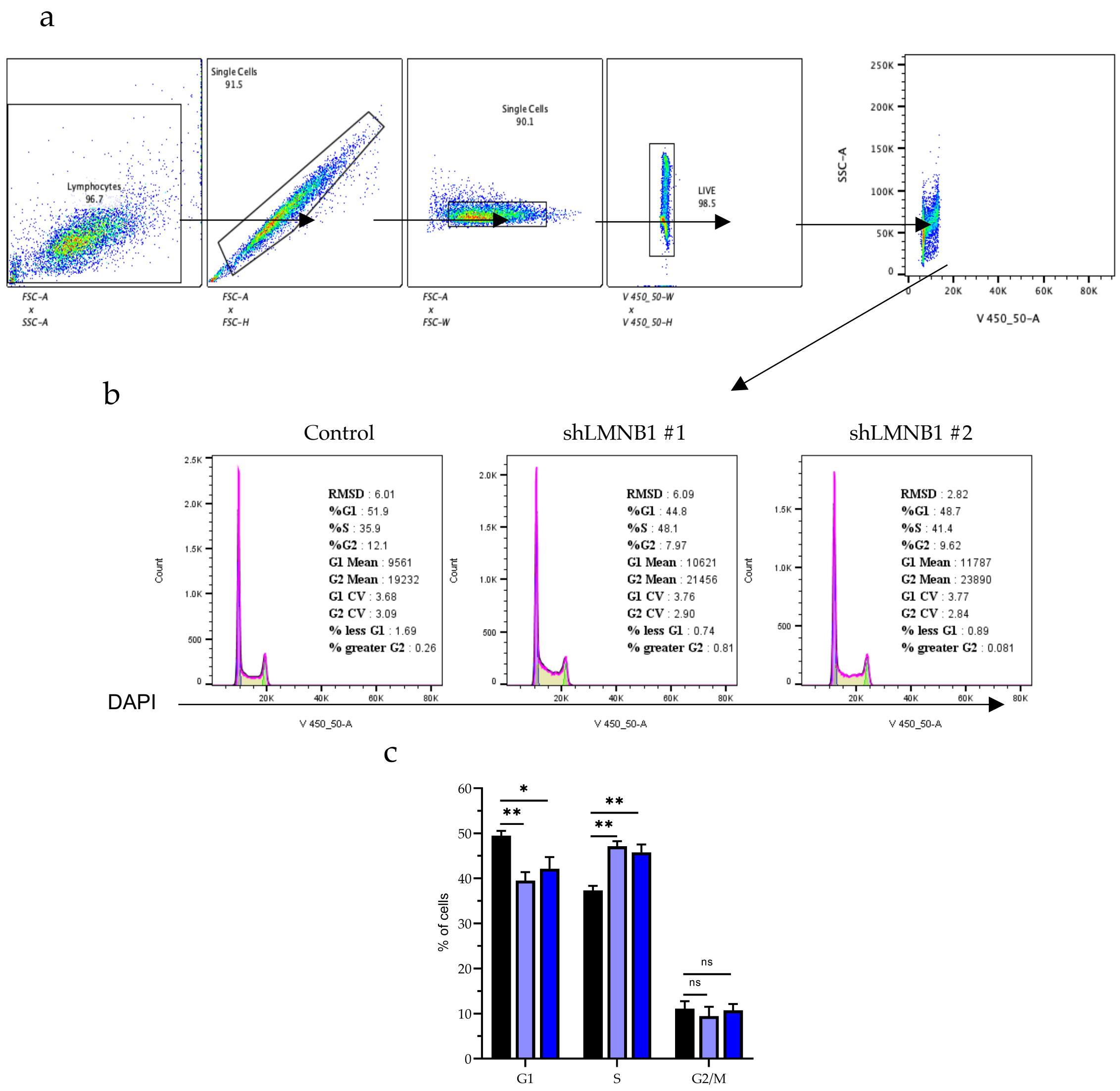

Figure 3.3.9.2 Cell cycle analysis of BL2 cells upon Lamin B1 knockdown. **(a)** Representative flow cytometry back gating strategy of cell population used for DAPI-based cell cycle analysis. **(b)** Representative cell cycle charts generated by FlowJo. **(c)** Bar chart showing the average proportion of BL2 cells within the cell cycle phase as measured by flow cytometry using DAPI staining of the DNA content (n=4). Error bars indicate s.e.m. Unpaired t-test was used for the statistical analysis. *$P \leq 0.05$; **$P \leq 0.01$; ns, not significant.

3.3.10 Validation of increased DNA damage upon Lamin B1 depletion in GC-derived B cell lymphoma cell line

For the validation experiments, OCI-Ly8 (GCB DLBCL) cells were transduced with shLMNB1 #1, which was found to result in a more prominent Lamin B1 knockdown. Transduction efficiency was assessed by flow cytometry, which confirmed successful transduction (90% GFP+ cells) (Figure 3.3.10.1). In agreement with elevated γH2AX as per flow cytometry, immunoblotting and intracellular staining of γH2AX revealed an elevated γH2AX signal in shLMNB1 treated OCI-Ly8 cells (Figure 3.3.10.1 b, c).

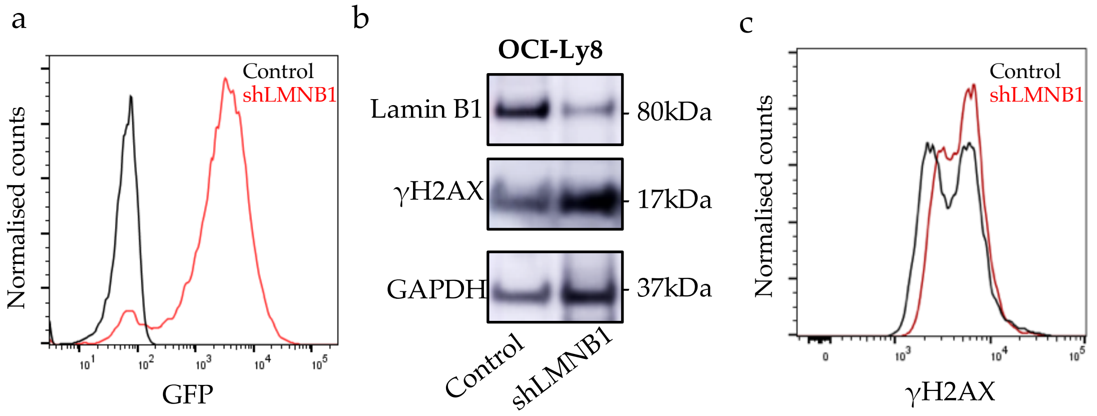

Figure 3.3.10.1 Validation of shRNA mediated Lamin B1 knockdown in OCI-Ly8 GCB DLBCL cell lines. **(a)** A representative flow cytometry chart shows the transduction efficiency by detecting the percentage of GFP+ OCI-Ly8 cells expressing shLMNB1 #1 24 hours after incubating with DOX. Untreated cells were used as a GFP- control. **(b)** Western blot image showing a decrease of total Lamin B1 levels and an increase of γH2AX in OCI-Ly8 shLMNB1 cells after incubation with DOX for 72 hours. GAPDH was used as a loading control. **(c)** Flow charts represent normalised count and fluorescent intensities of the γH2AX-PE channel.

Identically to BL2 cells, fixed OCI-LY8 cells were stained in parallel against Lamin B1(Alexa594) and γH2AX (Alexa488) to quantify the number of γH2AX foci and assess Lamin B1 nuclear incorporation (3.3.10.2). In agreement with γH2AX flow cytometry analysis, shLMNB1 OCI-Ly8 cells displayed a higher number of γH2AX foci per cell than in OCI-Ly8 control cells (Figure 3.3.10.2 b). Western blot analysis confirmed reduced depletion of Lamin B1 and increase of γH2AX (Figure 3.3.10.1 b). The cell cycle was also assessed by flow cytometry, but despite observing a similar cell cycle distribution as in BL2 cells, differences between shLMNB1 and control OCI-Ly8 cells were not significant (Figure 3.3.10.3).

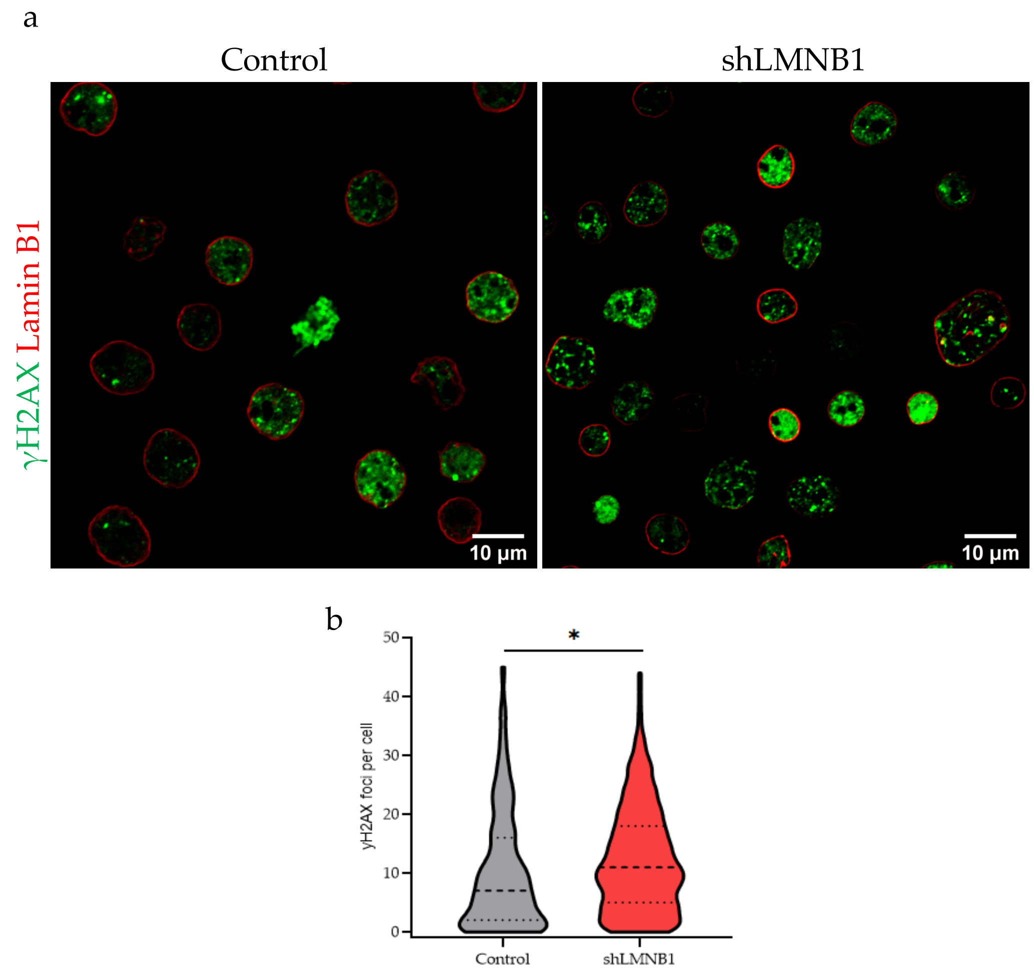

Figure 3.3.10.2 Lamin B1 depletion increases γH2AX foci in OCI-Ly8 cells. **(a)** Representative images of fixed OCI-Ly8 cells stained with anti-Lamin B1(Alexa594) and anti-γH2AX(Alexa488). Scale bar represents 10 μm. **(b)** Violin plot showing the number of γH2AX foci per cell in control and shLMNB1 BL2 cells. At least 100 nuclei were analysed. Dashed lines represent the mean from 3 independent experiments and a 95% confidence interval. Unpaired t-test was used for the statistical analysis. *$P \leq 0.05$. FoCo counter was used to quantify the number of foci per cell.

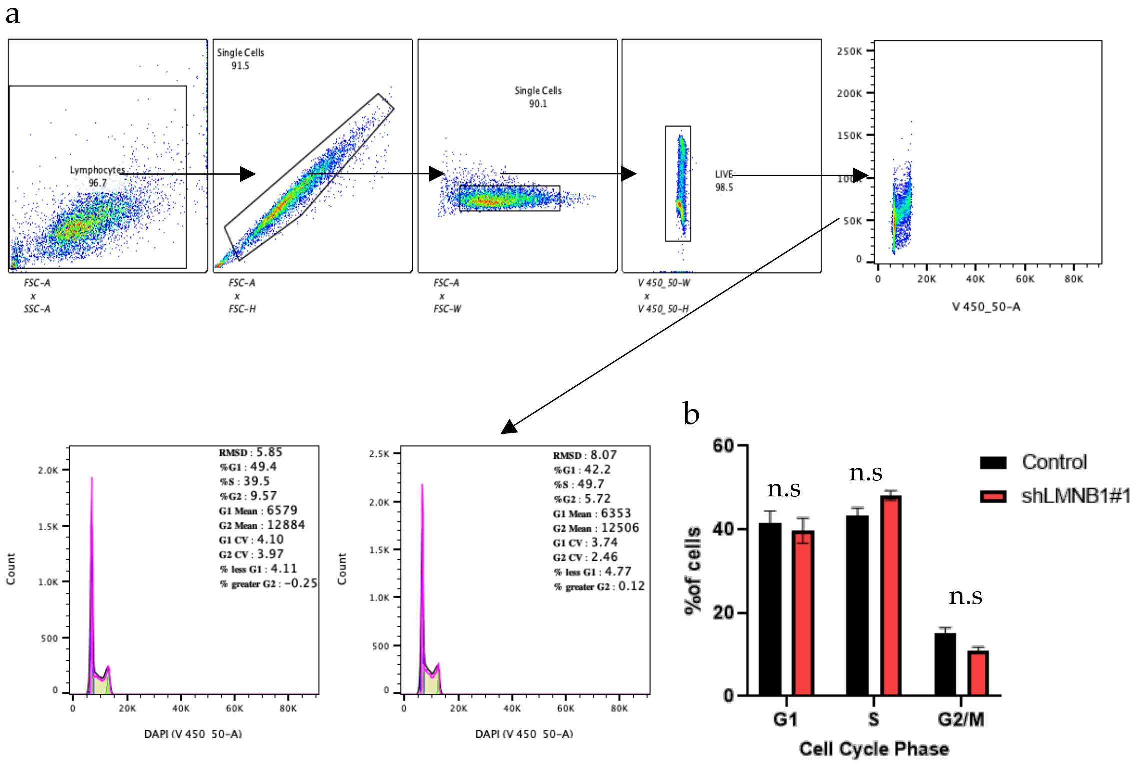

Figure 3.3.10.3 Cell cycle analysis of OCI-Ly8 cells upon Lamin B1 silencing. **(a)** Flow cytometry charts representing gating strategy for cell cycle analysis. **(b)** Quantification of cells within the specific phase of the cell cycle as measured by flow cytometry using DAPI staining of the DNA content (n=3). Unpaired t-test was used for the statistical analysis.

3.4 Discussion

In this chapter, I performed several experimental procedures that evaluated the impact of Lamin B1 depletion on genomic instability. First, I utilised previously generated WXS for the mutational analysis performed on three different cell lines (BL2 AID+, BL2 AID-, PCL12) after Lamin B1 knockdown. Furthermore, I engineered a novel *in vitro* Lamin B1 knockdown B cell lymphoma model, which was then used to assess DNA damage upon depletion of Lamin B1.

Accumulation of DNA damage in B cells is a key event of chromosomal translocations and genetic aberrations, which are likely to trigger lymphomagenesis. These genetic lesions include translocations of Ig gene with proto-oncogenes (*MYC*, *BCL6*, *BCL2*), resulting in constant expression of translocated genes. Little is known about the predispositions to chromosomal translocation and other genetic abnormalities. Therefore, capitalising on the previous work of our group, which established Lamin B1 as the epigenetic regulator of SHM in GC B cells, I further investigated the role of Lamin B1 in genomic instability.

WXS dataset was used to identify *de novo* SNVs upon Lamin B1 removal in AID-positive or AID-negative GC derived B cell lymphoma cells. Regardless of AID expression, all samples displayed an AID mutagenic signature upon siLMNB1 treatment. This observation suggests other APOBEC family members may be playing a role in this mutagenic activity. Particularly, APOBEC3G and ABPOBEC3C have relatively high expression in BL2 cells. Interestingly, high *APOBEC3G* expression was negatively associated with OS for R-CHOP treated DLBCL patients[220]. Furthermore, a recent study demonstrated *APOBEC3G* to be associated with increased DNA damage and mutagenesis in multiple myeloma patients[210]. Increased mutational burden in patients diagnosed with primary effusion lymphoma (PEL) is driven by *APOBEC3C*, which is upregulated in PEL compared to B cell lymphomas and is proposed to be a contributing factor to the development of PEL[221]. This data suggests other APOBEC family members may be responsible for the observed mutational signatures upon Lamin B1 knockdown. Interestingly, genome-wide mutational topology revealed clustering of SNVs upon depletion of Lamin B1 (Figure 3.3.3.1), likely due to increased chromatin accessibility upon reduced nuclear localisation of Lamin B1.

Several studies have previously demonstrated that Lamin B1 removal is known to cause changes in chromatin organization and accessibility, as shown by mapping of Lamin B1 and LADs[175,177,222]. Broader DNA accessibility can result in higher susceptibility to mutagenesis, as DNA is no longer protected by nuclear lamina. In this chapter, our data complement the previous studies[46,223,224], which demonstrated mutations are not uniformly distributed events across the genome. The question regarding the susceptibility of specific genomic regions to mutations has not been fully elucidated. Sources of mutational clusters can cause endogenous DNA damage – AID/APOBEC, error-prone repair by TLS[223], DNA motif sequence[225], DNA fragility and susceptibility to DSBs[142]. APOBEC cytidine deaminase targets unique sequences of DNA, resulting in the generation of clusters displaying APOBEC mutational signature[39,226,227]. Based on the data presented in this chapter, I provide further evidence that Lamin B1 plays a role in maintaining genomic stability, as suggested by WXS. COSMIC signature analysis and topology of mutations revealed Lamin B1 depletion induces SNVs groups independently of AID expression.

To overcome limitations of previously established RNAi Lamin B1 based cell lines, I further investigated the role of Lamin B1 in genomic instability by the generation of an efficient and inducible shRNA targeting Lamin B1, utilising a puromycin resistant gene, DOX dependent promoter, and TurboGFP reporter (Figure 3.3.4.1). The CMV promoter has been shown to have the highest activity in human cells[228]. Using the shRNA approach, Lamin B1 levels were reduced by up to 70% at the protein level, which agrees with other studies utilizing the shRNA-mediated knockdown in different cell models[164,176,177,168]. Upon successfully generating Lamin B1 knockdown in the B cell model, I demonstrated increased DNA damage by COMET assay and γH2AX analysis. Elevated γH2AX in shLMNB1 cells is consistent with data from osteosarcoma and hepatocellular carcinoma cells reported by Butin-Israeli et al. 2015[176]. Flow cytometry analysis of BL2 control and shLMNB1 cells revealed that two γH2AX cell populations exist, which might be directly related to the cell cycle phase and DNA content (Appendix Figure 10.1.3). Flow cytometry analysis of γH2AX suggests that there is a higher number of shLMNB1 cells in S and G2/M, which can be a contributing factor to elevated γH2AX. Therefore, a secondary quantitative analysis independent of the cell cycle phase (e.g. IF, western blotting) was required to assess the γH2AX levels. A study by Liu et al. demonstrated that Lamin B1 depletion represses RAD51 and sensitises cells to IR by Lamin B1-mediated stabilization of RAD51 after the induction of DNA damage. Consequently, I was interested in assessing DNA damage response in Lamin B1-depleted lymphoma cells. First, I assessed the HR pathway by evaluating RAD51 response, which remained unchanged in BL2 shLMNB1 cells compared to the control (Figure 3.3.7.1). Recent work by Van Steensel group has discovered that the choice of DSB repair pathway is dependent on the local chromatin environment, which directly influences the choice of DNA repair pathway[229]. Particularly, NHEJ has been shown to repair DSBs associated with euchromatin[229]. As previously described, Lamin B1 removal from the nuclear periphery disrupts LADs and contributes to chromatin relaxation, including the involvement of the NHEJ pathway[175,183].

Western blot analysis and confocal microscopy demonstrated an increase of 53BP1 in Lamin B1-depleted cells. However, while both approaches were consistent in BL2 shLMNB1 treated cells, western blot analysis showed very low levels of 53BP1 in control cells, which is contradictory to IF imaging. Increasing amount of protein loaded onto the gel and exposure time during image development could improve the sensitivity of the 53BP1 antibody in control samples. In line with our data, a recent study has uncovered that Lamin B1 sequesters 53BP1 in SV40-transformed human fibroblasts and U2OS cells, therefore preventing DNA repair response. I propose Lamin B1 depletion induces DSBs in B cells, which are subsequently repaired by NHEJ as a direct result of 53BP1 release from Lamin B1 suppressive environment. Consequently, the involvement of an error-prone repair pathway increases the likelihood of improper repair of DSBs, leading to point mutations, and an overall increase of genomic instability, as the mutational hotspots tend to conglomerate with DSBs[230,231].

Contrary to previous studies reporting an association of decreased Lamin B1 with reduced proliferation, proliferative capacity in BL2 cells was increased (Figure 3.3.9.1). This observation is in line with data previously published by our group in the siRNA Lamin B1 knockdown model[131]. To validate our data obtained from the BL2 shLMNB1 cell line in a different GC B cell-derived lymphoma cells, core experimental assays were performed in OCI-Ly8, which expresses lower basal levels of Lamin B1 protein and higher γH2AX compared to BL2 cell line (Figure 3.3.10.1, 3.3.10.2 & Appendix Figure 10.1.1). The observed phenotype in OCI-Ly8 was not as prominent as in BL2 cell line likely due to lower basal Lamin B1 expression seen in OCI-Ly8 cells. Taken together, these findings further signify the cell-type specificity and the role of Lamin B1 in B cell biology and genomic instability.

Chapter 4: Single Molecule Localisation Microscopy analysis of Lamin B1, γH2AX, and chromatin in BL2 cells

4.1 Introduction

In chapter 3, I demonstrated Lamin B1 silencing induces DNA damage in lymphoma cells. I was further interested to perform a spatial localisation analysis of γH2AX foci with respect to chromatin and Lamin B1. The spatial organization of the genome and chromatin accessibility are partly regulated by tethering to Lamin B1, forming lamina-associated domains (LADs), which are located primarily near the nuclear periphery[152,232]. However, recent studies revealed that Lamin B1 also colocalises with facultative and highly dynamic euchromatin regions[175]. Furthermore, localisation of DNA damage and repair was shown to rely on spatial organization and accessibility of chromatin[233]. Lamin B1 nuclear localisation has been previously studied by super-resolution microscopy (SRM) in various cell types[234–236]. The topology of γH2AX foci has been extensively studied by conventional microscopy techniques and single molecule localisation microscopy (SMLM)[237–241]. To our knowledge, no previous groups have visualised DNA damage and Lamin B1 in a single nucleus using SRM imaging. In a collaboration with colleagues from Germany, we used the state of the art microscopy for the SRM visualisation of Lamin B1 together with γH2AX foci and chromatin. Here, I optimised a dual-colour SMLM imaging for the localisation analysis of DSBs and chromatin with respect to Lamin B1. Chromatin was visualised using a DNA intercalator (Sytox Orange), which can be imaged by DNA structure fluctuation-assisted (fBALM) detection under specific pH conditions providing an accurate imaging of DNA-bound molecules at nanoscale level[242]. In this chapter, I describe the development and implementation of a novel comprehensive analytical approach for the assessment of Lamin B1, chromatin, and γH2AX in a single cell.

4.2 Chapter aims and hypothesis:

In this chapter, I developed a novel technique to study the nuclear lamina in relation to chromatin and DNA damage. Based results in chapter 3, we optimised a dual-colour SMLM imaging for comprehensive localisation and correlation analysis between DNA, Lamin B1, and γH2AX. I hypothesised that Lamin B1 and DNA would colocalise at the nuclear periphery and that the localisation of Lamin B1 would be negatively correlated with γH2AX in BL2 shLMNB1 cells.

Chapter aims:

1. Optimization of staining protocols for the SMLM of Lamin B1, DNA, and γH2AX.
2. Clustering and localisation analysis of γH2AX foci in Lamin B1 depleted nuclei.
3. Comprehensive topological analysis of DNA and Lamin B1.

4.3 Results

4.3.1 Super-resolution microscopy of Lamin B1 and γH2AX in BL2 cells

To develop dual-colour SRM imaging, I utilised the inducible shRNA Lamin B1 knockdown BL2 cell line established in Chapter 3. I first optimised the Lamin B1 staining protocol for SMLM using a combination of different fluorophores and embedding media that would allow me to image both antigens (Table 4.1). I detected a decrease of Lamin B1 mainly around the nuclear periphery in BL2 shLMNB1 cells (Figure 4.3.1.1 a, b), confirming the staining by confocal microscopy imaging before SRM imaging (Appendix Figure 10.2.2). As anticipated, Voronoi and radial distribution analysis revealed that BL2 control nuclei have a higher Lamin B1 density and more uniform distribution at the nuclear periphery compared to shLMNB1 nuclei (Figure 4.3.1.1). In line with our previous analysis in Chapter 3, SMLM imaging analysis confirmed the reduction of Lamin B1 is observed primarily around the nuclear periphery of BL2 shLMNB1 cells.

Antigen #1	Fluorophore #1	Antigen #2	Fluorophore #2	Embedding medium
Lamin B1	AF647	γH2AX	AF594	Prolong Gold
Lamin B1	AF647	DNA	Sytox Orange	PBS
Lamin B1	AF647	DNA	Sytox Orange	Prolong Gold
H3K9me3	AF594	LaminB1	AF647	Prolong Gold

Table 4.1 Summary of target antigens and detection fluorophores used for immunofluorescence staining and embedding buffer. Imaging of Sytox Orange required the addition of Glucose-Oxidase buffer prior to SMLM.

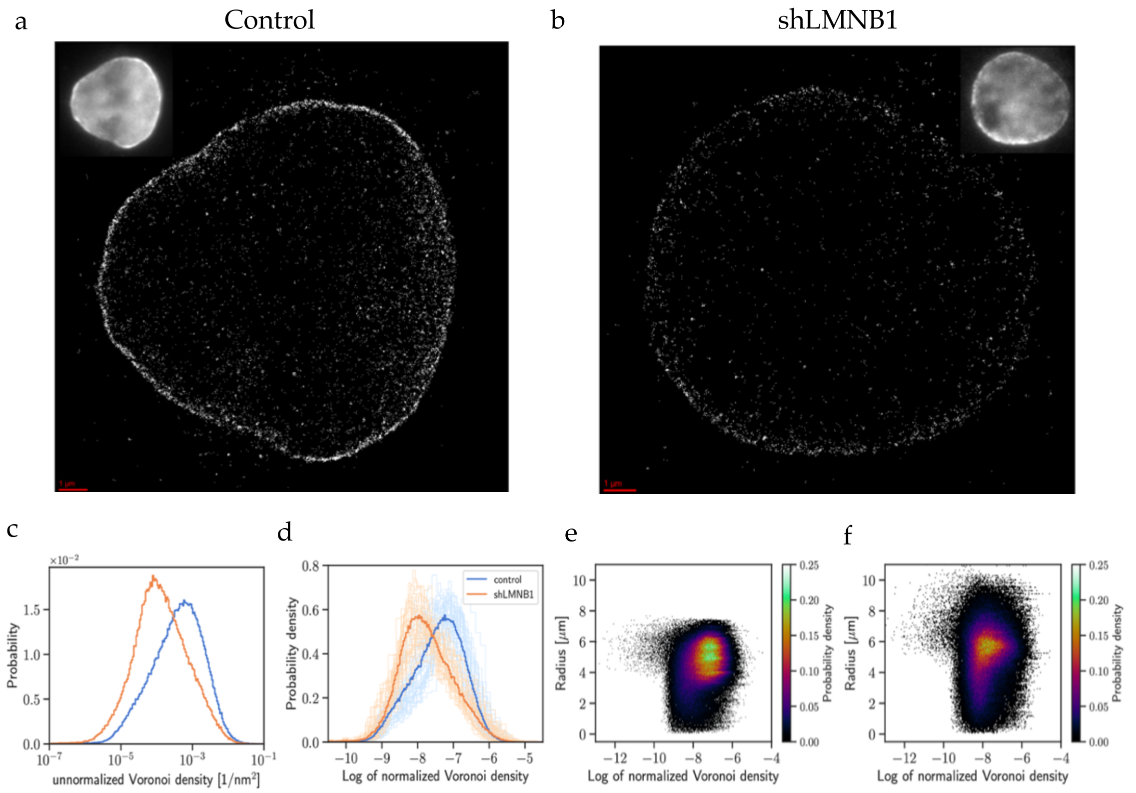

Figure 4.3.1.1 Voronoi analysis of LaminB1 for control and shLMNB1 nuclei. Representative SMLM images with their corresponding widefield images of **(a)** control and **(b)** shLMNB1 BL2 nucleus. **(c-d)** Histograms of the **(c)** unnormalised (absolute) and **(d)** normalised Voronoi density distributions. Curves represent the distribution across the measurements from 37 control and shLMNB1 nuclei each. **(e-f)** The radial density distributions of control **(e)** and shLMNB1 nuclei **(f)** are shown. Each point represents one localisation with its radial position and Voronoi density. The red scale bar shows 1 µm.

Next, SMLM was used to assess the localisation and distribution of γH2AX clusters in control and BL2 shLMNB1 nuclei (Figure 4.3.1.2). Complementary to confocal microscopy analysis in Chapter 3, shLMNB1 nuclei contained a higher number of γH2AX clusters (Figure 4.3.1.2 c). I was next interested whether higher foci frequency affects the relative distribution of γH2AX in BL2 shLMNB1 nuclei. Applying the Voronoi analysis, I did not observe any striking differences in γH2AX cluster density between the control and shLMNB1 nuclei (Figure 4.3.1.3 a, b). Radial distribution of Voronoi density revealed marginally sparser localisation of γH2AX clusters in shLMNB1 nuclei (Figure 4.3.1.3 c,d), suggesting increased scattering of γH2AX clusters throughout the Lamin B1 depleted nuclei.

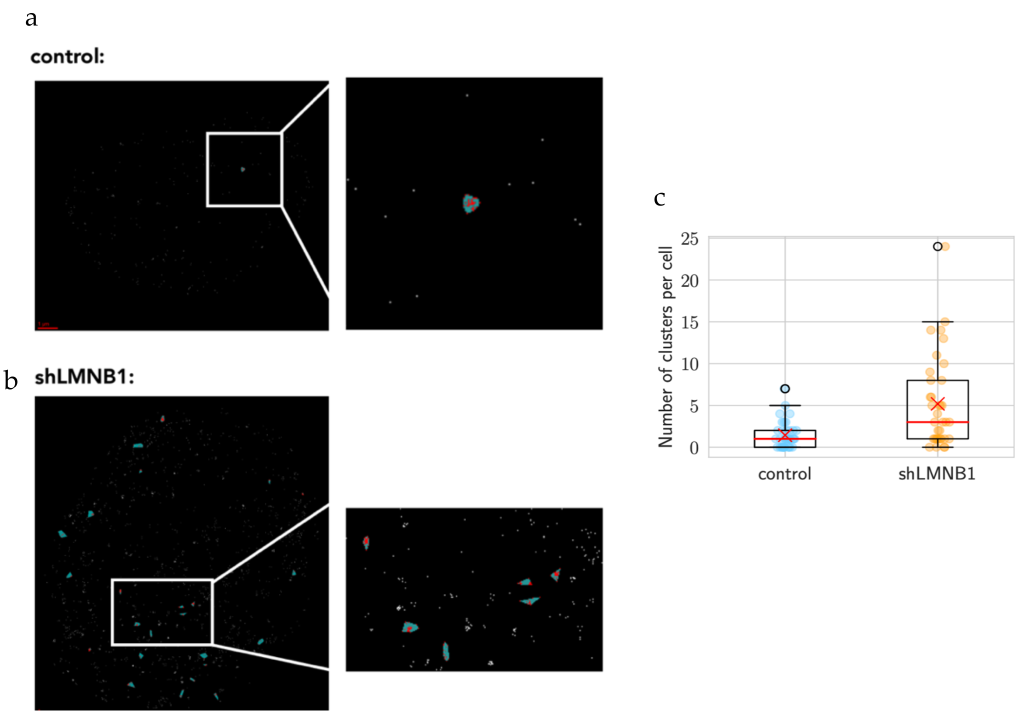

Figure 4.3.1.2 Representative SMLM images of γH2AX clusters in control **(a)** and shLMNB1 **(b)** BL2 nuclei. **(c)** Quantification of γH2AX clusters in control and shLMNB1 nuclei. A total of 37 control and shLMNB1 nuclei was analysed. Scale bar represents 1 µm.

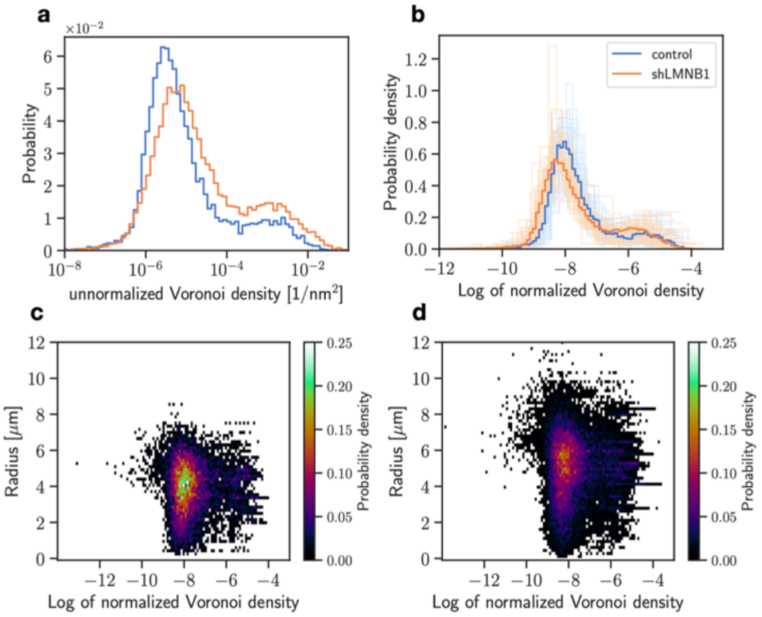

Figure 4.3.1.3 Voronoi density distributions of γH2AX. The difference is shown between the **(a)** unnormalised and **(b)** normalised Voronoi densities. The bold curves show the distribution considering all measurements, and the faint curves show the individual measurements of 37 control and shLMNB1 nuclei each. The normalised radial distribution of Voronoi densities is shown for control **(c)** and shLMNB1 **(d)** nuclei.

I further analysed the distribution of γH2AX molecules and Lamin B1. Previous reports have shown that DNA breaks within the euchromatin are repaired more effectively than to ones associated with the heterochromatin compartment due to easier access of DNA repair proteins[233,243]. I performed a topological analysis of Lamin B1 and γH2AX to address how Lamin B1 depletion influences the localisation of γH2AX. I hypothesised γH2AX would be particularly enriched at the nuclear periphery and within Lamin B1-free domains, likely corresponding to dynamic and accessible chromatin. Colocalisation analysis revealed a random distribution of γH2AX and Lamin B1 (Figure 4.3.1.4). Lower colocalisation of Lamin B1 and γH2AX signal in BL2 shLMNB1 suggests that DSBs are likely to locate within Lamin B1-free domains, which are commonly associated with the euchromatin structures (Figure 4.3.1.4 b). However, this observation may be attributed to the overall decrease of Lamin B1 molecules in BL2 shLMNB1 nuclei. Additionally, it must be noted that a single repair focus contains approximately 10 units of γH2AX enriched sub-cluster. This approach is currently unable to distinguish whether one γH2AX cluster corresponds to a single DSB break or several broken strands. Approximately 55% of the detected γH2AX signal was located along the Lamin B1 line (nuclear periphery) in BL2 control nuclei, while this proportion was even higher in BL2 shLMNB1 nuclei (65%) (Figure 4.3.1.4 c). To address whether γH2AX occurs within the euchromatin or heterochromatin domains, we optimised heterochromatin marker H3K9me3 and Sytox Orange to visualise DNA (Appendix Figure 10.2.1).

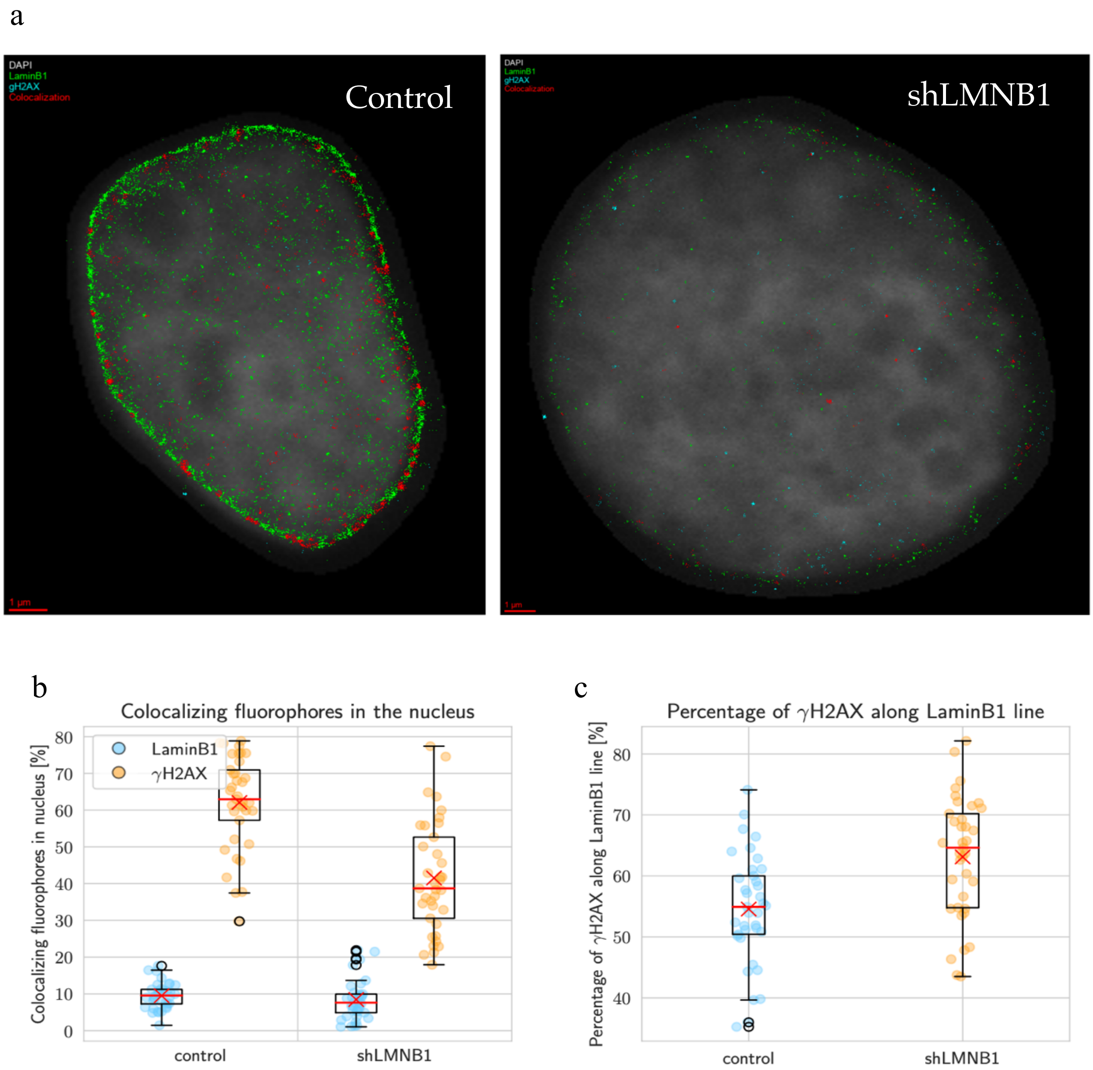

Figure 4.3.1.4 Colocalisation of Lamin B1 and γH2AX. **(a)** Representative SMLM colocalisation images of control and shLMNB1 nucleus. Lamin B1 (green) and γH2AX (cyan) signals are overlayed (red). **(b)** The percentage of colocalizing fluorophores in the nucleus is shown for control and shLMNB1 nuclei. **(c)** The percentage of γH2AX that is localised along the nuclear lamina is shown. The region of the nuclear lamina was defined by the Lamin B1 line. Grey background is a wide field image of DAPI.

4.3.2 SMLM of Lamin B1 and chromatin in the same nucleus

We performed a colocalisation analysis of Lamin B1 and chromatin structures stained with Sytox Orange. For this, we developed and optimised a novel dual-colour SRM imaging of Sytox Orange and Lamin B1 within the same nucleus (Figure 4.3.2.1 & 4.3.2.2). Colocalisation was quantified by the nearest neighbour distance frequency distribution for control and shLMNB1 nuclei. Calculated differences between the control (blue) and shLMNB1 (red) curves revealed a shift to larger distances in shLMNB1 samples, explained by a decreased colocalisation of Lamin B1 and Sytox Oranges, likely due to Lamin B1 knockdown (Figure 4.3.2.2). Several regions at the nuclear periphery displayed high colocalisation between Lamin B1 and DNA, which likely correspond to genomic regions containing LADs (Figure 4.3.2.2 and 4.3.2.3). Removal of Lamin B1 from the nuclear periphery naturally results in decreased Lamin B1/DNA binding, thus lower colocalisation is seen at the sites where LADs are normally located.

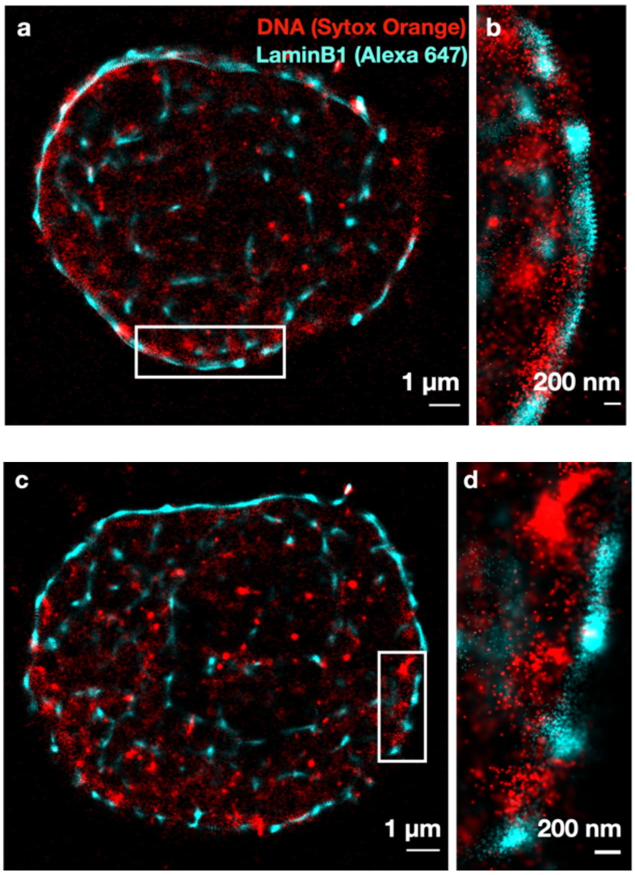

Figure 4.3.2.1 Dual colour super-resolution imaging of Lamin B1 and DNA. Merged dual-colour images of Sytox Orange (Red) and Lamin B1 (Cyan) of a control **(a)** and shLMNB1 **(c)** nucleus with inserts magnifying the nuclear periphery **(b,d)**. The images were reconstructed with ThunderSTORM, using Gaussian rendering with a non-forced lateral uncertainty of 20 nm and a magnification of 50×. Both images were reconstructed from 5000 frames. The shift between the two channels was manually corrected.

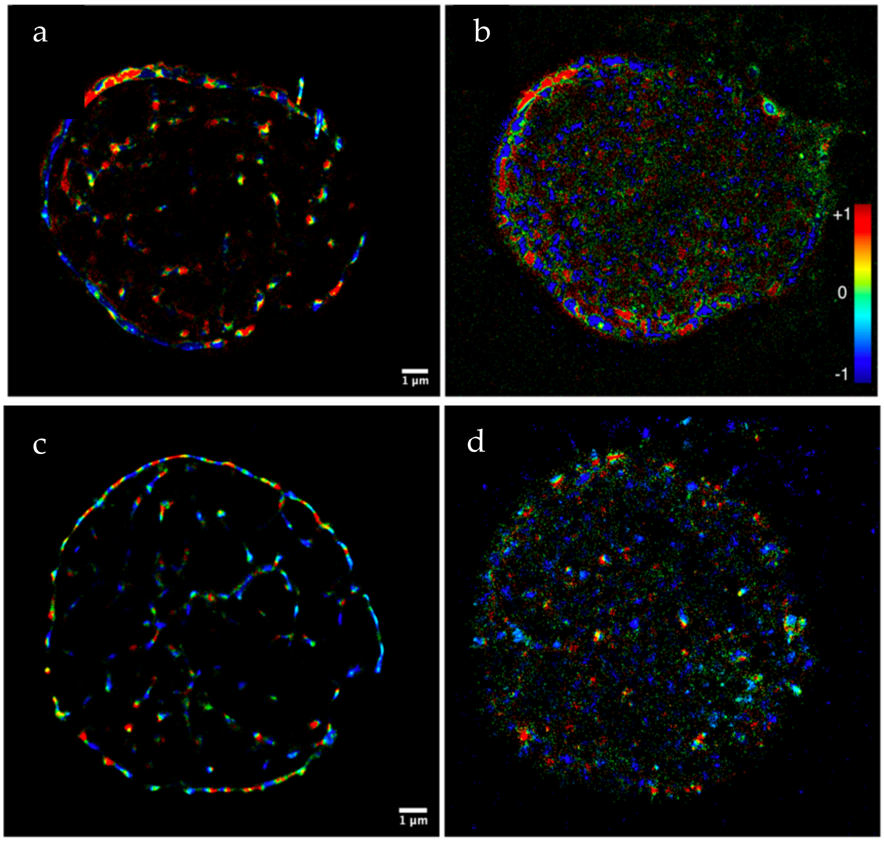

Figure 4.3.2.2 Spatial visualization of Lamin B1 and DNA colocalisation. The calculated colocalisation values of LaminB1 and Sytox Orange are shown both for a representative control **(a, b)** and shLMNB1 **(c, d)** nucleus. The colormap indicates the colocalisation value of each xy-position coordinate for LaminB1 molecules **(a, c)** and Sytox Orange molecules **(b, d).** Indicated values of +1 (red) show perfect alignment, -1 (blue) anti-correlation. A value of 0 (green) represents a low probability for colocalisation. The scale bars all show 1 µm.

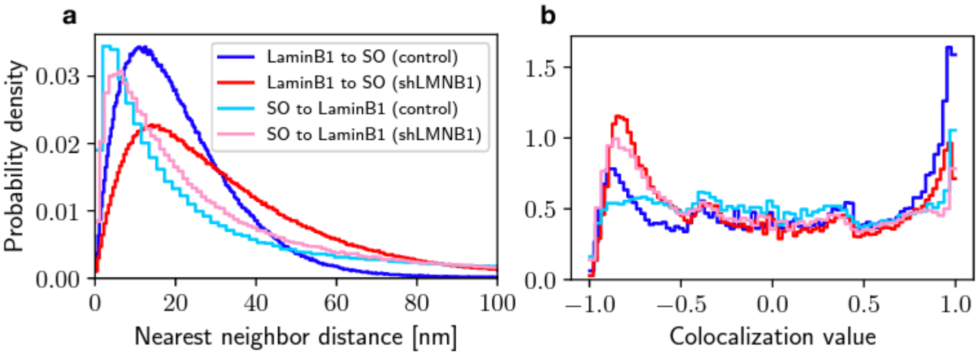

Figure 4.3.2.3 Colocalisation analysis of Lamin B1 and Sytox Orange. **(a)** Nearest neighbour distance frequency distributions for control (n=4) and shLMNB1 nuclei (n=8). The distributions were averaged over all measured nuclei and normalised. **(b)** Histograms of colocalisation values for control (n=4) and shLMNB1 (n=8) nuclei, averaged over all measured nuclei and normalised.

4.4 Discussion

In this chapter, I utilised a super-resolution microscopy analysis of Lamin B1 with respect to γH2AX and DNA in BL2 cells. To our knowledge, this is the first single-molecule localisation microscopy analysis of DNA content by Sytox Orange or γH2AX together with Lamin B1 in the same nuclei. First, SMLM validated confocal microscopy analysis described in Chapter 3. I was able to detect decreased Lamin B1 localisation at the nuclear periphery in BL2 shLMNB1 samples and increased frequency of γH2AX foci preferentially located around the nuclear periphery. This phenotype was observed particularly in shLMNB1 BL2 samples, suggesting DNA breaks occur in Lamin B1 deficient and highly dynamic chromatin regions. Additional colocalisation analysis revealed γH2AX signal was confined mainly to Lamin B1 negative regions, particularly in shLMNB1 BL2 cells, which can be explained by lower number of Lamin B1 localisation directly resulting from a Lamin B1 knockdown. I anticipated to detect genomic regions with low and high Lamin B1 localisation values corresponding to LADs. To further understand the association between Lamin B1, γH2AX, and chromatin, it would be necessary to perform a topological analysis of γH2AX and chromatin density. Ideal approach to study γH2AX and chromatin in relation to Lamin B1 would be to image all three target molecules in the single nuclei. To our knowledge, no such method has been developed.

In this chapter, I describe a novel imaging approach for visualisation of Lamin B1, DNA DSBs (marked by γH2AX), or chromatin in a single nucleus at the nanoscale level. Together with Prof. Hausmann and Prof. Cremer's lab, we developed a novel SMLM imaging methodology, which validated our increased frequency of γH2AX and decreased Lamin B1 at the nuclear periphery in BL2 shLMNB1 nuclei. Some of the preliminary analysis suggests that Lamin B1 and γH2AX are negatively correlated. A similar observation was made when assessing DNA (Sytox Orange) and Lamin B1. confirming the ability of dual-colour SMLM to identify LADs. To further utilise SMLM for a more quantitative approach, additional experiments are required to obtain enough nuclei for the statistical analysis. Furthermore, 3D-SRM could be useful for precise analysis of Lamin B1 distribution throughout the nucleus, as we were only able to image nuclei in a single plane. In addition to Lamin B1 and γH2AX analysis, we optimized a staining protocol for the heterochromatin (H3K9me3) marker with respect to Lamin B1 (Appendix Figure 10.2.1). In conclusion, we have developed a new methodology for a precise localisation microscopy imaging of DNA damage, nuclear lamina, and chromatin.

Chapter 5: Conditional deletion of Lamin B1 in mouse splenic GC B cells induces DNA damage

5.1 Introduction

Functional studies revealed that reducing Lamin B1 nuclear incorporation is associated with increased mutagenesis and DNA damage in germinal centre (GC) B cell-derived lymphoma cells. Our group previously demonstrated that Lamin B1 incorporation was reduced at the nuclear periphery of splenic GC B cells in mice[131]. To further translate and validate *in vitro* findings, I investigated the role of Lamin B1 in a novel *LMNB1* knockout *in vivo* model. Previous studies demonstrated that Lamin B1 is a vital developmental component of mammalian cells, as complete Lamin B1 knockout mice died immediately after birth due to defects in skeletal, neurological, and other organs[163,164,244]. While a complete Lamin B1 knockout caused lung defects and death immediately after birth, a haplo-insufficient Lamin B1 knockout resulted in a high incidence of spontaneous lung tumour formation in mice[164]. Contrary to the detrimental effect of Lamin B1 deletion during development, Lamin B1 deficient keratinocytes did not display any adverse phenotypic changes[245], further implying the role of Lamin B1 is cell-type dependent. Currently, there are no animal models with a genetically modulated Lamin B1 expression in GC B cells.

Considering the importance of Lamin B1 in cell development, I designed an experimental model that would allow me to investigate the role of Lamin B1 on genomic instability and adaptive immune response *in vivo*. Complementary to the hypomorphic Lamin B1 *in vitro* model, I intended to generate an inducible GC B cells-specific Lamin B1 knockout mouse model. Conditional Lamin B1 deletion can be accomplished by crossing *LaminB1*$^{fl/fl}$ mice with *Ighg1*(*C*γ*1*)-dependent *Cre* recombinase (*C*γ*1*$^{+/cre}$) mice (Figure 5.1). *Cre* recombinase mediates a deletion of a genomic location containing *loxP* sites within the Lamin B1 exon sequence[246]. The advantage of *C*γ*1*$^{+/cre}$ model is that Cre recombinase activity is strictly dependent on the endogenous expression of *C*γ*1* gene, which becomes transcribed specifically in GC B cells upon the stimulation of immune response[201]. Breeding of *C*γ*1*$^{+/cre}$ with *LaminB1*$^{fl/fl}$ generates the resultant *LaminB1*$^{fl/fl}$ *C*γ*1*$^{+/cre}$ genotype, and upon the subsequent NP-CGG immunization leads to a Cre-mediated deletion of Lamin B1 in GC B cells.

GC B cells normally undergo high rates of somatic hypermutation (SHM) and class-switch recombination (CSR) events, which are driven by the generation of

DNA double-strand breaks (DSBs) mediated by AID[188]. With the straightforward *in vitro* to *in vivo* translation, I intended to assess whether deletion of Lamin B1 specifically in GC B cells leads to increased DNA damage, changes in proliferation phenotype and B cell maturation with respect to adaptive immune response (Figure 5.1).

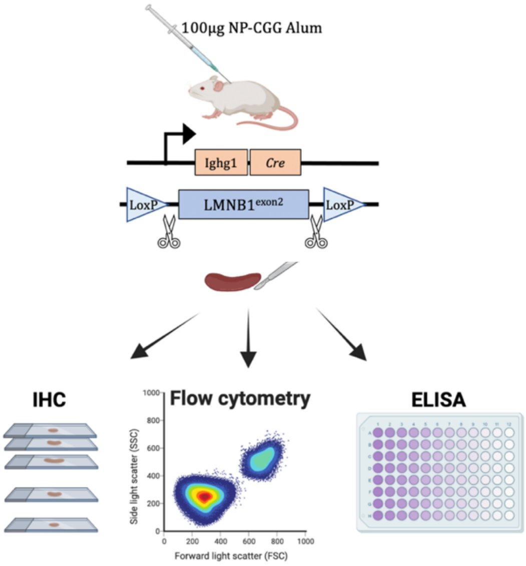

Figure 5.1 Generation of a GC B cell-specific Lamin B1 knockout mice. Schematic representation of the experimental approach to study the effect of Lamin B1 deletion in murine splenic GC B cells.

5.2 Aims and objectives

The purpose of the work described in this chapter is to study the effect of Lamin B1 deletion in GC B cells *in vivo.* The main objective is the generation of a GC B cell-specific Lamin B1 knockout *in vivo* model and validation of the *in vitro* data from Chapter 3. In addition to assessing DNA damage, I aimed to evaluate the impact of Lamin B1 deletion on humoral response. First, I hypothesised Lamin B1 deletion would lead to increased tolerable DNA damage and hyperproliferation of GCs. Further, I expected to detect a more robust humoral response upon deletion of Lamin B1 as a direct cause of hyperproliferation, mutagenesis, and class-switching. To address our hypothesis, I utilised immunohistochemistry (IHC) based analysis, high-throughput flow cytometry evaluation of cell surface markers, and ELISA assay for the assessment of antibody maturation.

Chapter aims:

1. Establishing a conditional GC B cell-specific Lamin B1 knockout mouse model.
2. Assessment of GC formation and DNA damage upon deletion of Lamin B1 in GC B cells by immunohistochemistry.
3. Immunophenotypic analysis of B cell repertoire by flow cytometry in Lamin B1 deficient mice.
4. Quantitatively measure IgG1 antibody affinity maturation upon Lamin B1 deletion.

5.3 Results

5.3.1 Generation of a conditional GC B cell-specific Lamin B1 knockout mouse model

Data published by our group showed Lamin B1 protein expression is reduced within the GCs of secondary lymphoid organs, suggesting Lamin B1 is involved in B cell-mediated adaptive immune response[131]. However, preceding experimental B cell models did not involve any genetic manipulation of Lamin B1 expression *in vivo*. Therefore, I aimed to expand on the results from previous experiments and I proposed to generate the first GC B cell-specific Lamin B1 knockout mouse model. Results from Chapter 3 demonstrated that Lamin B1 depletion induces DNA damage and increases the proliferative capacity of malignant B cells *in vitro*. Here, I hypothesised that in line with the shLMNB1 *in vitro* model, Lamin B1 knockout in the GC B cell would lead to increased genomic instability and hyperproliferative GC phenotype. I utilised a mouse model with a GC B cell-specific conditional deletion of the *LMNB1* gene ($LaminB1^{fl/fl}C\gamma 1^{+/cre}$) and a control heterozygous $C\gamma 1^{+/cre}$ genotype. All experimental mice aged 8-12 weeks old were immunised by intraperitoneal injection of 100 μg of 4-Hydroxy-3-nitrophenylacetyl-Chicken Gamma Globulin (NP-CGG) absorbed into Imject Alum to stimulate a mild immune response for 10 and 21 days. At the end of each time point, mice were culled, and spleens were processed for downstream analysis. First, GC B cells were characterised by Ki67 (proliferation marker) staining within lymphoid follicles of spleens (Figure 5.3.1.1 a). Subsequent sequential staining of Lamin B1 on the same tissue confirmed Lamin B1 deletion in GC B cells (Figure 5.3.1.1 b). In the *Cγ1*$^{+/cre}$ group, Lamin B1 was also decreased in the GC B cell (Ki67+) population compared to non-GC B cells (Ki67-), confirming the previous finding published data by our group (Figure 1.3.8.1).

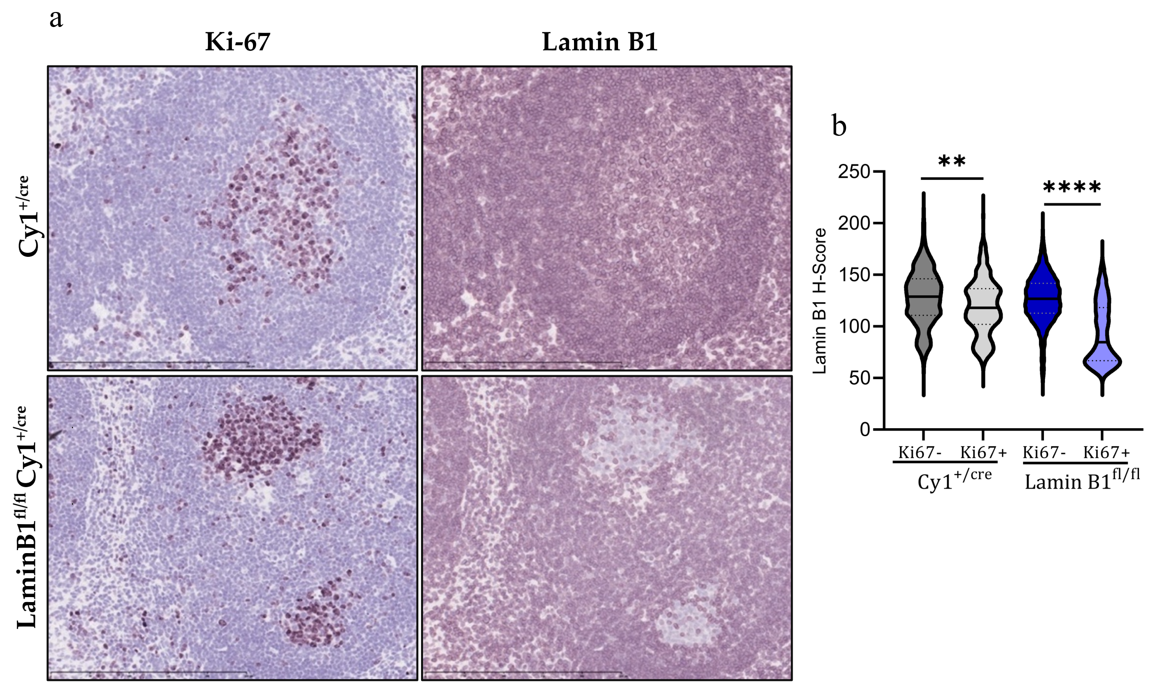

Figure 5.3.1.1 Lamin B1 deletion is achieved specifically in splenic GC. **(a)** Representative images of Ki-67 and Lamin B1 in spleen tissues from *Cγ1*$^{+/cre}$ and *LaminB1*$^{fl/fl}$ *Cγ1*$^{+/cre}$ 10 days after immunization. Vasoactive Intestinal Peptide (VIP) was used as the chromogen (pink). Scale bar represents 250 μm. **(b)** Bar chart showing the quantification of Lamin B1 signal intensity in GC B cells (Ki-67+) and non-GC B cells (Ki-67-) from 3 spleens per genotype. Unpaired t-test was used for the statistical analysis. $^{**}P \leq 0.01$, $^{****}P \leq 0.001$

5.3.2 Germinal centre formation is not impaired by Lamin B1 deletion

To evaluate the effect of Lamin B1 deletion on the proliferation and formation of GCs, I performed an immunohistochemical analysis of GCs in *Cγ1*$^{+/cre}$ and *LaminB1*$^{fl/fl}$*Cγ1*$^{+/cre}$ spleens. I did not find statistically significant differences between the number of GCs in *Cγ1*$^{+/cre}$ and *LaminB1*$^{fl/fl}$*Cγ1*$^{+/cre}$ mice 10 days (p=0.68) and 21 days (p=0.28) post-immunization, implying that Lamin B1 deletion does not restrain GC formation (Figure 5.3.2.1 a, b). Similarly, no significant differences were observed in the average size of GC in proportion to the total area of the spleen (Figure 5.3.2.1 c). Despite no differences found in the GC formation, *LaminB1*$^{fl/fl}$*Cγ1*$^{+/cre}$ (H-score) spleens displayed overall increased staining of proliferation marker Ki67 in comparison to $C\gamma 1^{+/cre}$ mice at day 10 post-immunization, suggesting a hyperproliferative phenotype might be associated with Lamin B1 depletion in B cells (Figure 5.3.2.1 d).

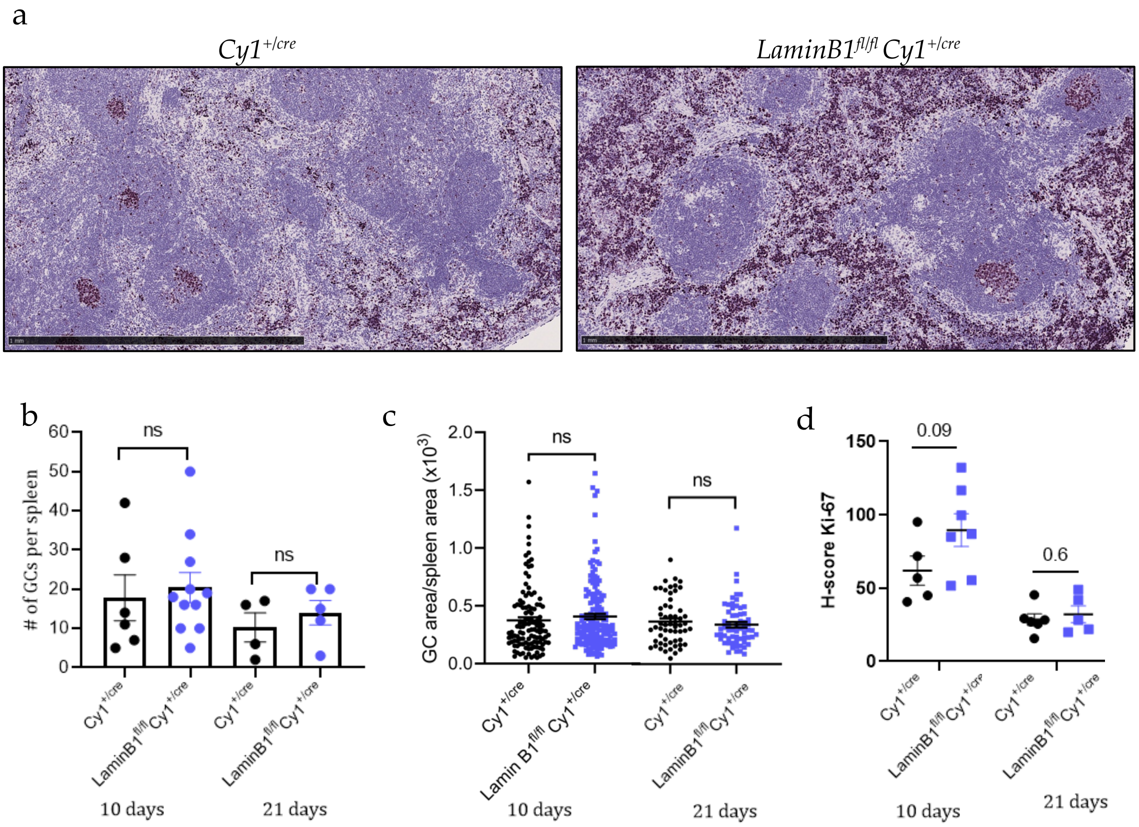

Figure 5.3.2.1 Lamin B1 loss does not affect GC formation. **(a)** Representative images of spleen tissues from $C\gamma 1^{+/cre}$ and $LaminB1^{fl/fl}$ $C\gamma 1^{+/cre}$ mice 10 days after immunization stained with anti-Ki67 antibody and haematoxylin. Scale bar represents 1 mm. **(b)** Bar charts showing the quantification of GCs per spleens in $C\gamma 1^{+/cre}$ (black) and $LaminB1^{fl/fl}$ $C\gamma 1^{+/cre}$ (blue) mice. **(c)** Chart showing the size of GCs divided by spleen area across all spleens 10 days and 21 days after immunization. Minimum of 5 mice per genotype were used for the analysis. **(d)** Ki-67 (H-Score) intensity across the entire spleen tissue. Unpaired t-test was used for statistical analysis. ns = not signigicant.

5.3.3 Loss of Lamin B1 in mouse GC B cells induces DNA damage

As previously mentioned, removal of Lamin B1 from the nuclear periphery has been observed in mouse splenic GC B cells upon immunization[131]. This phenomenon indicates that Lamin B1 removal and DNA accessibility provides the opportunity for mutagenic and recombination events within the Ig region in

B cells. Having described the effect of Lamin B1 depletion on genomic instability in GC-derived B cell lymphoma cell lines, I sought to validate *in vitro* data in the GC B cell-specific Lamin B1 knockout mouse model. I hypothesised that Lamin B1 deletion would result in elevated DNA damage due to more pronounced DNA accessibility and AID mutagenesis in GC B cells. First, I confirmed expression of AID, a cytosine deaminase controlling SHM and CSR, was upregulated specifically in GC B cells upon NP-CGG immunization (Figure 5.3.3.1). Next, IHC analysis was used to assess DNA damage upon Lamin B1 deletion by single cell multiplex analysis. Spleen tissues were sequentially stained with anti-Ki67, anti-LaminB1, and anti-γH2AX-ser139 antibodies (Figure 5.3.3.2 a & Appendix Figure 10.3.1). A higher intensity of γH2AX was detected in *LaminB1*$^{fl/fl}$*Cγ1*$^{+/cre}$ GC B cells (Ki67+ intrafollicular cells) ($p < 0.01$) compared to Cγ1$^{+/cre}$ after 10 days since the immunization (Figure 5.3.3.2 b). Notably, no differences were detected in non-GC B cells (Ki67- intrafollicular cells), which confirmed the observed phenotype specific to GC B cells is associated with Lamin B1's specific role in maintaining genomic stability (Figure 5.3.3.2 c).

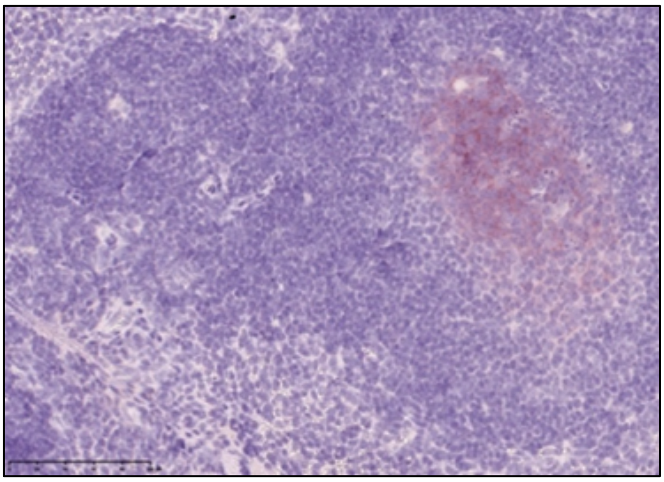

Figure 5.3.3.1 Immunohistochemical staining of AID in mice spleen. Representative image shows that AID is expressed specifically within the GC. Scale bar represents 100 μm.

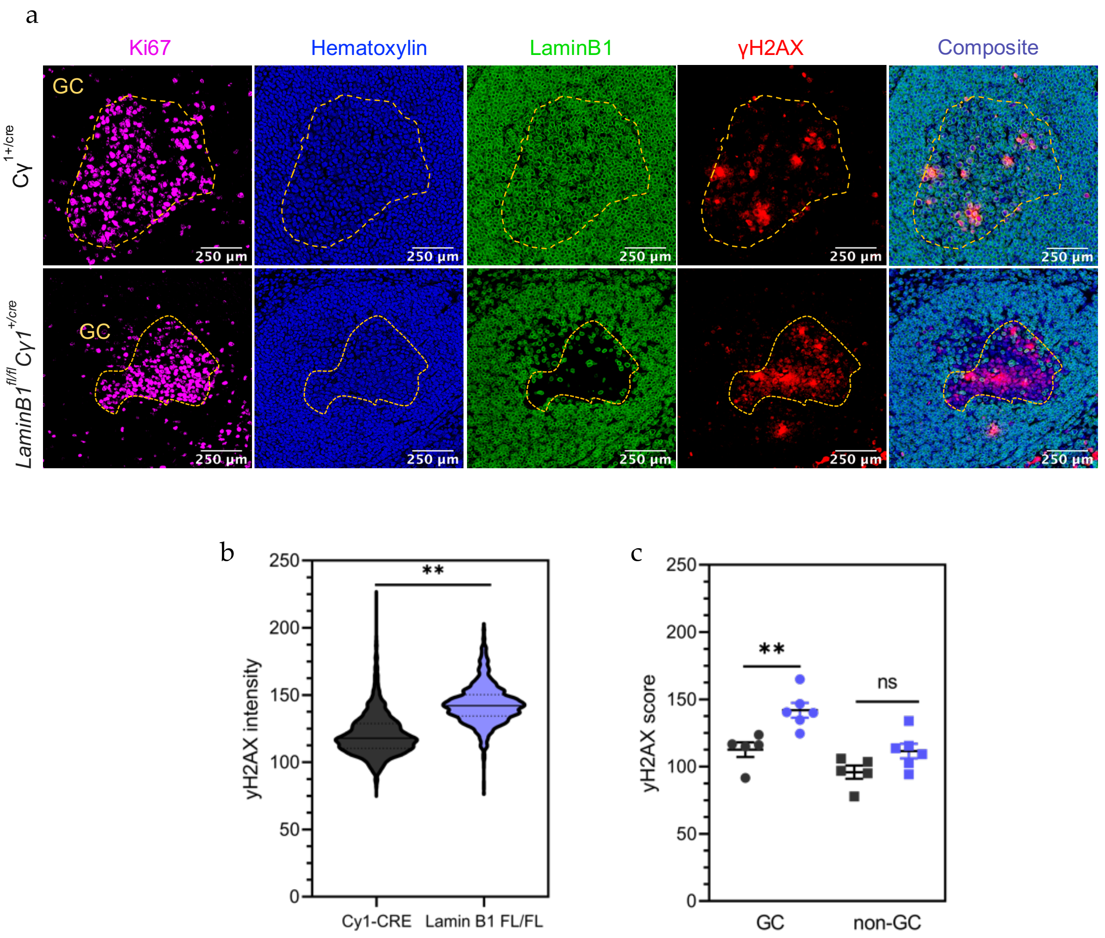

Figure 5.3.3.2 Lamin B1 deletion within splenic GC B cells leads to increased DNA damage. **(a)** Multiplex immunohistochemistry analysis of mouse spleens sequentially stained with haematoxylin (blue), Ki67 (magenta), Lamin B1 (green), and γH2AX (red). Scale bar represents 250 μm**.** **(b)** Violin plots representing γH2AX pixel intensities as single cells. Unpaired t-test of pooled data was used for statistical analysis. **(c)** Dot plots of γH2AX intensities represented as mean values in GC and non-GC cells of individual $C\gamma1^{+/cre}$ (black) and $LaminB1^{fl/fl}C\gamma1^{+/cre}$ (blue) mice. A minimum of 3 randomly selected GCs were analysed per replicate ($C\gamma1^{+/cre}$ N=5, $LaminB1^{fl/fl}C\gamma1^{+/cre}$ N=6). Error bars indicate s.e.m. Unpaired t-test was used for statistical analysis. $^{**}P \leq 0.01$; ns, not significant.

To ensure no signal from the previous staining remained on the tissues, a negative IHC control slide was included after each stripping of the staining (Appendix Figure 10.3.2). Complementary to the IHC analysis, I MACS separated peanut agglutinin positive (PNA+) GC B cells and performed IF confocal analysis of Lamin B1 and γH2AX (Figure 5.3.3.3). In line with IHC, *LaminB1*$^{fl/fl}$*Cγ1*$^{+/cre}$ PNA+ cells were predominantly negative for Lamin B1 and displayed increased γH2AX compared to *Cγ1*$^{+/cre}$ PNA+ cells. No evident differences were observed in PNA- populations between Cγ1$^{+/cre}$ and *LaminB1*$^{fl/fl}$*Cγ1*$^{+/cre}$ samples (Figure 5.3.3.3). Quantitative analysis was omitted due to the observed inconsistency of MACS-based PNA separation, which recurrently failed to enrich the PNA+ population efficiently. Increased DNA damage in Lamin B1 deficient cells prompted me to assess the downstream effect on the adaptive immune response.

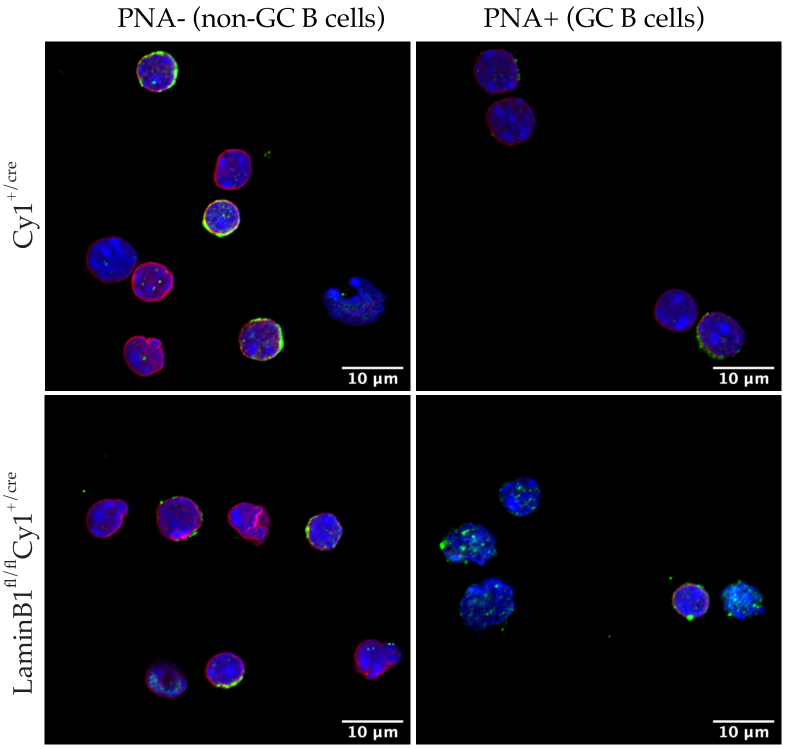

Figure 5.3.3.3 Qualitative analysis of PNA separated splenic B cells from *Cγ1*$^{+/cre}$ and *LaminB1*$^{fl/fl}$ *Cγ1*$^{+/cre}$ by IF confocal microscopy. Scale bar represents 10 µm. Representative images of PNA+ and PNA- populations stained against Lamin B1 (Alexa594-red), γH2AX (Alexa488-green), and DAPI (blue).

5.3.4 Lamin B1 deletion increases the proportion of GC B cells

Tolerated SHM and CSR-induced DNA damage during B cell activation is permissible due to the anti-apoptotic B cell lymphoma 6 (*BCL6*)-driven high proliferation of GC B cells and the inhibition of DNA damage response[207]. Increased DNA damage in Lamin B1 deficient GC B cells, prompted me to assess the impact of Lamin B1 deletion in the context of B cell differentiation (Figure

5.3.4.1). Complementary to GC IHC analysis, I compared the proportions of GC B cells (B220+, CD95+, GL7+) in $C\gamma 1^{+/cre}$ and $LaminB1^{fl/fl}/C\gamma 1^{+/cre}$ spleens. The flow cytometry provided a more comprehensive and sensitive detection of GC B cells ($B220^{+}$, $CD95^{+}$, $GL7^{+}$), as the staining was performed on a single cell suspension from the entire tissue, rather than just a single section in IHC. As demonstrated in Figure 5.3.4.2, no significant differences in GC B cells were detected between $C\gamma 1^{+/cre}$ and $LaminB1^{fl/fl} C\gamma 1^{+/cre}$ mice ($p = 0.20$) 10 days after the immunization. Contrary to the IHC analysis, 21 days post-immunization, I observed an increase of GC B cell proportion in $LaminB1^{fl/fl}$ $C\gamma 1^{+/cre}$ ($p=0.015$) compared to $C\gamma 1^{+/cre}$ on day 21 (Figure 5.3.4.2 b, d). This phenotypic change may be a result of increased proliferation or impairment of GC reaction in $LaminB1^{fl/fl}$ $C\gamma 1^{+/cre}$.

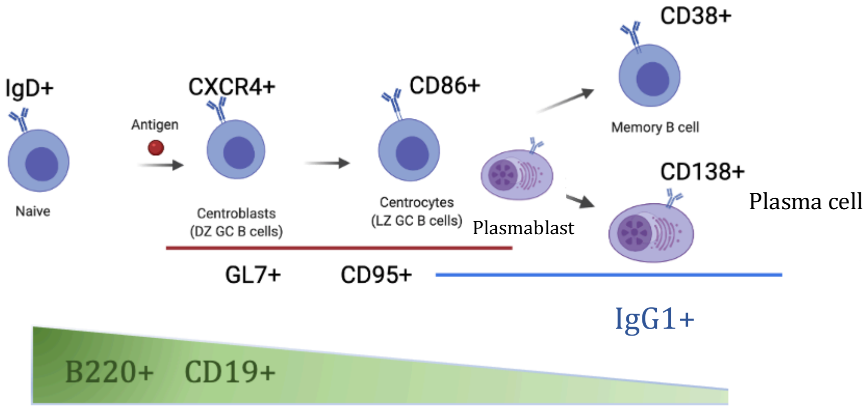

Figure 5.3.4.1 Expression of cell surface markers associated with differentiation stage of B cells in secondary lymphoid organs.

To address the increase of GC B cells on day 21, I was interested in whether the loss of Lamin B1 affects the GC compartmental distribution. Mature GCs are allocated into two GC microcompartments, centroblasts dark zone (DZ) GC B cells or light zone (LZ) GC B cells (centrocytes). Therefore, I analysed the distribution of DZ ($CXCR4^{high}CD86^{low}$) and LZ ($CXCR4^{low}CD86^{high}$) GC B cells as a ratio of DZ/LZ based using the established markers (Figure 5.3.4.1). Cell surface staining was performed on live cells on days 10 and 21 post-immunization. I did not observe significant differences in the distribution of DZ and LZ GC B cells, confirming that Lamin B1 deficient GC B cells progress through the GC reaction similarly to control cells (Figure 5.3.4.2 c, e). Upon class-switching and affinity selection, GC B cells further differentiate into a range of antibody-secreting cells.

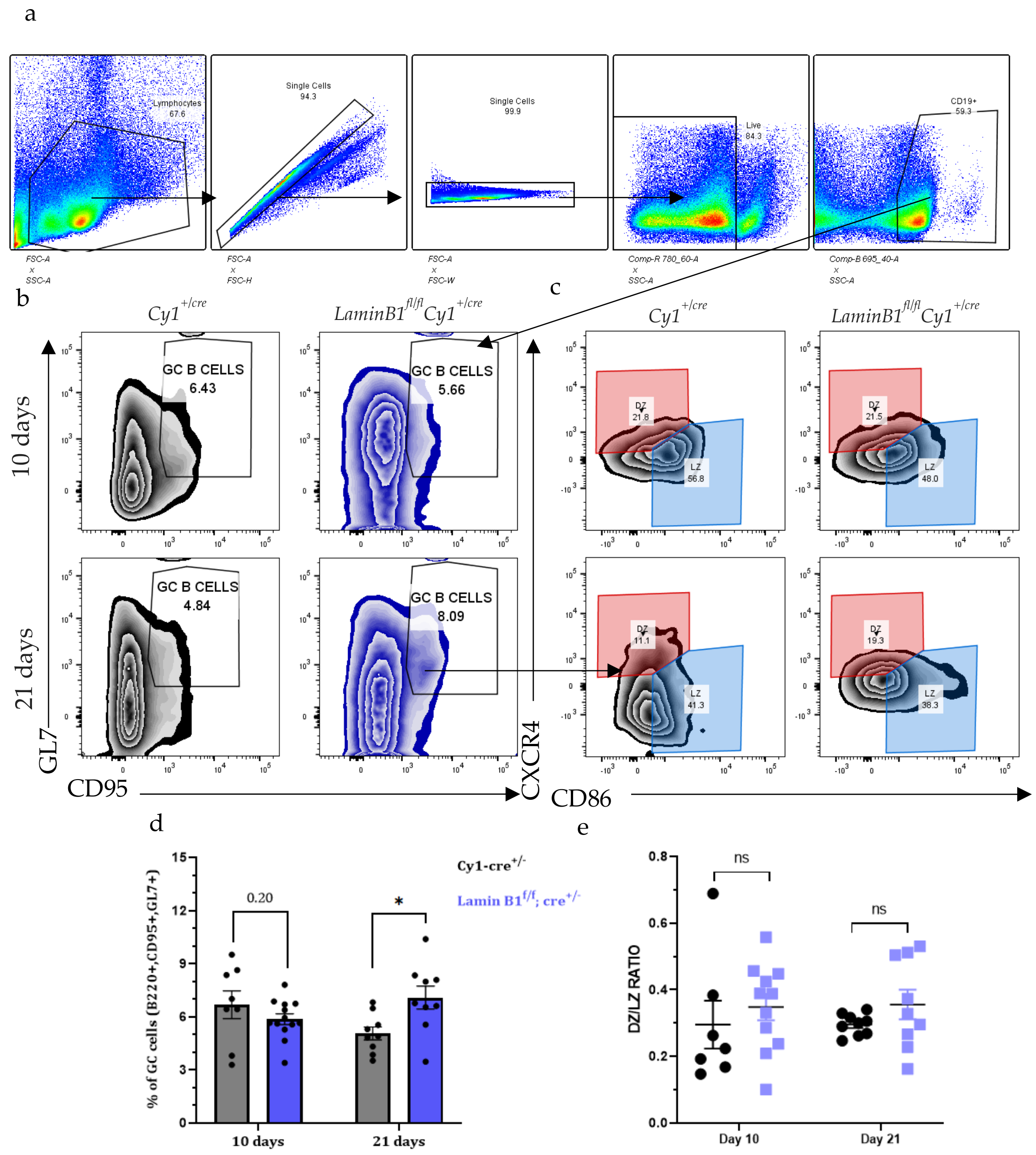

Figure 5.3.4.2 Lamin B1 deletion increases the proportion of GC B cells 21 days after immunization. **(a-c)** Flow cytometry analysis of GC B cell ($B220^{+}GL7^{+}CD95^{+}$) in NP-CGG injected mice 10 days and 21 days post-immunisation. **(b)** Representative contour plots of GC B cell gating and **(c)** DZ GC B cells ($CXCR4^{high}CD86^{low}$) and LZ GC B cells ($CXCR4^{low}CD86^{high}$) **(d)** Bar charts showing the quantification of GC B cell in *Cγ1*$^{+/cre}$ and *LaminB1*$^{fl/fl}$ *Cγ1*$^{+/cre}$ mice. **(e)** Dot plots showing the ratio of DZ/LZ ratio. Circles represent individual mice; error bars indicate s.e.m. Unpaired t-test comparisons shown are versus *Cγ1*$^{+/cre}$ mice; $*P \leq 0.05$; ns, not significant. All data are representative of at least two independent immunization experiments.

5.3.5 Lamin B1 deletion in GC B cell does not impair humoral response

Following the GC B cell analysis, I aimed to investigate whether Lamin B1 deletion and subsequent DNA damage affect the differentiation of antibody-secreting B cells. Within this context, flow cytometric high-throughput analysis was used to assess the established cell surface immunophenotypic markers of murine B cell populations including class-switched memory B cells, plasmablasts (PB), and plasma cells (PC) (Figure 5.3.4.1). I hypothesised that elevated DNA damage caused by Lamin B1 deletion would lead to more efficient CSR and an increased proportion of memory B cells and antibody-secreting cells (ASCs). First, I did not observe any significant changes in class-switched Memory B cells ($B220^+$, IgD^-, $CD138^-$, $IgG1^+$) between $C\gamma 1^{+/\mathrm{cre}}$ and $LaminB1^{\mathrm{fl/fl}}C\gamma 1^{+/\mathrm{cre}}$ demonstrated by the proportion of cells and mean IgG1+ staining intensity (Appendix Figure 10.3.3). Next, I analysed long-term (PC) and short-term (PB) ASCs by flow cytometry analysis, which revealed Lamin B1 deletion does not significantly impact the maturation of terminally differentiated PCs ($B220^{\mathrm{int}}$, $CD138^+$), despite observing a marginal increase in $LaminB1^{\mathrm{fl/fl}}C\gamma 1^{+/\mathrm{cre}}$ (9.2%) compared to $C\gamma 1^{+/\mathrm{cre}}$ ($p=0.08$) at day 21 (Figure 5.3.5.1). Interestingly, similarly to PCs, short-lived PBs, defined as ($B220^{\mathrm{high}}$,$CD138^+$,IgD^-)[247,248] remained unchanged at day 10, but there was a significant increase of PBs in Lamin B1 deficient mice compared to control mice 21 days after immunisation ($p < 0.05$) (Figure 5.3.5.2). To assess whether Lamin B1 deletion enhances antibody secretion and maturation, I performed ELISA-based analysis of NP-specific IgG1 antibodies.

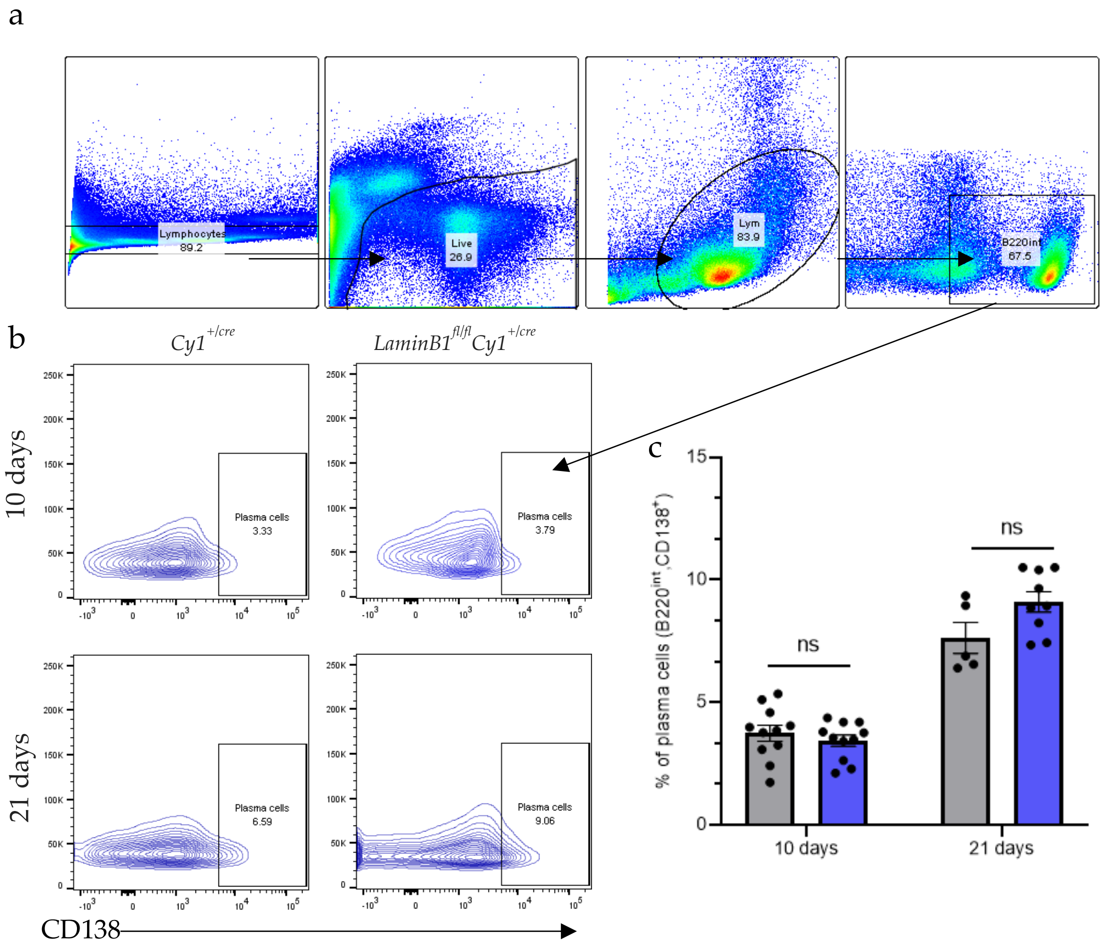

Figure 5.3.5.1 Flow cytometry analysis of PC differentiation upon Lamin B1 deletion in mouse GC B cells. **(a-b)** Representative flow cytometry charts showing the gating strategy of PC population (B220^{int}, CD138^{+}) in mice 10 days and 21 days post-immunisation with NP-CGG. **(b)** Representative contour plots of PC selected population gating and **(c)** Bar charts displaying the proportion of PC cells in spleens of *Cγ1*$^{+/cre}$ and *LaminB1*$^{fl/fl}$*Cγ1*$^{+/cre}$. Circles represent individual mice; error bars indicate SEM. Unpaired t-test comparisons are shown. ns, not significant. All data are representative of at least two independent immunization experiments.

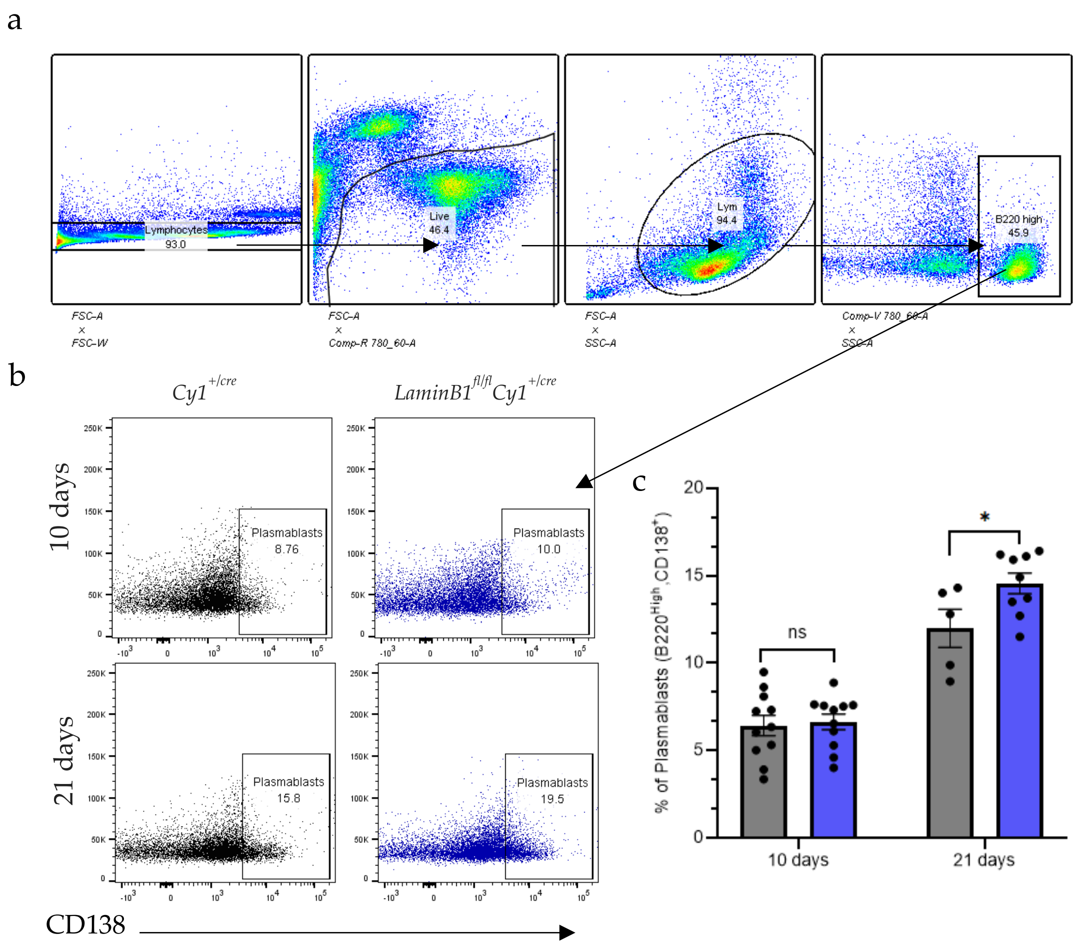

Figure 5.3.5.2 Flow cytometry analysis of PBs differentiation upon Lamin B1 deletion in mouse GC B cells. **(a-b)** Representative flow cytometry charts showing the gating strategy of PBs population (B220$^+$, CD138$^+$) in mice 10 days and 21 days post-immunisation with NP-CGG. **(b)** Representative contour plots of PBs in $C\gamma1^{+/\mathrm{cre}}$ and $LaminB1^{\mathrm{fl/fl}}C\gamma1^{+/\mathrm{cre}}$ at day 10 and 21 post-immunization. **(c)** Bar charts displaying the proportion of PBs in spleens of $C\gamma1^{+/\mathrm{cre}}$ and $LaminB1^{\mathrm{fl/fl}}C\gamma1^{+/\mathrm{cre}}$. Circles represent individual mice; error bars indicate SEM. Unpaired t-test comparisons shown are versus $C\gamma1^{+/cre}$ mice; $^*P \leq 0.05$; $^{**}P \leq 0.01$; ns, not significant. All data are representative of at least two independent immunization experiments.

5.3.6 Antibody maturation is not affected by Lamin B1 deletion

Increased DNA damage and PB differentiation prompted me to assess the titre of high-affinity (NP_{-9}) and low-affinity (NP_{-27}) IgG1 antibodies. I hypothesised Lamin B1 deletion associated with increased PBs would in turn lead to elevated high-affinity IgG1 antibodies. Serum was extracted from the peripheral blood of experimental mice on days 4,7,10, and 21 after NP-CGG immunization (Figure 5.3.6.1 a). Consistent with the increase in PBs proportion, IgG1 NP-specific antibodies remained unchanged on days 4, 7, and 10 post-immunizations (Figure 5.3.6.1 b and c). Surprisingly, I observed no difference in NP$_9$ and NP$_{27}$ IgG1-specific antibodies between $C\gamma1^{+/cre}$ and $LaminB1^{fl/fl}C\gamma1^{+/cre}$ on day 21. To compare changes in NP$_9$ and NP$_{27}$ IgG1 antibodies, I analysed the affinity ratio of NP$_9$/NP$_{27}$. Consistently with total levels of NP-specific antibodies, no differences were observed between $C\gamma1^{+/cre}$ and $LaminB1^{fl/fl}C\gamma1^{+/cre}$ samples (Figure 5.3.6.1 d), which suggests Lamin B1 deletion does not enhances antibody maturation.

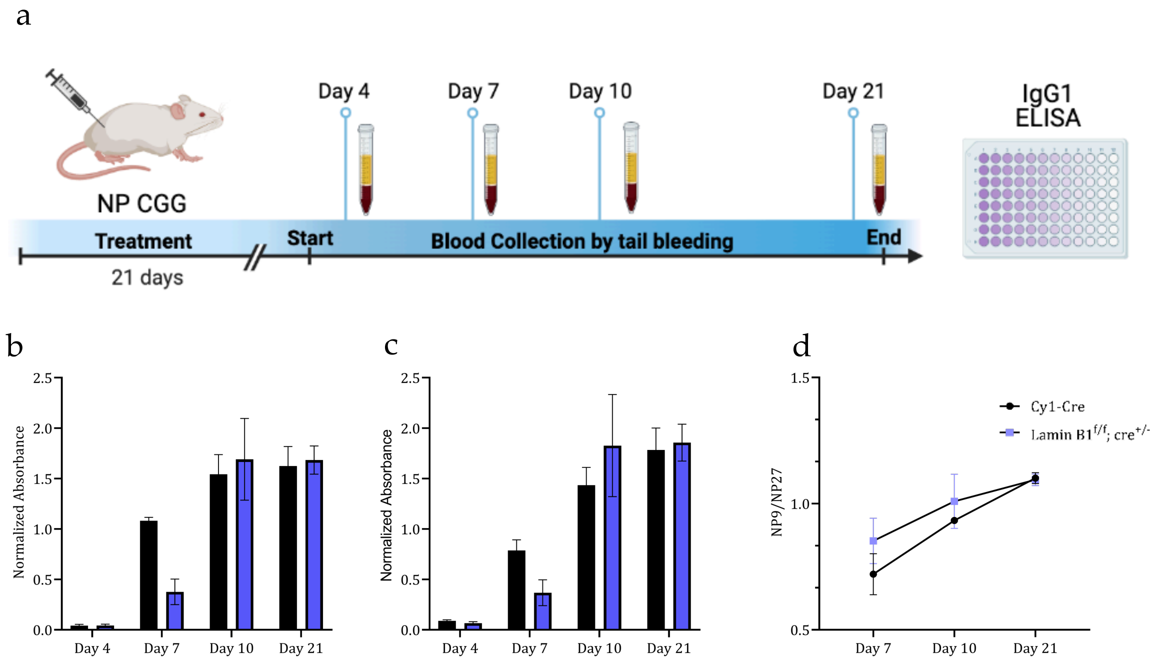

Figure 5.3.6.1 Lamin B1 deficiency does not impact antibody maturation. **(a)** Mice were immunised on day 0 with 100 µg NP-CGG: alum (1:1) by IP injection. Serum was collected by tail bleeding on day 4, 7, 10, 21 after immunization. **(b-c)** Anti-**(b)** NP-IgG$_1$ low (NP27) and **(c)** high (NP9) affinity antibody serum titers were determined by ELISA in $C\gamma1^{+/cre}$ (n=5) and $LaminB1^{fl/fl}C\gamma1^{+/cre}$ (n=5). **(d)** Ratio of anti-NP$_{(9)}$ or anti-NP$_{(27)}$ immunoglobulin isotype IgG1 are shown.

5.4 Discussion

Most human B cell non-Hodgkin's lymphomas (nHLs) are derived from germinal centres, where activated mature B cells undergo somatic hypermutation (SHM) and class switch recombination (CSR) as part of the adaptive immune response. Most nHL subtypes are often associated with distinct genetic lesions triggered particularly by CSR and SHM[59]. In this chapter, I intended to build up on the previous evidence of Lamin B1 mediated genomic instability using a newly established GC B cell-specific Lamin B1 knockout mouse model. In addition to the analysis of DNA damage, I investigated if Lamin B1 acts as a potent regulator of the humoral response. Considering the importance of Lamin B1 in cellular development, it was essential to limit any off-target phenotypes mediated by insufficient Lamin B1 expression. I generated a mouse model utilizing an inducible $C\gamma1$-dependent *Cre* recombinase, and loxP-flanked sites within the *LMNB1* gene. Upon stimulation of the immune response, transcriptional activation of $C\gamma1$ gene together with *Cre* recombinase would result in *Cre*-mediated deletion of Lamin B1, specifically in the GC B cells population (Figure 5.3.1.1). To my knowledge, this is the first GC B specific Lamin B1 knockout mouse model. Lamin B1 deletion did not have any detrimental phenotypic effects on the GC formation, as demonstrated by IHC analysis of spleens in $LaminB1^{fl/fl}C\gamma1^{+/cre}$ mice. The immunohistochemical approach used for the assessment of γH2AX revealed increased DNA damage present in the GC B cells. Current literature provides very limited evidence evaluating γH2AX response in murine spleens upon the stimulation of immune response. AID-induced DSBs within the IgH region are associated with phosphorylation of H2AX, a hallmark of DSBs, in B cells that are actively undergoing SHM. In agreement with our *in vitro* results in Chapter 3, single-cell multiplex staining analysis revealed an increase in DNA damage, specifically in Lamin B1 deficient GC B cells (Figure 5.3.3.2). Elevated DNA damage found within GC B cell populations could be attributed to greater DNA accessibility due to limited Lamin B1 bound chromatin, as suggested by chromatin accessibility sequencing assays[249,250].

GCs are sites of tolerable DNA damage induced by AID-driven SHM and CSR processes as part of adaptive immune response[40]. Previous research demonstrated AID deficient B cells failed to hypermutate *IgV* gene and undergo CSR due to insufficient DNA damage, as shown by reduced IgG1 production in γH2AX$^{-/-}$ mice[251]. The localisation of H2AX at the IgH locus is dependent on AID expression in GC B cells[251]. Therefore, based on the previously published studies, I expected to see a more robust antibody production as a direct consequence of reduced Lamin B1 and elevated DNA damage[28,188,208]. The observed hyperproliferative phenotype in BL2 shLMNB1 cells prompted to analyse GC B cell population in mouse spleen. Interestingly, $LaminB1^{fl/fl}C\gamma1^{+/cre}$ mice displayed a higher proportion of GC B cell 21 days after immunisation but did not show any differences in the distribution of DZ and LZ GC B cells, which implies that Lamin B1-depleted GC B cells undergo increased proliferation or do not properly egress the GC. Improper GC exit would consequently impair ASCs production, which is not evident from flow cytometry data. Several studies demonstrated that increase of proliferation is associated with DNA damage and mutagenesis[121,252,253]. Therefore, to determine if the proliferation is purely driven by Lamin B1 removal, an *ex vivo* assessment of GC B cell proliferation would allow to directly quantify proliferation rates with respect to Lamin B1 depletion. The mechanism behind Lamin B1-mediated increase of proliferation could be elucidated by transcriptome analysis of Lamin B1 deleted GC B Cells. Whether the increase of GC B cells and PBs translates into an elevated antibody production, I performed a quantitative analysis of IgG1 NP-specific high and low-affinity antibodies. Contrary to the elevated proportion of PBs, IgG1 antibody quantification did not indicate Lamin B1 deletion in GC B cells significantly impacts post-GC B cells maturation and antibody production. This observation is likely to be attributed to the constant expression of AID and already accessible DNA within the Ig region in control $C\gamma1^{+/cre}$ GC B cells, suggesting Lamin B1 removal does not increase DNA accessibility within the IgV.

Cell surface marker flow cytometry analysis of ASCs and IgG1 titre quantification did not indicate Lamin B1 deletion in GC B cells significantly impacts post-GC B cells maturation and antibody production. This observation is likely to be attributed to the constant AID expression and already accessible DNA sequence within the Ig region in control $C\gamma1^{+/cre}$ GC B cells, suggesting Lamin B1 removal does not increase DNA accessibility within the IgV. Nonetheless, more pronounced genome-wide DNA accessibility associated with Lamin B1 depletion may be responsible for genomic lesions in non-Ig regions, as suggested by elevated γH2AX staining in Lamin B1 deficient GC B cells. No differences in γH2AX levels detected in non-GC B cells between $C\gamma1^{+/cre}$ and $LaminB1^{fl/fl}C\gamma1^{+/cre}$ further confirmed the specificity of Lamin B1 induced DNA damage in GC B cells, which is likely related to AID activity within the non-Ig loci. There are several known AID off-target genomic regions which are associated with lymphomagenesis[41,254]. I further aimed to elucidate specific genomic locations of DNA DSBs in Lamin B1 deficient GC B cells. Here, I showed for the first time Lamin B1 deletion in GC B cells induced DNA damage while not impairing the adaptive immune response but rather compromising genomic integrity. Whether the source of DNA damage is a direct result of Lamin B1 deletion or increased proliferation is currently unclear. RNA-sequencing analysis of Lamin B1 knockout GC B cells would give an insight into transcriptional rewiring in these cells.

Chapter 6: Decreased Lamin B1 expression alters the transcriptional profile of BL2 cells

6.1 Chapter Introduction

Chromatin organization and accessibility are known to be partially regulated by Lamin B1 and lamina-associated domains (LADs), which contribute to regulation of gene transcription[169,255]. Studies have demonstrated the depletion of Lamin B1 alone modulates transcriptional profile in a range of cancer models[164,183]. Changes in transcription upon Lamin B1 silencing are likely due to the reorganization of LADs and increased DNA accessibility via chromatin relaxation at the periphery of the nucleus. Relocation of LADs and modulation of epigenetic marks is dependent on the cell type and differentiation state of the cell, as depicted in Diagram 5.1[148]. This concept is supported by the body of evidence showing that LADs together via Lamin B1 play the central role in silencing gene transcription within the heterochromatin compartment at the nuclear lamina[174,177,222]. However, recent data revealed a dynamic localisation of Lamin B1 within the euchromatin-enriched fraction of the genome, suggesting the presence of Lamin B1 within transcriptional sites is associated with gene transcription[175]. The accessibility transposase assay sequencing (ATAC-seq) and RNA-sequencing revealed Lamin B1 colocalises with open and actively expressed euchromatin regions[175].

Further evidence of Lamin B1 mediated gene regulation and chromatin accessibility was demonstrated in previously published work by our group[131]. Induction of somatic hypermutation (SHM) induced the removal of Lamin B1 from the nuclear periphery and subsequently led to decreased binding between Lamin B1 and DNA containing Immunoglobulin Heavy Chain Variable (*IGHV)* gene as revealed by the Lamin B1-chromatin immunoprecipitation sequencing (ChIP-seq). Accessibility of *IGHV* gene in turn promoted the acquisition of point mutations within the immunoglobulin sequence[131]. In addition to the mutagenesis mediated by Lamin B1 removal, the release of a kappa light chains from Lamin B1 suppressive environment led to the rescued expression upon SHM induction[131]. These findings confirmed previous evidence of Lamin B1 involvement in epigenetic regulation of gene transcription and DNA accessibility. Furthermore, a number of studies described that modulating Lamin B1 expression affects DNA damage response[176,180–182,256]. To understand the full extent of Lamin B1 mediated regulation of transcriptome, I carried out RNA-seq upon our shRNA-mediated Lamin B1 knockdown BL2 *in vitro* model. I aimed to identify genes and pathways controlled by Lamin B1 suppressive environment within the LADs in B cells.

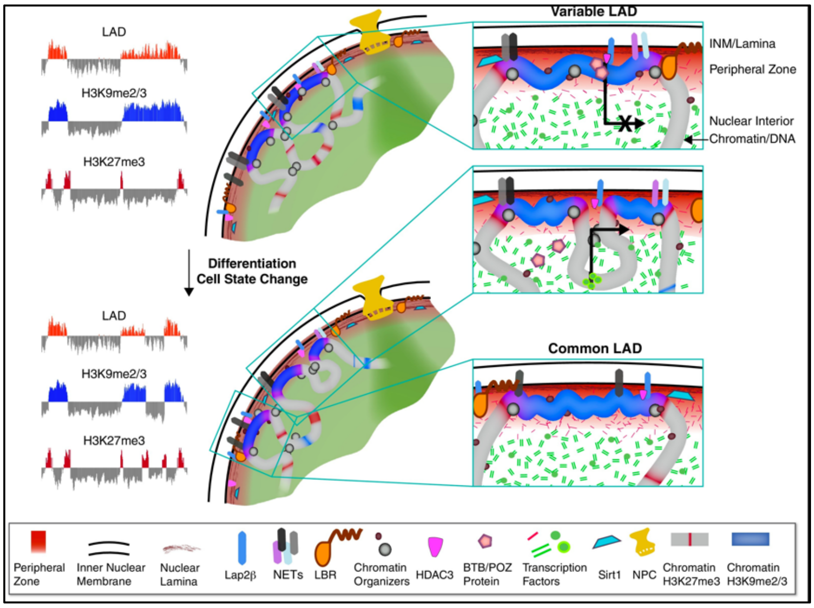

Figure 6.1 Schematic representation of chromatin association with the nuclear lamina. Scaffolding at the peripheral zone is cell type specific and dynamic throughout the differentiation. The nuclear lamina at the periphery facilitates gene regulation during differentiation and cell state changes via genome organization. Diagram was adapted from Luperchio et al.[232]

6.2 Chapter aims and hypothesis

The purpose of the work described in this chapter was to evaluate changes in gene expression by RNA-sequencing upon Lamin B1 silencing in BL2 cells. Based on the previous studies and results described in Chapter 3, I hypothesised Lamin B1 knockdown in B cells would display a high number of upregulated genes and enrichment of pathways associated with DNA damage pathway.

Chapter aims:

1. Analysis of transcription profile by RNA-sequencing in BL2 cells after Lamin B1 silencing.
2. Differential gene expression analysis and identification of significantly dysregulated genes.
3. Gene set enrichment analysis to identify pathways associated with Lamin B1 decrease.

6.3 Results

6.3.1 Changes in transcriptional profile upon Lamin B1 depletion

To gain a deeper insight into the changes of transcriptional prolife after depleting Lamin B1 in BL2 cells, I carried out RNA-seq experiment on two biological replicates from control and shLMNB1 treated BL2 cells. Prior to the sequencing, Lamin B1 knockdown was confirmed by western blotting as demonstrated in the Appendix Figure 10.4.1. First, raw data were pre-processed by trimming of adaptor sequences and aligning to the human genome 19 (hg19). Read alignment in all samples reached > 90% and qualitative assessment of aligned files (BAM-QC) was performed in QualiMap (Appendix Figure 10.4.1 b & Figure 10.4.3). FeatureCounts algorithm was used to count raw reads after the alignment for further differential expression analysis. Lamin B1 knockdown did not affect the expression of other nuclear lamins, eliminating any compensatory upregulation of *LMNB2* (Log2FC=-0.25) or *LMNA* (Log2FC=0.28) (Appendix Figure 10.4.2).

I utilised DESeq2 algorithm for differential gene expression (DEG) analysis of count data obtained from BL2 control and shLMNB1 samples. MA-plot was used to visualise the differences in log expression values between two biological conditions showing the significantly dysregulated genes in red (padj<0.05), as seen in Figure 6.3.1.1. After filtering out low expressed genes, I detected 177 significantly downregulated (padj<0.05, Log2FC <0.58) and 86 significantly upregulated genes (padj<0.05, Log2FC > 0.58) in BL2 shLMNB1 cells (Figure 6.3.1.1). DEG analysis revealed a dysregulated expression of several important transcription factors involved in tumorigenesis including *YAP1* (Log2FC=2.14), *PAX9* (Log2FC=-5.41), and *CCND2* (Log2FC=5.25) in BL2 shLMNB1 cells (Figure 6.3.1.2). The most prominently upregulated gene was a miRNA gene *miRNA196A2* (Log2FC=12.8), which has been previously implicated as an oncogenic miRNA range of cancers[257–259]. Some other notably deregulated genes were *CXCR5* involved in B cell migration and *RAG2*, a fundamental recombinase involved in B cell maturation and CSR. I next evaluated the expression of genes involved in DNA damage response and repair, which uncovered significant dysregulation in the expression of *AHNAK* and *DTX3L*, genes involved in the regulation of 53BP1.

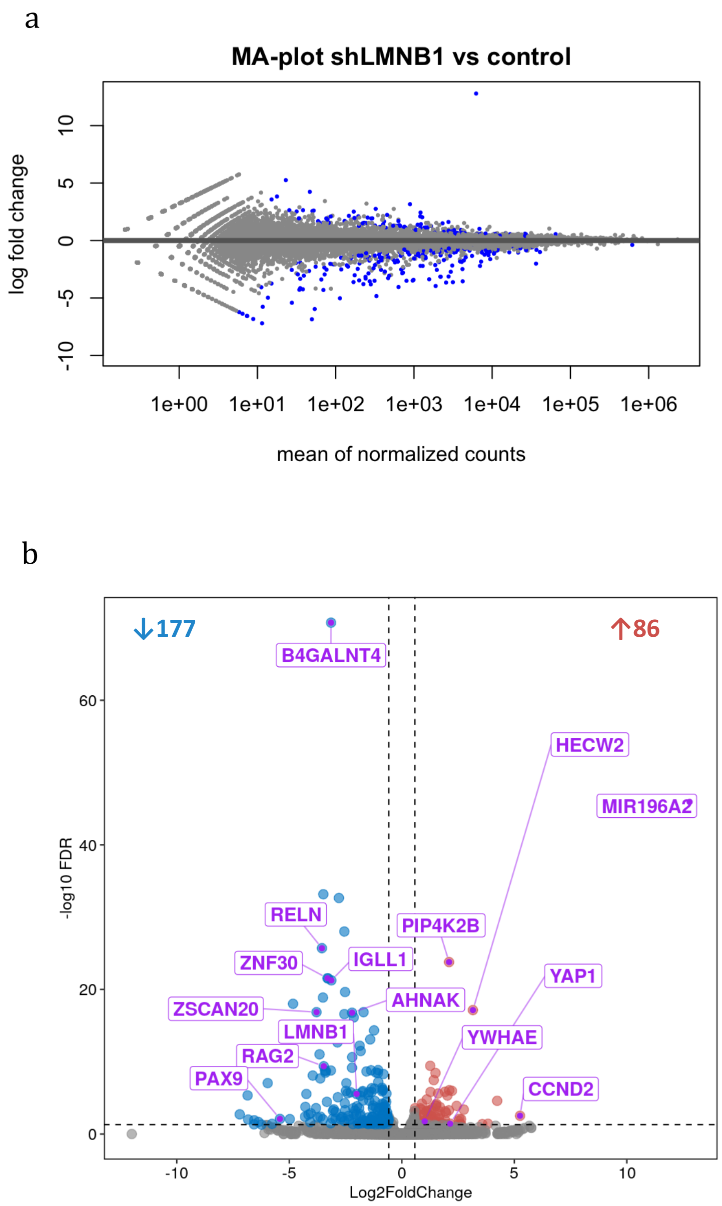

Figure 6.3.1.1 RNA-seq analysis of a transcriptional profile upon Lamin B1 knockdown in BL2 cells. **(a)** MA plot visualizing the differences between genes in control and shLMNB1 BL2 samples. Plotting of count data transformed the onto log fold change and mean average of normalised counts. Blue dots represent significant change of expression (padj < 0.05). DESeq2 was used to identify differentially expressed genes from two biological replicates of control and shLMNB1 BL2 cells. **(b)** Volcano plot showing DEGs (Log2FC< 0.58, Log2FC>0.58, and padj < 0.05).

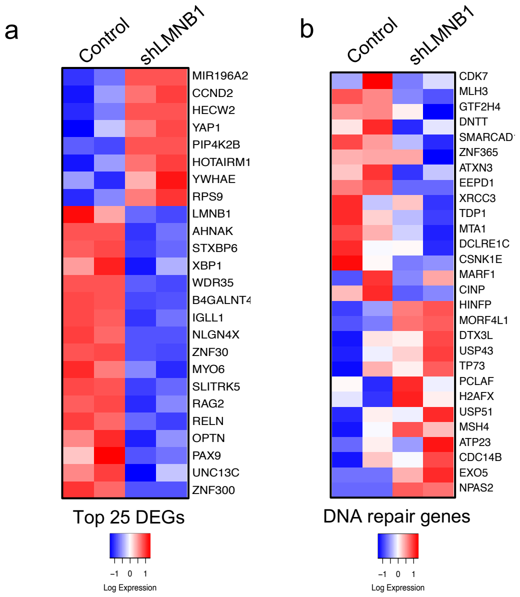

Figure 6.3.1.2 Deregulation of the transcriptional profile of BL2 cells after Lamin B1 nuclear disassembly. **(a-b)** Heatmap representation of selected **(a)** 25 significantly DEGs and **(b)** DNA repair genes with a Log2FC of +/- 0.5.

6.3.2 Gene set enrichment analysis of pathways affected by Lamin B1 silencing

In vitro experiments revealed an increase in DNA damage and proliferation upon Lamin B1 knockdown in BL2 cells. Therefore, I aimed to uncover cellular pathways dysregulated by Lamin B1 depletion. Normalised RNA-seq counts were used for GSEA of Hallmark pathways, and Gene Ontology (GO) sets. GSEA for Hallmark and KEGG gene sets revealed increased positive enrichment of pro-proliferative pathway MYC TARGETS V1 (NES = 1.42) and KEGG Ribosome pathway (NES = 2.47). Negatively enriched pathways were associated with "TNFA SIGNALLING VIA NfKB" and "EMT" genes (Figure 6.3.2 a). GSEA of GO Cellular components uncovered significant enrichment in pathways related to ribosomal processes and translation (Figure 6.3.2 b). I also analysed GO biological processes related to DNA damage response and repair, which showed insignificant positive enrichment genes involved in NHEJ (Figure 6.3.2 c). Conclusively, RNA-seq analysis revealed decreasing Lamin B1 expression modulates transcriptional landscape in BL2 cells. Next, I analysed pathways involved in DNA damage response and repair. GSEA analysis of GO DNA repair pathways revealed statistically insignificant enrichment in the expression of genes involved in regulation of NHEJ suggesting transcriptional regulation of

NHEJ pathway is not profoundly upregulated and post-translational signalling may be involved in response to DSBs in Lamin B1-deficient BL2 cells.

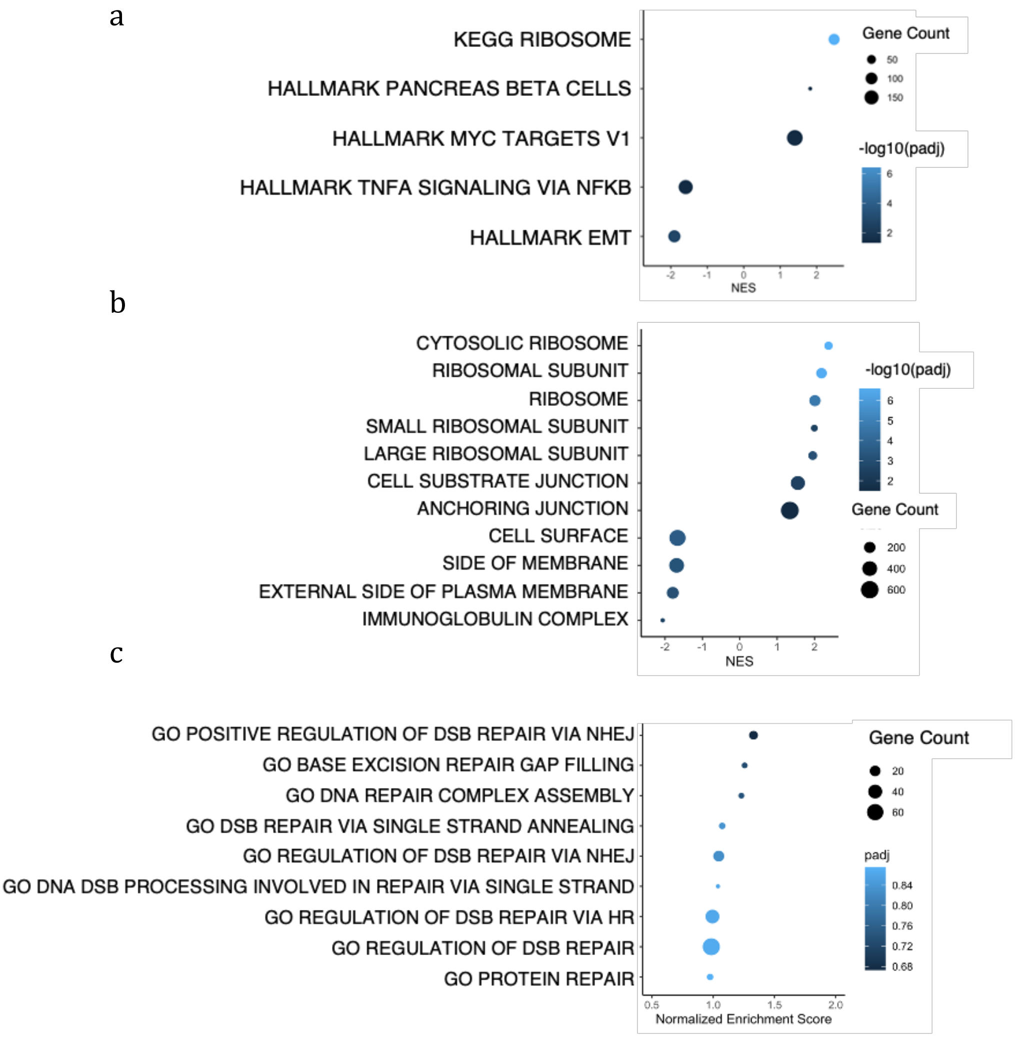

Figure 6.3.2.1 Gene set enrichment analysis for DNA repair gene set and NHEJ gene set **(a-c)** GSEA analysis of gene signatures related to **(a)** HALLMARK and KEGG gene sets **(b)** Gene Ontology (GO) Cellular components gene sets and **(c)** GO BP related to DNA repair. Gene sets with significant enrichment (padj<0.1) are shown in **(a)** and **(b)** and padj values are plotted as -log10, and untransformed padj values are shown in **(c)**. Normalised enrichment score (NES) is shown as BL2 shLMNB1 vs control samples.

6.3.3 DNA repair pathway signature correlates with aggressivity of B cell lymphoma

I sought to identify DNA Repair transcriptional signature changes in different subtypes of B cell lymphoma. To perform enrichment analysis, I utilised gene expression profiles in patients diagnosed with subtypes of B-cell lymphoma with increasing aggressiveness (Mantle Cell Lymphoma (MCL), Marginal Zone Lymphoma (MZL), Follicular Lymphoma (FL), Diffuse Large B Cell Lymphoma (DLBCL), Burkitt's lymphoma (BL)). GSEA analysis for the DNA Repair gene set (R-HSA-73894) was performed across different lymphoma cohorts. A positive enrichment of genes from the Reactome DNA repair gene set was observed in more aggressive B cell lymphoma subtypes. Significant positive enrichment was detected in BL patients compared with less aggressive FL (p=0.014) and MZL (p=0.01) (Figure 6.3.3). Insignificant the positive enrichment was observed in BL compared to DLBCL (p=0.075) and MCL (p=0.062) subtype (Figure 6.3.3).

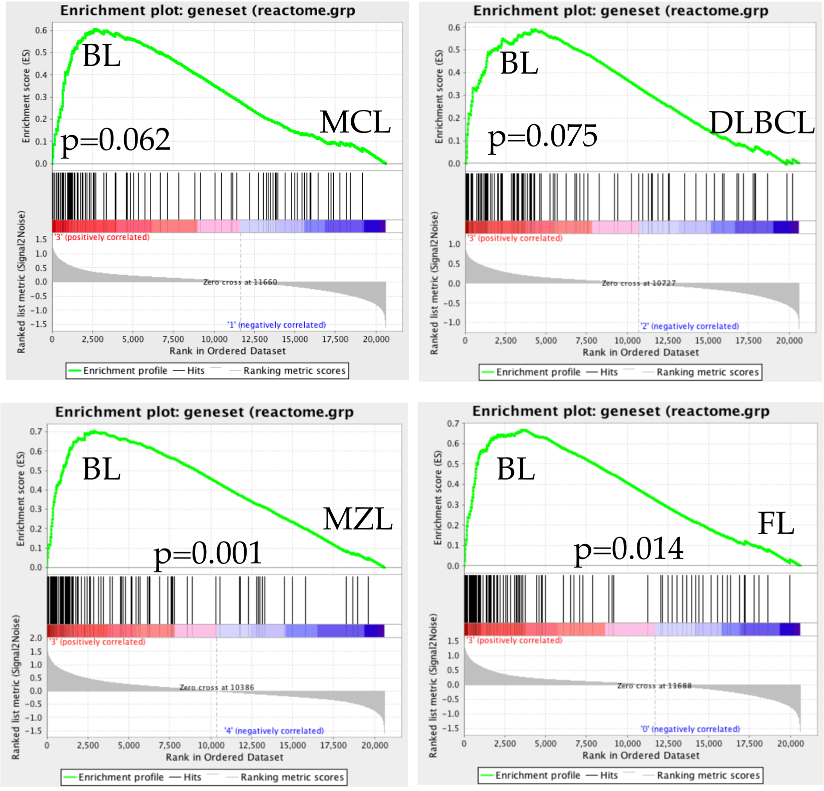

Figure 6.3.3 GSEA analysis of Reactome DNA repair pathway in B cell lymphoma subtypes. Gene expression profiles with matched NGS in B-cell non-Hodgkin lymphoma GSE132929. BL = Burtkitt's lymphoma, MCL = Mantle cell lymphoma, DLBCL = Diffuse large B cell lymphoma, FL = follicular lymphoma, MZL = Marginal zone lymphoma. Enrichment analysis was performed in GSEA v4.2.3.

6.4 Discussion

Previous studies demonstrated Lamin B1 contributes to repressing of transcription and its removal modulates gene expression landscape[164,255]. In this chapter, I aimed to elucidate the impact of Lamin B1 depletion on gene transcription in BL2 cells. I carried out RNA-seq analysis in control and shLMNB1 BL2 cells to investigate which pathways and genes are affected by changes in Lamin B1 expression. Contradictory to the repressive function of Lamin B1 on gene expression, I detected a higher number of significantly downregulated than upregulated genes (Figure 6.3.1.1), of which several genes (*YAP1*, *CCND2*, *miR196A2)* were previously shown to be upregulated in B cell lymphomas and other cancers[83,258,260,261]. Notably, an increased expression of *YAP1* was linked to disease progression and inferior survival outcome in DLBCL, likely mediated by pro-proliferative and anti-apoptotic role of *YAP1*[260,262]. Analogous to *YAP1*, *CCND2* increased expression is highly correlated with inferior survival of activated B-cell-like (ABC) DLBCL patients[261]. Increased expression of *CCND2* suggests Lamin B1 depletion may be responsible for a more aggressive phenotype resembling ABC subtype. Notably overexpressed hit in RNA-seq analysis was *miR196A2*, a microRNA involved in gene regulation of diverse biological processes involving cell cycle regulation, proliferation, apoptosis, development, and chromosome organization[258,263]. DEG gene analysis revealed Lamin B1 knockdown induces transcription changes in pro-proliferative genes often upregulated in B cell lymphomas and other cancers.

I was further interested in assessing the transcriptional changes in DNA repair genes upon Lamin B1 depletion. Previous findings demonstrated decreased expression of Lamin B1 impairs cell cycle progression and triggers a collapse of replication forks in osteosarcoma and colorectal cell lines[176,182]. Qin et al. described a positive correlation between Lamin B1 expression and homologous recombination repair genes in the majority of TCGA cancer types[256]. DEG analysis of DNA repair genes did not reveal any significant dysregulation of the genes as previously described in other cell cancer models. Interestingly, while *TP53BP1* expression remained unchanged, *DTX3L* and *AHNAK* genes involved in the recruitment and assembly of 53BP1 were dysregulated in BL2 shLMNB1 cells. Particularly, the upregulation of *DTX3L* contributes to monoubiquitinating Lysine-91 of histone H4 (H4K91ub), promoting rapid and specific recruitment of 53BP1 to the site of DNA damage[264]. Our findings are in agreement with data generated by Ghodke et al., which found that the loss of *AHNAK* promotes enhanced accumulation of 53BP1 on chromatin and promotes cell cycle phase separation[265]. RNA-seq revealed a significant downregulation *AHNAK* in BL2 shLMNB1, which may be responsible for increased presence of 53BP1 on chromatin. Furthermore, I detected a significant upregulation of HECW2, a HECT-type E3 ubiquitin ligase, which interacts with nuclear lamins and proliferating cell nuclear antigen (PCNA)[166]. Enzymatic activity of HECW2 mediates the ubiquitination of Lamin B1 and PCNA for proteasomal degradation in Hela cells[166]. Ubiquitination of PCNA also promotes replication of damaged DNA by recruiting lesion-bypass DNA polymerases[266,267].

To get a better understanding of Lamin B1 regulated transcriptional changes in DNA damage response genes, I performed GSEA analysis. First, GSEA analysis revealed a statistically insignificant positive enrichment of DNA Repair and NHEJ pathways in BL2 shLMNB1 cells. Transcriptional changes of DNA repair genes remain constant likely due to the persistent endogenous DNA damage in BL2 cells (Figure 3.3.3.1). Observing no significant changes in expression of DDR genes is not unexpected, considering the rapid post-translational signalling cascade via phosphorylation and ubiquitination is frequently utilised in response to DNA damage[219,268]. Moreover, the relatively unchanged transcriptional profile of DDR genes implies Lamin B1 depletion induces tolerable DNA damage and does not significantly impair transcription of DDR genes in BL2 cells. RNA-seq results are in line with a retrospective analysis of the transient Lamin B1 (siLMNB1) knockdown BL2 model, which also revealed a modest increase in NHEJ and DNA repair.

To explore the pathways driving the hyperproliferative phenotype associated Lamin B1 depletion in BL2 cells, I performed a GSEA analysis of Hallmark gene sets. While expression of *MYC* remained unchanged in Lamin B1-deficient BL2 cells, GSEA revealed a positive enrichment in "MYC TARGETS V1" gene sets, suggesting MYC target genes could be drivers of hyperproliferation in BL2 shLMNB1 samples. Interestingly, previous research has shown MYC target genes are associated with hyperproliferative phenotype and worse clinical outcome in Burkitt's lymphoma and other cancers[89,269,270]. Furthermore, gene ontology analysis revealed a significant positive enrichment in pathways related to ribosome biogenesis, which were also associated with the malignant transformation and progression of most spontaneous cancers[271,272].

Complementary to the analysis of DNA damage and repair genes, I was interested whether the upregulation of DDR correlated with aggressiveness of B cell lymphomas. Using previously published datasets, GSEA revealed a positive enrichment of DDR genes in more aggressive B cell lymphoma subtypes (Figure 6.3.3.1). These findings may provide a future tool to evaluate genomic instability arising from differential expression of DDR genes in B cell derived lymphomas.

In this chapter, RNA-seq analysis demonstrated Lamin B1 nuclear removal leads to transcriptional changes of several genes involved in B cell lymphoma and DSB repair response facilitated by NHEJ. Further, a positive enrichment of MYC target genes and ribosome pathways may be the driving force behind the proliferation boost observed in Lamin B1-deficient BL2 cells. Taken together, transcriptome analysis provides further evidence of Lamin B1 mediated gene regulation, DNA damage, and hyperproliferative phenotype in the malignant B cell. Translating our findings into a clinical setting using NGS dataset and clinical samples would be vital for the evaluation of Lamin B1 as a clinical marker in B cell derived lymphomas.

Chapter 7: Clinical evaluation of Lamin B1 in Diffuse Large B Cell Lymphoma patients

7.1 Introduction

The prognostic value of Lamin B1 in cancer remains unclear due to conflicting findings across cancer types (Table 7.1). Establishing Lamin B1 as a clinical biomarker remains a challenge due to the regulation of its expression taking place primarily at the post-transcriptional level[273]. While the assessment of Lamin B1 protein level may be a more reliable approach, utilising mRNA as a Lamin B1 expression readout is more prevalent due to the availability of NGS datasets and limited access to tissue biopsies (Table 7.1). Some of the previous studies found an increased Lamin B1 protein expression to be associated with inferior survival in pancreatic cancer, hepatocellular carcinoma, or prostate cancer[196–198,274].

Cancer type	Detection method	Lamin B1 expression
LUAD	mRNA and IHC	High[275]
PDAC	cDNA/protein	High[196]
Prostate cancer	NGS	High[197]
HCC	NGS	High[198]
CLL	NGS	Low[131]
FL	IHC	Low[131]
Colon cancer	RT-qPCR	High[195]
Gastric cancer	IHC	Low[199]
Breast cancer	RT-qPCR	Low[276]
AML	NGS	Low[277]

Table 7.1 Dysregulated expression of Lamin B1 in cancer. Summary of studies demonstrating Lamin B1 expression to be associated with worse clinical outcome. LUAD=Lung adenoma carcinoma, PDAC=Pancreatic duct adenocarcinoma, HCC=Hepatocellular carcinoma, CLL=Chronic lymphocytic leukaemia, FL=Follicular lymphoma. AML=Acute Myeloid Leukaemia.

While in solid tumours overexpression of Lamin B1 is associated with worse prognosis, low Lamin B1 is linked to poor survival in haematological malignancies (Figure 1.3.10.1)[131,277]. Transcriptome analysis used for the clinical evaluation of Lamin B1 in nHL patients revealed that low Lamin B1 is associated with an adverse overall survival (OS) and progression-free survival (PFS) in Chronic Lymphocytic Leukaemia (CLL) patients, regardless of the administered treatment regime (Figure 1.3.10.1). In addition to the inferior survival outcome, Lamin B1 mRNA expression was decreased specifically in genomically instable (GI) CLL cohort and correlated with higher expression of DNA-editing proteins apolipoprotein B mRNA editing enzyme catalytic polypeptide-like (APOBECs) (Figure 1.3.7, Figure 1.3.10.1). At the protein level, decreased Lamin B1 expression was associated with the transformation of follicular lymphoma (FL) into a more aggressive counterpart, as demonstrated by immunohistochemical (IHC) analysis of Lamin B1 (Figure 1.3.10.2). Due to the complexity of nHL, above mentioned evidence supports the clinical value of Lamin B1 in just a fraction of nHL subtypes. Therefore, to assess the clinical significance of Lamin B1 and the association with DNA damage in the most prevalent B cell lymphoma subtype, I used tissue microarrays (TMAs) from diffuse large B cell lymphoma (DLBCL) patients to quantify Lamin B1 protein expression by IHC for the assessment of clinical outcome (Appendix Table 10.5.1). To our knowledge, few studies have examined DNA damage in B cell lymphomas, which demonstrated that constitutive DNA damage and defective DDR are linked to worse clinical outcome[125,127,278,279]. Defective DNA repair mechanisms might likely be factors contributing to worse clinical prognosis due to a high number of genomic aberrations often presented in DLBCL patients[125,280]. Therefore, defining the relationship between γH2AX and Lamin B1 protein level by IHC analysis would allow me to translate findings from the functional studies into the clinical setting. In addition to assessing Lamin B1 in DLBCL TMAs, I obtained a publicly available DLBCL transcriptome dataset to investigate a potential gene expression rewiring related to Lamin B1 expression (Appendix Table 10.5.2).

7.2 Chapter aims and hypothesis

In this chapter, I aimed to evaluate Lamin B1 expression and DNA damage in the clinical setting using DLBCL TMAs. In line with published literature and our previously described data, I hypothesised that decreased Lamin B1 protein expression would be associated with increased γH2AX levels and worse prognostic outcomes in DLBCL patients.

Chapter aims:

1. Immunohistochemical analysis of Lamin B1 and γH2AX in DLBCL patients.

2. Assessing the clinical value of Lamin B1 protein expression in diagnosis and survival prognosis.
3. Evaluation of γH2AX expression as a prognostic marker in the DLBCL cohort.
4. Gene expression evaluation in DLBCL patients using a TCGA dataset.

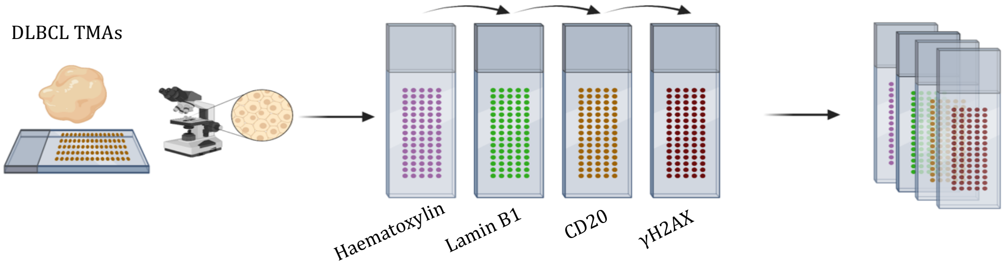

Figure 7.2 Schematic representation of sequential immunohistochemical staining in DLBCL TMAs. TMA slides were sequentially stained with the corresponding antibody and scanned. Each staining was stripped, and the protocol was repeated using a different antibody.

7.3 Results

7.3.1 Immunohistochemical analysis revealed a fluctuating Lamin B1 expression in DLBCL patients

Decreased Lamin B1 expression in patients diagnosed with FL or CLL was associated with a disease transformation and worse clinical prognosis, respectively[131]. To further evaluate Lamin B1 as a prognostic factor in GC-derived B cell lymphomas, I have performed an immunohistochemical analysis of Lamin B1 on diagnostic TMAs obtained from DLBCL patients (Figure 7.2 and 7.3.1 a). I hypothesised that germinal centre B cell-like (GCB) DLBCL patients would display decreased Lamin B1 expression compared to activated B cell-like (ABC) DLBCL subtype and healthy donors. The staining intensity score (H-score) revealed a broad range of Lamin B1 protein expression across the DLBCL cohort (N=50) (Figure 7.3.1 b). Utilizing the available algorithmic classification (Hans algorithm) of DLBCL patients, I stratified patients based on the cell-of-origin (COO) as ABC (N=17) or GCB DLBCL subtypes (N=32)[82,281]. The COO subtype stratification of the cohort revealed no significant changes in Lamin B1 staining (H-score) between COO subtypes ($p = 0.073$). However, a more pronounced difference was observed in the non-ABC cohort compared to lymph nodes from healthy donors (p = 0.08) (Figure 7.3.1 c), suggesting that Lamin B1 is highly dysregulated at the protein level in DLBCL patients.

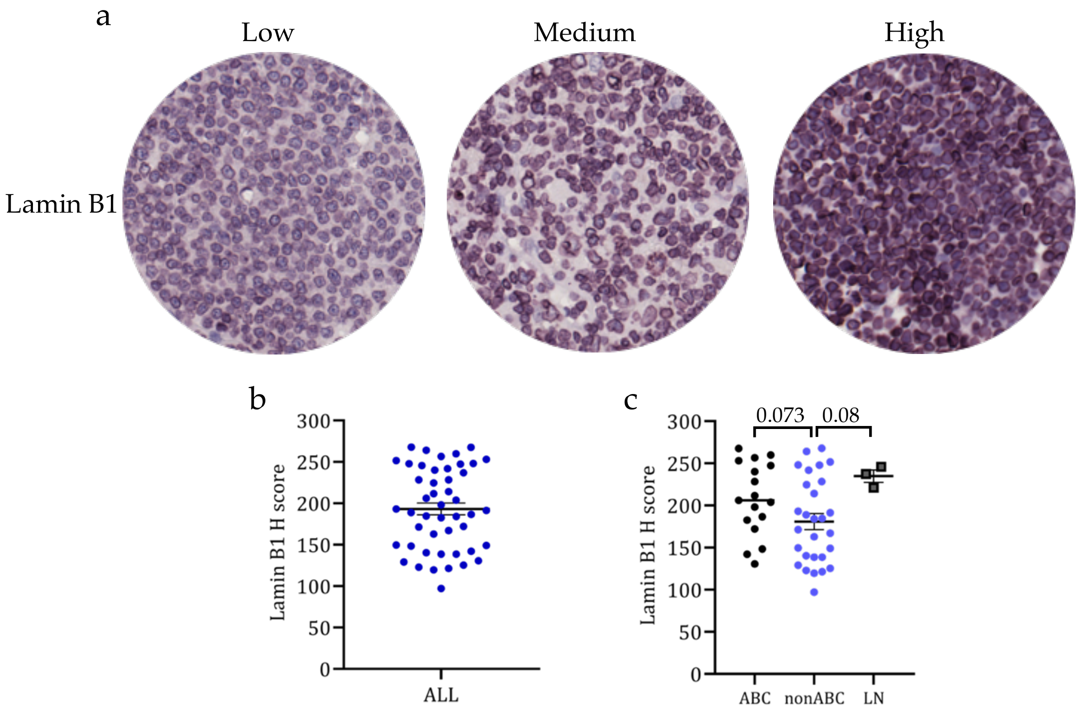

Figure 7.3.1 Lamin B1 is dysregulated in DLBCL patients. **(a)** Representative images of DLBCL TMAs stained with anti-Lamin B1 antibody showing a differential Lamin B1 protein expression. VIP chromogen was used for signal detection and tissues were counterstained with haematoxylin for the detection of nuclei. **(b)** Plot showing the heterogeneity of Lamin B1 protein expression (H-score) across all DLBCL TMAs; N=47. **(c)** Lamin B1 H-score across cell-of-origin DLBCL subtypes after COO stratification; N = 48. Unpaired t-test was used for statistical analysis with p-values indicated in the plots. LN=Lymph node.

7.3.2 Decrease in Lamin B1 is not associated with elevated DNA damage in DLBCL patients

To translate my previous *in vitro* and *in vivo* findings of a negative correlation between Lamin B1 expression and DNA damage, I performed sequential staining for Lamin B1, CD20 (B-cell marker), and γH2AX-ser139 (Figure 7.3.2.1). Considering the previous findings from CLL patients (Figure 1.3.7 & 1.3.10.1) and functional studies (Chapters 3 & 5), I hypothesised that DLBCL patients with decreased Lamin B1 nuclear incorporation would present with elevated γH2AX signal. Immunohistochemical staining of Lamin B1 was used to dichotomise

DLBCL patients by the median Lamin B1 H-score (High > 186, N=26 and Low <186, N=25). Surprisingly, the assessment of γH2AX revealed that Lamin B1^{high} patients display increased DNA damage (Figure 7.3.2.2). This observation suggests that other factors than Lamin B1 alone contribute to the elevated DNA damage in DLBCL.

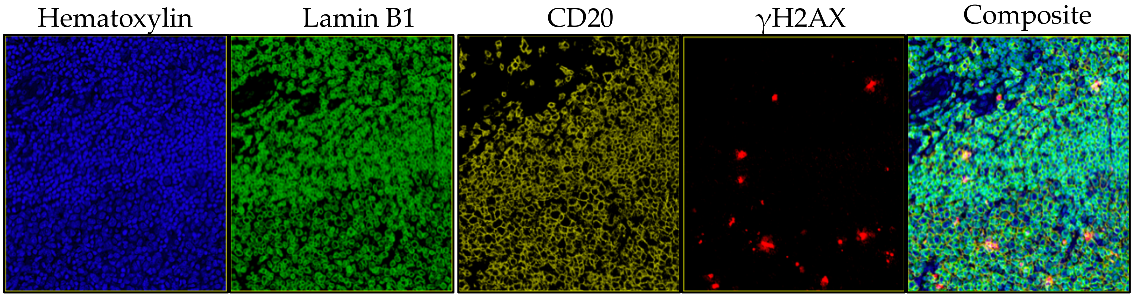

Figure 7.3.2.1 Immunohistochemical staining of DLBCL tissue microarrays. Representative images of DLBCL TMAs stained with anti-Lamin B1, anti-CD20, and anti-γH2AX showing a range of Lamin B1 expression. VIP chromogen was used for signal detection and tissues were counterstained with haematoxylin.

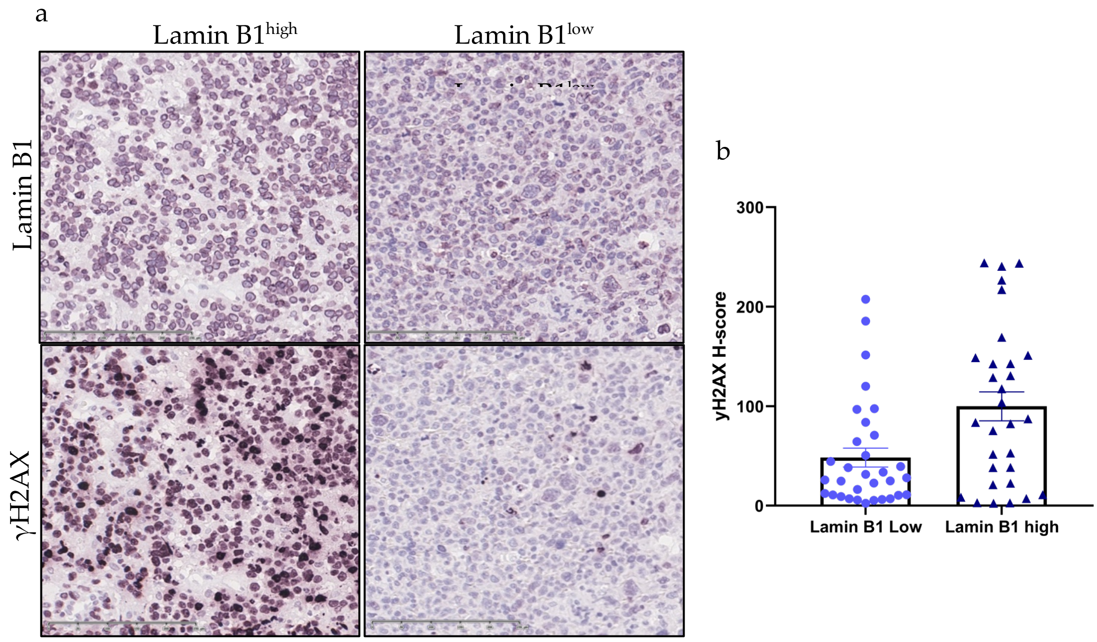

Figure 7.3.2.2 Lamin B1 is positively correlated with γH2AX in DLBCL patients. **(a)** Representative images of DLBCL TMAs stained with anti-Lamin B1 and anti-γH2AX **(b)** Dot plot showing γH2AX (H-score) in Lamin B1-high and Lamin B1-low DLBCL patients (N = 50). Scale bar represents 250 μm.

7.3.3 GCB DLBCL patients have lower Lamin B1 expression in later diagnostic stage

To further evaluate Lamin B1 in the clinical setting, I used the available diagnostic data and clinical history from the available database. I hypothesised that decreased Lamin B1 expression would be associated with a more advanced clinical stage of the disease and worse survival outcomes. There was no association between decreased Lamin B1 and advanced diagnostic stages in DLBCL patients independently of the COO stratification (Figure 7.3.3.1 a). A marginal difference was observed between Lamin B1 in DLBCL patients diagnosed at a later stage (H-score=175.1) and healthy lymph node tissues (H-score=242.5, p=0.16), as shown in Figure 7.3.3.1. After I excluded ABC subtypes, I observed a more noticeable decrease in Lamin B1 expression in late (H-score=167.3, p=0.2) vs early (H-score=187.3) diagnostic stages in non-ABC DLBCL cohort (Figure 7.3.3.1 b). Lamin B1 expression in healthy lymph nodes (H-score=234.5) was insignificantly higher compared to non-ABC DLBC patients diagnosed at a later stage (H-score=173.3, p-value 0.07) (Figure 7.3.3.1 b), which implies Lamin B1 may have a clinical implication in DLBCL disease progression when looking at a larger cohort.

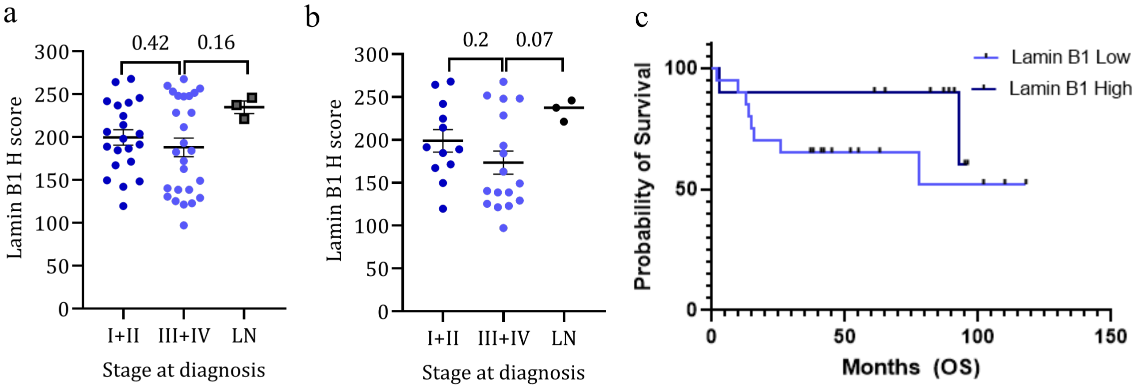

Figure 7.3.3.1 Analysis of Lamin B1 expression in DLBCL patients across diagnostic stages. **(a)** Boxplot showing Lamin B1 H-score at the stage at diagnosis (Ann-Arbor stage) in all DLBCL subtypes (N = 51) **(b)** Boxplot showing Lamin B1 H-score at a diagnostic stage in non-ABC DLBCL subtypes (N = 32). **(c)** Kaplan-Meyer curve showing OS based on dichotomization of γH2AX H-score at diagnostic stage in DLBCL patients (N = 47). LN = Lymph node.

Next, I analysed the impact of Lamin B1 expression on the survival outcome. In line with the previous findings in the CLL cohort, I hypothesised that lower Lamin B1 expression would be associated with inferior OS in DLBCL patients. DLBCL patients were dichotomised based on Lamin B1 H-score for the OS analysis. Kaplan Mayer curve shows an insignificant inferior OS in Lamin B1^{low} compared to Lamin B1^{high} DLBCL patients (p=0.09) (Figure 7.3.3.1 c). Due to the limited sample size and associated clinical data, all DLBCL patients regardless of the COO stratification were included in the analysis. Mantel-Cox test

In addition to Lamin B1, I also utilised γH2AX for the clinical evaluation in DLBCL patients. I hypothesised that elevated γH2AX, as a result of persistent DNA damage, would be associated with disease progression and poor survival outcomes. Interestingly, γH2AX staining did not reveal any significant correlation with the clinical diagnostic stage in DLBCL patients (Figure 7.3.3.2 a,b). Similarly, dichotomization of the cohort based on γH2AX expression for the survival analysis revealed no difference in OS between γH2AX-high and γH2AX-low expressing DLBCL patients (Figure 7.3.3.2 c).

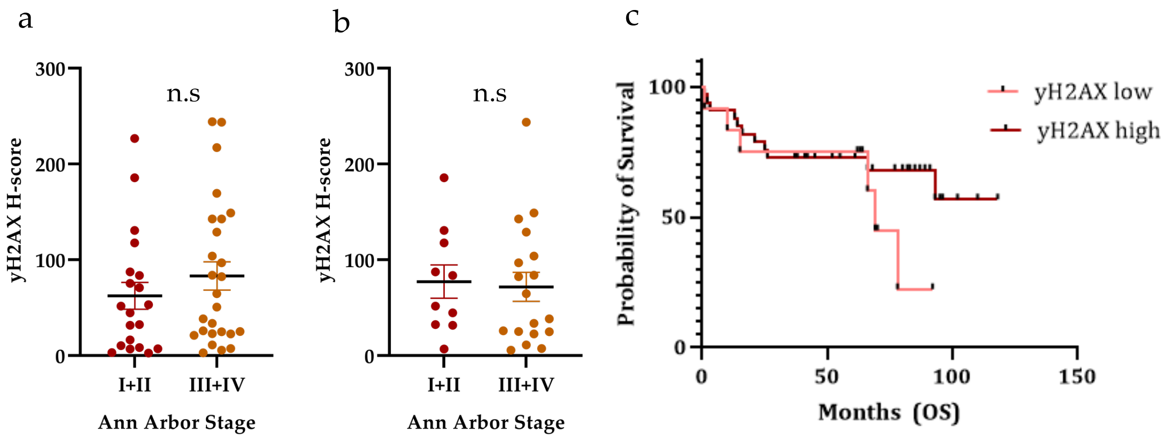

Figure 7.3.3.2 Survival analysis of DLBCL patients as a factor of γH2AX expression. **(a)** Boxplot showing γH2AX (H-score) at an early or late diagnostic stage in all subtypes (N=46) **(b)** Boxplot showing γH2AX (H-score) at an early or late diagnostic stage in non-ABC DLBCL subtypes (N=28). **(c)** Kaplan-Meyer curve showing OS based on dichotomization of γH2AX H-score at diagnostic stage (Ann-Arbor stage) in all DLBCL subtypes (N=47); n.s, not significant.

7.3.4 Clinicopathological analysis of Lamin B1 expression in DLBCL patients

Due to the limited number of DLBCL TMA samples, I implemented a large RNA-seq DLBCL (N=485) dataset to increase the size of the DLBCL cohort. Using a transcriptomics approach, I aimed to further evaluate Lamin B1 as a clinical biomarker in GC-derived B cell lymphoma. Normalised read counts were obtained from the TCGA database and DLBCL patient COO stratification (ABC, GCB) was implemented from a previously published analysis by Schmitz et al. 2018[205]. Normalised *LMNB1* expression (Log2 CPM) was analysed across COO subtypes and diagnostic stages of DLBCL patients. ABC and GCB DLBCL subtypes displayed similar *LMNB1* expression (Figure 7.3.4 a). No significant difference in LMNB1 expression was observed across diagnostic stages ABC DLBCL subtype (Figure 7.3.4 a). Contrary to the ABC subtype, *LMNB1* expression was significantly decreased in stages 2 and 3 compared to stage 1 in the GCB DLBCL cohort, while the difference between stage 1 and stage 4 was not statistically significant in the GCB cohort (Figure 7.3.4 b). Observed differences in the GCB DLBCL cohort further indicate that Lamin B1 has a specific role in GC B cell-derived lymphomas and B cell biology.

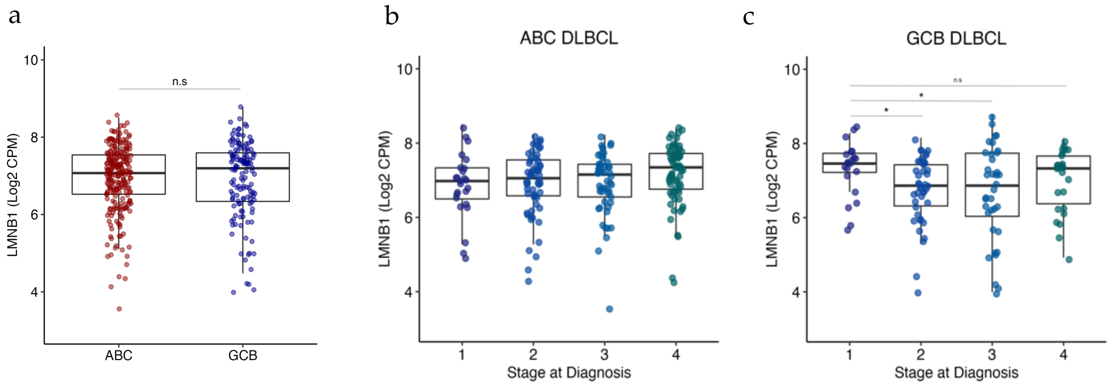

Figure 7.3.4 Analysis of *LMNB1* mRNA expression in DLBCL patients across diagnostic stages using RNA-seq dataset. **(a)** *LMNB1* expression (Log2 CPM) in DLBCL patients stratified based on the cell of origin. **(b-c)** *LMNB1* expression (Log2 CPM) across the diagnostic stage in **(b)** ABC DLBCL subtype (N=243) and **(c)** GCB DLBCL subtype (N=139). Unpaired t-test was used for statistical analysis. $^{*}P \leq 0.05$; $^{**}P \leq 0.01$; ns, not significant.

7.3.5 Gene set enrichment analysis GCB DLBCL patients

The transcriptome analysis of shLMNB1 BL2 cells in Chapter 6 revealed an enrichment of several pathways associated with ribosome biogenesis, translation, and *Myc* target genes. To assess cellular pathways correlated with *LMNB1* expression, I performed a single-sample Gene Set Enrichment Analysis (ssGSEA) using log-normalised CPM counts from GCB DLBCL patients. Normalised enrichment scores of Hallmark gene sets were used for hierarchical clustering (Figure 7.3.5.1). A comparative analysis of NES for Hallmark gene sets in the Lamin B1^{low} and Lamin B1^{high} patients. Contrary to the GSEA analysis in BL2 shLMNB1 cells, gene sets including "MYC TARGETS V1", "MYC TARGETS V2", "E2F TARGETS", "MITOTIC SPINDLE" were positively enriched in Lamin B1^{high} DLBCL patients (Figure 7.3.5.1 & Appendix 10.5). Interestingly, upregulation of the "OXIDATIVE PHOSPHORYLATION" was found in DLBCL patients expressing low *LMNB1* (Figure 7.3.5.1 & Appendix Table 10.5.3). Surprisingly, the ssGSEA analysis further revealed a significant positive enrichment of REACTOME gene sets related to DNA REPAIR, HOMOLOGY DIRECTED REPAIR" and "DNA DOUBLE STRAND BREAK REPAIR" in Lamin B1^{high} DLBCL cohort (Figure 7.3.5.2 & Appendix Figure 10.5).

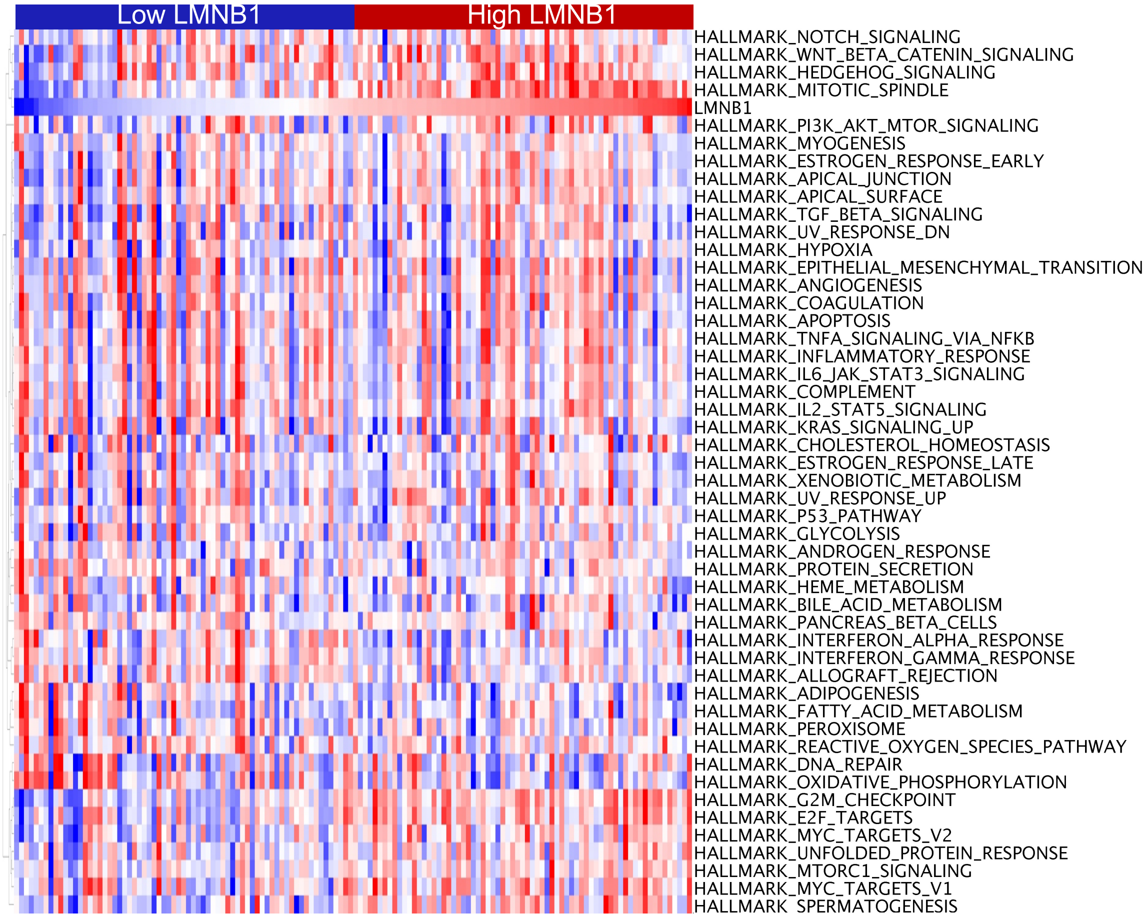

Figure 7.3.5.1 Gene expression analysis of Hallmark pathways and LMNB1 in GCB DLBCL patients. The ssGSEA was performed on log-transformed CPM read counts. Heatmap showing NES for Hallmark gene sets in Lamin B1 high and Lamin B1 low GCB DLBCL patients. Hierarchical clustering was performed on rows using Pearson correlation in GenePattern. N =138.

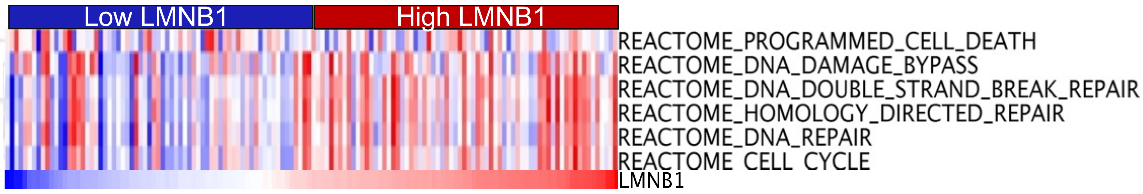

Figure 7.3.5.2 Gene expression analysis of Reactome DDR gene sets and *LMNB1* in GCB DLBCL patients. Heatmaps showing NES for Reactome DNA DAMAGE response gene set in Lamin B1 high and Lamin B1 low GCB DLBCL patients. The ssGSEA was performed on log-transformed CPM read counts. Hierarchical clustering was performed on rows using Pearson correlation in GenePattern. N =138.

7.3.6 Upregulation of ribosome biogenesis is associated with decreased Lamin B1

GSEA analysis in BL2 shLMNB1 cells uncovered the upregulation of genes associated with ribosomal biogenesis. Therefore, I assessed these findings in the DLBCL cohort by ssGSEA and Gene Ontology (GO) Cellular Component (CC) comprising of genes involved in subcellular structures and cellular organization. The ssGSEA revealed a positive enrichment of gene involved in ribosome biogenesis in low *LMNB1* expressing patients (Figure 7.3.6 & and Appendix 10.5.1). Opposingly, genes associated with the “Nuclear periphery” and “Nuclear Periphery were significantly downregulated in the low *LMNB1* group. This data further confirms Lamin B1 expression has a broad impact on gene transcription and cell components.

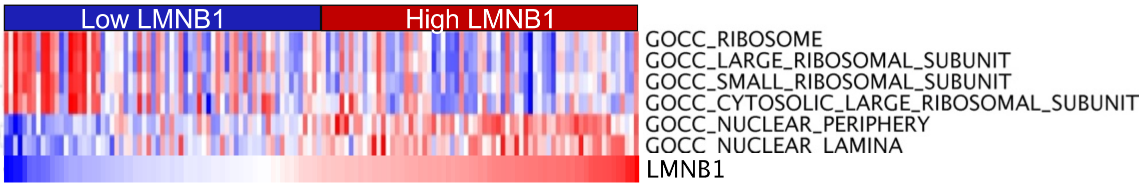

Figure 7.3.6 Gene expression analysis of GO Cellular Components and *LMNB1* in GCB DLBCL patients. Heatmaps showing NES for GO CC gene set in Lamin B1 high and Lamin B1 low GCB DLBCL patients. The ssGSEA and hierarchical clustering were performed in GenePattern. N =138.

7.3.7 Evaluation of Lamin B1 expression as a prognostic marker of survival outcome in DLBCL cohort

To complement the limited survival data from the TMA DLBCL cohort, I performed a PFS analysis in the DLBCL cohort obtained from TCGA. Based on the previously published data in the CLL cohort, I hypothesised that decreased mRNA Lamin B1 expression would be correlated with a worse clinical prognosis, particularly in the GCB DLBCL subtype. Independently of COO subtype, DLBCL patients were first stratified based on quartile *LMNB1* expression, which revealed a significantly decreased overall PFS (p=0.023) in *LMNB1*^{low} expressing patients (Figure 7.3.7.1). The overall PFS analysis of patients dichotomised patients based on the median *LMNB1* expression did not reveal a significant difference in PFS survival (not shown). However, a significantly lower 5-year PFS (p=0.026) was found to be associated with low *LMNB1* expression in DLBCL patients (Figure 7.3.7.1 b).

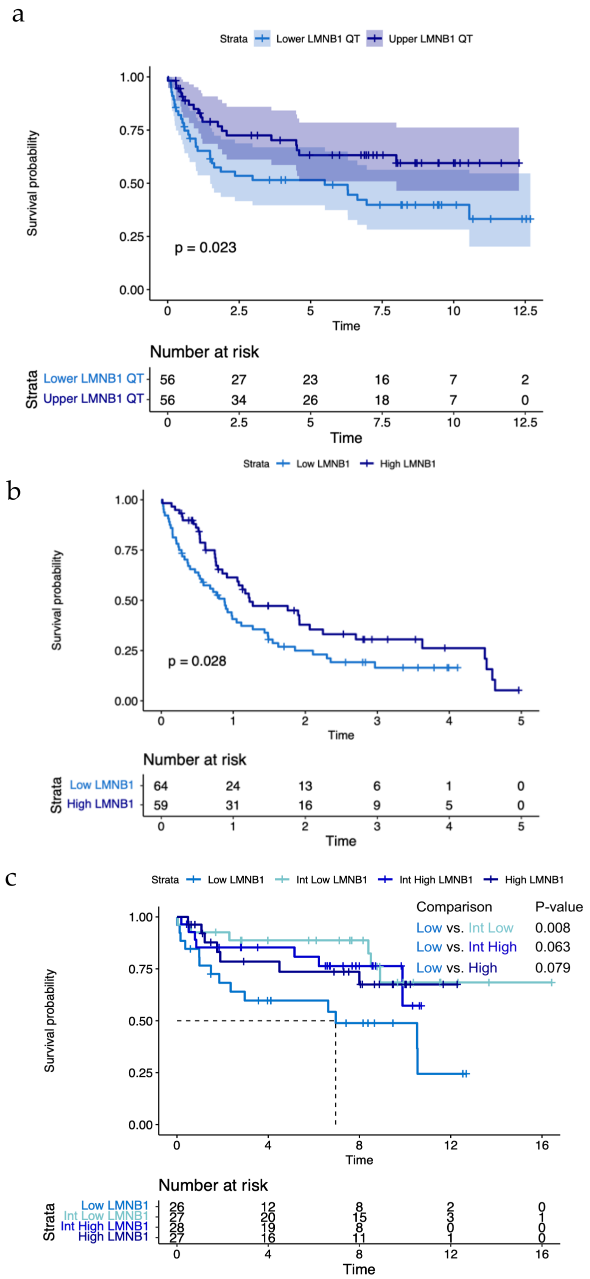

Figure 7.3.7.1 Survival analysis of DLBCL patients as a factor of LMNB1 expression. **(a-b)** Kaplan-Meyer curve estimates of **(a)** overall PFS (95% confidence intervals) in DLBCL patients as a factor of quartile *LMNB1* expression (N=112) and **(b)** 5-Year PFS in DLBCL patients dichotomised based on median *LMNB1* expression (N=123). **(c)** Kaplan-Meyer curve estimates of overall PFS based on quartile LMNB1 expression in the GCB DLBCL subtype (N=113).

Interestingly, according to the COO DLBCL subtyping, low *LMNB1* expression was associated with poor survival in GCB DLBCL patients (Figure 7.3.7.1 c), but not in ABC-classified patients (not shown). Therefore, I was interested to analyse patients that were defined as "unclassified". Due to the low sample size, patients with available clinical data and falling into the unclassified group were split into equally sized groups (n=14 each) based on *LMNB1* expression. Remarkably, low *LMNB1* expression in unclassified DLBCL patients was associated with a significantly shorter PFS (Fig. 7.3.7.2 a). A borderline insignificant difference was observed when stratifying unclassified patients based on median *LMNB1* expression (Figure 7.3.7.2 b). Analysis of diagnostic stages and survival indicates that decreased *LMNB1* expression may be associated with disease progression and inferior clinical outcomes in DLBCL patients, particularly in the GCB subtype and unclassified patients.

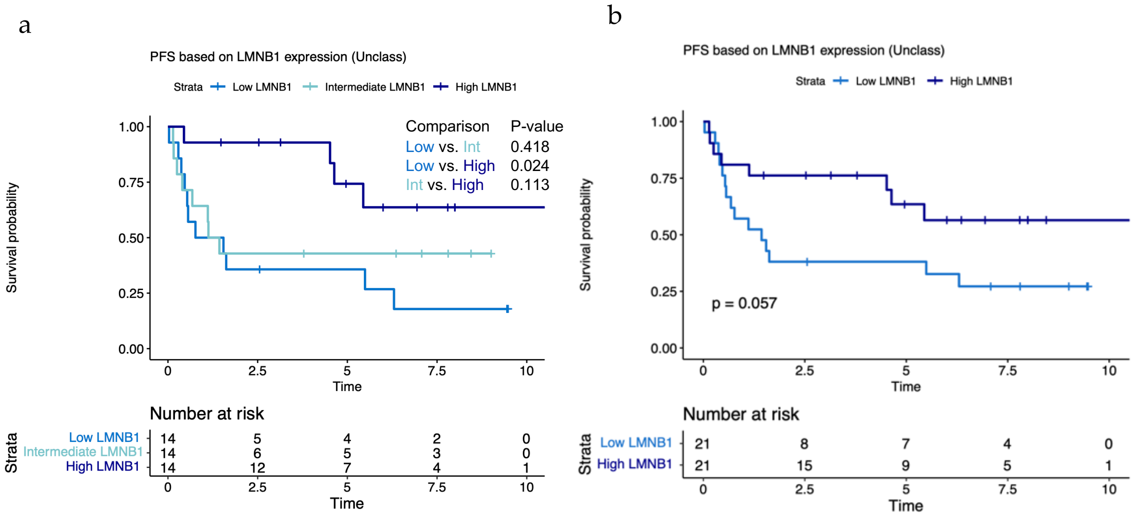

Figure 7.3.7.2 Survival analysis of unclassified DLBCL patients as a factor of *LMNB1* expression. **(a)** Kaplan-Meyer curve estimates of overall PFS of unclassified DLBCL patients after stratifying patients into three groups based on *LMNB1* expression (N=42). **(b)** Kaplan-Meyer curve estimates of overall PFS of unclassified DLBCL patients dichotomised based median *LMNB1* expression (N=42).

7.4 Discussion

In this chapter, I translated findings from functional studies into the clinical setting by utilising a collection of DLBCL tissue microarrays and publicly available gene expression dataset. Functional studies revealed depletion of

Lamin B1 leads to increased DNA damage and mutagenesis in human lymphoma cells and normal mouse GC B cells (Chapters 3 & 5). Insufficient repair of DNA damage may result in genetic lesions, including point mutations, deletions, and translocations[282]. Elevated physiological DNA damage in B cells and genomic aberrations are likely factors contributing to the malignant transformations and tumorigenesis[59]. Therefore, I investigated whether decreased Lamin B1 expression is associated with elevated DNA damage and worse clinical prognosis in B cell-derived lymphoma.

The immunohistochemical methodology has become a standard diagnostic tool in lymphomas. Currently, there are collective prognostic markers in DLBCL; however, a single biomarker has not yet been established[76,78]. IHC analysis of Lamin B1 protein expression in TMAs revealed a broad range of Lamin B1 expression across the DLBCL cohort, which suggests that Lamin B1 might be regulated at the transcriptional and post-translational level. Among other subtypes, NGS-based gene expression profiling is used to classify the most common molecular DLBCL subtypes (ABC or GCB)[28,205,281,283,]. The stratification of DLBCL based on GEP is also reproducible by IHC and algorithmic-based analysis using established phenotypic markers[281]. For that reason, I implemented the patient stratification based on the COO, which revealed marginally lower Lamin B1 protein levels in the GCB cohort compared to the ABC subtype and lymph node tissue from healthy donors.

Contrary to our previous findings in Chapters 3 & 5, I found the levels of γH2AX to be positively correlated with Lamin B1 in DLBCL patients. This finding could be due to other factors stimulating DNA damage in highly mutated tumours, including the complexity of the tumour environment or endogenous factors (e.g. oncogene-induced replication, oxidative stress, AID activity, or defective DNA repair mechanisms)[87,125,127,210]. Despite not detecting an inverse relationship between Lamin B1 expression and γH2AX, the clinicopathological analysis of Lamin B1 across diagnostic stages showed that in Lamin B1 protein expression, particularly in GCB DLBCL subtype. A low Lamin B1 protein expression was not associated significantly with an inferior survival likely due to a small sample size. Therefore, it would be necessary to have a larger sample size and ideally obtain corresponding gene expression profiles to determine whether the regulation of

Lamin B1 occurs at the transcriptional and post-translational level. Several proposed mechanisms of Lamin B1 regulation exist, including post-translational modifications (farnesylation, acetylation) and degradation via autophagic or proteasomal machinery[159,165,166,179]. In addition to the OS analysis, a comparison of the clinical outcome based on γH2AX expression showed no significant differences, which is contrary to the previously published data[127] and could be attributed to the smaller sample size.

Analogous to the differential Lamin B1 protein expression in DLBCL TMAs, differential *LMNB1* mRNA expression was also seen in DLBCL patients LMNB1, which suggests that Lamin B1 is regulated also at the transcriptional level. A recent study demonstrated that AML patients carrying 5q deletion, which often contains *LMNB1* locus at 5q23.2, have significantly decreased *LMNB1* expression[200]. Interestingly, deletion of 5q arm has been detected in a proportion of refractory and relapsed DLBCL (rrDLBCL), potentially a contributing factor of decreased *LMNB1* expression[283]. The clinicopathological analysis indicates that low *LMNB1* is associated with advanced disease stages and inferior survival outcomes, specifically in the GCB and unclassified DLBCL subtypes. These findings are contrary to the analysis of various solid tumour tissues, which demonstrated *LMNB1* that upregulation is generally linked to poor survival and the advanced stage of the disease[256,284].

In this study, hallmark enrichment analysis revealed a positive association of *LMNB1* and pathways associated with MYC TARGETS, MITOTIC SPINDLE, and E2F TARGETS, which was in contrast with GSEA analysis from RNA-seq BL2 shLMNB1 cells. Upregulation of genes associated with "OXIDATIVE PHOSPHORYLATION" was correlated with low Lamin B1. The analysis in the DLBCL cohort is in agreement with comprehensive *LMNB1* gene expression analysis in prostate adenocarcinoma (PRAD) patients[256]. The comparison of the DNA damage repair transcriptional profile revealed positive enrichment of DDR-related REACTOME gene sets ("DNA REPAIR", "HOMOLOGY DIRECTED REPAIR", "DNA DOUBLE STRAND BREAK REPAIR") in LMNB1-high expressing cohort. Comparably to previous studies, our analysis revealed a strong association between DNA repair genes and *LMNB1* expression at the transcriptional level, which indicates Lamin B1 is involved in regulating DNA damage repair[180,182,256,284].

In addition to Hallmark gene sets, GO CC term analysis revealed that genes involved in ribosome biogenesis and protein translation are significantly upregulated in patients with low *LMNB1* expression, which agrees with previous findings in the BL2 cell line. Structural constituents of ribosomes are vital subcellular structures involved in protein translation required to meet the needs of hyperproliferative malignant cells. Lamin B1 together with nuclear lamina have been shown to maintain the functional plasticity of the nucleolus, a major site of ribosome biogenesis[285–287]. Therefore, this data suggests a potential link between Lamin B1 mediated regulation of ribosome, protein translation, and the nucleolus organization. In conclusion, data presented in this chapter further confirmed that Lamin B1 has an important function in DLBCL regarding the regulation of gene transcription associated with cell proliferation, DNA damage response, and clinical prognosis.

Chapter 8: Genome-wide analysis of double-strand breaks in Lamin B1 depleted cells

8.1 Introduction

A broad range of exogenous factors, including bacterial infection, genotoxic drugs, X-rays, and ultraviolet (UV) radiation, contribute to the formation of DNA double-strand breaks (DSBs)[288,289]. In addition to exogenous factors, endogenous cellular mechanisms, such as replicative stress, reactive oxygen species (ROS), or activation-induced deaminase (AID) driven somatic hypermutations (SHM) can result in the formation of DSBs[120]. Particularly in normal germinal centre (GC) B cells, reduced Lamin B1 expression and AID activity induces programmed and tightly controlled DNA damage in the secondary lymphoid organs[42,131]. In line with previous reports demonstrating Lamin B1 mediated genomic instability in osteosarcoma cell line[176], I have shown that reducing Lamin B1 expression induces DSBs in normal and malignant GC B cells (Chapters 3 & 5). Further, whole-exome sequencing (WXS) analysis revealed mutational clusters in Lamin B1-depleted cells (Figure 3.3.1.3). Due to the limited number of reports in the literature extensively examining Lamin B1-mediated DNA damage, I wanted to define the topology of DSBs formed upon Lamin B1 depletion. Identifying DSB hotspots as a direct result of Lamin B1 depletion in B cells would provide additional evidence of Lamin B1 as an upstream modulator of B cell mutagenesis and potentially lymphomagenesis.

To perform an in-depth analysis of DSBs induced by Lamin B1 depletion, I adapted the sBLISS (in-suspension breaks labelling in situ and sequencing) method of genome-wide DSB profiling, which can be used to detect DSBs at a single nucleotide level to identify fragile chromatin regions[290]. sBLISS is an innovative technology capable of tagging DSBs by a unique molecular identifier (UMI)-adaptor labelling, amplification, and subsequent next-generation sequencing (NGS). The versatility of the sBLISS has been previously used for the identification of genomic regions susceptible to etoposide-induced DSBs[142]. Etoposide-induced DSBs were associated with increased transcriptional output and proximity to loop anchors, which were attributed to leukaemia-driving gene fusions detected in mixed-lineage leukaemia (MLL) patients[142]. Another study identified the association of colibactin-induced DNA damage signature with increased mutagenesis colorectal cancer[225]. The sBLISS identified unique DNA sequences enriched particularly in AT-rich hexamer motif to be susceptible to DSBs induced by colibactin toxin from E. coli. Using a similarly modified approach, I implemented the sBLISS method to generate genome-wide profiles of DSBs to uncover fragile chromatin sequences prone to DNA damage induced by Lamin B1 depletion in normal and malignant B cells.

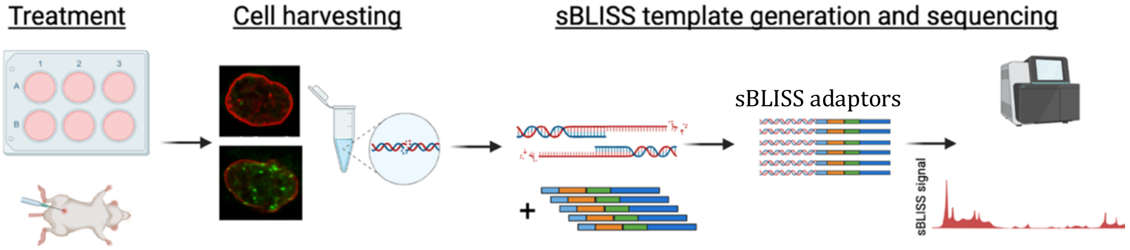

Figure 8.1 Experimental approach of genome-wide DSB profiling using the sBLISS methodology. BL2 shLMNB1 and LaminB1$^{fl/fl}$Cγ1$^{+/cre}$ FACS sorted mouse cells were fixed and lysed for sBLISS template generation. Blunted DSB ends were ligated to barcode-specific sBLISS UMI-containing adaptors. The generated template was sonicated and used for RT-PCR and library preparation. Single-end 1x76 bp was used for sequencing of the sBLISS libraries. Prior to UMI-DSB analysis, reads were filtered based on unique barcodes for each sample.

8.2 Chapter aims and hypothesis:

In this chapter, our main objective was to identify genomic regions susceptible to DSBs formed by the depletion of Lamin B1 at the nuclear periphery in B cells. I utilised *in vivo and in vitro* Lamin B1 silencing models for the sBLISS analysis of genome-wide DSBs profile. Using sBLISS approach, I intended to precisely identify genomic regions prone to DSBs. Identification of DSB hotspots is essential for a better understanding of Lamin B1-mediated genome protection in B cells.

Chapter aims:

1. Analysis of genome-wide DSB profile by sBLISS in BL2 cells after Lamin B1 silencing.
2. Analysis of genome-wide DSB profile in GC B cells after Lamin B1 deletion.
3. Comparison of transcriptional output and prevalence of DSBs.
4. Motif sequence analysis of DNA around DSB sites.

8.3 Results

8.3.1 Genome wide DSB analysis in BL2 cells upon depletion of Lamin B1

To further study the specificity and localisation of Lamin B1-induced DNA damage, I implemented the sBLISS method to human lymphoma cells. Untreated, shLMNB1-induced, and Etoposide-treated BL2 cells were used in triplicates for the sBLISS experiment. Cells treated with Etoposide at the concentration of 20 µM for 2 hours were used as a positive control of DSBs induction. All samples were treated and harvested simultaneously to avoid intersample variation during the generation of sBLISS template as described in the methods section 2.9.1. Lamin B1 knockdown and induction of DNA damage were confirmed by flow cytometry and western blot analysis shown in Figure 7.1.1 of the Appendix. Libraries were sequenced at single-end 1x76 base pairs (bp). Raw sBLISS reads were processed and mapped to the human genome 19 (hg19) using an adapted pipeline developed specifically for sBLISS[142,290]. First, qualitative analysis was performed to assess sequencing depth and saturation across all biological samples and replicates. Total reads, mapped reads, and DSB counts for each sample in triplicates displayed a high mapping score (QC>60) and similarities between biological replicates (Figure 8.3.1.1 a). UMI-DSB counts represent the number of unique DSBs at a unique genomic location, which was used for downstream analysis. The proportion of UMI-DSBs per total reads suggests the complexity of the library and sequencing saturation (~30%) was sufficient for the analysis as per Bouwman et al. 2020 (Figure 8.3.1.1 b)[290]. Read count balance between UMI-DSBs mapped to the positive and negative strands displays a balanced distribution of reads derived from the sense and antisense strand within the identified DSBs (Figure 8.3.1.1 c)

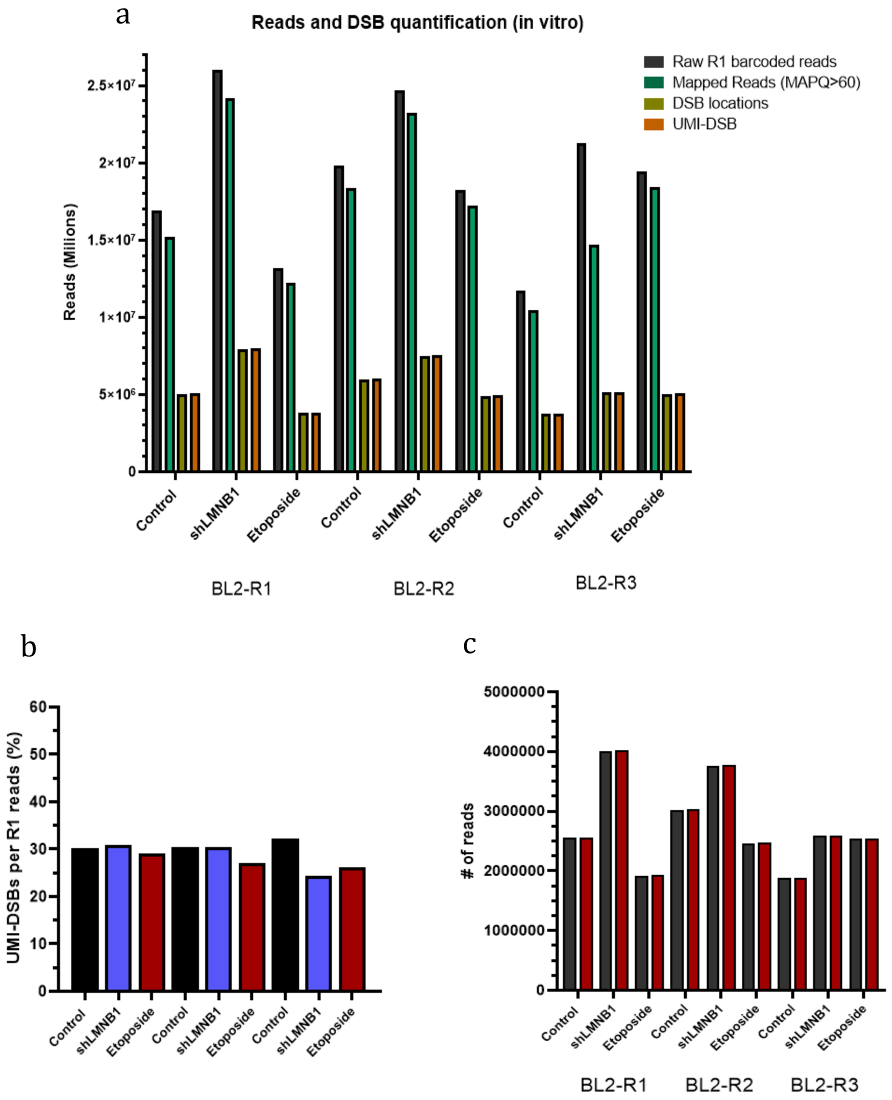

Figure 8.3.1.1 Pre-processing analysis of read and UMI-DSB counts. **(a)** Reads and DSB counts for each sample in the three libraries at subsequent steps of: raw R1 reads with prefix, mapped reads (mapping quality (MAPQ) ≥ 60), number of detected DSB locations genome-wide (not considering UMI frequency), and number of UMI-DSBs genome-wide (reads with a unique UMI and location) **(b)** Ratio of UMI-DSBs counts of identified DSBs with a unique UMI and unique location genome per number of reads with a prefix used for saturation and library complexity estimation. **(c)** Read count balance between UMI-DSBs mapped to the positive (grey) and negative (red) strands.

Next, I performed Pearson's correlation analysis of the DSBs load in the 10 kilobase-pair (kb) genomic bins, which revealed a high correlation between biological replicates and a lower correlation between treatment conditions, as expected (Figure 8.3.1.2 a). Further, I identified the number of DSB locations associated with the minimum number of distinct UMIs (unique DSBs) found per given location (Figure 8.3.1.2 b). The number of DSB locations containing a high number of unique UMIs confirms the occurrence of DSB clustering. No differences were found in DSB distribution across promoter, gene, and intergenic regions in control and shLMNB1 as demonstrated by pie charts in (Figure 8.3.1.3). Etoposide-treated BL2 samples showed a marginally lower proportion of DSBs found in intergenic regions as compared to control and shLMNB1, confirming Etoposide-induced DSBs have a bias towards gene transcription. Along with BL2 cells, I implemented the sBLISS to splenocytes obtained from our mouse models.

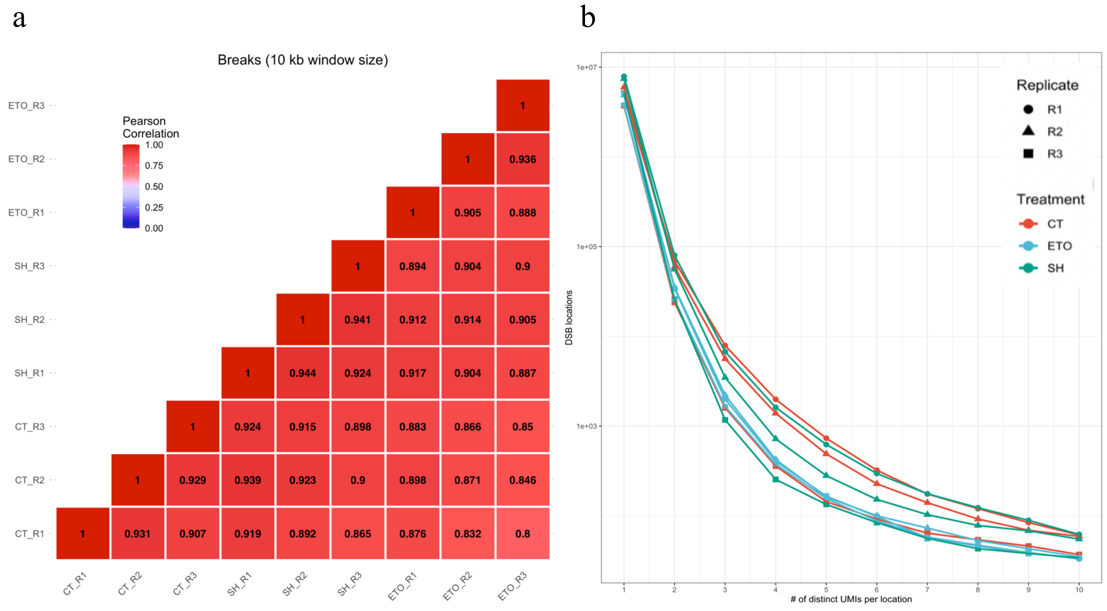

Figure 8.3.1.2 The sBLISS analysis of variation between replicates and biological conditions in BL2 cells. **(a)** Pearson's correlation coefficient of the DSB load in 10-kb genomic windows, calculated between all replicates and samples for BL2 sBLISS data. **(b)** The number of identified DSB locations filtered by the minimum number of distinct UMIs found per location for BL2 samples. CT (Control), ETO (Etoposide-treated), SH (shLMNB1).

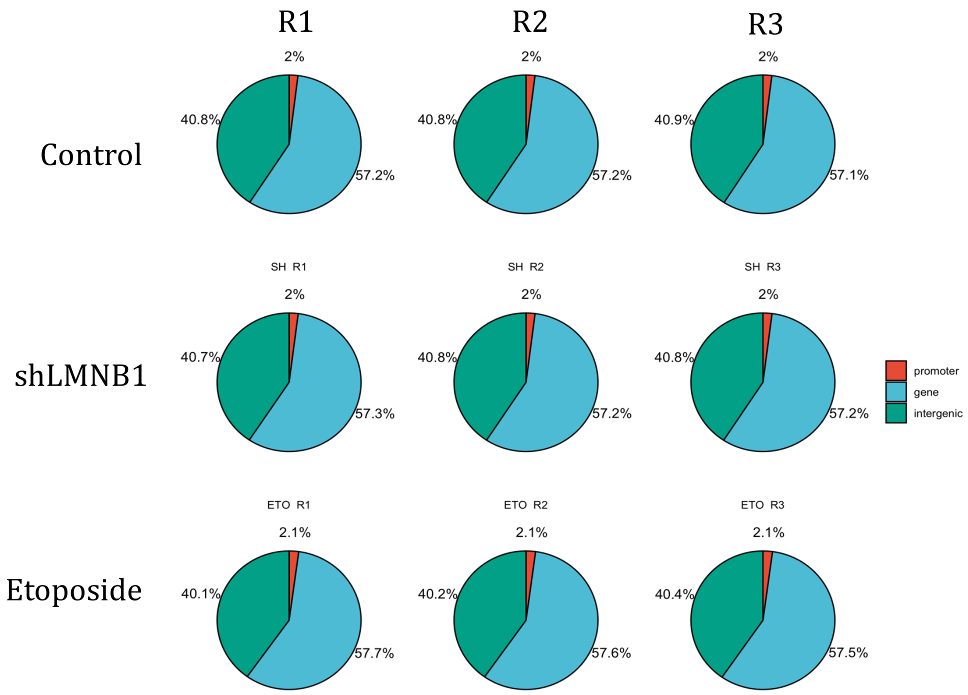

Figure 8.3.1.3 DSB distribution across genomic features does not change significantly change upon Lamin B1 depletion or Etoposide treatment. Pie charts showing the DSB distribution of the identified DSB ends across promoters, genes, and the intergenic region for all BL2 samples. Genes are considered from the transcription start to transcription end site, and promoters are defined as the 2kb upstream of the transcription start site. The intergenic region is defined as the remainder of the genome.

8.3.2 Genome-wide DSB analysis in murine Lamin B1 deficient GC B cells

For the *in vivo* sBLISS analysis, *Cγ1*$^{+/cre}$ and *LaminB1*$^{fl/fl}$*Cγ1*$^{+/cre}$ mice were immunised as in Chapter 5 using two different immunization rounds, each including a minimum of four mice per condition. After ten days, mouse spleens were processed, GC B cells fraction was enriched by PNA (peanut agglutinin antigen) beads and sorted by fluorescence-associated cell sorting (FACS) prior to the generation of sBLISS template (Figure 8.3.2.1). In addition to GC B cells (B220+, CD95-, GL7-), the naïve B cell population (B220+, CD95-, GL7-, IgD+, IgM-) was FACS sorted and used as a negative control. Analogous to the sBLISS analysis of BL2 samples, mouse reads were processed, and qualitative analysis was performed to confirm sequencing depth and saturation (Figure 8.3.2.2). Total reads, mapped reads, and DSB counts for each sample in two different libraries show similar values between biological replicates. A higher number of reads was detected in $LaminB1^{fl/fl}C\gamma1^{+/cre}$ samples, suggesting a more complex sBLISS library likely due to the increased frequency of DSBs. Opposingly, Naïve B cells samples in library M1 showed a very low number of reads, likely due to the low library complexity caused by a low number of DSB present in the particular biological sample (Figure 8.3.2.2 & 8.2.2.3). The proportion of UMI-DSBs per total reads suggested sufficient library complexity was obtained in most of the samples except for $C\gamma1^{+/cre}$ (M1) and Naïve B cell (M1) samples. Read count balance between UMI-DSBs mapped to the positive and negative strands display equal distribution.

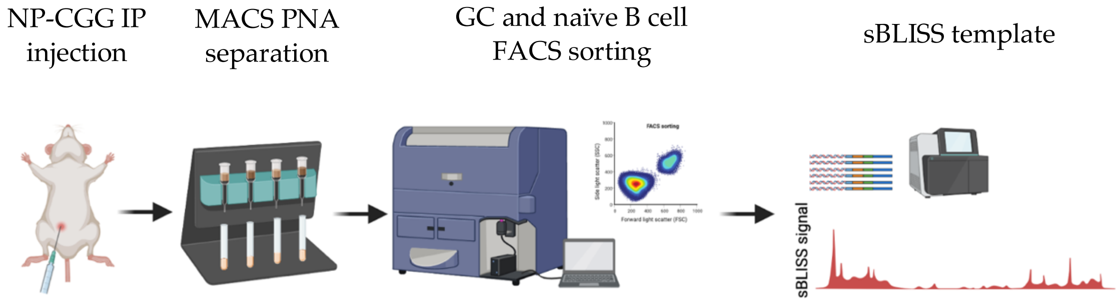

Figure 8.3.2.1 Schematic representation of genome-wide DNA DSB profiling sBLISS methodology using mouse samples. Mice were immunised with NP-CGG to stimulate the immune response for ten days. On day 10, splenocytes were harvested, MACS separated by PNA positivity and FACS-sorted based on GC B cell markers and naïve B cell markers. Immediate post-sorting, cells were fixed and processed for sBLISS template generation.

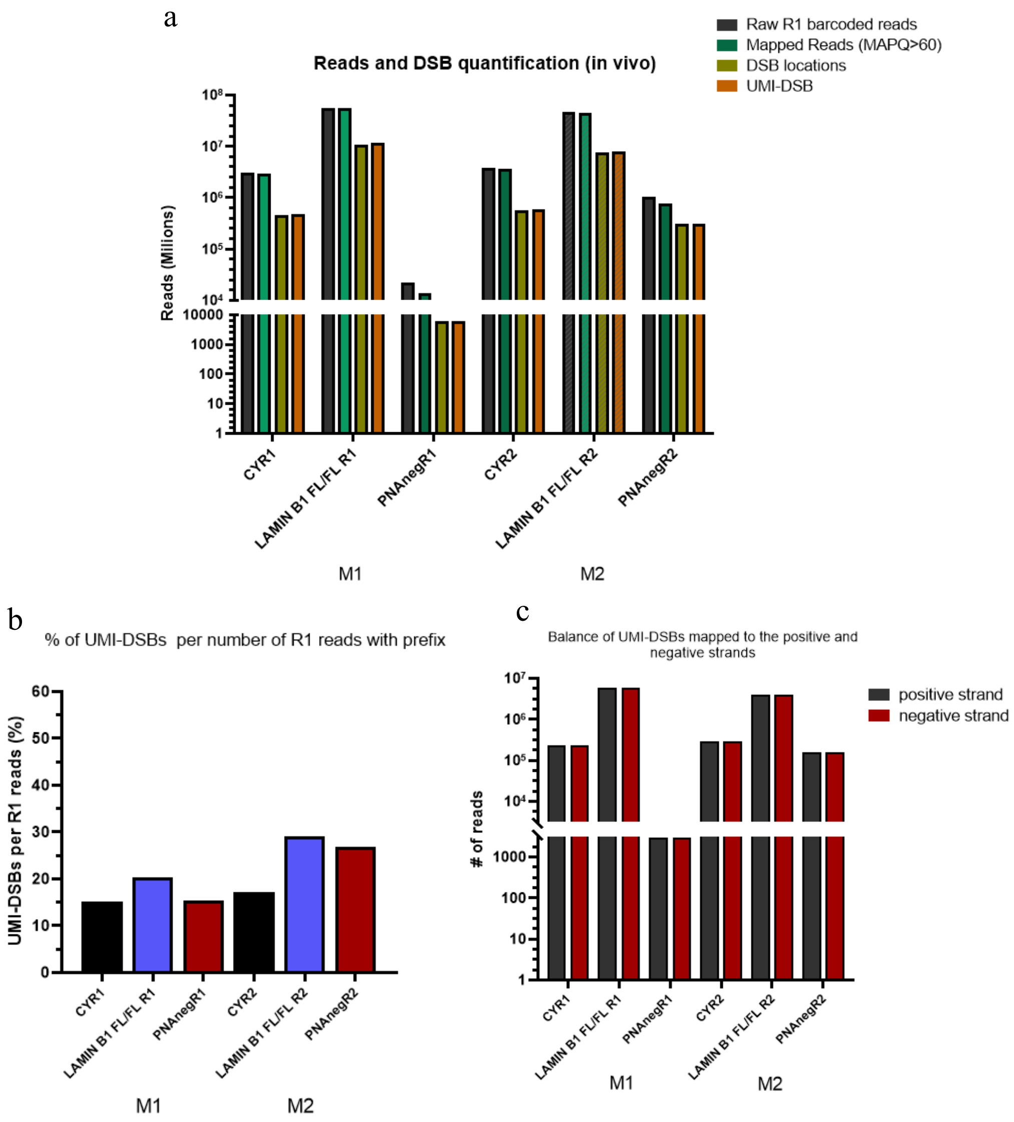

Figure 8.3.2.2 Qualitative analysis of reads and UMI-DSB counts. **(a)** Pearson's correlation coefficient of the DSB load in 10-kb genomic windows, calculated between all replicates and samples for mouse sBLISS data **(b)** Ratio of UMI-DSBs counts of identified DSBs with a unique UMI and unique location genome per number of reads with a prefix used for saturation and library complexity estimation. **(c)** Read count balance between UMI-DSBs mapped to the positive (+; Watson) and negative (−; Crick) strands.

Increased variation between samples was confirmed by Pearson's correlation analysis of DSBs distribution in the 10-kb genomic bins (Figure 8.3.2.3 a). LaminB1$^{fl/fl}$Cγ1$^{+/cre}$ samples displayed a high correlation (0.9), while Cγ1$^{+/cre}$ samples had a lower correlation (0.459). Due to the significantly lower read count in the naïve B cells sample (M1), no correlation (0.022) was observed between M1 and M2 samples between the two replicates (Figure 8.3.2.3 a). Further, I identified the number of DSB locations associated with the minimum number of distinct UMIs found per location, representative of a unique DSB (Figure 8.3.2.3 b). Notable differences between Lamin B1 deficient and control samples were detected when comparing the number of unique DSBs per distinct location, suggesting a high number of DSB hotspots in Lamin B1-deficient GC B cells (Figure 8.3.2.3 b). As expected, sBLISS of naïve B cells samples had a lower number of detected unique UMI-DSBs as compared to samples derived from GC B cells. Whether DSBs in mouse samples are associated with particular genomic features, I compared the distribution of DSBs across promoter, intergenic, and gene coding regions. Localisation of DSBs in naïve B cells across the gene-coding DNA sequences (47.7%) was lower compared to GC B cell samples, particularly Lamin B1$^{fl/fl}$ GC B cells (50.6%), suggesting gene coding regions are more susceptible to DSBs in cells with decreased Lamin B1 expression (Figure 8.3.2.4).

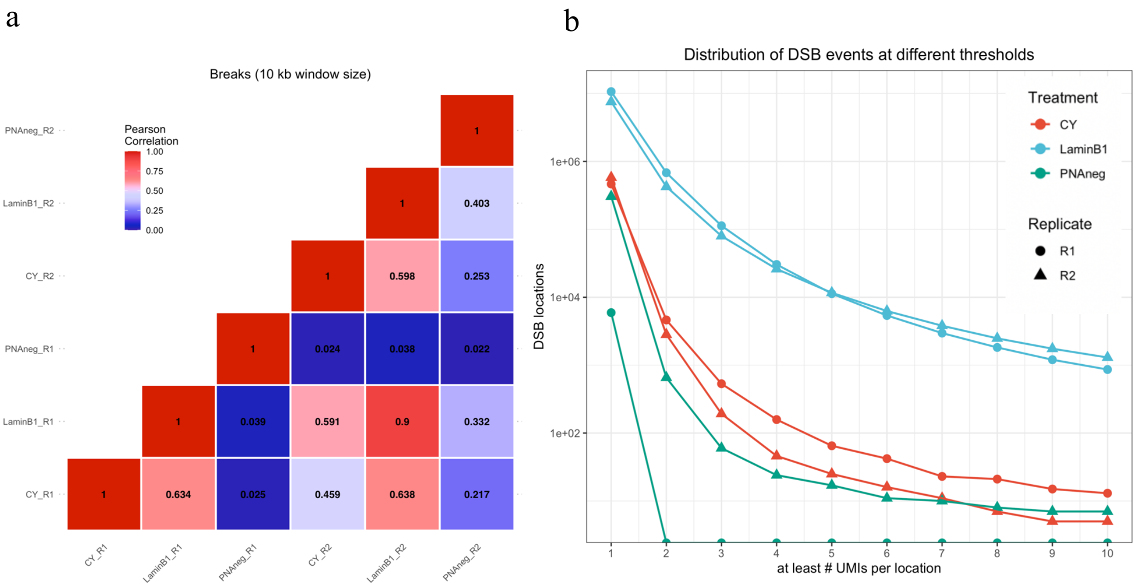

Figure 8.3.2.3 sBLISS analysis of variation between replicates and biological conditions in mouse samples. **(a)** Pearson's correlation coefficient of the DSB load in 10-kb genomic windows, calculated between all replicates and samples for mouse samples sBLISS data. **(b)** The number of identified DSB locations filtered by the minimum number of distinct UMIs found per location for splenic GC B cells and Naïve B cells from mouse samples.

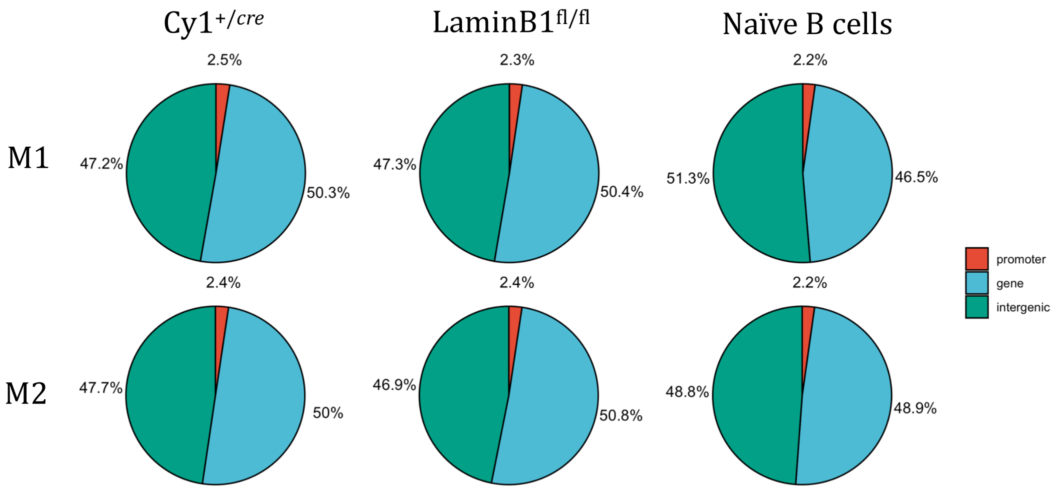

Figure 8.3.2.4 DSB distribution across genomic features upon Lamin B1 deletion in GC B cells and Naïve B cell populations. Pie charts showing the DSB distribution of the identified DSB ends genomic regions in GC B cells and Naïve B cell samples. M1 and M2 represent separate libraries. Genes are considered from transcription start to transcription end site, and promoters are defined as the 2 kb upstream of the transcription start site. The intergenic region is defined as the remainder of the genome.

8.3.3 DSBs induced by Lamin B1 depletion localise preferentially around TSS of highly expressed genes

Previous reports demonstrated a positive correlation between gene transcription and the frequency of DSBs[142]. To assess whether DSBs are associated with transcriptional output upon Lamin B1 depletion, I implemented the RNA-seq dataset from BL2 cells generated in Chapter 5. As described in Chapter 1.3.4, Lamin B1 removal from the nuclear lamina is associated with decreased DNA binding of Lamin B1, chromatin relaxation, and subsequent active gene transcription[184,232,255]. Thus, I hypothesised that cells depleted of Lamin B1 would contain an increased frequency of DSBs within the highly transcribed genes. I performed enrichment analysis of sBLISS signal across top 10% and low bottom 10% transcribed genes as per RNA-seq analysis in Chapter 5. The sBLISS signal was increased in highly expressed genes compared to lowly expressed genes in all biological samples (Figure 8.3.3). In agreement with previously published data, sBLISS signal was found to be increased in the highly transcribed genes in etoposide-treated cells compared to control (Figure 8.3.3 a)[142]. No apparent differences in sBLISS signal distribution were observed between BL2 shLMNB1 and control samples. Interestingly, sBLISS signal in low-transcribed genes was constant across all biological samples, further indicating DSBs tend to occur preferentially in actively transcribed genes. Due to the observed DSBs peak around the transcription start site (TSS), I compared sBLISS signal around TSS. In fact, when enrichment was focused primarily around TSS (± 2.5 kb of TSS), I observed an increased sBLISS signal around TSSs in shLMNB1 BL2 cells compared to control BL2 cells (Figure 8.3.3 b). Etoposide-treated samples displayed more robust localisation of DSBs around TSSs as previously reported. I did not find any differences in sBLISS signal in the bottom 10% of the expressed genes across all biological samples, confirming the association between DSBs and active transcription.

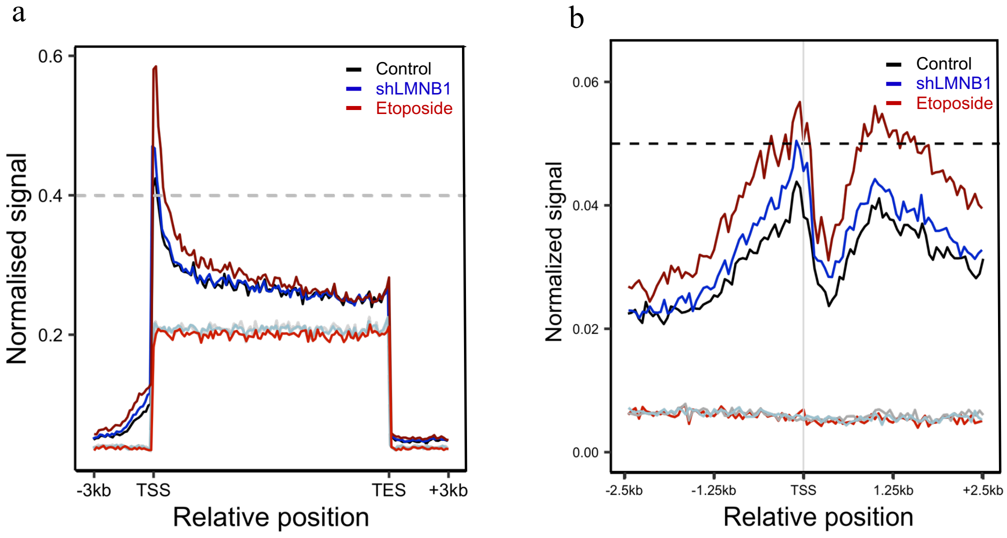

Figure 8.3.3 DSB localisation is associated with transcriptional output and Lamin B1 expression in BL2 cells. **(a)** Plot of the average DSBs per kilobase pair (Kbp) in the top 10% and bottom 10% expressed genes shown across gene bodies, transcription start site (TSS) and transcription end site (TES) **(b)** DSB distribution across the 5-kb region around the TSSs of the top 10% and bottom 10% expressed genes. Normalised sBLISS signal is shown for 100 bins per gene body. Gene body size is calculated by binning each region into 100 bins and then normalizing the signal by the library size and bin width. The fixed-size (3-kb) flanking up- and downstream regions of the gene are binned into 25 bins and normalised in the same way. Top and bottom expressed genes are defined based on the average gene expressed from the RNA-seq dataset in Chapter 6.

8.3.4 Identification of DSB hotspots associated with Lamin B1 depletion

To visualise the genome-wide localisation of DSBs, I used Circos plots for DSBs profiling at the genome-wide scale (Figure 8.3.4.1). sBLISS peaks calling using Macs2 was performed to identify DSB hotspot clusters associated with Lamin B1 depletion. Differential Macs2 peak calling on DSB-UMIs identified several DSB clusters across the genome in Etoposide-treated and shLMNB1 BL2 cells (Figure 8.3.4.2 a & Appendix Figure 10.6.4 a). The number of identified DSB hotspots associated with Etoposide treatment was 733, double the amount in BL2 shLMNB1 cells (352). Circos plots also revealed that Etoposide-induced DSBs clusters are much more dispersed than BL2 shLMNB1 (Figure 8.3.4.2 b) samples. In addition to BL2 samples, a much higher number of DSB hotspots was observed in Lamin B1 depleted GC B cells than in control samples, suggesting a complete deletion of Lamin B1 has a more profound effect on DSB susceptibility in GC B cells (Figure 8.3.4.2 b & Appendix Figure 10.6.4 c). Interestingly, no obvious clustering pattern can be observed in mouse Lamin B1 compared to human BL2 shLMNB1 samples (Figure 8.3.4.2 b).

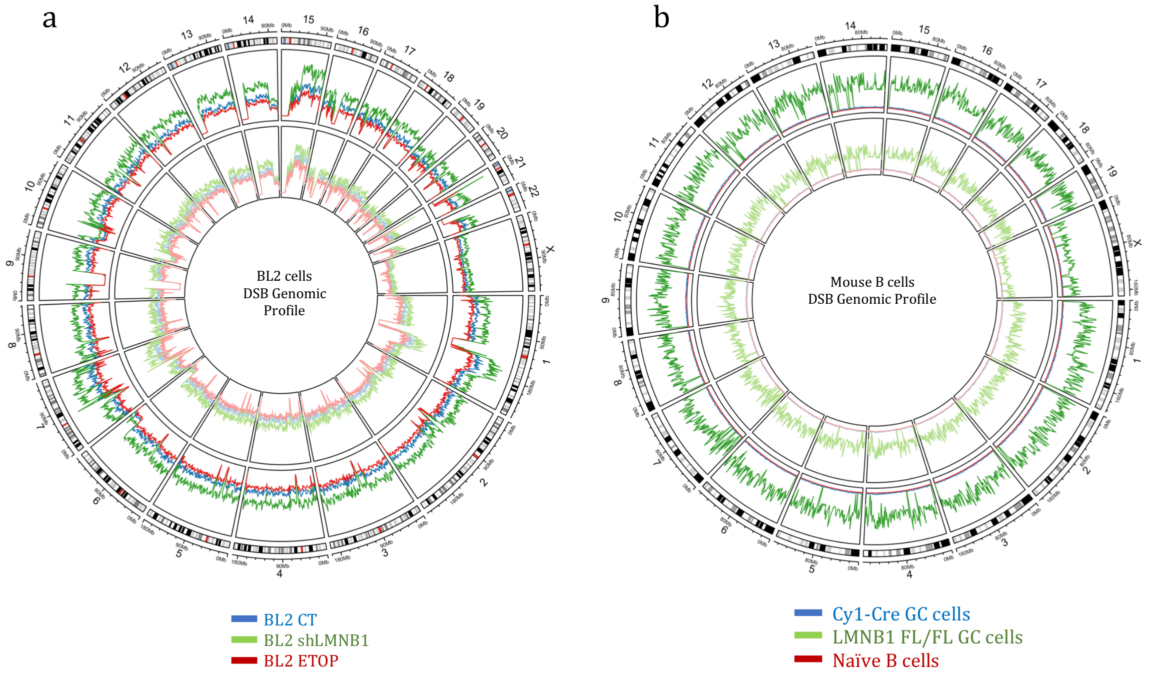

Figure 8.3.4.1 Circos plots visualizing the genome-wide distribution of identified DSB events in **(a)** BL2 cells and **(b)** mouse splenocytes. The genome is binned at 1 Mb. For visualization purposes, a hard upper limit (mean + 3× standard deviation) was set for the maximum DSB signal of each experiment. Two experimental replicates are plotted on top of each other; the outer track shows replicate 1, inner track shows replicate 2.

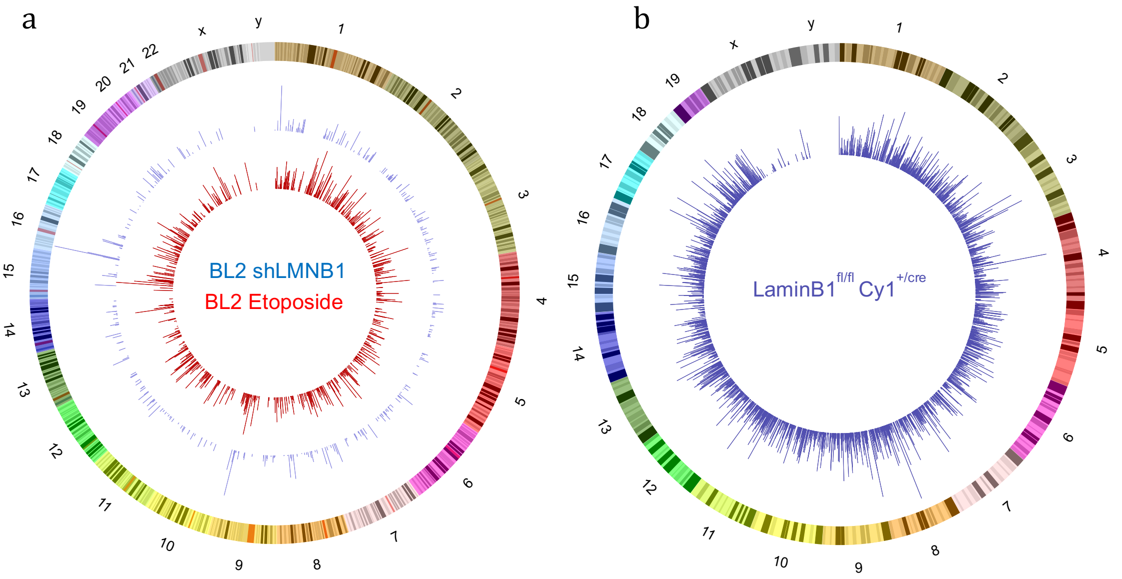

Figure 8.3.4.2 Identification of DSB hotspots in Lamin B1 deficient or Etoposide treated **(a)** BL2 cells and **(b)** mouse Lamin B1 knockout GC B cells. Macs2 (version 2.1.1.20160309) was used to call peaks from the BED files of UMI-DSB. The following algorithm parameters were used for peak calling (--no background model, --no cross-correlation between strands around the hotspots, -- shift the reads by -100 bp and extend them 200 bp to recreate the original fragment). DSB hotspots were as peaks identified by Macs2 peaks with fold enrichment >4, FDR<0.05, Pileup (height at the peak of the summit) >10).

8.3.5 Comparison of DSBs clusters with mutational hotspots and genomic aberrations in nHL lymphomas

Detection of DSBs clusters was used to compare sBLISS peaks with the genomic locations of SNVs called by WXS upon Lamin B1 silencing, as demonstrated in Chapter 3. I was interested in identifying any existing common genomic sites of DSBs and mutational clusters in BL2 cells. Using Circos plots, I visualised DSBs profile and SNVs from Lamin B1-depleted BL2 sample (Figure 8.3.5 a), which revealed several DSB hotspots tend to localise near the identified mutational clusters, particularly in Chr.1, 7, 10, 19. Whether the identified DSB hotspots contained any genes associated with lymphomagenesis, I mapped the most frequently mutated DLBCL genes generated by Ryan Morin lab and aligned them to sBLISS peaks from BL2 shLMNB1 samples. I found four genes (*CIITA, NLRC5, VPS13B, UNC5D)* to be containing DSBs hotspots in Lamin B1 depleted cells (Figure 8.3.5 b & Appendix Figure 10.6.4 c).

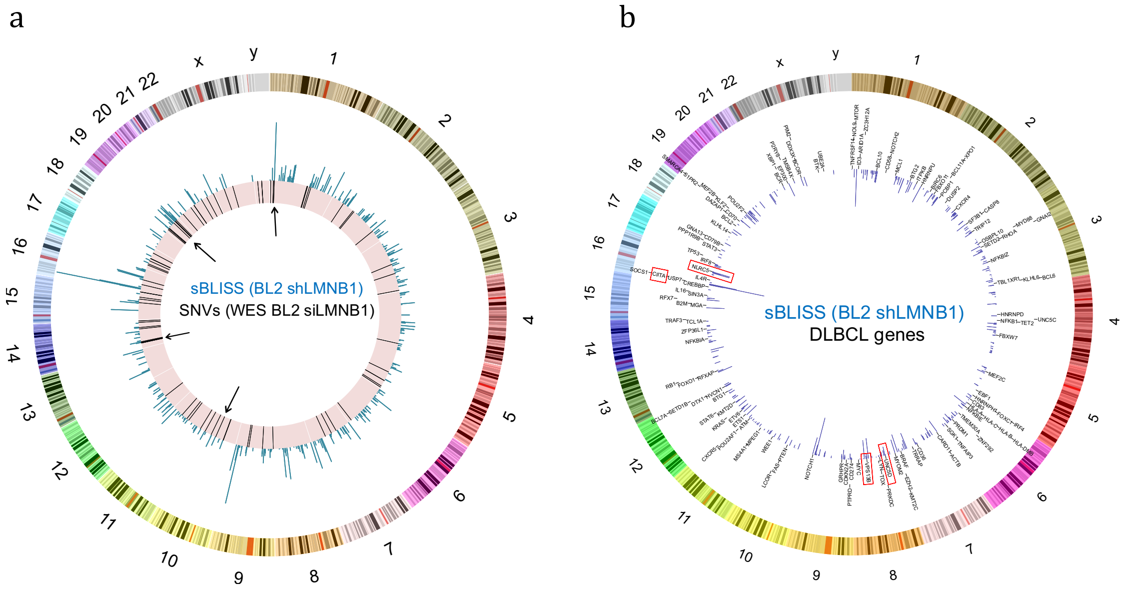

Figure 8.3.5 Mapping of DSB hotspots. Comparison of DSB hotspots identified in Lamin B1 deficient BL2 cells and **(a)** SNVs detected by WXS in Chapter 3 BL2 cells and **(b)** frequently mutated genes in DLBCL. List of genes is shown in the Appendix Table 10.6.5

8.3.6 DNA Motif analysis around DSBs

AID preferentially deaminates cytosine (C) within a specific DNA target sequence, so-called AID "hotspots" (WRC, WRCY, WGCW) and less frequently within SYC (GC/CT/C) motif sequence, known as AID "cold spots". In addition to IgV regions, AID induces reproducible DSBs at several genomic regions outside of IgV loci in B cells. Therefore, I was interested to analyse DNA motif sequences around detected DSBs. To scan DNA motifs around DSBs, DNA sequences (±10bp/±5bp) around each UMI-DSB location were used for a set of enrichment analysis using MEME Suite algorithms. First, I was interested to evaluate the enrichment and localisation of AID target motifs within DNA sequences around DSBs induced upon Lamin B1 deletion in BL2 cells and mouse splenocytes. I utilised the Simple Enrichment Analysis (SEA) algorithm to count the frequency of AID target motifs within DNA sequences around DSBs detected by sBLISS. Considering the similar frequency of single nucleotide variants (SNVs) found in AID- and AID+ BL2 cells (Chapter 3), I did not expect to find an abnormal enrichment of AID target motifs near DSBs. Interestingly, SEA revealed 44% of DSBs found in BL2 control and 47% in shLMNB1 BL2 samples contained AID "hotspot" (WRC) (Figure 8.3.6 a). Opposingly, AID cold-spots (SYC) motifs were present in around 1.5% of the DSBs, suggesting nearly half of the DSBs can be contributed to the activity of AID. Considering the reduced Lamin B1 expression and AID activity in mouse GC B cells, I hypothesised DSBs found in GC B cell samples would have a higher proportion of AID "hotspot" target motifs around DSBs compared to Naïve B cell samples. In both GC B cell-derived samples, SEA revealed a prominent enrichment of WRC motifs around DSBs compared to naïve B cells (Figure 8.3.6 b) sequences contained. Contrary to SEA analysis in BL2 cells, SYC motifs were found in a third of DNA sequences around DSBs in all mouse samples, including Naïve B cells (Figure 8.3.6 b). Given the removal of Lamin B1 in GC B cells of $LaminB1^{fl/fl}C\gamma1^{+/cre}$ mice, I hypothesise greater chromatin accessibility would result in a higher enrichment of AID hotspots near DSBs locations in $LaminB1^{fl/fl}C\gamma1^{+/cre}$ GC B cells compared to $C\gamma1^{+/cre}$ GC B cells. SEA revealed only a marginal increase of WRC motifs within DNA sequences around DSBs found in Lamin B1 depleted GC B cells (61%) compared to control samples (59%). Similar differences were found in other AID target motifs, WRCY and WGCW, which were present in approximately 45% and 15% of the DNA sequences, respectively.

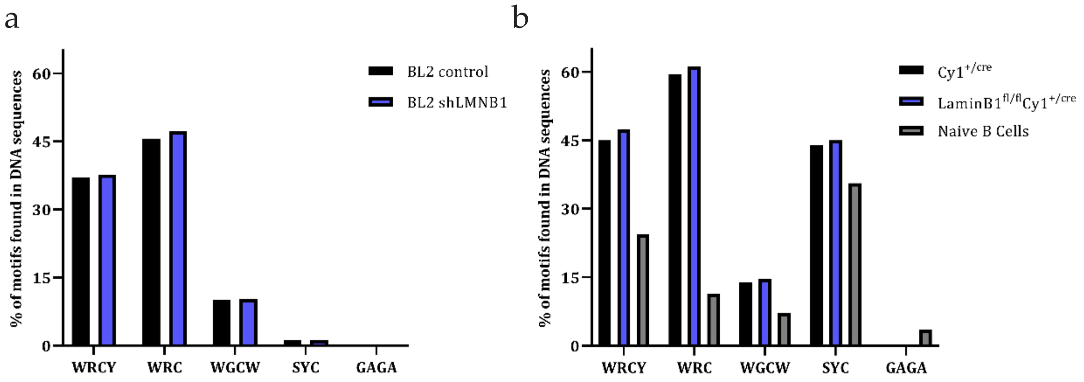

Figure 8.3.6 SEA analysis of AID target motifs in sequences associated with sBLISS detected DSBs **(a-b)** Bar charts displaying the percentage AID motifs found in DNA sequences around DSBs **(a)** in BL2 control and shLMNB1 samples and in **(b)** mouse samples from $C\gamma1^{+/cre}$ and $LaminB1^{fl/fl}C\gamma1^{+/cre}$. SEA algorithm was used to perform enrichment analysis on given AID motifs in DSB associated DNA sequences from all samples. (W = A/T, R = A/G, Y = C/T, G=Guanine, C=Cγtosine). AID "cold-spots" are SYC (GC/CT/C) or the third Cs in the trinucleotides: TTC, CAC, GGC and GAC.

8.3.7 Localisation of AID motif sequences around DSBs

To determine the precise location of AID motifs within the DSB DNA sequence, I utilised the Centrimo algorithm to calculate the localisation probability of a given motif within the DNA sequence. I hypothesised AID target motifs be preferentially located at the centre of the DSB DNA sequence, near the original DNA breakage site. First, I observed a slightly higher localisation of AID motifs (WRC, WRCY, WGCW) within DNA sequences around DSBs in BL2 samples (Figure 8.3.7 a), while the position of the non-AID motif was constant across the DNA sequence. More pronounced differences were found in control and Lamin B1-deficient GC B cells, which both revealed a preferential localisation of AID target motifs in the centre of the DNA sequence (Figure 8.3.7 b). The probability of AID motif to be found near DSB in Lamin B1-deficient GC B cells was marginally higher compared to control GC B cells. Comparable to BL2 samples, a random DNA motif sequence (GAGA) was preferentially found at the periphery of the DSB sequence (Figure 8.3.7 c), confirming the specificity of AID motif localisation using the Centrimo algorithm. When comparing Lamin B1 deficient GC B cells and Naïve B cell samples, I observed more profound differences in the location probability of AID target motifs in the centre of the sequence around DSBs. Furthermore, no preferential localisation of AID target motifs was found in Naïve B cell samples, indicating nearly half of the detected DSBs are attributed to the activity of AID in mouse GC B cells.

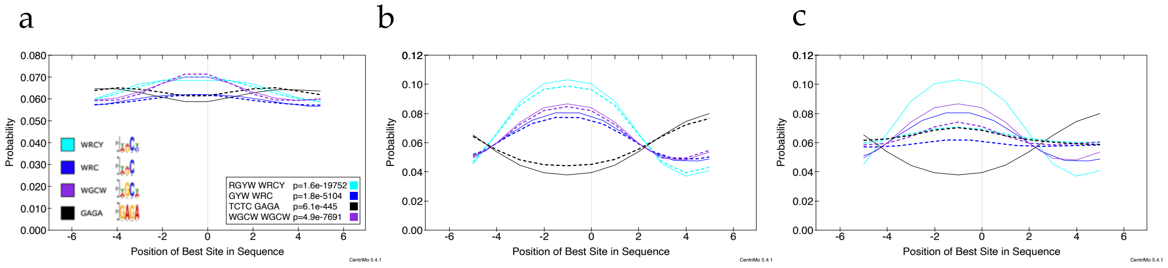

--- BL2 control
— BL2 shLMNB1

--- GC B cell Cy1$^{+/cre}$
— GC B cell LaminB1$^{fl/fl}$Cy1$^{+/cre}$

--- Naïve B cell
—GC B cell (LaminB1$^{fl/fl}$Cy1$^{+/cre}$)

Figure 8.3.7 AID target motif is preferentially located at the DNA DSB breakage site in mouse GC B cells. **(a-c)** Centrimo plot showing localisation probability of AID target motif in the DNA sequence at DSB sites in **(a)** BL2 control and shLMNB1 samples, **(b)** in GC B cell of $LaminB1^{fl/fl}C\gamma1^{+/cre}$ **(c)** GC B cell ($LaminB1^{fl/fl}C\gamma1^{+/cre}$) and Naïve B cells. Position "0" represents the original DNA breakage site.

8.4. Discussion

In this chapter, I investigated which genomic sites are prone to DSBs upon Lamin B1 depletion in normal and malignant GC B cells. For this, I utilised sBLISS methodology to detect DSBs at a genome-wide scale in human BL2 cells and normal mouse splenocytes models established in Chapter 3 and 5, respectively. Induction of DNA damage is dependent on several factors, such as spatial chromatin organization and accessibility, DNA motif sequence, or even transcription state[142,282,291]. Chromatin undergoes several conformational changes prior to the proper recruitment of DNA repair factors to the damaged site. Among other factors, the majority of spontaneous DSBs occur due to DNA replication errors or due to the enzymatic activity of AID and Type II DNA topoisomerase (TOP2)[291,292]. AID is known to preferentially deaminates the cytosine in single stranded DNA within specific motif sequences WRC & WRCY[227]. Recent studies also revealed Etoposide treatment-induced DSBs occur primarily within the open chromatin sites around TSS of highly transcribed genes, further confirming DNA DSBs are randomly distributed genetic lesions[142,292]. Elevated DNA damage analysis described in the previous chapters established the role of Lamin B1 in maintaining genomic stability in B cells. Whole exome sequencing (WXS) analysis of Lamin B1 silencing using *in vitro* and *in vivo* GC B cell models revealed a genome-wide non-random clustering of single nucleotide variants and increased incidence of DSBs formation (Chapter 3 & 5). However, the characteristics of genomic regions susceptible to DSBs induced upon Lamin B1 depletion remain unknown. In this chapter, I investigated the specificity of endogenous DSBs induced by the removal of Lamin B1 from the nuclear periphery in human and mouse B cells by the NGS approach.

Qualitative analysis of sBLISS reads revealed that library complexity and sequencing saturation was correlated between biological replicates and consistent with the previous studies[290,293]. Only sample displaying a low number of detected DSBs was the naïve B cell sample which is likely due to the low levels of endogenous DSBs in this cell population compared to GC B cells. Despite observing a higher read count in Lamin B1 depleted conditions, I did not perform any quantitative comparisons of absolute DSB counts between different biological samples. Instead, normalised sBLISS data (UMI-DSB) were used for a comprehensive analysis of DSB distribution across the genome.

The majority of DSBs identified by sBLISS were mapped to gene coding regions and no differences were found between control and Lamin B1-deficient BL2 and mouse GC B cells. I was able to identify a high number of DSB-enriched genomic regions in Lamin B1-depleted BL2 and mouse GC B cells. The number of peaks in GC B cells obtained from *LaminB1$^{fl/fl}$Cγ1$^{+/cre}$* was greater than in BL2 shLMNB1, likely due to a complete deletion of Lamin B1 in mouse GC B cells. In BL2 shLMNB1 cells, I was able to find shared genomic regions containing SNV and DSB clusters identified by WXS and sBLISS, respectively. To further determine the genome features of DSBs, I analysed transcriptional rate and DNA sequence around DSBs detected by sBLISS.

Previous studies reported that DSBs are often present in actively transcribed genes, particularly around their TSSs and promoter regions[142,208,294]. Integrating the RNA-seq analysis from Chapter 6 with the sBLISS data, DSB hotspots induced by the depletion of Lamin B1 were enriched exclusively around TSS of highly transcribed genes compared to control BL2 samples. In agreement with previously published data, Etoposide-induced DSBs were also mainly localised around TSSs and across gene bodies of highly expressed genes[142]. Interestingly, Lamin B1 was previously associated with a euchromatin-enriched genome fraction around TSSs of highly expressed genes in mouse cells primed to undergo epithelial-mesenchymal transition[175]. Artificial removal of Lamin B1 may disrupt these dynamic euchromatin Lamin B1 domains, making them more susceptible to DSBs. To address this hypothesis, Lamin B1 ChIP-seq and RNA-seq analysis in mouse GC B cells would provide more insight into DNA DSBs formation within eLAD. Taken together, genome-wide analysis of DSBs by sBLISS implies Lamin B1 depletion together with increased transcription has a synergistic negative effect on genomic instability in BL2 cells.

AID mutational activity in non-Ig genes is dependent on several factors, including transcriptional rate, frequency of AID target hotspots, and recruitment of AID to certain genomic sites, such as Ig region[34,187,295]. Increased AID activity and repeated targeting of certain genomic regions in turn lead to high mutation frequencies. I analysed DNA motif sequences around DSBs in BL2 cells and mouse B cells, and whether the induction of DNA breaks in B cells is driven by AID activity. The primary function of AID is the deamination of cytosines in DNA, causing the induction of DSBs or point mutations. AID preferentially targets cytosine within certain DNA motifs, known as AID target hotspots (WRC, WRCY, WGCW). Therefore, I performed enrichment and localisation analysis of AID target motifs around the DSBs.

SEA analysis revealed that AID target motifs (WRC) were enriched in approximately half of all DSBs detected by sBLISS in BL2 and mouse GC B cells, and only a marginal increase was detected in Lamin B1 depleted cells. Further, WRC motif was less abundant in naïve B cells samples, which corresponds with AID expression in GC B cells. Opposingly, the AID cold spot motif (SYC) was absent in the DSB sequences in BL2 cells (2%) but detected in nearly 40% of DSB sequences found in mouse B cells. While mouse immunisation induces AID-driven SHM in the WRC motif, the previous study has shown immunisation can induce DSBs and mutations at the cold spot because of the potential diversification of Ig repertoire. In line with the positive enrichment of AID motifs around DSBs, the Centrimo algorithm confirmed AID motif sequences are preferentially located near the DSB site, suggesting the DNA break is indeed the result of AID activity. Lamin B1-depleted GC B cells showed a slightly higher probability of AID motifs being localised near the original breakage site.

In conclusion, the sBLISS was used to identify genomic regions susceptible to DSBs upon Lamin B1 deletion. DSBs were more enriched around TSSs of highly expressed genes in Lamin B1-depleted BL2 cells compared to control cells. Furthermore, I detected a marginally higher enrichment of AID hotspots target motifs around DSBs detected in Lamin B1-depleted BL2 cells and mouse GC B cells. This observation was confirmed by the localisation of AID motifs near the DSBs. Here I report that Lamin B1 depletion, transcriptional output, and AID activity are all contributing factors to DNA damage within certain genomic regions in B cells.

Chapter 9: Discussion of Key Findings and Final Remarks

9.1 Key findings and future directions

This work describes novel findings regarding the role of Lamin B1 in maintaining genome stability in normal and malignant B cells. The association of Lamin B1 and DNA damage has been previously investigated in a limited range of cell lines[176,180,182]. In B cells, Lamin B1 is an upstream epigenetic regulator of AID-mediated mutagenesis in the IgV region and is a negative prognostic factor of survival in CLL patients[131]. In this study, I implemented several experimental methodologies that allowed me to investigate the role of Lamin B1 in B cells and in the clinical setting.

A comprehensive analysis of a published CLL study revealed that decreased Lamin B1 is associated with GI signature. Complementary to these findings, previously generated unpublished whole exome sequencing data from our lab revealed that Lamin B1 silencing induces a nonuniform distribution of *de novo* mutations, which primarily consisted of cytosine to thymine (C>T) nucleotide substitution independently of the AID expression status. The mutational signature in AID-negative cells suggests that other APOBEC3 genes could be driving the observed phenotype. These preliminary findings from the CLL cohort and transient Lamin B1 knockdown lymphoma cell lines were further addressed by the implementation of hypomorphic Lamin B1 *in vitro* and *in vivo* B cell models. Due to limitations (e.g., nucleoporation and knockdown efficiency, siRNA stability) of a transient Lamin B1 silencing, I generated stable doxycycline-inducible Lamin B1 knockdown cell lines, which efficiently and consistently reduced Lamin B1 incorporation at the nuclear periphery. Stable Lamin B1 knockdown cell lines have been previously established in a limited number of cancer models (NMuMG, U2OS and HCC116)[164,175,176], but to my knowledge, this is the first instance of a stable Lamin B1 knockdown in B cell lymphoma cells. Downstream functional assays revealed that Lamin B1 depletion leads to elevated endogenous DNA damage, which is in agreement with previously published findings from HCC116 and U2OS cells[176]. While in those studies Lamin B1 silencing impaired proliferation, this phenotype was not observed in lymphoma cells. Elevated DNA damage was accompanied by increased localisation of 53BP1 foci, which indicates that cells utilise the NHEJ pathway to resolve DSBs induced by Lamin B1 depletion[191,296]. Complementing the findings of increased 53BP1 foci upon Lamin B1 knockdown, a recent study found that

Lamin B1 directly interacts with 53BP1 and therefore prevents its recruitment to the damaged site upon exposure to ionizing radiation (IR)[180]. To monitor 53BP1 localisation, I generated an mAPPLE-53BP1 reporter cell line for the time-lapse imaging of live BL2 shLMNB1 cells, but the sensitivity of the reporter was not high enough for a reliable readout. Utilising an NHEJ reporter would be potentially a suitable method to obtain a direct information of the NHEJ-mediated repair. However, Schep et al. demonstrated that the NHEJ pathway is biased towards DSBs associated with the relaxed euchromatin, which is commonly coupled with the absence of Lamin B1[174,229]. Therefore, cells containing an intrachromosomal substrate and meganuclease (I-SceI) as a part of the NHEJ reporter may not provide an accurate readout of the DSB repair associated specifically with Lamin B1 depletion, but rather the efficacy of NHEJ repair of artificially induced DSBs by I-SceI.

Lamin B1 is known to regulate gene expression through the reorganization of chromatin at the nuclear periphery[148,175,177,184]. In this study, I performed RNA-sequencing after depleting Lamin B1 expression in BL2 cells. The RNA-seq analysis uncovered 262 dysregulated genes, including oncogenes (*YAP1*, *CCND2*) implicated with unfavourable outcomes in B cell lymphomas[260,261]. Other notably dysregulated genes in cancer included *YWHAE*, *miR196A2*, and *USP2*[263,297,298]. Interestingly, a ubiquitin-ligase (*HECW2*) responsible for the ubiquitination and proteasomal degradation of proliferating cell nuclear antigen (*PCNA*) and Lamin B1 was upregulated in shLMNB1 BL2 samples[166,299]. The loss of PCNA, an essential component of DNA replication and repair, has been associated with increased levels γH2AX and genomic instability in HEK293T cells[166,300]. Therefore, it would be interesting to assess the levels of PCNA protein in shLMNB1 cells. The expression of the transcription factor *Myc* was not significantly changed, a high enrichment of genes associated with MYC targets, protein translation, and ribosome biogenesis was seen in shLMNB1 cells. This is particularly interesting as *Myc* and Lamin B1 are known to be involved in the regulation of protein translation and ribosome biogenesis[270,287,301]. Therefore, assessment of protein synthesis would directly answer the question if Lamin B1 depletion upregulates translation. RNA-seq did not reveal a significant enrichment of DDR genes in shLMNB1 BL2 cells, which contradicts some of the reported findings[176,181,182]. One possible explanation is that the DDR signalling is regulated primarily by rapid post-translation modifications (PTMs). Therefore, the robust transcriptional changes of DNA repair genes in response to endogenous DNA damage may not be as prominent as in contrast to artificially induced DNA damage. Within this context, genes (*DTX3L* and *AHNAK),* involved in the regulation of NHEJ and 53BP1 were differentially expressed in Lamin B1 depleted cells[264,265]. For future experiments, it would be vital to perform RNA-seq in triplicates to increase the statistical power for differential expression analysis. As DDR is primarily regulated by PTMs, a quantitative phosphoproteomic analysis would be a suitable approach to elucidate pathways involved in DNA damage repair. Complementing the bulk RNA-seq in BL2 shLMNB1 model, single-cell RNA-seq in Lamin B1 knockout GC B cells would provide a better understanding of Lamin B1-mediated regulation of gene expression in normal GC B cells. Furthermore, Lamin B1 ChIP-seq in BL2 shLMNB1 cells could determine if Lamin B1 depletion leads to changes of chromatin and Lamin B1 binding particularly in dysregulated genes.

Loss of Lamin B1 and subsequent elevated DNA damage did not have any detrimental effects on the GC formation and downstream adaptive immune response. Based on previous studies utilising chromatin accessibility sequencing methods, findings in the study suggest that Lamin B1 removal increases DNA accessibility and susceptibility to tolerable DNA damage in the GC B cell population[249,250]. An increased proportion of GC B cells and plasmablasts was observed 21 days after immunisation, but this did not significantly affect IgG1 antibody maturation. I hypothesise that this observation is likely attributed to the expression of *AID* in the GC B cells and accessible DNA sequence within the immunoglobulin region in control $C\gamma1^{+/\mathrm{cre}}$ mice, and this is not further impacted by the loss of Lamin B1. To directly address this, I performed a single cell ATAC-seq, but I failed to sequence enough cells for downstream analysis. The IHC analysis of DNA damage implies more accessible DNA across the genome due to Lamin B1 deletion likely induces genomic lesions outside of the IgV cluster. The mechanism and topology of DNA breaks (γH2AX) outside of Ig loci in Lamin B1 deficient GC B cells remain unknown. To determine genomic regions susceptible to DSBs in Lamin B1 knockout GC B cells, I implemented the sBLISS methodology for the topological mapping of endogenous DSBs in normal and malignant B cells. The sBLISS revealed several genomic regions and transcriptionally active sites susceptible to DSBs associated with Lamin B1 depletion. Identified sequences around DSBs contained motifs associated with the mutagenic activity of AID, suggesting that a high proportion of detected DNA damage is a consequence of AID-mediated cytosine deamination. To determine if Lamin B1 deletion increases chromatin accessibility and whether DSBs localise within the accessible chromatin regions, I performed scATAC-seq, but as previously mentioned I did not obtain a sufficient sequencing depth. Lamin B1 ChIP-seq would allow to elucidate if DSBs are likely to be associated with Lamin B1-free chromatin, which could provide further evidence of Lamin B1-mediated genome protection. Mapping of genes frequently mutated in DLBCL revealed that genomic regions prone to DSB in Lamin B1-depleted cells contain with several mutated genes in lymphoma. To further investigate the susceptibility of genome to DSB, the sBLISS should be performed in a range of lymphoma cells lines and ideally primary DLBCL cells. It must be noted that the sBLISS approach can be used for a quantitative analysis after normalisation of the read counts and that currently only DSBs that are not bound be DNA repair complexes can be detected. Therefore, this dataset does not include DSBs that are being actively repaired. 53BP1 or yH2AX ChIP-seq analysis could be potentially used as an alternative approach for the detection of genomic regions susceptible to DNA damage.

I translated the findings from *in vitro* and *in vivo* models into the clinical setting by expanding previously analysed lymphoma cohorts (CLL & FL). Contrary to the functional studies, IHC analysis revealed increased γH2AX staining in Lamin B1 high-expressing cohort. In clinical samples, numerous factors that influence the extent of endogenous DNA damage should be considered, including DDR mutational status, replication stress, and the complexity of tumour environment, which are all known drivers of genomic instability[120,302]. Due to a small size of the DLBCL cohort and limited survival data, the assessment of Lamin B1 protein expression in DLBCL patients did not reveal any significant findings. Therefore, I implemented a complementary analytical approach involving a comprehensive assessment of the publicly available gene expression dataset of 485 DLBCL patients. Interestingly, GCB DLBCL patients diagnosed at a later clinical stage showed decreased *LMNB1* expression, while no changes were observed ABC subtype. Prognostic evaluation of *LMNB1* mRNA expression revealed significant differences in progression-free survival (PFS) in DLBCL patients, more strikingly in GCB subtype. To elucidate the pathways that may be contributing to poor clinical outcome, I performed single-sample Gene Set Enrichment Analysis (ssGSEA) in low and high *LMNB1*-expressing GCB DLBCL patients. The ssGSEA revealed a positive correlation between *LMNB1* and hallmark pathways, including "MYC Targets", "Mitotic Spindle", "mTOR Signalling". Opposingly, a negative correlation was seen between *LMNB1* and genes associated with "Oxidative Phosphorylation", which is often reprogrammed in cancer cells and associated with a distinct metabolic signature in a subset of DLBCL[303,304]. The analysis of GO CC term revealed "ribosomal biogenesis" and "nuclear periphery" pathways were highly correlated with *LMNB1* expression in the DLBCL cohort, which agrees with RNA-seq analysis in BL2 shLMNB1 cells. Ribosome biogenesis is an important cellular process for the generation of subcellular structures involved in protein translation in order to meet the needs of hyperproliferative malignant cells[272]. Interestingly, previous studies demonstrated that Lamin B1 maintains the functional plasticity of the nucleolus, which is a major site of ribosome biogenesis[285–287]. Therefore, this data further emphasises the link between Lamin B1 removal and structural reorganization, and regulation of gene expression. Within this context, Lamin B1 has been previously linked to modulated gene expression involved in DNA damage response[176,182,284]. The GSEA revealed a significant positive enrichment of DDR-associated gene sets in *LMNB1*-high expressing patients, which is in agreement with recently published pan-cancer dataset analysis[256]. In *LMNB1*-low expressing patients, a decreased expression of DDR genes may lead to increased genomic instability due to the inability to repair genomic lesions. Most DDR signalling cascade occurs at the post-translational level. Therefore, the phosphoproteomic approach or IHC analysis of the main DNA repair markers would provide more accurate insight into the DNA damage response in DLBCL patients. These results demonstrate that Lamin B1 is not expressed at steady levels in DLBCL patients. Incorporation of WXS or WGS datasets would be a useful approach to correlate *LMNB1* expression and the mutational burden in individual patients. Genetic aberration within individual patients DLBCL would provide a direct link between the mutational load and Lamin B1.

Data presented in this study show that a sufficient level of Lamin B1 in the nucleus is required for the maintenance of genomic stability in normal and malignant B cells and that Lamin B1 expression is associated with adverse clinical outcome in DLBCL patients, which potentially implicates Lamin B1 acts as a tumour suppressor in the context of B cell biology. The impact of *LMNB1* deletion on lymphomagenesis needs to be assessed using established lymphoma mouse models. Our data suggests other APOBEC family members might play a crucial role in mediating genomic instability. Future studies would be required to determine which specific APOBEC deaminase drives mutagenesis and whether this mutagenesis is signified in Lamin B1 depleted nuclei. Whether Lamin B1 removal permits mutagenesis and incidence of DSBs in regard to open and accessible chromatin is still to be elucidated. ATAC-seq or Hi-C sequencing would be adequate methods to assess chromatin accessibility and three-dimensional spatial chromatin organisation, respectively.

9.2 Proposed experiments and directions

Based on the findings presented in this study, several questions remain to be answered. Below listed proposals could further elucidate the impact of decreased Lamin B1 expression in B cells.

Experimental directions to be addressed regarding data in Chapter 3:

1. Study the effect of NHEJ inhibition on DNA damage upon Lamin B1 depletion
2. Assessment of DNA damage in BL2 AID-/- shLMNB1 cell lines.
3. Evaluate the effect of Lamin B1 knockout on B cell proliferation and viability.
4. Measure DNA damage after overexpressing Lamin B1 in BL2 cells.
5. Generation of NHEJ reporter cell lines to monitor DDR response in a time-dependent manner.

Experimental proposals to be addressed regarding data in Chapter 4:

1. Performing a colocalisation analysis of 53BP1 and Lamin B1 at the nanoscale level.

2. Three-dimensional analysis of nuclear lamina, chromatin compaction, and γH2AX localisation by SMLM.

Experimental proposals s to be addressed regarding data in Chapter 5:

1. To address whether Lamin B1 has a protective role in lymphomagenesis by generating B cell lymphoma Lamin B1 knockout model.
2. Assess the spontaneous occurrence of lymphoma genesis upon prolonged Lamin B1 knockout model
3. Measure the engrafting potential of BL2 shLMNB1 in irradiated mice?

Experimental proposals and questions to be addressed regarding data in Chapter 6:

1. Phosphoproteomic analysis in BL2 shLMNB1 cell to understand changes in phosphorylation of DNA repair pathways in response to DNA damage
2. Validation of RNA-seq hits (*AHNAK*, *HECW2*, *miR196a2*) and further investigation of their role in genomic instability and proliferation.

Experimental proposals and questions to be addressed regarding data in Chapter 7:

1. Expanding of TMAs from nHL patients and assessing the expression of DNA damage response genes (*BRCA1*, *RAD51*, *TP53*, *TP53BP1*)
2. Analysing the mutational burden in Lamin B1 low and high DLBCL patients

Experimental proposals and questions to be addressed regarding data in Chapter 8:

1. Single-cell ATAC-sequencing analysis to map the chromatin accessibility in Lamin B1 depleted cells and within the DSB hotspots
2. ChIP-seq correlation analysis of Lamin B1 in BL2 and mouse splenic GC B cells.

9.3 Final Remarks

Findings in this study provide additional evidence of Lamin B1's role in maintaining genomic stability in GC B cells and malignant counterparts (Chapters 3 & 5). These findings revealed that the removal of Lamin B1 from the nuclear periphery induces DNA DSBs, the most severe form of genetic lesions, in B cell lymphoma cells (Chapter 3). Artificial Lamin B1 downregulation led to increased proliferative capacity without activating the cell cycle checkpoint mechanisms. The generated Lamin B1 knockdown *in vitro* model has proven to be a reliable and versatile tool for studying the effect of differential Lamin B1 expression. RNA-sequencing analysis revealed pathways dysregulated by Lamin B1 removal in BL2 cells (Chapter 6), which was supplemented by the genome-wide analysis of DSBs in human and mouse B cells (Chapter 8).

Lamin B1 has been previously proposed as a biomarker in several malignancies, including CLL. Considering the need for more precise biomarkers in B cell-derived lymphomas, I translated the findings from the functional studies into the clinical setting (Chapter 7). The complementary approach of utilising Lamin B1 protein and RNA expression revealed that Lamin B1 has a prognostic value in DLBCL. Additional experiments are needed to decipher the precise mechanisms of Lamin B1-mediated genomic instability in B cells. Findings in this study signify the distinct role of Lamin B1 in B cell biology and B cell-derived lymphomas.

Chapter 10: Appendix

10.1 Appendix Chapter 3

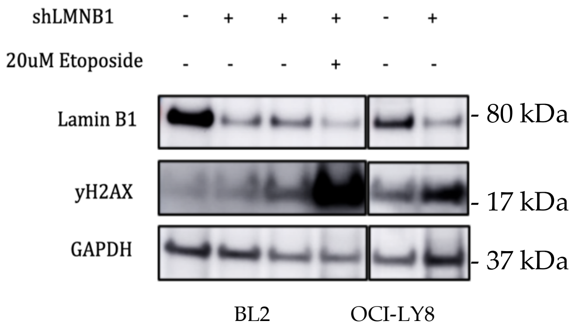

Figure 10.1.1 Lamin B1 protein expression negatively correlates with γH2AX. Western blot analysis of protein lysates extracted from control BL2 and OCI-LY8 cells and cells transduced with shLMNB1. Etoposide treated cells were used as a positive control DSBs. GAPDH was used as a loading control.

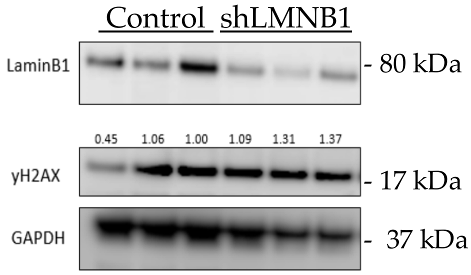

Figure 10.1.2 Western blot analysis shows Lamin B1 knockdown is associated with increased yH2AX expression. GAPDH was used as a loading control.

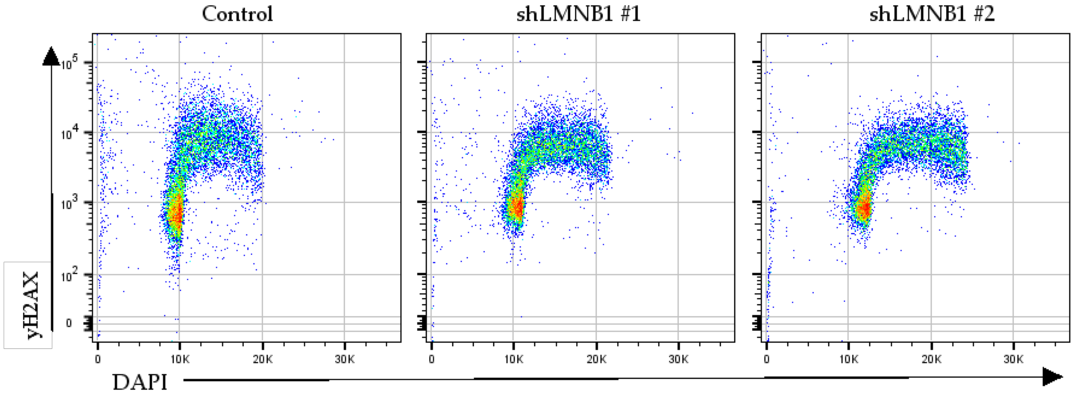

Figure 10.1.3 Analysis of yH2AX expression and DNA content in BL2 cells.

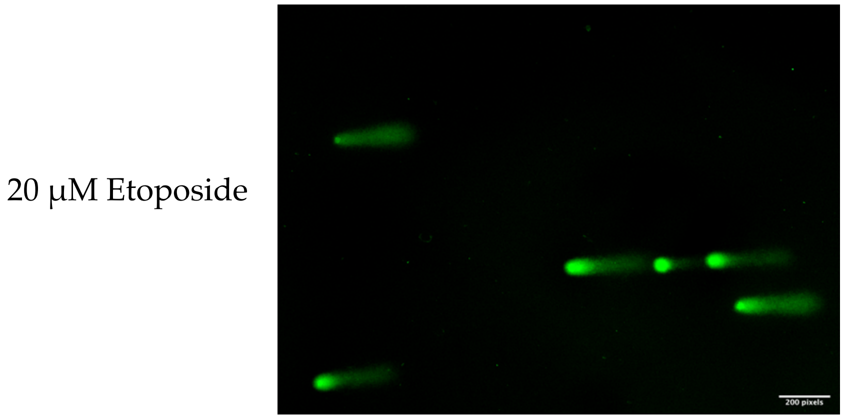

Figure 10.1.4 Representative COMET image of BL2 cells treated with 20 µM Etoposide for 3 hours.

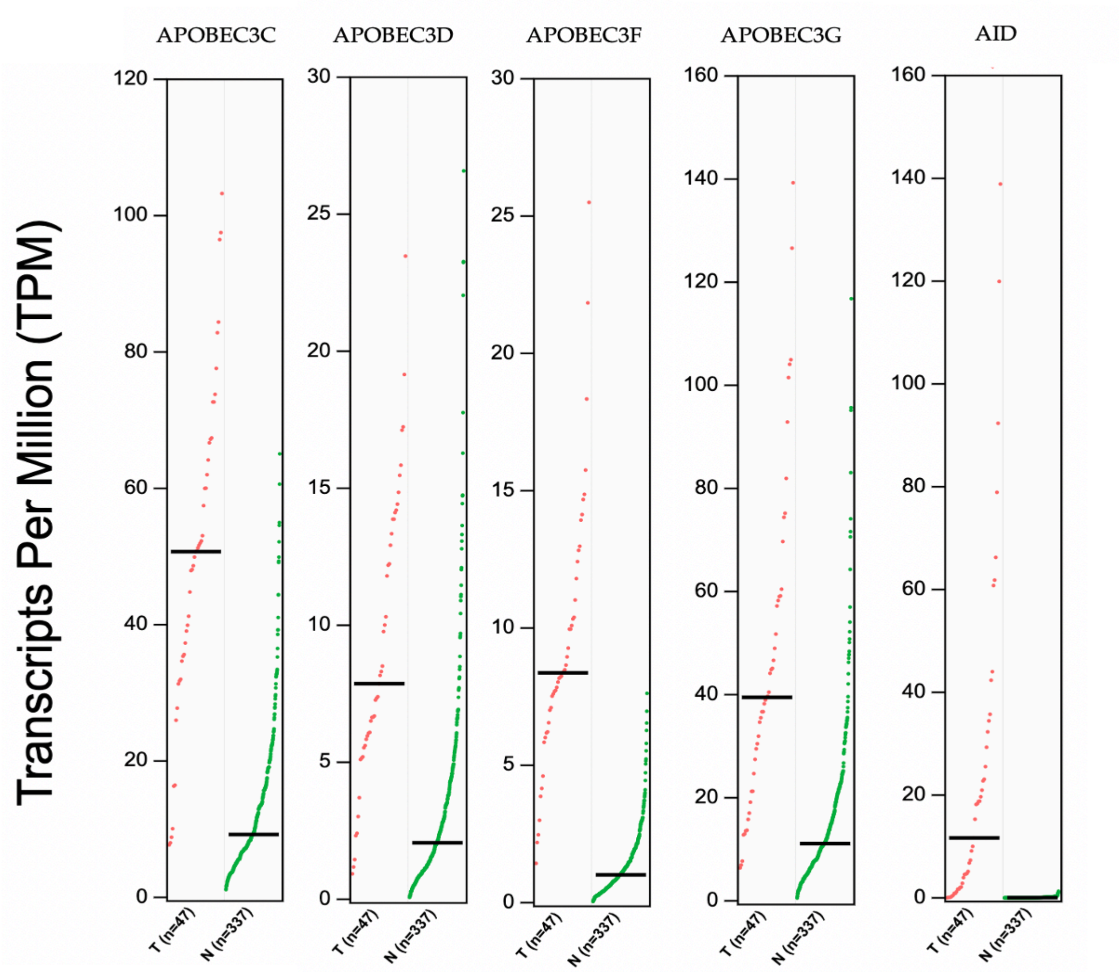

Figure 10.1.5 APOBEC3 expression is upregulated in DLBCL patients compared to healthy donors. Comparison analysis of APOBEC3 genes and AID expression (TPM) in DLBCL patients and healthy donor tissues from GEPIA2 database. T = Tumour; N = Normal.

10.2 Appendix Chapter 4

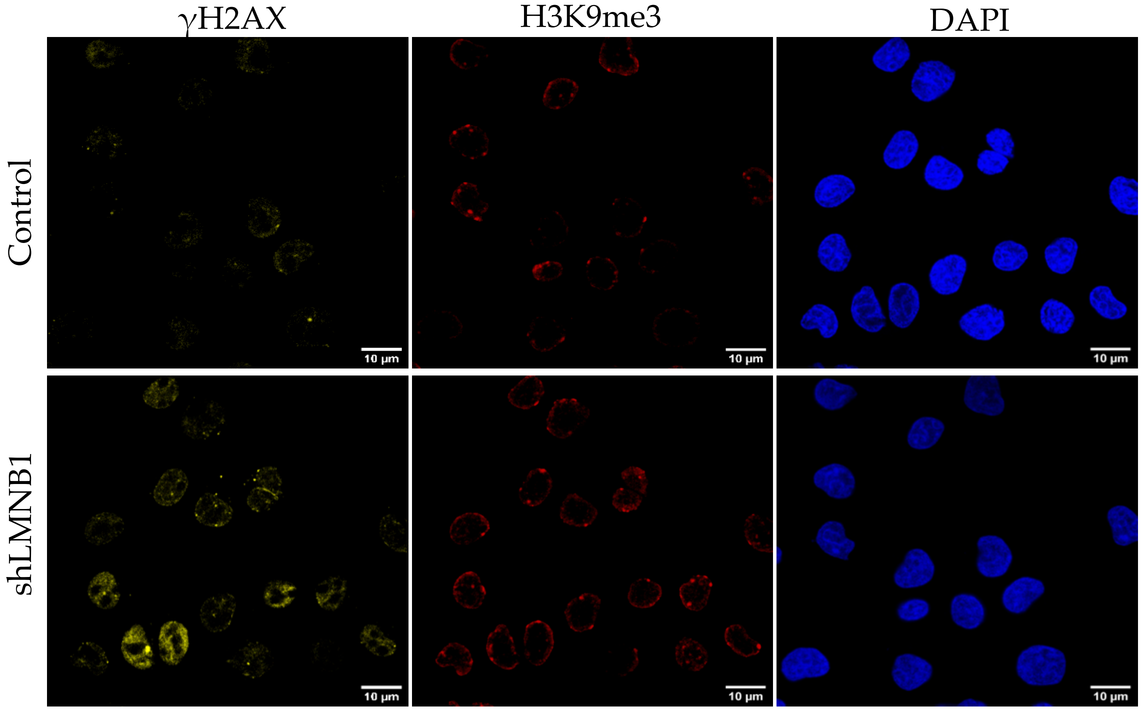

Figure 10.2.1 Confocal microscopy of γH2AX (Alexa647) and H3K9me3 (Alexa594) in control and shLMNB1 treated BL2 cells.

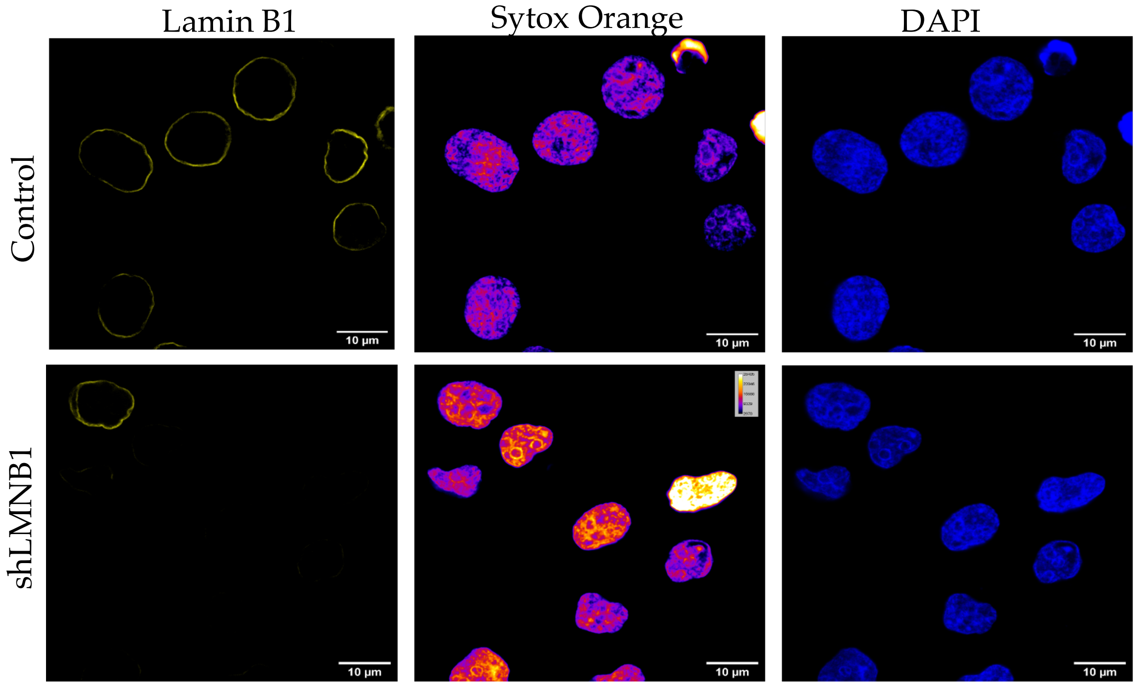

Figure 10.2.2 Confocal microscopy of Sytox Orange and Lamin B1 (Alexa 647) in control and shLMNB1 treated BL2 cells.

10.3 Appendix Chapter 5

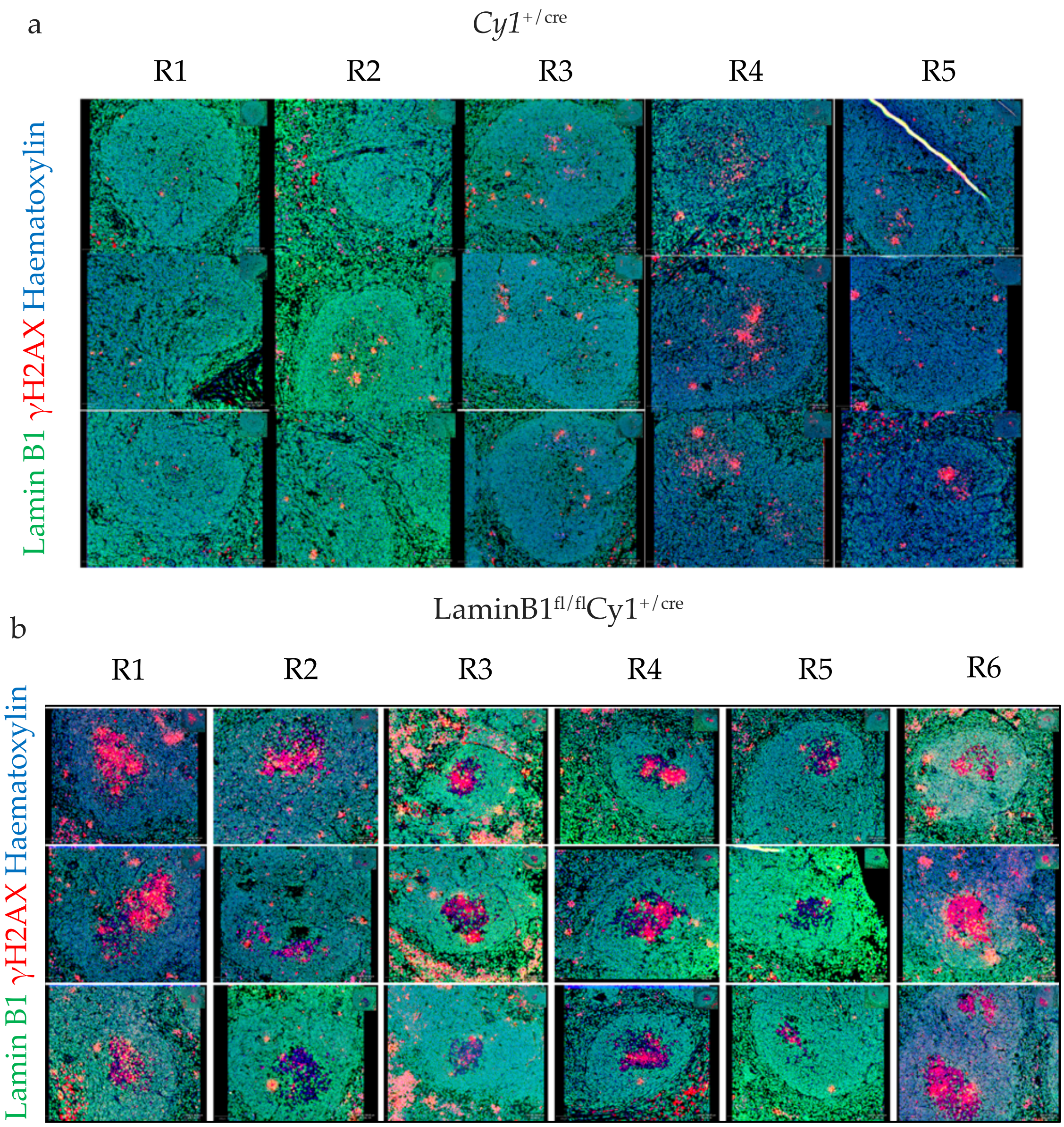

Figure 10.3.1 Multiplex analysis of γH2AX and Lamin B1 in mouse spleens. Minimum of 3 randomly selected GCs were analysed per individual mouse spleen ($C\gamma1^{+/cre}$ N=5, *LaminB1*$^{fl/fl}$*C*γ*1*$^{+/cre}$ N=6. Representative images of GCs from **(a)** $C\gamma1^{+/cre}$ and **(b)** *LaminB1*$^{fl/fl}$*C*γ*1*$^{+/cre}$ spleens used for analysis in Figure 5.3.1.2 showing Lamin B1, γH2AX, and haematoxylin staining.

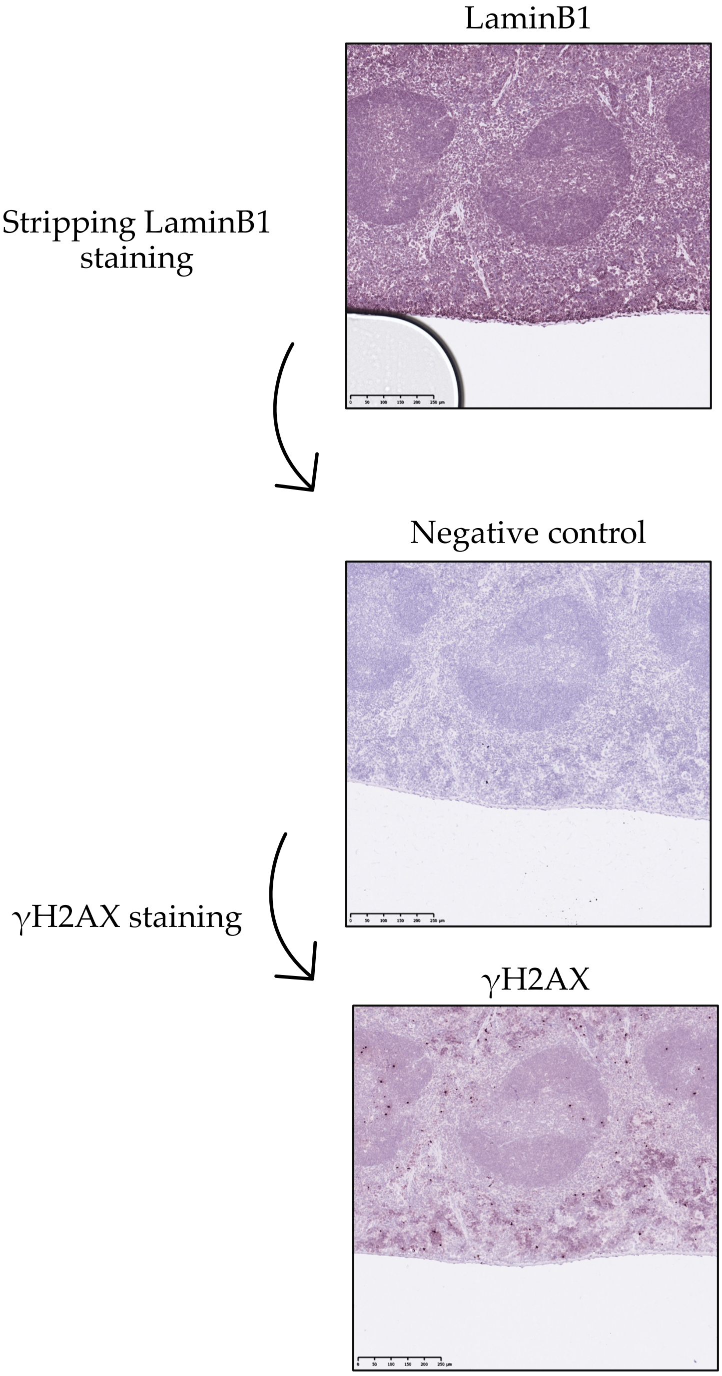

Figure 10.3.2 Stripping of VIP staining from tissue by antigen retrieval step. Example of a sequential staining after stripping Lamin B1 staining. Negative control slide was stained using the same protocol without the addition of primary antibody incubation.

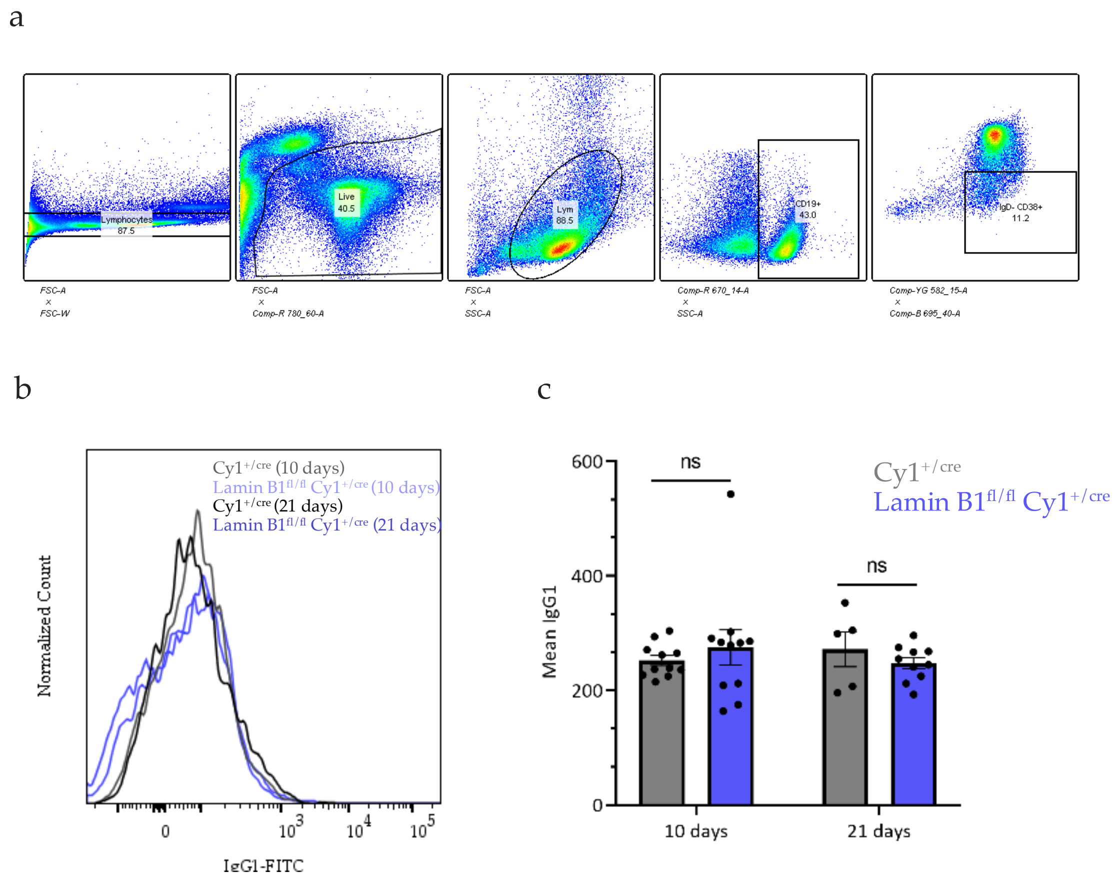

Figure 10.3.3 Flow cytometry analysis of class-switched Memory B cells upon Lamin B1 deletion in mouse GC B cells. **(a-b)** Representative flow cytometry charts showing gating strategy of class-switched Memory B cell population (CD19^{+}, IgD^{-}, CD38^{+}) in mice 10 days and 21 days post-immunisation with NP-CGG. **(b)** Representative histograms of IgG1 channel in $C\gamma 1^{+/\mathrm{cre}}$ and $LaminB1^{\mathrm{fl/fl}}$ $C\gamma 1^{+/\mathrm{cre}}$ mice on day 10 and day 21 **(c)** Bar charts showing mean IgG1 intensity within CD19^{+}, IgD^{-}, CD38^{+} cell populations obtained from splenocytes from $C\gamma 1^{+/\mathrm{cre}}$ and $C\gamma 1^{+/\mathrm{cre}}/LaminB1^{\mathrm{fl/fl}}$. Circles represent individual mice; error bars indicate SEM. Test comparisons shown are versus $C\gamma 1^{+/cre}$ mice, ns, not significant. All data are representative of at least two independent immunization experiments.

10.4 Appendix Chapter 6

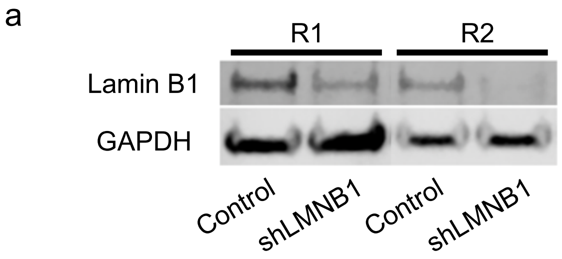

b

Sample	Total reads	# of read after trimming	% of reads after trimming	% of Paired READS	HISAT alignment %	# aligned 1 time	% aligned 1 time
Control R1	94513905	94329882	99.81%	84.7%	95.45%	80260097	85.08%
Control R2	88003179	87845998	99.82%	85.3%	95.62%	74538277	84.85%
shLMNB1 R1	129860748	129595784	99.80%	83.4%	94.82%	111320792	85.90%
shLMNB1 R2	130979998	130764895	99.84%	84.0%	94.96%	112137445	85.76%

Figure 10.4.1 RNA-seq analysis upon Lamin B1 silencing in BL2 cells. **(a)** Western blot confirmation of Lamin B1 knock-down in BL2 cells used for RNA-seq analysis. GAPDH was used as an internal loading control **(b)** RNA-seq read counts table from two independent experiments showing the proportion of reads after adaptor trimming and alignment to hg19.

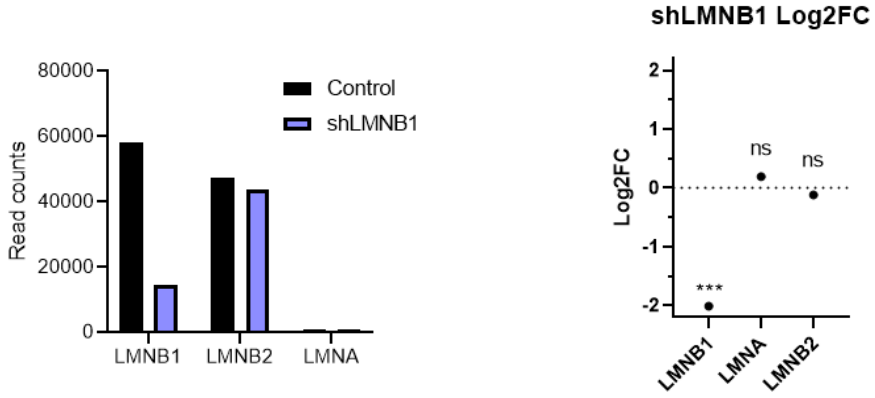

Figure 10.4.2 Assessing expression of nuclear lamins by RNA-seq. **(a)** Raw read counts of nuclear lamins upon Lamin B1 specific knockdown from two independent replicates. **(b)** Log2 fold change expression of nuclear lamins confirms a significant downregulation of Lamin B1. Lamin B2 and Lamin AC remained unchanged. Expression data normalised and converted to CPM+1 and transformed into Log2 values. Box plots show quantification of LMNB1 expression as Log2(CPM+1). Unpaired t-test was used for statistical analysis. ***$P \leq 0.001$; ns, not significant.

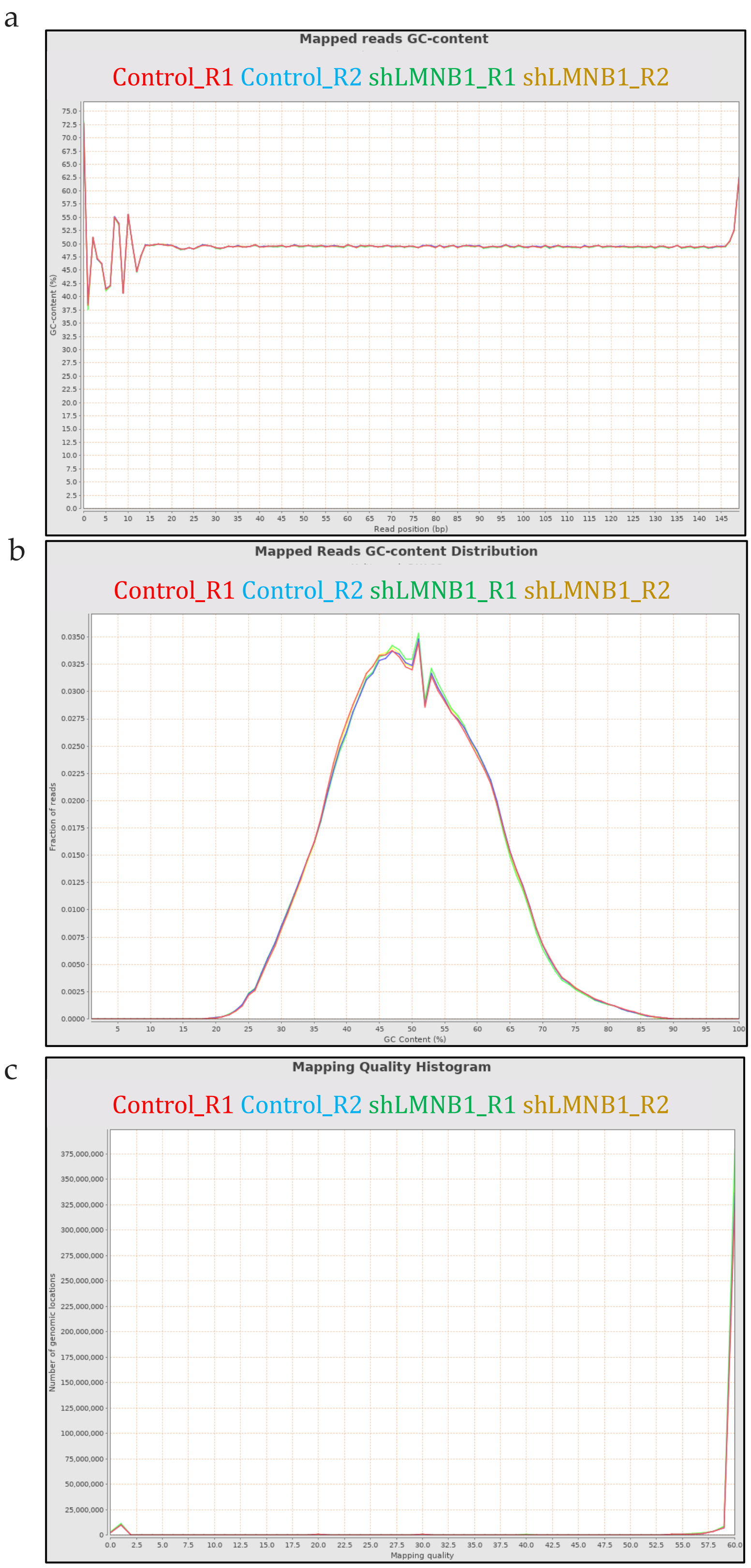

Figure 10.4.3 BAM-QC analysis of aligned reads from RNA-seq. QualiMap Multi BAM QC analysis of **(a)** mapped reads GC content across read position quality **(b)** GC content distribution and **(c)** mapping quality histogram showing number of genomic regions associated with quality score of mapped reads. Most of the reads have high mapping quality of 60.

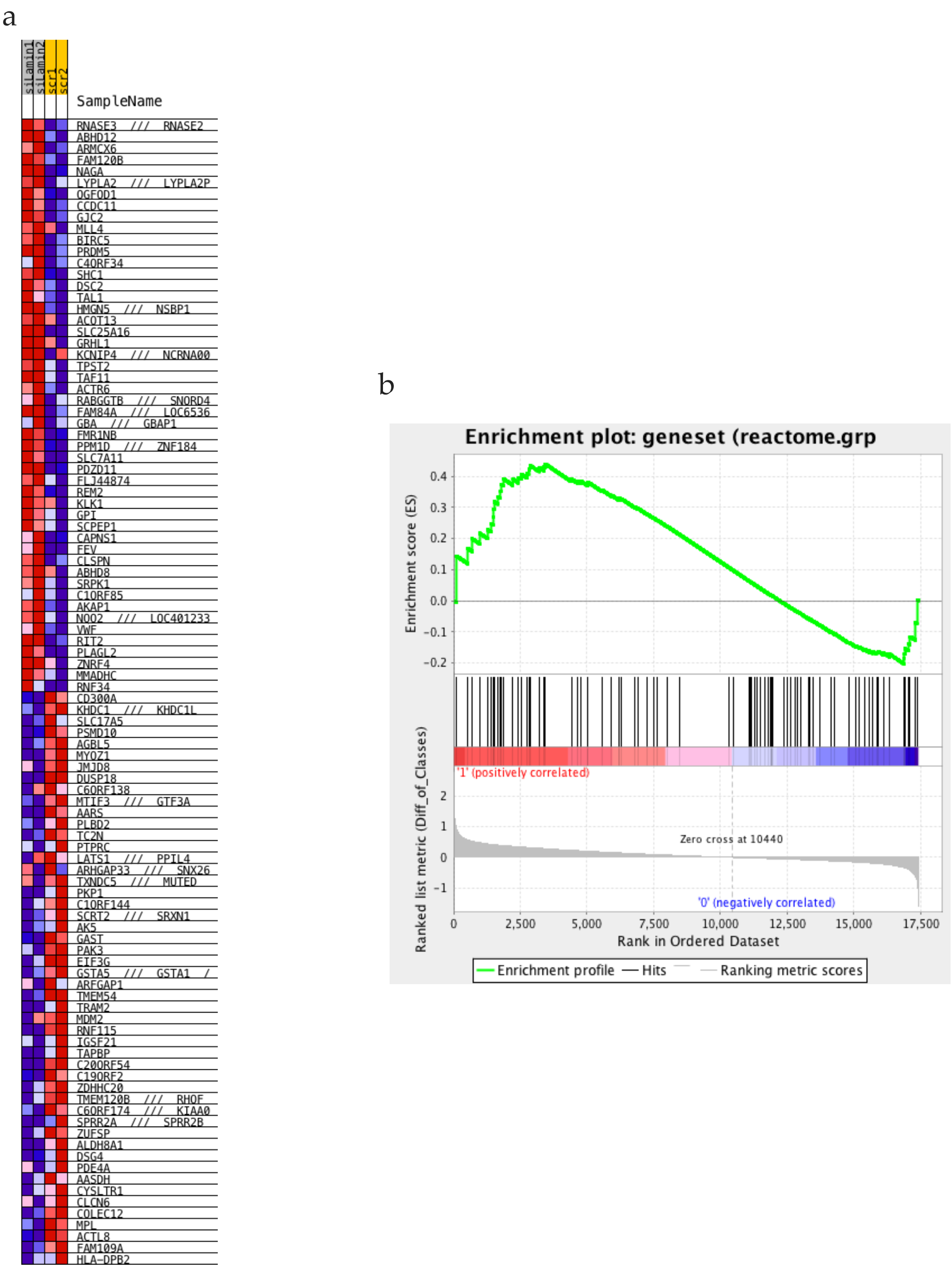

Figure 10.4.4 DNA damage and repair analysis in siLMNB1 BL2 cells. **(a)** Heatmap showing expression of genes in DNA repair gene set from two independent replicates in BL2 cells treated with siLMNB1 or scrambled sequence[131]. **(b)** Gene set enrichment analysis was performed on 'C7: DNA repair gene set (Reactome:HSA-73894) signature gene sets compiled at the Molecular Signatures Database, Broad Institute. BL2 cells were analysed for mRNA expression using the Affymetrix Gene Chip Human Exon 1.0 ST Array (Affymetrix, Santa Clara, CA, USA). Processed gene expression data were obtained from Gene Expression Omnibus (GEO) with (accession number GSE98529).

10.5 Appendix Chapter 7

Clinical feature	Parameters	n
Gender	Male Female NA	32 17 1
Median Age		60 (19-86)
COO classification	ABC nonABC	17 32
Ann Arbor Stage	1 2 3 4 NA	11 10 13 12 4
Median OS		62 months n=36
Median Lamin B1 H-score		190.15 (97.18-267.93) n=50

Table 10.5.1 Description of clinicopathological features of DLBCL patients analysed by IHC. Tumour biopsies were obtained from the Tissue Bank at Barts Cancer Institute.

Clinical feature	Parameters	n
Gender	Male Female	289 201
Median Age		63 (14-92)
COO classification	ABC GCB Unclassified	248 140 101
Ann Arbor Stage	0 1 2 3 4 NA 1.5 2.5	1 59 122 115 131 58 1 1
Median PFS		3.625 years n=235
LMNB1 expression (Log2 CPM)		7.09 (3.52-8.79) n=481
IPI Group (International Prognostic Index)	Low Intermediate High NA	104 187 72 125

Table 10.5.2 Description of clinicopathological features of DLBCL patients. Dataset was obtained from TCGA and Schmitz et al.

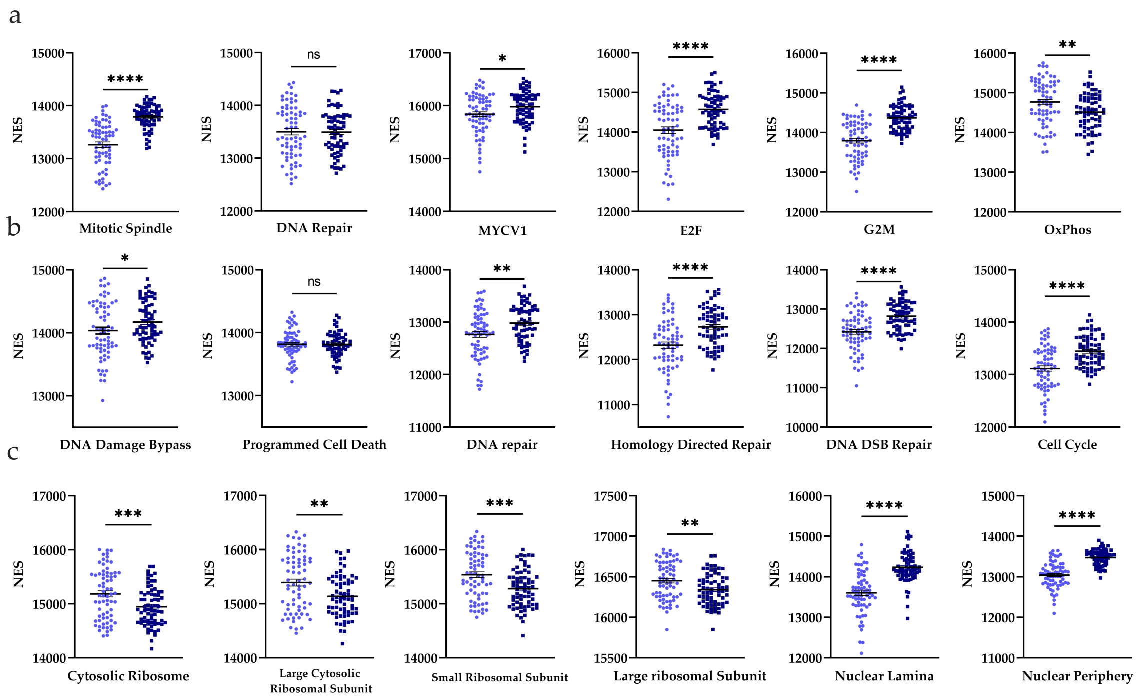

Figure 10.5 GSEA of significantly enriched pat in LMNB1-high and LMNB1-low expressing GCB DLBCL patients. **(a-c)** GSEA dotplots of enrichment scores for gene sets related to **(a)** Hallmark **(b)** Reactome associated DNA damage pathways and **(c)** Gene Ontology Cellular Components. N=138. Unpaired t-test was used for the statistical analysis. *$P \leq 0.05$, **$P \leq 0.01$,***$P \leq 0.001$; ns, not significant. Normalized enrichment score was obtained by single sample GSEA analysis in Gene Pattern. Lamin B1-high (dark blue) and Lamin B1-low (light blue) DLBCL patients are shown.

10.6 Appendix Chapter 8

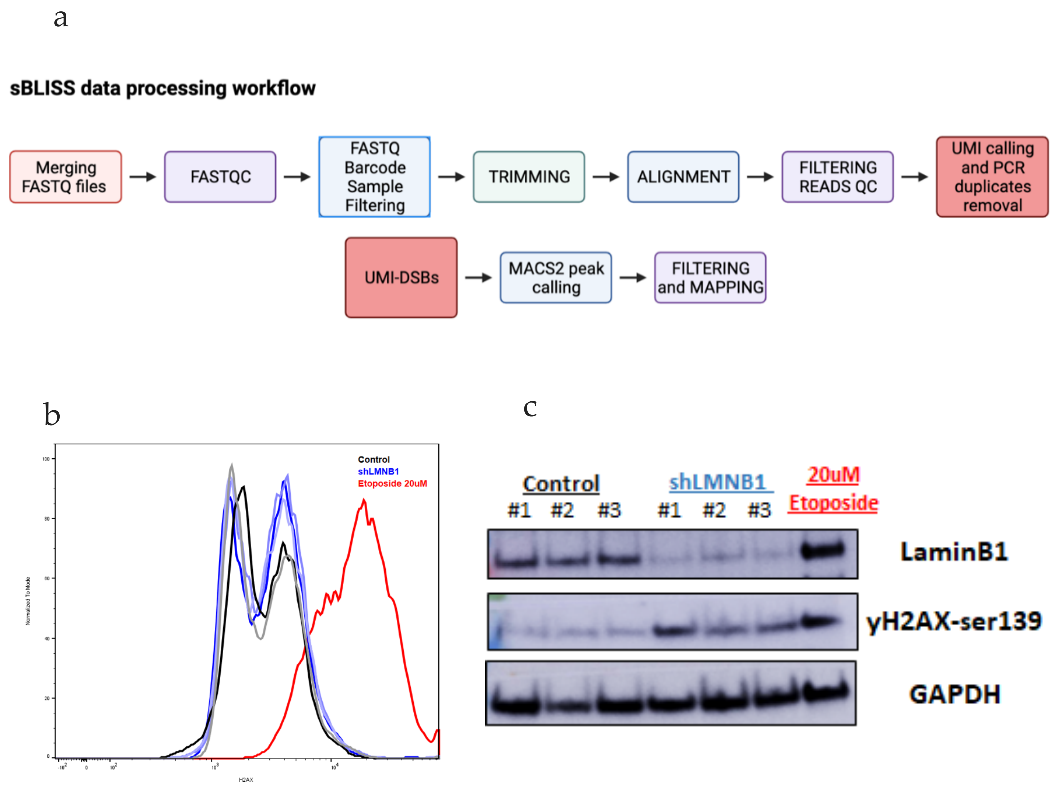

Figure 10.6.1 Validation of Lamin B1 knockdown in BL2 cells used for sBLISS analysis. **(a)** Description of sBLISS analysis pipeline. Analysis was carried out using Python and R Studio **(b)** Flow cytometry chart showing cells stained with anti-γH2AX antibody **(c)** Western blot analysis of protein levels of Lamin B1 and γH2AX upon Lamin B1 knockdown or Etoposide treatment. GAPDH was used as a loading control.

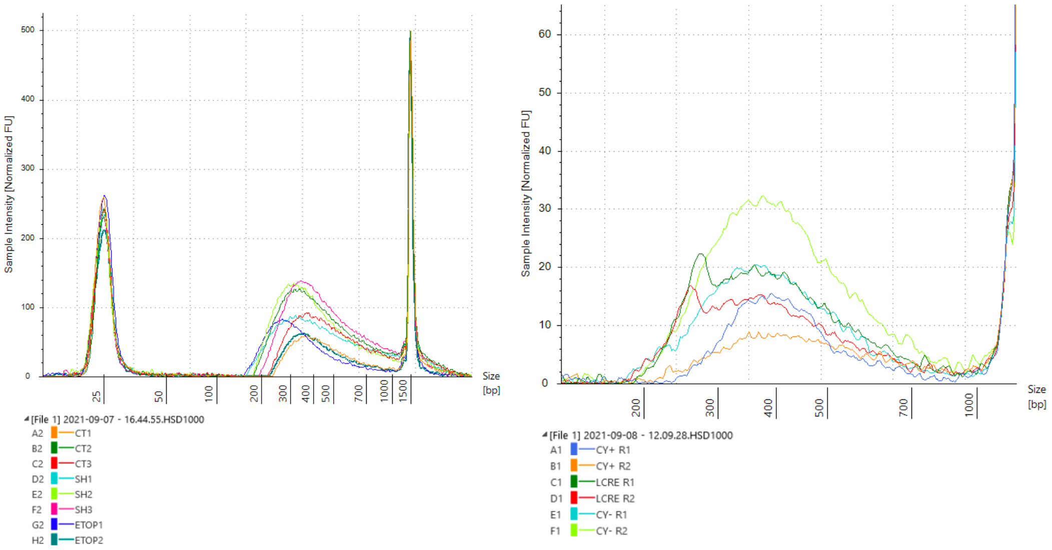

Figure 10.6.2 DNA Tapestation profiles after sBLISS template purification and sonication of BL2 samples and mouse samples. Templates were diluted to <10 ng/µL before loading onto the Bioanalyzer chip. Profiles were generated after one round of double-sided bead purification and showed the main peak between 200bp and 800bp. CT=control, SH=shLMNB1, ETOP=Etoposide, CY+=Cγ1-Cre, LCRE=LaminB1$^{fl/fl}$ Cγ1-Cre, CY= naïve B cells

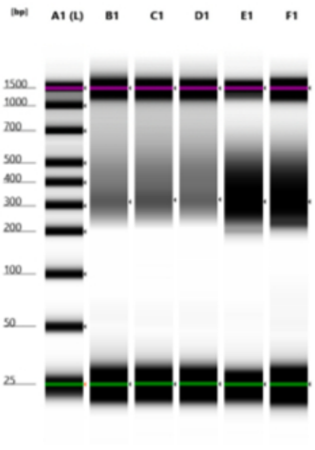

Default image (Contrast 100%), Image is Scaled to Sample

Sample Info

Well	Conc. [ng/µl]	Sample Description	Alert	Observations
A1	23.0	Ladder		Ladder
B1	0.550	BL2-1		
C1	0.626	BL2-2		
D1	0.472	BL2-3		
E1	6.08	M1		
F1	2.10	M2		

Figure 10.6.3 DNA profiles after library generation and purification. Templates were diluted to < 10 ng/µL before loading onto the Bioanalyzer chip. Profiles were generated after one round of double-sided bead purification and show a main peak between 200 bp and 800 bp.

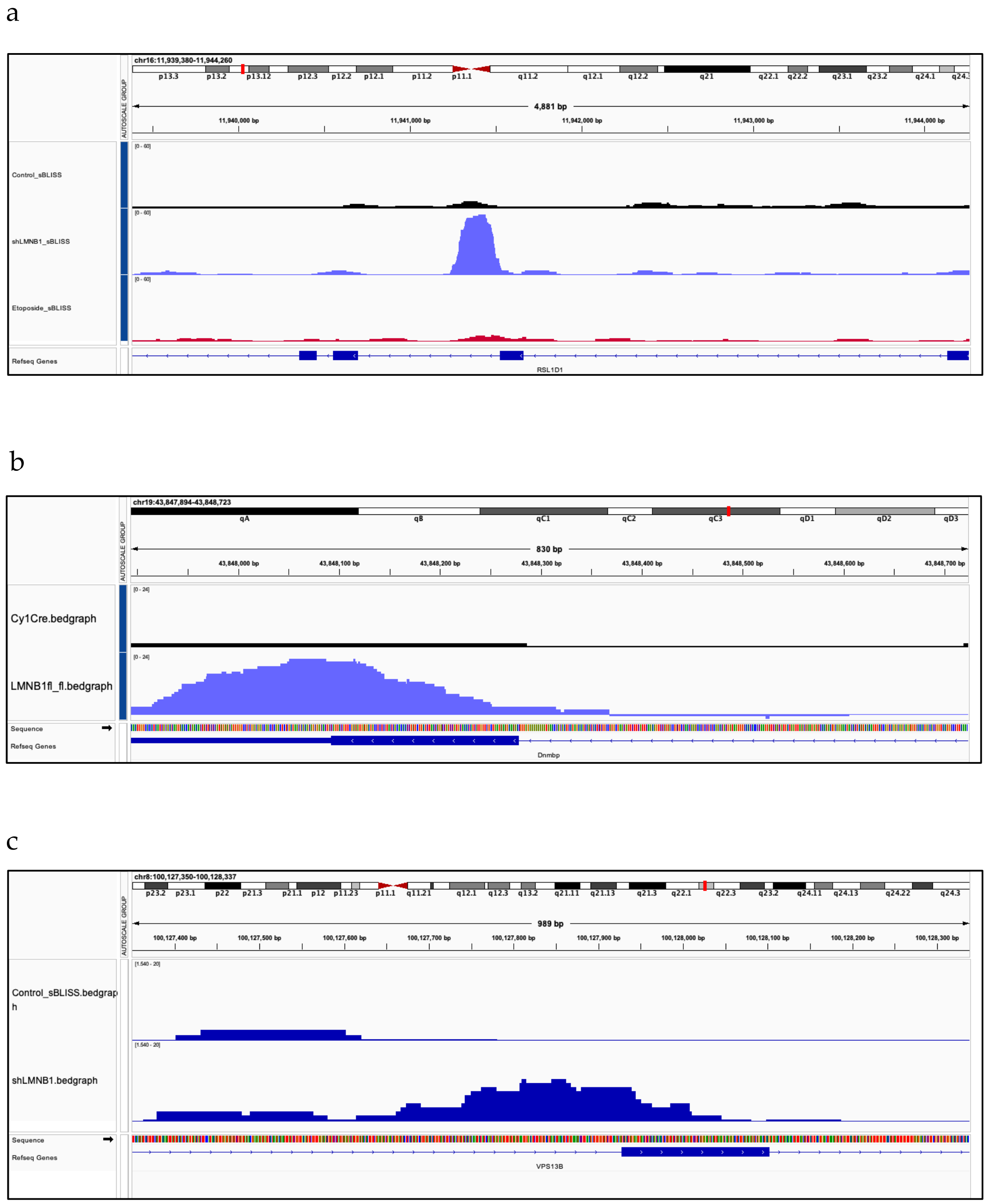

Figure 10.6.4 Visualization of sBLISS peaks in the genome browser. **(a-b)** MAC2 called peaks (DSB hotspots) in Lamin B1 depleted **(a)** BL2 cells and **(b)** mouse GC B cells. **(c)** Comparison of DSB hotspot in shLMNB1 BL2 samples and frequently mutated DLBCL gene (*VPS13*).

ENSG00000075624	ACTB
ENSG00000117713	ARID1A
ENSG00000149311	ATM
ENSG00000166710	B2M
ENSG00000142867	BCL10
ENSG00000119866	BCL11A
ENSG00000171791	BCL2
ENSG00000113916	BCL6
ENSG00000110987	BCL7A
ENSG00000183337	BCOR
ENSG00000186716	BCR
ENSG00000115760	BIRC6
ENSG00000157764	BRAF
ENSG00000133639	BTG1
ENSG00000159388	BTG2
ENSG00000010671	BTK
ENSG00000198286	CARD11
ENSG00000064012	CASP8
ENSG00000112576	CCND3
ENSG00000120217	CD274
ENSG00000135218	CD36
ENSG00000116815	CD58
ENSG00000125726	CD70
ENSG00000007312	CD79B
ENSG00000112149	CD83
ENSG00000147889	CDKN2A
ENSG00000179583	CIITA
ENSG00000005339	CREBBP
ENSG00000121966	CXCR4
ENSG00000071626	DAZAP1
ENSG00000215301	DDX3X
ENSG00000135144	DTX1
ENSG00000158050	DUSP2
ENSG00000164330	EBF1
ENSG00000100393	EP300
ENSG00000134954	ETS1
ENSG00000139083	ETV6
ENSG00000106462	EZH2
ENSG00000026103	FAS
ENSG00000138081	FBXO11
ENSG00000109670	FBXW7
ENSG00000054598	FOXC1
ENSG00000150907	FOXO1
ENSG00000120063	GNA13
ENSG00000114353	GNAI2
ENSG00000137106	GRHPR
ENSG00000184357	HIST1H1B
ENSG00000187837	HIST1H1C
ENSG00000124575	HIST1H1D
ENSG00000168298	HIST1H1E
ENSG00000180573	HIST1H2AC
ENSG00000233224	HIST1H2AM
ENSG00000180596	HIST1H2BC
ENSG00000197903	HIST1H2BK
ENSG00000124693	HIST1H3B
ENSG00000184678	HIST2H2BE
ENSG00000206503	HLA-A
ENSG00000234745	HLA-B
ENSG00000204525	HLA-C
ENSG00000204257	HLA-DMA
ENSG00000242574	HLA-DMB
ENSG00000138668	HNRNPD
ENSG00000169045	HNRNPH1
ENSG00000153187	HNRNPU
ENSG00000122986	HVCN1
ENSG00000117318	ID3
ENSG00000172349	IL16
ENSG00000077238	IL4R
ENSG00000137265	IRF4
ENSG00000140968	IRF8
ENSG00000143772	ITPKB
ENSG00000127528	KLF2
ENSG00000197705	KLHL14
ENSG00000172578	KLHL6
ENSG00000055609	KMT2C
ENSG00000167548	KMT2D
ENSG00000133703	KRAS
ENSG00000196233	LCOR
ENSG00000227507	LTB
ENSG00000254087	LYN
ENSG00000143384	MCL1
ENSG00000213999	MEF2B
ENSG00000081189	MEF2C
ENSG00000174197	MGA
ENSG00000197629	MPEG1
ENSG00000156738	MS4A1
ENSG00000198793	MTOR
ENSG00000136997	MYC
ENSG00000172936	MYD88
ENSG00000036448	MYOM2
ENSG00000196498	NCOR2
ENSG00000109320	NFKB1
ENSG00000100906	NFKBIA
ENSG00000146232	NFKBIE
ENSG00000144802	NFKBIZ
ENSG00000140853	NLRC5
ENSG00000162408	NOL9
ENSG00000148400	NOTCH1
ENSG00000134250	NOTCH2
ENSG00000144645	OSBPL10
ENSG00000182162	P2RY8
ENSG00000169564	PCBP1
ENSG00000137193	PIM1
ENSG00000102096	PIM2
ENSG00000110777	POU2AF1
ENSG00000028277	POU2F2
ENSG00000108819	PPP1R9B
ENSG00000057657	PRDM1
ENSG00000253729	PRKDC
ENSG00000171862	PTEN
ENSG00000153707	PTPRD
ENSG00000139687	RB1
ENSG00000181827	RFX7
ENSG00000133111	RFXAP
ENSG00000067560	RHOA
ENSG00000116954	RRAGC
ENSG00000267534	S1PR2
ENSG00000139718	SETD1B
ENSG00000181555	SETD2
ENSG00000115524	SF3B1
ENSG00000118515	SGK1
ENSG00000169375	SIN3A
ENSG00000127616	SMARCA4
ENSG00000185338	SOCS1
ENSG00000065526	SPEN
ENSG00000168610	STAT3
ENSG00000166888	STAT6
ENSG00000177565	TBL1XR1
ENSG00000100721	TCL1A
ENSG00000168769	TET2
ENSG00000112697	TMEM30A
ENSG00000205542	TMSB4X
ENSG00000118503	TNFAIP3
ENSG00000157873	TNFRSF14
ENSG00000198846	TOX
ENSG00000141510	TP53
ENSG00000131323	TRAF3
ENSG00000153827	TRIP12
ENSG00000196367	TRRAP
ENSG00000077721	UBE2A
ENSG00000182168	UNC5C
ENSG00000156687	UNC5D
ENSG00000187555	USP7
ENSG00000132549	VPS13B
ENSG00000166483	WEE1
ENSG00000100219	XBP1
ENSG00000082898	XPO1
ENSG00000163874	ZC3H12A
ENSG00000185650	ZFP36L1
ENSG00000188994	ZNF292
ENSG00000160683	CXCR5
ENSG00000168394	TAP1

Table 10.6.5 List of the most frequently mutated genes in DLBCL. Gene list was generated by Ryan Morin's lab and downloaded from the Github depository. Ensembl gene ids and associated gene symbols are shown.

From Figure 3.3.6.2 and 3.3.10.1

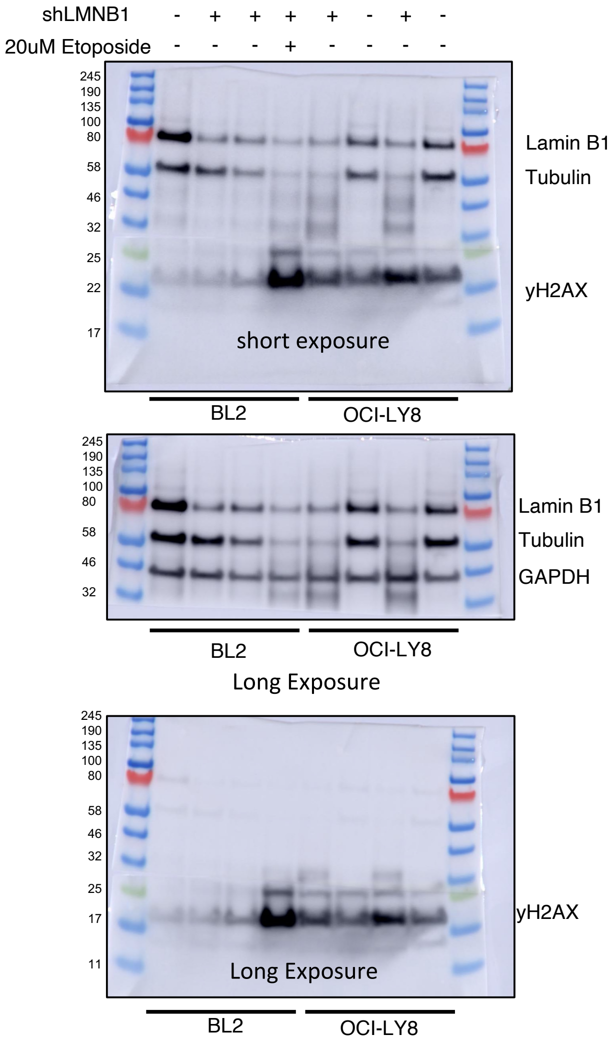

From Figure 10.4.1

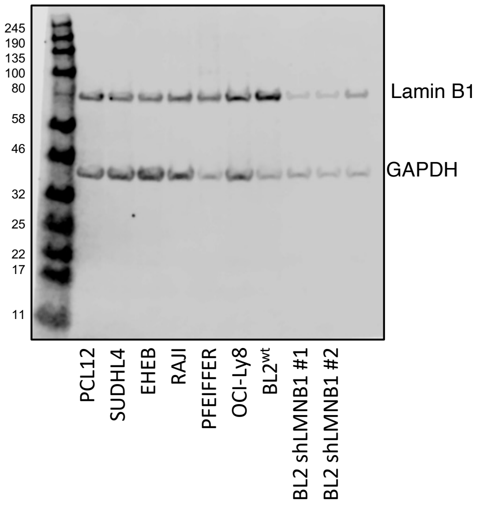

From Figure 3.3.8.2

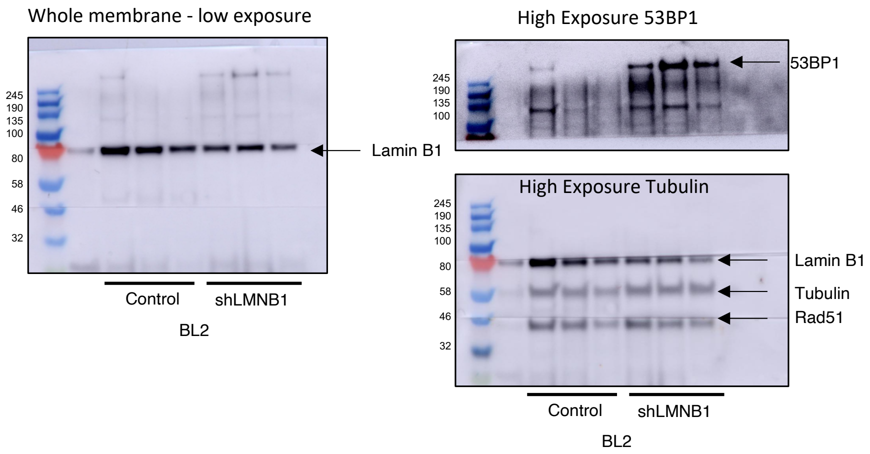

From Figure 10.4.1

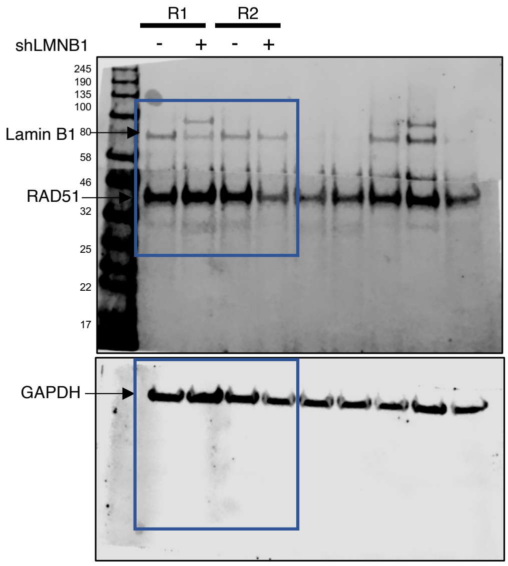

From Figure 10.6.1

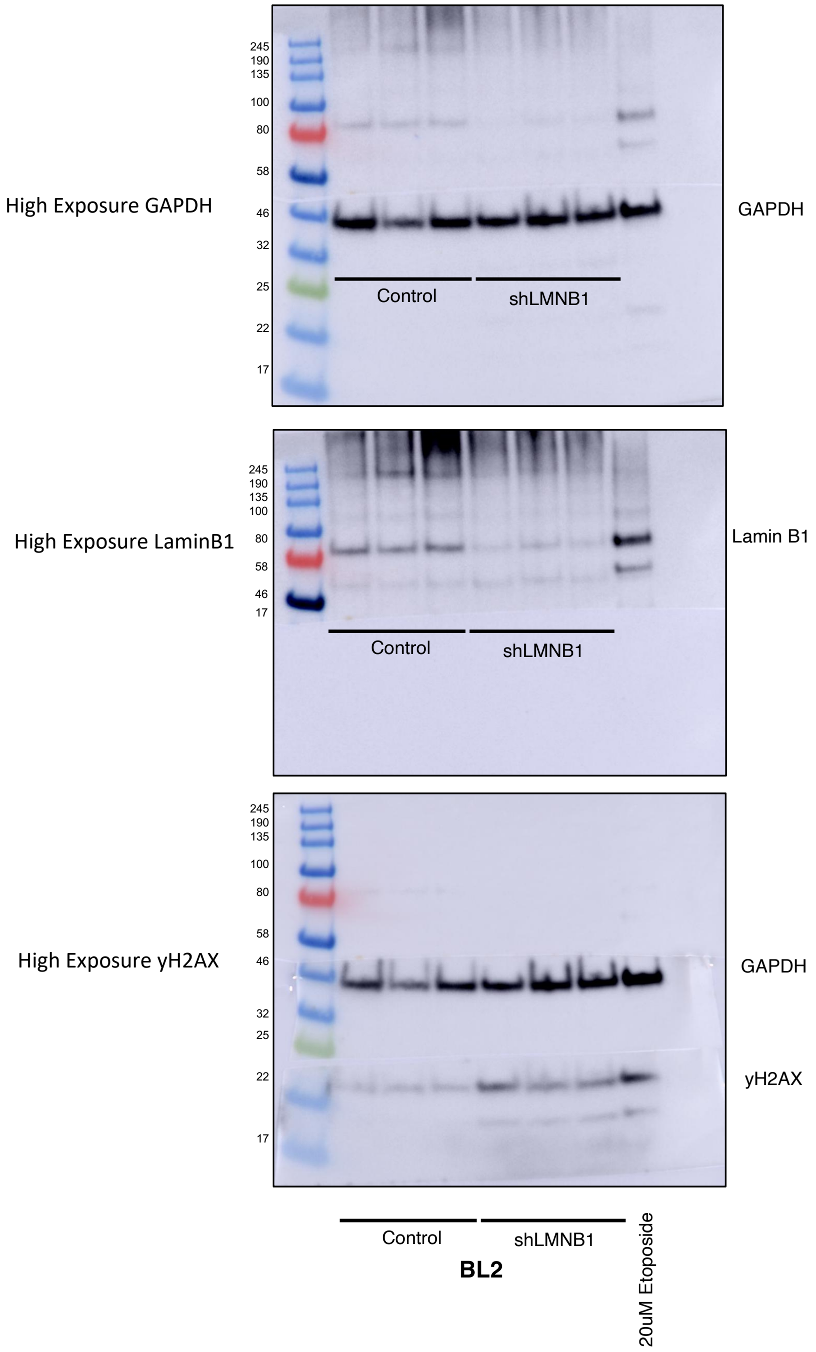

Figure 10.7 Supplementary images of uncropped western blot images.

Chapter 11: Bibliography

1. Tiselius, A. & Kabat, E. A. Electrophoresis of immune serum. *Science* **87**, 416–417 (1938).
2. Fagraeus, A. Plasma cellular reaction and its relation to the formation of antibodies in vitro [1]. *Nature* (1947) doi:10.1038/159499a0.
3. Becker, A. J., McCulloch, E. A. & Till, J. E. Cytological demonstration of the clonal nature of spleen colonies derived from transplanted mouse marrow cells. *Nature* (1963) doi:10.1038/197452a0.
4. Cooper, M. D., Peterson, R. D. A. & Good, R. A. Delineation of the thymic and bursal lymphoid systems in the chicken. *Nature* (1965) doi:10.1038/205143a0.
5. Mitchell, G. F. & Miller, J. F. Cell to cell interaction in the immune response. II. The source of hemolysin-forming cells in irradiated mice given bone marrow and thymus or thoracic duct lymphocytes. *The Journal of experimental medicine* (1968) doi:10.1084/jem.128.4.821.
6. GOOD, R. A. & ZAK, S. J. Disturbances in gamma globulin synthesis as experiments of nature. *Pediatrics* (1956).
7. Fröland, S., Natvig, J. B. & Berdal, P. Surface-bound immunoglobulin as a marker of B lymphocytes in man. *Nature New Biology* (1971) doi:10.1038/newbio234251a0.
8. Coombs, R. R., Feinstein, A. & Wilson, A. B. Immunoglobulin determinants on the surface of human lymphocytes. *Lancet* (1969) doi:10.1097/00007890-197007000-00015.
9. Raff, M. C., Megson, M., Owen, J. J. T. & Cooper, M. D. Early production of intracellular IgM by B-lymphocyte precursors in mouse. *Nature* (1976) doi:10.1038/259224a0.
10. Gathings, W. E., Lawton, A. R. & Cooper, M. D. Immunofluorescent studies of the development of pre-B cells, B lymphocytes and immunoglobulin isotype diversity in humans. *European Journal of Immunology* (1977) doi:10.1002/eji.1830071112.
11. Tyan, M. L., Cole, L. J. & Herzenberg, L. A. Fetal Liver:A Source of Immunoglobulin Producing Cells in the Mouse. *Proceedings of the Society for Experimental Biology and Medicine* (1967) doi:10.3181/00379727-124-31951.
12. Cumano, A., Furlonger, C. & Paige, C. J. Differentiation and characterization of B-cell precursors detected in the yolk sac and embryo body of embryos beginning at the 10- to 12-somite stage. *Proceedings of the*

National Academy of Sciences of the United States of America (1993) doi:10.1073/pnas.90.14.6429.

13. Schofield, R. The relationship between the spleen colony-forming cell and the haemopoietic stem cell. A hypothesis. *Blood Cells* (1978).
14. Ciriza, J., Thompson, H., Petrosian, R., Manilay, J. O. & García-Ojeda, M. E. The migration of hematopoietic progenitors from the fetal liver to the fetal bone marrow: Lessons learned and possible clinical applications. *Experimental Hematology* (2013) doi:10.1016/j.exphem.2013.01.009.
15. Kincade, P. W., Lawton, A. R., Bockman, D. E. & Cooper, M. D. Suppression of immunoglobulin G synthesis as a result of antibody-mediated suppression of immunoglobulin M synthesis in chickens. *Proceedings of the National Academy of Sciences of the United States of America* (1970) doi:10.1073/pnas.67.4.1918.
16. Jacob, J., Kelsoe, G., Rajewsky, K. & Weiss, U. Intraclonal generation of antibody mutants in germinal centres. *Nature* (1991) doi:10.1038/354389a0.
17. Kondo, M., Weissman, I. L. & Akashi, K. Identification of clonogenic common lymphoid progenitors in mouse bone marrow. *Cell* (1997) doi:10.1016/S0092-8674(00)80453-5.
18. Medina, K. L. *et al.* Assembling a gene regulatory network for specification of the B cell fate. *Developmental Cell* (2004) doi:10.1016/j.devcel.2004.08.006.
19. Adams, B. *et al.* Pax-5 encodes the transcription factor BSAP and is expressed in B lymphocytes, the developing CNS, and adult testis. *Genes and Development* (1992) doi:10.1101/gad.6.9.1589.
20. Nutt, S. L., Heavey, B., Rolink, A. G. & Busslinger, M. Commitment to the B-lymphoid lineage depends on the transcription factor Pax5. *Journal of Immunology* (2015) doi:10.1038/44076.
21. Hardy, R. R., Carmack, C. E., Shinton, S. A., Kemp, J. D. & Hayakawa, K. Resolution and characterization of pro-B and pre-pro-B cell stages in normal mouse bone marrow. *Journal of Experimental Medicine* (1991) doi:10.1084/jem.173.5.1213.
22. Schatz, D. G., Oettinger, M. A. & Baltimore, D. The V(D)J recombination activating gene, RAG-1. *Cell* (1989) doi:10.1016/0092-8674(89)90760-5.
23. Oettinger, M. A., Schatz, D. G., Gorka, C. & Baltimore, D. RAG-1 and RAG-2, adjacent genes that synergistically activate V(D)J recombination. *Science* (1990) doi:10.1126/science.2360047.

24. Tsubata, T. & Reth, M. The products of pre-B cell-specific genes (λ5 and VpreB) and the immunoglobulin μ chain form a complex that is transported onto the cell surface. *Journal of Experimental Medicine* (1990) doi:10.1084/jem.172.3.973.
25. Brack, C., Hirama, M., Lenhard-Schuller, R. & Tonegawa, S. A complete immunoglobulin gene is created by somatic recombination. *Cell* (1978) doi:10.1016/0092-8674(78)90078-8.
26. ALT, F. W., Blackwell, T. K., Depinho, R. A., Reth, M. G. & Yancopoulos, G. D. Regulation of Genome Rearrangement Events during Lymphocyte Differentiation. *Immunological Reviews* (1986) doi:10.1111/j.1600-065X.1986.tb01470.x.
27. Radbruch, A. *et al.* Competence and competition: The challenge of becoming a long-lived plasma cell. *Nature Reviews Immunology* (2006) doi:10.1038/nri1886.
28. Muramatsu, M. *et al.* Class switch recombination and hypermutation require activation-induced cytidine deaminase (AID), a potential RNA editing enzyme. *Cell* (2000) doi:10.1016/S0092-8674(00)00078-7.
29. Reynaud, C. A., Aoufouchi, S., Faili, A. & Weill, J. C. What role for AID: Mutator, or assembler of the immunoglobulin mutasome? *Nature Immunology* (2003) doi:10.1038/ni0703-631.
30. Cattoretti, G. *et al.* BCL-6 protein is expressed in germinal-center B cells. *Blood* (1995) doi:10.1182/blood.v86.1.45.bloodjournal86145.
31. Inoue, T. *et al.* The transcription factor Foxo1 controls germinal center B cell proliferation in response to T cell help. *Journal of Experimental Medicine* (2017) doi:10.1084/jem.20161263.
32. Wöhner, M. *et al.* Molecular functions of the transcription factors E2A and E2-2 in controlling germinal center B cell and plasma cell development. *Journal of Experimental Medicine* (2016) doi:10.1084/jem.20152002.
33. Klein, U. *et al.* Transcriptional analysis of the B cell germinal center reaction. *Proceedings of the National Academy of Sciences of the United States of America* (2003) doi:10.1073/pnas.0437996100.
34. Bransteitter, R., Pham, P., Calabrese, P. & Goodman, M. F. Biochemical analysis of hypermutational targeting by wild type and mutant activation-induced cytidine deaminase. *Journal of Biological Chemistry* **279**, (2004).
35. Dominguez-Sola, D. *et al.* The proto-oncogene MYC is required for

selection in the germinal center and cyclic reentry. *Nature Immunology* (2012) doi:10.1038/ni.2428.

36. Bhattacharya, D. Regulation of Ig class switch recombination by NF-kappaB: retroviral expression of RelB in activated B cells inhibits switching to IgG1, but not to IgE. *International Immunology* (2002) doi:10.1093/intimm/dxf066.
37. Roco, J. A. *et al.* Class-Switch Recombination Occurs Infrequently in Germinal Centers. *Immunity* **51**, (2019).
38. Kumar, S. *et al.* Flexible ordering of antibody class switch and V(D)J joining during B-cell ontogeny. *Genes and Development* **27**, (2013).
39. Conticello, S. G. The AID/APOBEC family of nucleic acid mutators. *Genome Biology* vol. 9 (2008).
40. Muramatsu, M. *et al.* Specific expression of activation-induced cytidine deaminase (AID), a novel member of the RNA-editing deaminase family in germinal center B cells. *Journal of Biological Chemistry* (1999) doi:10.1074/jbc.274.26.18470.
41. Ramiro, A. R. *et al.* AID is required for c-myc/IgH chromosome translocations in vivo. *Cell* **118**, (2004).
42. Dorsett, Y. *et al.* A role for AID in chromosome translocations between c-myc and the IgH variable region. *Journal of Experimental Medicine* **204**, (2007).
43. Klein, I. A. *et al.* Translocation-capture sequencing reveals the extent and nature of chromosomal rearrangements in B lymphocytes. *Cell* **147**, (2011).
44. Conticello, S. G., Thomas, C. J. F., Petersen-Mahrt, S. K. & Neuberger, M. S. Evolution of the AID/APOBEC family of polynucleotide (deoxy)cytidine deaminases. *Molecular Biology and Evolution* **22**, (2005).
45. Alexandrov, L. B. *et al.* Signatures of mutational processes in human cancer. *Nature* **500**, (2013).
46. Lada, A. G. *et al.* AID/APOBEC cytosine deaminase induces genome-wide kataegis. *Biology Direct* (2012) doi:10.1186/1745-6150-7-47.
47. Monroe, J. G. *et al.* Positive and negative selection during B lymphocyte development. *Immunologic Research* (2003) doi:10.1385/IR:27:2-3:427.
48. Norvell, A., Mandik, L. & Monroe, J. G. Engagement of the antigen-receptor on immature murine B lymphocytes results in death by apoptosis. *Journal of Immunology* (1995).

49. Sandel, P. C. & Monroe, J. G. Negative selection of immature B cells by receptor editing or deletion is determined by site of antigen encounter. *Immunity* (1999) doi:10.1016/S1074-7613(00)80029-1.
50. Cyster, J. G. & Goodnow, C. C. Antigen-induced exclusion from follicles and anergy are separate and complementary processes that influence peripheral B cell fate. *Immunity* (1995) doi:10.1016/1074-7613(95)90059-4.
51. Victora, G. D. *et al.* Identification of human germinal center light and dark zone cells and their relationship to human B-cell lymphomas. *Blood* (2012) doi:10.1182/blood-2012-03-415380.
52. Smith, A. *et al.* Lymphoma incidence, survival and prevalence 2004-2014: Sub-type analyses from the UK's Haematological Malignancy Research Network. *British Journal of Cancer* (2015) doi:10.1038/bjc.2015.94.
53. Küppers, R. Mechanisms of B-cell lymphoma pathogenesis. *Nature Reviews Cancer* (2005) doi:10.1038/nrc1589.
54. Cleary, M. L., Smith, S. D. & Sklar, J. Cloning and structural analysis of cDNAs for bcl-2 and a hybrid bcl-2/immunoglobulin transcript resulting from the t(14;18) translocation. *Cell* (1986) doi:10.1016/0092-8674(86)90362-4.
55. Tsujimoto, Y., Gorham, J., Cossman, J., Jaffe, E. & Croce, C. M. The t(14;18) chromosome translocations involved in B-cell neoplasms result from mistakes in VDJ joining. *Science* (1985) doi:10.1126/science.3929382.
56. Tsai, A. G. *et al.* Human Chromosomal Translocations at CpG Sites and a Theoretical Basis for Their Lineage and Stage Specificity. *Cell* (2008) doi:10.1016/j.cell.2008.10.035.
57. Summers, K. E. *et al.* Frequency of the Bcl-2/IgH rearrangement in normal individuals: Implications for the monitoring of disease in patients with follicular lymphoma. *Journal of Clinical Oncology* (2001) doi:10.1200/JCO.2001.19.2.420.
58. Roulland, S. *et al.* Early Steps of Follicular Lymphoma Pathogenesis. in *Advances in Immunology* (2011). doi:10.1016/B978-0-12-385991-4.00001-5.
59. Pasqualucci, L. Molecular pathogenesis of germinal center-derived B cell lymphomas. *Immunological Reviews* (2019) doi:10.1111/imr.12745.
60. Kanzler, H., Küppers, R., Hansmann, M. L. & Rajewsky, K. Hodgkin and Reed-Sternberg cells in Hodgkin's disease represent the outgrowth of a dominant tumor clone derived from (crippled) germinal center B cells.

Journal of Experimental Medicine (1996) doi:10.1084/jem.184.4.1495.

61. Pileri, S. A. *et al.* Primary mediastinal B-cell lymphoma: High frequency of BCL-6 mutations and consistent expression of the transcription factors OCT-2, BOB.1, and PU.1 in the absence of immunoglobulins. *American Journal of Pathology* (2003) doi:10.1016/S0002-9440(10)63815-1.
62. Meeker, T. *et al.* Emergence of Idiotype Variants during Treatment of B-Cell Lymphoma with Anti-Idiotype Antibodies. *New England Journal of Medicine* (1985) doi:10.1056/NEJM198506273122602.
63. Kraus, M., Alimzhanov, M. B., Rajewsky, N. & Rajewsky, K. Survival of resting mature B lymphocytes depends on BCR signaling via the Igα/β heterodimer. *Cell* (2004) doi:10.1016/j.cell.2004.05.014.
64. Gemenetzi, K. *et al.* B Cell Receptor Immunogenetics in B Cell Lymphomas: Immunoglobulin Genes as Key to Ontogeny and Clinical Decision Making. *Frontiers in Oncology* (2020) doi:10.3389/fonc.2020.00067.
65. Coiffier, B. *et al.* Long-term outcome of patients in the LNH-98.5 trial, the first randomized study comparing rituximab-CHOP to standard CHOP chemotherapy in DLBCL patients: A study by the Groupe d'Etudes des Lymphomes de l'Adulte. *Blood* (2010) doi:10.1182/blood-2010-03-276246.
66. Fisher, S. G. & Fisher, R. I. The epidemiology of non-Hodgkin's lymphoma. *Oncogene* (2004) doi:10.1038/sj.onc.1207843.
67. Darwiche, W., Gubler, B., Marolleau, J. P. & Ghamlouch, H. Chronic lymphocytic leukemia B-cell normal cellular counterpart: Clues from a functional perspective. *Frontiers in Immunology* (2018) doi:10.3389/fimmu.2018.00683.
68. Seifert, M. *et al.* Cellular origin and pathophysiology of chronic lymphocytic leukemia. *Journal of Experimental Medicine* (2012) doi:10.1084/jem.20120833.
69. Coiffier, B. & Sarkozy, C. Diffuse large B-cell lymphoma: R-CHOP failure-what to do? *Hematology* (2016) doi:10.1182/asheducation-2016.1.366.
70. UK, C. R. No Title.
71. Linch, D. C. Burkitt lymphoma in adults. *British Journal of Haematology* (2012) doi:10.1111/j.1365-2141.2011.08877.x.
72. S.S., D. & T., F. Non-Hodgkin's lymphoma time trends: United States and international data. *Cancer Research* (1992).
73. Global Data. B-Cell Non-Hodgkin's Lymphoma: Epidemiology Forecast to

2027 No Title. in (GlobalData, 2019).

74. NICE. *Non-Hodgkin's Lymphoma: Diagnosis and Management.* (2016).
75. Li, Q. *et al.* Integrative analysis of hub genes and key pathway in two subtypes of diffuse large B-cell lymphoma by bioinformatics and basic experiments. *Journal of Clinical Laboratory Analysis* **35**, (2021).
76. Sehn, L. H. *et al.* The revised International Prognostic Index (R-IPI) is a better predictor of outcome than the standard IPI for patients with diffuse large B-cell lymphoma treated with R-CHOP. *Blood* (2007) doi:10.1182/blood-2006-08-038257.
77. Solal-Céligny, P. *et al.* Follicular lymphoma international prognostic index. *Blood* (2004) doi:10.1182/blood-2003-12-4434.
78. Sun, R., Medeiros, L. J. & Young, K. H. Diagnostic and predictive biomarkers for lymphoma diagnosis and treatment in the era of precision medicine. *Modern Pathology* **29**, (2016).
79. Baron, B. W. *et al.* Identification of the gene associated with the recurring chromosomal translocations t(3;14)(q27;q32) and t(3;22)(q27;q11) in B-cell lymphomas. *Proceedings of the National Academy of Sciences of the United States of America* (1993) doi:10.1073/pnas.90.11.5262.
80. Montoto, S. & Fitzgibbon, J. Transformation of indolent B-cell lymphomas. *Journal of Clinical Oncology* (2011) doi:10.1200/JCO.2010.32.7577.
81. Kanungo, A., Medeiros, L. J., Abruzzo, L. V. & Lin, P. Lymphoid neoplasms associated with concurrent t(14;18) and 8q24/c-MYC translocation generally have a poor prognosis. *Modern Pathology* (2006) doi:10.1038/modpathol.3800500.
82. Alizadeh, A. A. *et al.* Distinct types of diffuse large B-cell lymphoma identified by gene expression profiling. *Nature* (2000) doi:10.1038/35000501.
83. Blenk, S. *et al.* Germinal center B cell-Like (GCB) and activated B cell-like (ABC) type of diffuse large B cell lymphoma (DLBCL): Analysis of molecular predictors, signatures, cell cycle state and patient survival. *Cancer Informatics* (2007) doi:10.1177/117693510700300004.
84. Karmali, R. & Gordon, L. I. Molecular Subtyping in Diffuse Large B Cell Lymphoma: Closer to an Approach of Precision Therapy. *Current Treatment Options in Oncology* (2017) doi:10.1007/s11864-017-0449-1.
85. Ye, B. H. *et al.* Alterations of a zinc finger-encoding gene, BCL-6, in diffuse

large-cell lymphoma. *Science* (1993) doi:10.1126/science.8235596.

86. Taub, R. *et al.* Translocation of the c-myc gene into the immunoglobulin heavy chain locus in human Burkitt lymphoma and murine plasmacytoma cells. *Proceedings of the National Academy of Sciences of the United States of America* (1982) doi:10.1073/pnas.79.24.7837.
87. Ruhe, M. *et al.* Molecular biomarkers of DNA damage in diffuse large-cell lymphoma—a review. *Journal of Laboratory and Precision Medicine* (2019) doi:10.21037/jlpm.2019.01.01.
88. Morin, R. D. *et al.* Somatic mutations altering EZH2 (Tyr641) in follicular and diffuse large B-cell lymphomas of germinal-center origin. *Nature Genetics* (2010) doi:10.1038/ng.518.
89. Dave, S. S. *et al.* Molecular Diagnosis of Burkitt's Lymphoma. *New England Journal of Medicine* **354**, (2006).
90. Zech, L., Haglund, U., Nilsson, K. & Klein, G. Characteristic chromosomal abnormalities in biopsies and lymphoid-cell lines from patients with burkitt and non-burkitt lymphomas. *International Journal of Cancer* (1976) doi:10.1002/ijc.2910170108.
91. Dalla-Favera, R. *et al.* Human c-myc onc gene is located on the region of chromosome 8 that is translocated in Burkitt lymphoma cells. *Proceedings of the National Academy of Sciences of the United States of America* (1982) doi:10.1073/pnas.79.24.7824.
92. Hummel, M. *et al.* A biologic definition of Burkitt's lymphoma from transcriptional and genomic profiling. *New England Journal of Medicine* (2006) doi:10.1056/NEJMoa055351.
93. Klein, U., Rajewsky, K. & Küppers, R. Human immunoglobulin (Ig)M+IgD+ peripheral blood B cells expressing the CD27 cell surface antigen carry somatically mutated variable region genes: CD27 as a general marker for somatically mutated (memory) B cells. *Journal of Experimental Medicine* (1998) doi:10.1084/jem.188.9.1679.
94. Moreno, C. & Montserrat, E. Genetic lesions in chronic lymphocytic leukemia: What's ready for prime time use? *Haematologica* (2010) doi:10.3324/haematol.2009.016873.
95. Calin, G. A. *et al.* Frequent deletions and down-regulation of micro-RNA genes miR15 and miR16 at 13q14 in chronic lymphocytic leukemia. *Proceedings of the National Academy of Sciences of the United States of America*

(2002) doi:10.1073/pnas.242606799.

96. Stankovic, T. *et al.* ATM mutations and phenotypes in ataxia-telangiectasia families in the British Isles: Expression of mutant ATM and the risk of leukemia, lymphoma, and breast cancer. *American Journal of Human Genetics* (1998) doi:10.1086/301706.

97. Dicker, F. *et al.* The detection of TP53 mutations in chronic lymphocytic leukemia independently predicts rapid disease progression and is highly correlated with a complex aberrant karyotype. *Leukemia* (2009) doi:10.1038/leu.2008.274.

98. Montoto, S. *et al.* Risk and clinical implications of transformation of follicular lymphoma to diffuse large B-cell lymphoma. *Journal of Clinical Oncology* (2007) doi:10.1200/JCO.2006.09.3260.

99. González-Rincón, J. *et al.* Unraveling transformation of follicular lymphoma to diffuse large B-cell lymphoma. *PLoS ONE* (2019) doi:10.1371/journal.pone.0212813.

100. Okosun, J. *et al.* Integrated genomic analysis identifies recurrent mutations and evolution patterns driving the initiation and progression of follicular lymphoma. *Nature Genetics* (2014) doi:10.1038/ng.2856.

101. Okosun, J., Montoto, S. & Fitzgibbon, J. The routes for transformation of follicular lymphoma. *Current Opinion in Hematology* (2016) doi:10.1097/MOH.0000000000000255.

102. Fuchs, D. Diffuse large B-cell lymphoma. *Memo - Magazine of European Medical Oncology* (2019) doi:10.1007/s12254-018-0457-2.

103. Sandlund, J. T. Burkitt lymphoma: Staging and response evaluation. *British Journal of Haematology* (2012) doi:10.1111/j.1365-2141.2012.09026.x.

104. Coleman, M. Chemotherapy for large-cell lymphoma: Optimism and caution. *Annals of Internal Medicine* (1985) doi:10.7326/0003-4819-103-1-140.

105. Patriarca, A. & Gaidano, G. Investigational drugs for the treatment of diffuse large B-cell lymphoma. *Expert Opinion on Investigational Drugs* vol. 30 (2021).

106. Shipp, M. A. *et al.* Diffuse large B-cell lymphoma outcome prediction by gene-expression profiling and supervised machine learning. *Nature Medicine* **8**, (2002).

107. Coiffier, B. *et al.* Chop chemotherapy plus rituximab compared with chop alone in elderly patients with diffuse large-B-cell lymphoma. *New England*

Journal of Medicine (2002) doi:10.1056/NEJMoa011795.

108. McLaughlin, P. *et al.* Rituximab chimeric anti-CD20 monoclonal antibody therapy for relapsed indolent lymphoma: Half of patients respond to a four-dose treatment program. *Journal of Clinical Oncology* (1998) doi:10.1200/JCO.1998.16.8.2825.
109. Maloney, D. G. *et al.* Idec-c2b8: Results of a phase I multiple-dose trial in patients with relapsed non-Hodgkin's lymphoma. *Journal of Clinical Oncology* (1997) doi:10.1200/JCO.1997.15.10.3266.
110. Pishko, A. & Nasta, S. D. The role of novel immunotherapies in non-Hodgkin lymphoma. *Translational Cancer Research* (2017) doi:10.21037/tcr.2017.01.08.
111. Albinger, N., Hartmann, J. & Ullrich, E. Current status and perspective of CAR-T and CAR-NK cell therapy trials in Germany. *Gene Therapy* vol. 28 (2021).
112. Sarkozy, C., Traverse-Glehen, A. & Coiffier, B. Double-hit and double-protein-expression lymphomas: Aggressive and refractory lymphomas. *The Lancet Oncology* (2015) doi:10.1016/S1470-2045(15)00005-4.
113. Ribrag, V. *et al.* Rituximab and dose-dense chemotherapy for adults with Burkitt's lymphoma: a randomised, controlled, open-label, phase 3 trial. *The Lancet* (2016) doi:10.1016/S0140-6736(15)01317-3.
114. Short, N. J. *et al.* Outcomes of adults with relapsed or refractory Burkitt and high-grade B-cell leukemia/lymphoma. *American Journal of Hematology* (2017) doi:10.1002/ajh.24720.
115. Mori, S. *et al.* Utilization of pathway signatures to reveal distinct types of B lymphoma in the Eμ-myc model and human diffuse large B-cell lymphoma. *Cancer Research* (2008) doi:10.1158/0008-5472.CAN-08-1329.
116. Cattoretti, G. *et al.* Deregulated BCL6 expression recapitulates the pathogenesis of human diffuse large B cell lymphomas in mice. *Cancer Cell* (2005) doi:10.1016/j.ccr.2005.03.037.
117. Egle, A., Harris, A. W., Bath, M. L., O'Reilly, L. & Cory, S. VavP-Bcl2 transgenic mice develop follicular lymphoma preceded by germinal center hyperplasia. *Blood* (2004) doi:10.1182/blood-2003-07-2469.
118. Nilsson, K. & Pontén, J. Classification and biological nature of established human hematopoietic cell lines. *International Journal of Cancer* (1975) doi:10.1002/ijc.2910150217.

119. Ford, R. J., Goodacre, A., Ramirez, I., Mehta, S. R. & Cabanillas, F. Establishment and characterization of human B-cell lymphoma cell lines using B-cell growth factor. *Blood* (1990) doi:10.1182/blood.v75.6.1311.bloodjournal7561311.

120. Tubbs, A. & Nussenzweig, A. Endogenous DNA Damage as a Source of Genomic Instability in Cancer. *Cell* vol. 168 (2017).

121. Halazonetis, T. D., Gorgoulis, V. G. & Bartek, J. An oncogene-induced DNA damage model for cancer development. *Science* (2008) doi:10.1126/science.1140735.

122. Klein, U. & Dalla-Favera, R. Germinal centres: Role in B-cell physiology and malignancy. *Nature Reviews Immunology* (2008) doi:10.1038/nri2217.

123. Cunnigham. Targeting the CINful genome: Stategies to overcome tumore heterogeneity. *Progress in Biophysics and Molecular Biology* **147**, 77–91 (2019).

124. Hanahan, D. & Weinberg, R. A. Hallmarks of cancer: The next generation. *Cell* vol. 144 (2011).

125. De Miranda, N. *et al.* DNA repair genes are selectively mutated in diffuse large B cell lymphomas. *Journal of Experimental Medicine* (2013) doi:10.1084/jem.20122842.

126. Bakhoum, S. F., Danilova, O. V., Kaur, P., Levy, N. B. & Compton, D. A. Chromosomal instability substantiates poor prognosis in patients with diffuse large B-cell lymphoma. *Clinical Cancer Research* (2011) doi:10.1158/1078-0432.CCR-11-2049.

127. Derenzini, E. *et al.* Constitutive activation of the DNA damage response pathway as a novel therapeutic target in diffuse large B-cell lymphoma. *Oncotarget* (2015) doi:10.18632/oncotarget.2720.

128. Pasqualucci, L. *et al.* BCL-6 mutations in normal germinal center B cells: Evidence of somatic hypermutation acting outside Ig loci. *Proceedings of the National Academy of Sciences of the United States of America* (1998) doi:10.1073/pnas.95.20.11816.

129. Khodabakhshi, A. H. *et al.* Recurrent targets of aberrant somatic hypermutation in lymphoma. *Oncotarget* (2012) doi:10.18632/oncotarget.653.

130. Liu, M. & Schatz, D. G. Balancing AID and DNA repair during somatic hypermutation. *Trends in Immunology* vol. 30 (2009).

131. Klymenko, T. *et al.* Lamin B1 regulates somatic mutations and progression

of B-cell malignancies. *Leukemia* (2018) doi:10.1038/leu.2017.255.

132. Gonzalez-Sandoval, A. & Gasser, S. M. On TADs and LADs: Spatial Control Over Gene Expression. *Trends in Genetics* vol. 32 (2016).
133. Zheng, H. & Xie, W. The role of 3D genome organization in development and cell differentiation. *Nature Reviews Molecular Cell Biology* vol. 20 (2019).
134. Schoonhoven, A. van, Huylebroeck, D., Hendriks, R. W. & Stadhouders, R. 3D genome organization during lymphocyte development and activation. *Briefings in Functional Genomics* **19**, (2020).
135. Ochs, F. *et al.* Stabilization of chromatin topology safeguards genome integrity. *Nature* **574**, (2019).
136. Valton, A. L. & Dekker, J. TAD disruption as oncogenic driver. *Current Opinion in Genetics and Development* vol. 36 (2016).
137. Lupiáñez, D. G. *et al.* Disruptions of topological chromatin domains cause pathogenic rewiring of gene-enhancer interactions. *Cell* **161**, (2015).
138. Nagano, T. *et al.* Cell-cycle dynamics of chromosomal organization at single-cell resolution. *Nature* **547**, (2017).
139. Ryba, T. *et al.* Evolutionarily conserved replication timing profiles predict long-range chromatin interactions and distinguish closely related cell types. *Genome Research* **20**, (2010).
140. Dixon, J. R. *et al.* Topological domains in mammalian genomes identified by analysis of chromatin interactions. *Nature* **485**, (2012).
141. Pommier, Y., Sun, Y., Huang, S. Y. N. & Nitiss, J. L. Roles of eukaryotic topoisomerases in transcription, replication and genomic stability. *Nature Reviews Molecular Cell Biology* vol. 17 (2016).
142. Gothe, H. J. *et al.* Spatial Chromosome Folding and Active Transcription Drive DNA Fragility and Formation of Oncogenic MLL Translocations. *Molecular Cell* (2019) doi:10.1016/j.molcel.2019.05.015.
143. Canela, A. *et al.* Genome Organization Drives Chromosome Fragility. *Cell* **170**, (2017).
144. Noordermeer, S. M. *et al.* The shieldin complex mediates 53BP1-dependent DNA repair. *Nature* **560**, (2018).
145. van Steensel, B. & Belmont, A. S. Lamina-Associated Domains: Links with Chromosome Architecture, Heterochromatin, and Gene Repression. *Cell* vol. 169 (2017).
146. Guelen, L. *et al.* Domain organization of human chromosomes revealed by

mapping of nuclear lamina interactions. *Nature* **453**, (2008).

147. Gruenbaum, Y. *et al.* The nuclear lamina and its functions in the nucleus. *International Review of Cytology* **226**, (2003).
148. Lochs, S. J. A., Kefalopoulou, S. & Kind, J. Lamina Associated Domains and Gene Regulation in Development and Cancer. *Cells* **8**, (2019).
149. Aebi, U., Cohn, J., Buhle, L. & Gerace, L. The nuclear lamina is a meshwork of intermediate-type filaments. *Nature* **323**, (1986).
150. Meuleman, W. *et al.* Constitutive nuclear lamina-genome interactions are highly conserved and associated with A/T-rich sequence. *Genome Research* **23**, (2013).
151. Hatch, E. M., Fischer, A. H., Deerinck, T. J. & Hetzer, M. W. Catastrophic Nuclear Envelope Collapse in Cancer Cell Micronuclei. *Cell* **154**, (2013).
152. Dechat, T. *et al.* Nuclear lamins: Major factors in the structural organization and function of the nucleus and chromatin. *Genes and Development* vol. 22 (2008).
153. Briand, N. & Collas, P. Lamina-associated domains: Peripheral matters and internal affairs. *Genome Biology* vol. 21 (2020).
154. Moir, R. D., Montag-Lowy, M. & Goldman, R. D. Dynamic properties of nuclear lamins: Lamin B is associated with sites of DNA replication. *Journal of Cell Biology* **125**, (1994).
155. Dreesen, O., Ong, P. F., Chojnowski, A. & Colman, A. The contrasting roles of lamin B1 in cellular aging and human disease. *Nucleus* **4**, (2013).
156. Young, S. G., Jung, H. J., Coffinier, C. & Fong, L. G. Understanding the roles of nuclear A- and B-type lamins in brain development. *Journal of Biological Chemistry* vol. 287 (2012).
157. Lammerding, J. *et al.* Lamins a and C but not lamin B1 regulate nuclear mechanics. *Journal of Biological Chemistry* **281**, (2006).
158. Adam, S. A., Butin-Israeli, V., Cleland, M. M., Shimi, T. & Goldman, R. D. Disruption of lamin B1 and lamin B2 processing and localization by farnesyltransferase inhibitors. *Nucleus (United States)* **4**, (2013).
159. Jung, H. J. *et al.* Farnesylation of lamin B1 is important for retention of nuclear chromatin during neuronal migration. *Proceedings of the National Academy of Sciences of the United States of America* (2013) doi:10.1073/pnas.1303916110.
160. Hocevar, B. A., Burns, D. J. & Fields, A. P. Identification of protein kinase

C (PKC) phosphorylation sites on human lamin B. Potential role of PKC in nuclear lamina structural dynamics. *Journal of Biological Chemistry* **268**, (1993).

161. Maske, C. P. *et al.* A carboxyl-terminal interaction of lamin B1 is dependent on the CAAX endoprotease Rce1 and carboxymethylation. *Journal of Cell Biology* **162**, (2003).
162. Mathieson, T. *et al.* Systematic analysis of protein turnover in primary cells. *Nature Communications* **9**, (2018).
163. Coffinier, C. *et al.* Deficiencies in lamin B1 and lamin B2 cause neurodevelopmental defects and distinct nuclear shape abnormalities in neurons. *Molecular Biology of the Cell* (2011) doi:10.1091/mbc.E11-06-0504.
164. Jia, Y. *et al.* Lamin B1 loss promotes lung cancer development and metastasis by epigenetic derepression of RET. *Journal of Experimental Medicine* (2019) doi:10.1084/jem.20181394.
165. Dou, Z. *et al.* Autophagy mediates degradation of nuclear lamina. *Nature* **527**, (2015).
166. Krishnamoorthy, V., Khanna, R. & Parnaik, V. K. E3 ubiquitin ligase HECW2 targets PCNA and lamin B1. *Biochimica et Biophysica Acta - Molecular Cell Research* (2018) doi:10.1016/j.bbamcr.2018.05.008.
167. Freund, A., Laberge, R. M., Demaria, M. & Campisi, J. Lamin B1 loss is a senescence-associated biomarker. *Molecular Biology of the Cell* **23**, (2012).
168. Dreesen, O. *et al.* Lamin B1 fluctuations have differential effects on cellular proliferation and senescence. *Journal of Cell Biology* (2013) doi:10.1083/jcb.201206121.
169. Peric-Hupkes, D. *et al.* Molecular Maps of the Reorganization of Genome-Nuclear Lamina Interactions during Differentiation. *Molecular Cell* **38**, (2010).
170. Pickersgill, H. *et al.* Characterization of the Drosophila melanogaster genome at the nuclear lamina. *Nature Genetics* **38**, (2006).
171. Polioudaki, H. *et al.* Histones H3/H4 form a tight complex with the inner nuclear membrane protein LBR and heterochromatin protein 1. *EMBO Reports* **2**, (2001).
172. Kind, J. *et al.* Single-cell dynamics of genome-nuclear lamina interactions. *Cell* **153**, (2013).
173. Kumaran, R. I. & Spector, D. L. A genetic locus targeted to the nuclear

periphery in living cells maintains its transcriptional competence. *Journal of Cell Biology* **180**, (2008).

174. Gesson, K. *et al.* A-type Lamins bind both hetero- and euchromatin, the latter being regulated by lamina-associated polypeptide 2 alpha. *Genome Research* **26**, (2016).

175. Pascual-Reguant, L. *et al.* Lamin B1 mapping reveals the existence of dynamic and functional euchromatin lamin B1 domains. *Nature Communications* (2018) doi:10.1038/s41467-018-05912-z.

176. Butin-Israeli, V. *et al.* Role of Lamin B1 in Chromatin Instability. *Molecular and Cellular Biology* (2015) doi:10.1128/mcb.01145-14.

177. Shah, P. P. *et al.* Lamin B1 depletion in senescent cells triggers large-scale changes in gene expression and the chromatin landscape. *Genes and Development* (2013) doi:10.1101/gad.223834.113.

178. Shimi, T. *et al.* The role of nuclear lamin B1 in cell proliferation and senescence. *Genes and Development* **25**, (2011).

179. Murray-Nerger, L. A., Justice, J. L., Rekapalli, P., Hutton, J. E. & Cristea, I. M. Lamin B1 acetylation slows the G1 to S cell cycle transition through inhibition of DNA repair. *Nucleic Acids Research* **49**, (2021).

180. Etourneaud, L. *et al.* Lamin B1 sequesters 53BP1 to control its recruitment to DNA damage. *Science Advances* (2021) doi:10.1126/sciadv.abb3799.

181. Butin-Israeli, V., Adam, S. A. & Goldman, R. D. Regulation of Nucleotide Excision Repair by Nuclear Lamin B1. *PLoS ONE* **8**, (2013).

182. Liu, N. A. *et al.* Regulation of homologous recombinational repair by lamin B1 in radiation-induced DNA damage. *FASEB Journal* **29**, (2015).

183. Chang, L. *et al.* Nuclear peripheral chromatin-lamin B1 interaction is required for global integrity of chromatin architecture and dynamics in human cells. *Protein and Cell* (2020) doi:10.1007/s13238-020-00794-8.

184. Sadaie, M. *et al.* Redistribution of the Lamin B1 genomic binding profile affects rearrangement of heterochromatic domains and SAHF formation during senescence. *Genes and Development* (2013) doi:10.1101/gad.217281.113.

185. Di Noia, J. M. & Neuberger, M. S. Molecular mechanisms of antibody somatic hypermutation. *Annual Review of Biochemistry* vol. 76 (2007).

186. Liu, M. *et al.* Two levels of protection for the B cell genome during somatic hypermutation. *Nature* **451**, (2008).

187. Pham, P., Bransteitter, R., Petruska, J. & Goodman, M. F. Processive AID-catalysed cytosine deamination on single-stranded DNA simulates somatic hypermutation. *Nature* **424**, (2003).

188. Stavnezer, J., Kinoshita, K., Muramatsu, M. & Honjo, T. Molecular Mechanism of Class Switch Recombination. in *Molecular Biology of B Cells* (2003). doi:10.1016/B978-012053641-2/50021-6.

189. Bothmer, A. *et al.* 53BP1 regulates DNA resection and the choice between classical and alternative end joining during class switch recombination. *Journal of Experimental Medicine* **207**, (2010).

190. Sundaravinayagam, D. *et al.* 53BP1 Supports Immunoglobulin Class Switch Recombination Independently of Its DNA Double-Strand Break End Protection Function. *Cell Reports* **28**, (2019).

191. Gupta, A. *et al.* Role of 53BP1 in the regulation of DNA double-strand break repair pathway choice. *Radiation Research* vol. 181 (2014).

192. Reina-San-Martin, B., Chen, H. T., Nussenzweig, A. & Nussenzweig, M. C. ATM is required for efficient recombination between immunoglobulin switch regions. *Journal of Experimental Medicine* **200**, (2004).

193. Chapman, J. R. *et al.* RIF1 Is Essential for 53BP1-Dependent Nonhomologous End Joining and Suppression of DNA Double-Strand Break Resection. *Molecular Cell* **49**, (2013).

194. Padiath, Q. S. *et al.* Lamin B1 duplications cause autosomal dominant leukodystrophy. *Nature Genetics* **38**, (2006).

195. Izdebska, M., Gagat, M. & Grzanka, A. Overexpression of lamin B1 induces mitotic catastrophe in colon cancer lovo cells and is associated with worse clinical outcomes. *International Journal of Oncology* **52**, (2018).

196. Li, L. *et al.* Lamin B1 is a novel therapeutic target of betulinic acid in pancreatic cancer. *Clinical Cancer Research* **19**, (2013).

197. Luo, F. *et al.* Lamin B1 promotes tumor progression and metastasis in primary prostate cancer patients. *Future Oncology* **17**, 663–673 (2021).

198. Abdelghany, A. M. *et al.* Using lamin B1 mRNA for the early diagnosis of hepatocellular carcinoma: A cross-sectional diagnostic accuracy study [version 1; peer review: 2 approved]. *F1000Research* **7**, (2018).

199. Yu, Z. Y. *et al.* Lamin b1 deficiency promotes malignancy and predicts poor prognosis in gastric cancer. *Neoplasma* **67**, (2020).

200. Reilly, A. *et al.* Loss of Lamin B1 in Myeloid Neoplasms with 5q Deletion

Causes Myeloid-Biased Hematopoiesis and Pelger-Huet Nuclear Anomaly. *Blood* **138**, (2021).

201. Casola, S. *et al.* Tracking germinal center B cells expressing germ-line immunoglobulin $\gamma 1$ transcripts by conditional gene targeting. *Proceedings of the National Academy of Sciences of the United States of America* **103**, (2006).
202. Grüll, F., Kirchgessner, M., Kaufmann, R., Hausmann, M. & Kebschull, U. Accelerating image analysis for localization microscopy with FPGAs. in *Proceedings - 21st International Conference on Field Programmable Logic and Applications, FPL 2011* (2011). doi:10.1109/FPL.2011.11.
203. Ester, M., Kriegel, H.-P., Sanger, J. & Xu, X. A Density Based Notion of Clusters in Large Spatial Databases with Noise. in *Conference on Knowledge Discovery and Data Mining* (1996).
204. Malkusch, S. *et al.* Coordinate-based colocalization analysis of single-molecule localization microscopy data. *Histochemistry and Cell Biology* **137**, (2012).
205. Schmitz, R. *et al.* Genetics and Pathogenesis of Diffuse Large B-Cell Lymphoma. *New England Journal of Medicine* **378**, (2018).
206. Basso, K. & Dalla-Favera, R. Germinal centres and B cell lymphomagenesis. *Nature Reviews Immunology* (2015) doi:10.1038/nri3814.
207. Phan, R. T. & Dalla-Favera, R. The BCL6 proto-oncogene suppresses p53 expression in germinal-centre B cells. *Nature* (2004) doi:10.1038/nature03147.
208. Chaudhuri, J. *et al.* Transcription-targeted DNA deamination by the AID antibody diversification enzyme. *Nature* (2003) doi:10.1038/nature01574.
209. Tate, J. G. *et al.* COSMIC: The Catalogue Of Somatic Mutations In Cancer. *Nucleic Acids Research* (2019) doi:10.1093/nar/gky1015.
210. Talluri, S. *et al.* Dysregulated APOBEC3G causes DNA damage and promotes genomic instability in multiple myeloma. *Blood Cancer Journal* (2021) doi:10.1038/s41408-021-00554-9.
211. Shen, H. M., Peters, A., Baron, B., Zhu, X. & Storb, U. Mutation of BCL-6 gene in normal B cells by the process of somatic hypermutation of Ig genes. *Science* (1998) doi:10.1126/science.280.5370.1750.
212. Singh, N. P., McCoy, M. T., Tice, R. R. & Schneider, E. L. A simple technique for quantitation of low levels of DNA damage in individual cells. *Experimental Cell Research* (1988) doi:10.1016/0014-4827(88)90265-0.

213. Fairbairn, D. W., Olive, P. L. & O'Neill, K. L. The comet assay: a comprehensive review. *Mutation Research/Reviews in Genetic Toxicology* (1995) doi:10.1016/0165-1110(94)00013-3.
214. Kuo, L. J. & Yang, L. X. γ-H2AX- A novel biomaker for DNA double-strand breaks. *In Vivo* (2008).
215. Kobayashi, J. Molecular mechanism of the recruitment of NBS1/hMRE11/hRAD50 complex to DNA double-strand breaks: NBS1 binds to γ-H2AX through FHA/BRCT domain. *Journal of Radiation Research* (2004) doi:10.1269/jrr.45.473.
216. Hoeijmakers, J. H. J. Genome maintenance mechanisms for preventing cancer. *Nature* vol. 411 (2001).
217. Deriano, L., Merle-Béral, H., Guipaud, O., Sabatier, L. & Delic, J. Mutagenicity of non-homologous end joining DNA repair in a resistant subset of human chronic lymphocytic leukaemia B cells. *British Journal of Haematology* (2006) doi:10.1111/j.1365-2141.2006.06071.x.
218. Panier, S. & Boulton, S. J. Double-strand break repair: 53BP1 comes into focus. *Nature Reviews Molecular Cell Biology* vol. 15 (2014).
219. Houtgraaf, J. H., Versmissen, J. & van der Giessen, W. J. A concise review of DNA damage checkpoints and repair in mammalian cells. *Cardiovascular Revascularization Medicine* **7**, (2006).
220. Jais, J. P. *et al.* The expression of 16 genes related to the cell of origin and immune response predicts survival in elderly patients with diffuse large B-cell lymphoma treated with CHOP and rituximab. *Leukemia* (2008) doi:10.1038/leu.2008.188.
221. Wagener, R. *et al.* Analysis of mutational signatures in exomes from B-cell lymphoma cell lines suggest APOBEC3 family members to be involved in the pathogenesis of primary effusion lymphoma. *Leukemia* (2015) doi:10.1038/leu.2015.22.
222. Noguchi, A. *et al.* Decreased Lamin B1 Levels Affect Gene Positioning and Expression in Postmitotic Neurons. *Neuroscience Research* (2021) doi:10.1016/j.neures.2021.05.011.
223. Stone, J. E., Lujan, S. A., Kunkel, T. A. & Kunkel, T. A. DNA polymerase zeta generates clustered mutations during bypass of endogenous DNA lesions in Saccharomyces cerevisiae. *Environmental and Molecular Mutagenesis* (2012) doi:10.1002/em.21728.

224. Qian, J. *et al.* B cell super-enhancers and regulatory clusters recruit AID tumorigenic activity. *Cell* **159**, (2014).

225. Dziubańska-Kusibab, P. J. *et al.* Colibactin DNA-damage signature indicates mutational impact in colorectal cancer. *Nature Medicine* (2020) doi:10.1038/s41591-020-0908-2.

226. Roberts, S. A. *et al.* An APOBEC cytidine deaminase mutagenesis pattern is widespread in human cancers. *Nature Genetics* **45**, (2013).

227. Kohli, R. M. *et al.* Local sequence targeting in the AID/APOBEC family differentially impacts retroviral restriction and antibody diversification. *Journal of Biological Chemistry* **285**, (2010).

228. Qin, J. Y. *et al.* Systematic comparison of constitutive promoters and the doxycycline-inducible promoter. *PLoS ONE* (2010) doi:10.1371/journal.pone.0010611.

229. Schep, R. *et al.* Impact of chromatin context on Cas9-induced DNA double-strand break repair pathway balance. *Molecular Cell* (2021) doi:10.1016/j.molcel.2021.03.032.

230. Nesta, A. V., Tafur, D. & Beck, C. R. Hotspots of Human Mutation. *Trends in Genetics* vol. 37 717–729 (2021).

231. Shee, C., Gibson, J. L. & Rosenberg, S. M. Two Mechanisms Produce Mutation Hotspots at DNA Breaks in Escherichia coli. *Cell Reports* **2**, (2012).

232. Luperchio, T. R., Wong, X. & Reddy, K. L. Genome regulation at the peripheral zone: Lamina associated domains in development and disease. *Current Opinion in Genetics and Development* vol. 25 (2014).

233. Lorat, Y. *et al.* Beyond repair foci: DNA double-strand break repair in euchromatic and heterochromatic compartments analyzed by transmission electron microscopy. *PLoS ONE* **7**, (2012).

234. Stiekema, M. *et al.* Super-resolution imaging of the a- and b-type lamin networks: A comparative study of different fluorescence labeling procedures. *International Journal of Molecular Sciences* **22**, (2021).

235. Kittisopikul, M., Virtanen, L., Taimen, P. & Goldman, R. D. Quantitative analysis of nuclear lamins imaged by super-resolution light microscopy. *Cells* vol. 8 (2019).

236. Creech, M. K., Wang, J., Nan, X. & Gibbs, S. L. Superresolution imaging of clinical formalin fixed paraffin embedded breast cancer with single molecule localization microscopy. *Scientific Reports* **7**, (2017).

237. Bach, M. *et al.* Super-resolution localization microscopy of γ-H2AX and heterochromatin after folate deficiency. *International Journal of Molecular Sciences* **18**, (2017).

238. Podhorecka, M., Skladanowski, A. & Bozko, P. H2AX phosphorylation: Its role in DNA damage response and cancer therapy. *Journal of Nucleic Acids* vol. 2010 (2010).

239. Hofmann, A., Krufczik, M., Heermann, D. W. & Hausmann, M. Using persistent homology as a new approach for super-resolution localization microscopy data analysis and classification of γH2AX foci/clusters. *International Journal of Molecular Sciences* **19**, (2018).

240. Varga, D., Majoros, H., Ujfaludi, Z., Erdélyi, M. & Pankotai, T. Quantification of DNA damage induced repair focus formation: Via super-resolution dSTORM localization microscopy. *Nanoscale* **11**, (2019).

241. Natale, F. *et al.* Identification of the elementary structural units of the DNA damage response. *Nature Communications* **8**, (2017).

242. Szczurek, A. *et al.* Super-resolution binding activated localization microscopy through reversible change of dna conformation. *Nucleus* **9**, (2018).

243. Goodarzi, A. A. & Jeggo, P. A. The heterochromatic barrier to DNA double strand break repair: How to get the entry visa. *International Journal of Molecular Sciences* vol. 13 (2012).

244. Vergnes, L., Péterfy, M., Bergo, M. O., Young, S. G. & Reue, K. Lamin B1 is required for mouse development and nuclear integrity. *Proceedings of the National Academy of Sciences of the United States of America* (2004) doi:10.1073/pnas.0401424101.

245. Yang, S. H. *et al.* An absence of both lamin B1 and lamin B2 in keratinocytes has no effect on cell proliferation or the development of skin and hair. *Human Molecular Genetics* **20**, (2011).

246. Barlow, C. *et al.* Targeted expression of Cre recombinase to adipose tissue of transgenic mice directs adipose-specific excision of loxP-flanked gene segments. *Nucleic Acids Research* **25**, (1997).

247. Vijay, R. *et al.* Infection-induced plasmablasts are a nutrient sink that impairs humoral immunity to malaria. *Nature Immunology* **21**, (2020).

248. Musaigwa, Fungai; Kamdem, Severin Donald; Mpotje, Thabo; Mosala, Paballo; Aziz, Nada Abdel; Herbert, D. R. . et al. Cell death in CD138+

plasmablasts and plasma B cells from schistosomiasis-infected and anti-poliovirus vaccinated animals. *PLOS Pathogens* (2022).

249. Chen, X. *et al.* ATAC-see reveals the accessible genome by transposase-mediated imaging and sequencing. *Nature Methods* **13**, (2016).
250. Alcalá-Vida, R. *et al.* Neuron type-specific increase in lamin B1 contributes to nuclear dysfunction in Huntington's disease. *EMBO Molecular Medicine* **13**, (2021).
251. Petersen, S. *et al.* AID is required to initiate Nbs1/γ-H2AX focus formation and mutations at sites of class switching. *Nature* **414**, (2001).
252. Kiraly, O., Gong, G., Olipitz, W., Muthupalani, S. & Engelward, B. P. Inflammation-Induced Cell Proliferation Potentiates DNA Damage-Induced Mutations In Vivo. *PLoS Genetics* **11**, (2015).
253. Ogrunc, M. *et al.* Oncogene-induced reactive oxygen species fuel hyperproliferation and DNA damage response activation. *Cell Death and Differentiation* **21**, (2014).
254. Pasqualucci, L. *et al.* AID is required for germinal center-derived lymphomagenesis. *Nature Genetics* **40**, (2008).
255. Reddy, K. L., Zullo, J. M., Bertolino, E. & Singh, H. Transcriptional repression mediated by repositioning of genes to the nuclear lamina. *Nature* **452**, (2008).
256. Qin, H. *et al.* Pan-cancer analysis identifies LMNB1 as a target to redress Th1/Th2 imbalance and enhance PARP inhibitor response in human cancers. *Cancer cell international* **22**, 101 (2022).
257. Sun, M. *et al.* MiR-196a is upregulated in gastric cancer and promotes cell proliferation by downregulating p27 kip1. *Molecular Cancer Therapeutics* **11**, (2012).
258. Liu, X. hua *et al.* MicroRNA-196a promotes non-small cell lung cancer cell proliferation and invasion through targeting HOXA5. *BMC Cancer* **12**, (2012).
259. Hamta, A. & Hajihassani, F. The Molecular Analysis of rs11614913 Polymorphism from miRNA196a Gene and Its Relationship with TNF-α Gene Expression in Cervical Cancer. *Jentashapir Journal of Cellular and Molecular Biology* **11**, (2020).
260. Zhou, X. *et al.* Regulation of Hippo-YAP signaling by insulin-like growth factor-1 receptor in the tumorigenesis of diffuse large B-cell lymphoma.

Journal of Hematology and Oncology **13**, (2020).

261. Wang, D., Zhang, Y. & Che, Y. Q. CCND2 mRNA Expression Is Correlated With R-CHOP Treatment Efficacy and Prognosis in Patients With ABC-DLBCL. *Frontiers in Oncology* **10**, (2020).

262. Cottini, F. *et al.* Rescue of Hippo coactivator YAP1 triggers DNA damage-induced apoptosis in hematological cancers. *Nature Medicine* **20**, 599–606 (2014).

263. Bastami, M. *et al.* Critical roles of microRNA-196 in normal physiology and non-malignant diseases: Diagnostic and therapeutic implications. *Experimental and Molecular Pathology* vol. 122 (2021).

264. Yang, C. S. *et al.* Ubiquitin Modification by the E3 Ligase/ADP-Ribosyltransferase Dtx3L/Parp9. *Molecular Cell* **66**, (2017).

265. Ghodke, I. *et al.* AHNAK controls 53BP1-mediated p53 response by restraining 53BP1 oligomerization and phase separation. *Molecular Cell* **81**, (2021).

266. Andersen, P. L., Xu, F. & Xiao, W. Eukaryotic DNA damage tolerance and translesion synthesis through covalent modifications of PCNA. *Cell Research* vol. 18 (2008).

267. Motegi, A. *et al.* Polyubiquitination of proliferating cell nuclear antigen by HLTF and SHPRH prevents genomic instability from stalled replication forks. *Proceedings of the National Academy of Sciences of the United States of America* **105**, (2008).

268. Huen, M. S. Y. & Chen, J. The DNA damage response pathways: At the crossroad of protein modifications. *Cell Research* vol. 18 (2008).

269. Jung, M. S. *et al.* A Myc activity signature predicts poor clinical outcomes in Myc-associated cancers. *Cancer Research* **77**, (2017).

270. Schulze, A., Oshi, M., Endo, I. & Takabe, K. Myc targets scores are associated with cancer aggressiveness and poor survival in er-positive primary and metastatic breast cancer. *International Journal of Molecular Sciences* **21**, (2020).

271. Pecoraro, A., Pagano, M., Russo, G. & Russo, A. Ribosome biogenesis and cancer: Overview on ribosomal proteins. *International Journal of Molecular Sciences* vol. 22 (2021).

272. Pelletier, J., Thomas, G. & Volarevi, S. Ribosome biogenesis in cancer: New players and therapeutic avenues. *Nature Reviews Cancer* vol. 18 (2017).

273. Simon, D. N. & Wilson, K. L. Partners and post-translational modifications of nuclear lamins. *Chromosoma* vol. 122 (2013).

274. Sun, W. *et al.* Proteome analysis of hepatocellular carcinoma by two-dimensional difference gel electrophoresis. *Molecular and Cellular Proteomics* **6**, (2007).

275. Li, W. *et al.* Lamin B1 overexpresses in lung adenocarcinoma and promotes proliferation in lung cancer cells via akt pathway. *OncoTargets and Therapy* **13**, (2020).

276. Wazir, U. *et al.* The clinicopathological significance of lamin A/C, lamin B1 and lamin B receptor mRNA expression in human breast cancer. *Cellular and Molecular Biology Letters* **18**, (2013).

277. Reilly, A. *et al.* Lamin B1 deletion in myeloid neoplasms causes nuclear anomaly and altered hematopoietic stem cell function. *Cell Stem Cell* **29**, (2022).

278. Ramachandiran, S. *et al.* Chromosome instability in diffuse large B cell lymphomas is suppressed by activation of the noncanonical NF-κB pathway. *International Journal of Cancer* (2015) doi:10.1002/ijc.29301.

279. Maguire, A. *et al.* Enhanced DNA repair and genomic stability identify a novel HIV-related diffuse large B-cell lymphoma signature. *International Journal of Cancer* **145**, (2019).

280. Pasqualucci, L. *et al.* Analysis of the coding genome of diffuse large B-cell lymphoma. *Nature Genetics* **43**, (2011).

281. Hans, C. P. *et al.* Confirmation of the molecular classification of diffuse large B-cell lymphoma by immunohistochemistry using a tissue microarray. *Blood* **103**, (2004).

282. Cannan, W. J. & Pederson, D. S. Mechanisms and Consequences of Double-Strand DNA Break Formation in Chromatin. *Journal of Cellular Physiology* vol. 231 (2016).

283. Rushton, C. *et al.* The Copy Number Landscape of Relapsed and Refractory Diffuse Large B-Cell Lymphoma. *Blood* **136**, (2020).

284. Hua, Y., He, Z. & Zhang, X. A pan-cancer analysis based on weighted gene co-expression network analysis identifies the biomarker utility of lamin B1 in human tumors. *Cancer Biomarkers* (2021) doi:10.3233/cbm-203247.

285. Louvet, E., Yoshida, A., Kumeta, M. & Takeyasu, K. Probing the stiffness of isolated nucleoli by atomic force microscopy. *Histochemistry and Cell*

Biology **141**, (2014).

286. Dubois, M. L. & Boisvert, F. M. The nucleolus: Structure and function. in *The Functional Nucleus* (2016). doi:10.1007/978-3-319-38882-3_2.
287. Martin, C. *et al.* Lamin B1 maintains the functional plasticity of nucleoli. *Journal of Cell Science* **122**, (2009).
288. McKinnon, P. J. & Caldecott, K. W. DNA strand break repair and human genetic disease. *Annual Review of Genomics and Human Genetics* vol. 8 (2007).
289. Mills, K. D., Ferguson, D. O. & Alt, F. W. The role of DNA breaks in genomic instability and tumorigenesis. *Immunological Reviews* vol. 194 (2003).
290. Bouwman, B. A. M. *et al.* Genome-wide detection of DNA double-strand breaks by in-suspension BLISS. *Nature Protocols* **15**, (2020).
291. Staszewski, O. *et al.* Activation-Induced Cytidine Deaminase Induces Reproducible DNA Breaks at Many Non-Ig Loci in Activated B Cells. *Molecular Cell* **41**, (2011).
292. Morimoto, S. *et al.* Type II DNA topoisomerases cause spontaneous double-strand breaks in genomic DNA. *Genes* vol. 10 (2019).
293. Mosler, T. *et al.* R-loop proximity proteomics identifies a role of DDX41 in transcription-associated genomic instability. *Nature Communications* **12**, 7314 (2021).
294. Machour, F. E. & Ayoub, N. Transcriptional Regulation at DSBs: Mechanisms and Consequences. *Trends in Genetics* vol. 36 (2020).
295. Goyenechea, B. *et al.* Cells strongly expressing Igκ transgenes show clonal recruitment of hypermutation: A role for both MAR and the enhancers. *EMBO Journal* **16**, (1997).
296. Zimmermann, M. & De Lange, T. 53BP1: Pro choice in DNA repair. *Trends in Cell Biology* vol. 24 (2014).
297. Yang, Y. F. *et al.* YWHAE promotes proliferation, metastasis, and chemoresistance in breast cancer cells. *Kaohsiung Journal of Medical Sciences* **35**, (2019).
298. Qu, Q. *et al.* USP2 promotes cell migration and invasion in triple negative breast cancer cell lines. *Tumor Biology* **36**, (2015).
299. Shumaker, D. K. *et al.* The highly conserved nuclear lamin Ig-fold binds to PCNA: Its role in DNA replication. *Journal of Cell Biology* **181**, (2008).
300. Groehler, A. L. & Lannigan, D. A. A chromatin-bound kinase, ERK8,

protects genomic integrity by inhibiting HDM2-mediated degradation of the DNA clamp PCNA. *Journal of Cell Biology* **190**, (2010).

301. Barna, M. *et al.* Suppression of Myc oncogenic activity by ribosomal protein haploinsufficiency. *Nature* **456**, (2008).
302. Gizem Sonugür, F. & Akbulut, H. The role of tumor microenvironment in genomic instability of malignant tumors. *Frontiers in Genetics* **10**, (2019).
303. Caro, P. *et al.* Metabolic Signatures Uncover Distinct Targets in Molecular Subsets of Diffuse Large B Cell Lymphoma. *Cancer Cell* **22**, (2012).
304. Lebleu, V. S. *et al.* PGC-1α mediates mitochondrial biogenesis and oxidative phosphorylation in cancer cells to promote metastasis. *Nature Cell Biology* **16**, (2014).